



HAL
open science

Influence of thermal forces on asteroids populations

Wen-Han Zhou

► **To cite this version:**

Wen-Han Zhou. Influence of thermal forces on asteroids populations. Astrophysics [astro-ph]. Université Côte d'Azur, 2024. English. NNT : 2024COAZ5074 . tel-04902667

HAL Id: tel-04902667

<https://theses.hal.science/tel-04902667v1>

Submitted on 21 Jan 2025

HAL is a multi-disciplinary open access archive for the deposit and dissemination of scientific research documents, whether they are published or not. The documents may come from teaching and research institutions in France or abroad, or from public or private research centers.

L'archive ouverte pluridisciplinaire **HAL**, est destinée au dépôt et à la diffusion de documents scientifiques de niveau recherche, publiés ou non, émanant des établissements d'enseignement et de recherche français ou étrangers, des laboratoires publics ou privés.

UNIVERSITÉ
CÔTE D'AZUR

ÉCOLE DOCTORALE
SCIENCES
FONDAMENTALES
ET APPLIQUÉES

$$\rho \left(\frac{\partial v}{\partial t} + v \cdot \nabla v \right) = -\nabla p + \nabla \cdot T + f$$

$$e^{i\pi} + 1 = 0$$

THÈSE DE DOCTORAT

Influence des forces thermiques sur les populations d'astéroïdes

Wen-Han ZHOU

Laboratoire J.-L. Lagrange · Observatoire de la Côte d'Azur

**Présentée en vue de l'obtention
du grade de docteur en Sciences de la
Planète et de l'Univers
d'Université Côte d'Azur**

Dirigée par : Patrick Michel
Soutenue le : 10 Décembre, 2024

Devant le jury, composé de :
Alessandro Rossi, Professeur, IFAC-CNR,
Florence, Italy
Stefania Soldini, Professeure Agrégé,
University of Liverpool, UK
Paolo Tanga, Astronome, Observatoire de
la Côte d'Azur, Nice, France
Federica Spoto, Professeure Agrégé,
Harvard University, Boston, USA
Patrick Michel, Directeur de recherche,
Université Côte d'Azur, Nice, France

Influence des forces thermiques sur les populations d'astéroïdes

Influence of thermal forces on asteroids populations

Directeur

Patrick Michel

Directeur de recherche, Université Côte d'Azur, Nice, France

Rapporteurs

Alessandro Rossi

Professeur, IFAC-CNR, Florence, Italy

Stefania Soldini

Associate Professor, Department of Mechanical & Aerospace Engineering, University of Liverpool, Liverpool, UK

Examineurs

Paolo Tanga

Astronome, Observatoire de la Côte d'Azur, Nice, France

Federica Spoto

Associate Professor Harvard-Smithsonian Center for Astrophysics, Harvard University, Boston, USA

Dedicated to the loving memory of Qi-Chu Zhou.

1942 – 2024

RESUMÉ Les astéroïdes sont des planétésimaux rocheux résiduels qui n'ont pas réussi à former des planètes et ont subi une évolution collisionnelle subséquente. L'étude des astéroïdes est cruciale pour comprendre des problèmes fondamentaux tels que la formation, l'évolution et l'origine de la vie dans notre système solaire et les systèmes exoplanétaires.

Après l'élimination du gaz du disque protoplanétaire et les instabilités subséquentes des planètes géantes, les astéroïdes de la ceinture principale (MBA) se stabilisent à leur emplacement actuel. Une petite fraction des astéroïdes de la ceinture principale est transportée de façon continue vers l'orbite terrestre, formant une population appelée la population des astéroïdes géocroiseurs (NEA). Elle suscite beaucoup d'attention en raison de son histoire passée et de la menace future d'un impact sur notre planète. Les principaux mécanismes dynamiques qui façonnent la ceinture d'astéroïdes moderne et qui contribuent à leur transport vers la région proche de la Terre incluent les collisions, l'interaction planétaire et les effets thermiques, à savoir les effets Yarkovsky et YORP. Ces effets thermiques sont le sujet central de cette thèse.

L'effet Yarkovsky est la force radiative produite par le rayonnement thermique du côté après-midi d'un objet en rotation en orbite autour du Soleil. Cet effet sur un objet unique a été bien décrit mathématiquement à la fin du siècle dernier. Cependant, son rôle sur un système d'astéroïdes binaire n'a pas été complètement compris et est souvent négligé. Dans cette thèse, je construis un cadre théorique de base pour l'effet « Yarkovsky binaire ». Le principe de l'effet Yarkovsky binaire est de faire migrer à la fois le composant primaire et secondaire vers l'orbite synchrone où la période de rotation est égale à la période orbitale mutuelle. Nous proposons que l'effet Yarkovsky binaire sur l'astéroïde secondaire (BYS) est le principal mécanisme de synchronisation des astéroïdes secondaires, et que l'effet Yarkovsky binaire sur l'astéroïde primaire (BYP) continue de réduire les orbites de la plupart des astéroïdes binaires découverts. Les futures recherches sur l'évolution à long terme des systèmes binaires devraient prendre en compte le BYP et le BYS.

L'effet YORP est le couple radiatif produit par le rayonnement thermique provenant de la surface irrégulière des astéroïdes. Il gouverne l'évolution de la rotation des petits astéroïdes. Les récentes études photométriques de la mission Gaia, ont trouvé un groupe excessif de rotateurs lents et un fossé les séparant des rotateurs plus rapides, inexpliqué par les théories actuelles. J'ai développé un modèle d'évolution de la rotation des astéroïdes capable de reproduire la distribution observée, tenant compte de l'effet YORP, des collisions et des effets d'amortissement du frottement interne. Ce modèle suggère que cette distribution est régulée par la compétition entre les collisions et l'amortissement du frottement interne des « basculeurs » - des astéroïdes avec des vecteurs de rotation instables, et que le groupe des rotateurs lents est principalement peuplé de basculeurs. Nous contraignons le produit de la rigidité et du facteur de qualité, qui se rapporte à la viscosité du corps, à 4×10^9 Pa. Ce nombre, deux ordres de grandeur plus petit que celui supposé pour les blocs monolithiques, implique que les astéroïdes dont la structure est en agrégat pourraient subir des effets de marée plus forts que ce que l'on pensait auparavant en raison de leur porosité et de leur couche de régolithe.

Un autre problème lié à l'effet YORP concerne sa sensibilité aux structures de surface telles que les cratères d'impact. Le couple YORP d'un astéroïde change fréquemment en raison des collisions, rendant difficile l'étude de l'évolution à long terme de la rotation. Dans le but de résoudre ce problème, j'ai développé des solutions analytiques, vérifiées par des solutions numériques, pour les couples YORP induits par les cratères, qui seront utilisés pour étudier le comportement de marche aléatoire de la rotation des astéroïdes à l'avenir.

Mots clés astéroïdes · dynamique · effets thermiques

ABSTRACT Asteroids are rocky leftover planetesimals that failed to form planets and experienced subsequent collisional evolution. Most of the asteroids are distributed in the so-called "Main Belt" located from 2.1 to 3.2 astronomical units (au). Studying asteroids is crucial to understand fundamental problems such as the formation, evolution and life origin of our Solar system and exoplanetary systems.

After the gas depletion of the protoplanetary disk and the subsequent giant planet instabilities, Main belt asteroids (MBAs) settle down at their modern location. A small fraction of MBAs is continuously delivered to the near Earth orbit, forming a population called near-Earth asteroids (NEAs) that gain a lot of attention due to their previous history and future threat of impacting our planet. Major dynamical mechanisms shaping the modern asteroid belt and the delivery to the near-Earth space include collisions, planetary interaction and thermal effects, namely the Yarkovsky and YORP effects. These thermal effects are the focus of this thesis.

The Yarkovsky effect is the radiative force produced by the thermal radiation in the afternoon side of a spinning object that orbits around the Sun. This effect on a single object has been well described mathematically in the end of the last century. However, its role on a binary asteroid system was not completely understood and often overlooked. In this thesis, I build a basic theoretical framework for the "Binary Yarkovsky" effect. The principle of the Binary Yarkovsky effect is to migrate both the primary and secondary components towards the synchronous orbit where the spin period equals the mutual orbital period. We propose that the Binary Yarkovsky effect on the secondary asteroid (BYS) is the major mechanism to synchronise the secondary asteroids, and Binary Yarkovsky effect on the primary asteroid (BYP) is still shrinking the orbits of most discovered binary asteroids. Future investigation on the long-term evolution of binaries should take BYP and BYS into account.

The YORP effect is the radiative torque produced by the thermal radiation from the irregular surface of asteroids. It governs the rotational evolution of small asteroids. Recent photometric surveys from the Gaia mission, allowing observation of long-period asteroids, found an excessive group of slow rotators and a gap separating them from faster rotators, which is unexplained by current theories. I developed an asteroid rotational evolution model capable of reproducing the observed distribution, accounting for the YORP effect, collisions and internal friction damping effects. The model suggests that this distribution is regulated by the competition between collisions and internal friction dampening of "tumblers" -asteroids with unstable rotation vectors, and that the slow rotator group of asteroids is mainly populated by tumblers. We constrain the product of the rigidity and quality factor, which relates to the body's viscosity, to 4×10^9 Pa. This number, two orders of magnitude smaller than the one assumed for monolithic boulders, implies that rubble pile asteroids could undergo stronger tidal effects than previously thought due to a porous structure and regolith layer.

Another puzzle of the YORP effect relates to its sensitivity to the surface structures such as impact craters. The YORP torque of an asteroid frequently changes due to collisions, making it difficult to study its long-term rotational evolution. As an attempt to solve this problem, I developed analytical solutions, verified by numerical solutions, for crater-induced YORP torques, which will be used to study the random-walk behaviour of asteroids' rotation in the future.

Keywords asteroids · dynamics · thermal effects

ACKNOWLEDGEMENTS

About 3 years ago, finishing my master's degree at the University of Hong Kong, I was looking for Ph.D. opportunities. Thanks to the introduction of Yun Zhang, a postdoc at Observatoire de la Côte d'Azur at that time, Patrick Michel kindly agreed to be my Ph.D. supervisor in Nice. Since then, Patrick has given me invaluable support at each step of my career. Patrick's insightful feedback, patience, and expertise have been invaluable in shaping my work and helping me grow both academically and personally. It has been an enormous privilege working with him these past years.

During my Ph.D, I had the incredible opportunity to communicate with researchers in Nice. Each of them is a great master in their field. In particular, I am very honored to be part of the TOP team and appreciate every team member. In particular, I would like to thank Alessandro Morbidelli and other permanent members in the team for their patience in discussing with me and offering help. I would like to give a special thanks to Marco Delbo, a great expert in the thermal modeling of asteroids, not only because of his kind treat of pizza, but also his constantly warm-hearted support for early-career students like me. Without Marco, I could not have achieved what I have. I would like to thank my collaborators in the team: Harrison Agrusa, who generously offers valuable suggestions on our work, and Bin Ren, who offers great help in science and beyond (including the chance to pet his cat). I would like to thank Julia Maia for providing me with the template of this PhD thesis. Last but not least, I would like to thank the chef Khaled's team in the OCA canteen, who offers delicious food, motivating me a lot to work at the observatory. Everything that happened during these three years will remain a precious memory in my life.

A heartfelt appreciation goes out to my awesome thesis committee. First, I must thank Alessandro Rossi and Stefania Soldini for the thoughtful reviews of my thesis manuscripts. I am also very grateful to Federica Spoto who discussed with me on the asteroid family evolution.

Lastly, I would like to thank my family and friends for the love and support during my long spatial and temporal journey towards my Ph.D. degree.

CONTENTS

| | | |
|------------|--|-----------|
| I | INTRODUCTION | 1 |
| 1 | INTRODUCTION | 3 |
| 1.1 | Observation features of asteroids | 3 |
| 1.1.1 | Size-frequency distribution (SFD) | 3 |
| 1.1.2 | Spectroscopic classes | 4 |
| 1.1.3 | Orbital elements | 4 |
| 1.1.4 | Spin distribution | 5 |
| 1.2 | Origin and long-term evolution | 5 |
| 1.3 | Yarkovsky effect | 7 |
| 1.3.1 | Mechanism | 7 |
| 1.3.2 | Detection | 9 |
| 1.3.3 | Application | 10 |
| 1.3.4 | Unsolved Issues | 11 |
| 1.4 | YORP effect and rotational evolution | 11 |
| 1.4.1 | Mechanism | 11 |
| 1.4.2 | Detection | 13 |
| 1.4.3 | Application | 13 |
| 1.4.4 | Unsolved Issues | 14 |
| II | YARKOVSKY EFFECT AND ORBITAL EVOLUTION | 17 |
| 2 | BINARY YARKOVSKY EFFECT ON THE SECONDARY ASTEROID | 19 |
| 3 | BINARY YARKOVSKY EFFECT ON THE PRIMARY ASTEROID | 31 |
| III | YORP EFFECT AND ROTATIONAL EVOLUTION | 39 |
| 4 | A ROTATIONAL EVOLUTION MODEL EXPLAINING THE OBSERVED SPIN DISTRIBUTION | 41 |
| 5 | CRATER-INDUCED YORP EFFECT WITH ZERO THERMAL INERTIA | 63 |
| 6 | CRATER-INDUCED YORP EFFECT WITH FINITE THERMAL INERTIA | 77 |
| IV | CONCLUSION AND PROSPECTS | 91 |
| 7 | CONCLUSIONS AND PROSPECTS | 93 |
| | BIBLIOGRAPHY | 95 |

Part I

INTRODUCTION

INTRODUCTION

Asteroids are rocky leftover planetesimals that failed to form planets and subsequently experienced collisional evolution. Most of the asteroids are distributed in the so-called “Main Belt” located from 2.1 to 3.2 astronomical units (au). The total mass of main belt asteroids (MBAs) is roughly 0.045 % of Earth mass (Krasinsky et al., 2002; Somenzi et al., 2010; Kuchynka and Folkner, 2013), with most of the mass concentrated in a few large asteroids like 1 Ceres, 2 Pallas and 4 Vesta. A small fraction of asteroids are delivered to orbits intersecting with Earth’s orbit, forming Near-Earth Asteroids (NEAs).

This thesis focuses on the Yarkovsky and YORP effects, both of which are caused by radiative force, on the long-term evolution of main belt asteroids. By briefly introducing the observational features of the current main belt asteroids in Sec. 1.1 and the origin and history of asteroids in Sec. 1.2, we will have a basic idea of what roles the Yarkovsky and YORP effect are playing during the evolution of asteroids and how they help people understand the Solar system history and possible evolution of exo-planetary systems. We then review the current knowledge of Yarkovsky and YORP in Sec. 1.3 and Sec. 1.4, respectively, which leads to the major part of this thesis in the following chapters that try to answer the unsolved problems in the field. Chapters 2 and 3 will concentrate on the Yarkovsky effect and Chapters 4, 5 and 6 will concentrate on the YORP effect

1.1 OBSERVATION FEATURES OF ASTEROIDS

Major observational features can be summarized below.

1.1.1 *Size-frequency distribution (SFD)*

For asteroids without sufficient thermal infrared emission data, the size of asteroids is inferred from the absolute magnitudes

$$D = 1329 \frac{10^{-H/5}}{\sqrt{p_V}} \text{ km} \quad (1.1)$$

Here D is the diameter, H is the absolute magnitude, a measure of an asteroid’s brightness, and p_V is the visual geometric albedo, defined as the proportion of total incoming power reflected to the source direction when accounting for the visible wavelength.

A typical SFD of debris disks is characterized by a power law:

$$N_{>D} \sim D^\alpha \quad (1.2)$$

where $N_{>D}$ is the cumulative number of asteroids with a diameter larger than D . For collision-dominating debris disks, $\alpha = -2.5$ (Dohnanyi, 1969; Wyatt et al., 2011). Observation reports a broken power law for MBAs: $\alpha = -2.6$ for $D \leq 0.1$ km, $\alpha = -1.3$ for $0.2 \text{ km} \leq D \leq 5 \text{ km}$, and $\alpha = -3$ for $5 \text{ km} \leq D \leq 40 \text{ km}$ (Cheng, 2004; Bottke et al., 2005; Bottke et al., 2020; Heinze et al., 2019). This wavy distribution is speculated to result from the size-dependent strength of asteroids and the size distribution of collisional fragments (Bottke et al., 2005). The steeper slope in the range $D > 100$ km and the elbow at $D \sim 130$ km are considered as the primordial distribution of planetesimals (Morbidelli et al., 2009).

1.1.2 Spectroscopic classes

In general, asteroids are spectroscopically classified to C-type, which is carbonaceous and has a low albedo, S-type which is silicate-rich and has a higher albedo, and M-type which is metal-rich and has moderately high albedos (DeMeo2019; Tholen, 1984; Mahlke et al., 2022). C-type asteroids contain primitive materials that are less thermal altered. S-type asteroids are more evolved than C-types, having undergone processes such as differentiation. This suggests that they may be fragments of larger bodies that once had molten interiors. M-type asteroids are believed to be the remnants of the metallic cores of larger differentiated bodies that were shattered by collisions.

The composition of asteroids shows dependence on the distance to the Sun (e.g. see Fig. 3 in DeMeo and Carry, 2014). S-type asteroids are dominating at the inner main belt (2.2 - 2.5 au), while the central main belt (2.5 - 3.2 au) is dominated by C-types asteroids. Farther regions are dominated by P-type and D-type asteroids, which are similar to the spectra of comet nuclei. This spatial trend is considered to result from the thermal gradient in the protoplanetary disk where planetesimals formed. However, there is a mixing of different types of asteroids in the semi-major axis, implying a complicated dynamical evolution in the past. The early migration of giant planets could be an answer to this mixing, while the timing of the giant planet instability is yet determined (Walsh et al., 2011; Morbidelli et al., 2015).

1.1.3 Orbital elements

The semimajor axes of main belt asteroids are mainly distributed from 2.1 to 3.2 au. The inner edge is related to the secular resonance between the precession frequency of the perihelion of asteroids and the g_6 planetary frequency. The outer edge is related to the 2:1 mean motion resonance with Jupiter. There are several gaps located at 2.5, 2.8 au, namely Kirkwood gaps where asteroids are depleted, which separate the main belt to the inner belt, middle belt and outer belt.

Their eccentricities range from 0 to 0.3 and inclinations range from 0 to 33 degrees. This indicates an excitation process in the past since the planetesimals are considered to form in circular and co-planar orbits (Johansen et al., 2015; Morbidelli et al., 2015).

1.1.4 Spin distribution

The spin rate of large asteroids (e.g. the radius $R > 50$ km) basically follows a Maxwell distribution with the peak corresponding to a period of ~ 6 hours (Pravec and Harris, 2000). Observation on asteroids larger than 1 km shows an upper limit of the spin rate corresponding to a rotational period of ~ 2.2 hours for asteroids, beyond which the centrifugal forces will overcome the self-gravity and therefore lead to rotational disruption. This spin limit can be well described by

$$P_{\min} = \sqrt{\frac{3\pi}{\rho G}} = 3.3\rho^{-1/2} \text{ h} \quad (1.3)$$

according to Pravec and Harris (2000). Here G is the gravitational constant and ρ is the bulk density of asteroids. This is seen as evidence of a rubble pile structure instead of a monolithic structure. For asteroids smaller than 1 km, there are fast rotators whose spin rate exceeds the above spin limit, indicating a monolithic structure with internal cohesion > 1 kPa (Hu et al., 2021).

For small main belt asteroids (range from 1 km to 50 km), two observational features are distinguishable: the excess of fast rotators (e.g. period $P < 3$ hours) and the excess of the slow rotators (e.g. period $P > 1$ day) (Pravec and Harris, 2000). The former is considered to arise from the accumulation of asteroids near the spin limit, which could avoid destruction by mass shedding and maintain a relatively fast rotation, when it starts to spin faster than the spin limit (Zhang18). The excess of slow rotators still lacks a well-recognized explanation. Recent observations by Gaia have shown that, in the period-diameter diagram of main belt asteroids, there is a visible gap separating the slow rotators from the faster ones, which makes the problem even more complicated (Ďurech and Hanuš, 2023).

1.2 ORIGIN AND LONG-TERM EVOLUTION

Theories that attempt to decipher the history of main belt asteroids have to be subject to the observational features above. Planetesimals, the progenitors of asteroids, can grow up to 10^3 km in the protoplanetary disk due to accreting collisions and self-gravity. They form in the concentrated region of the dust where the gas-particle instabilities such as the streaming instability can be triggered (Youdin and Goodman, 2005). Theoretically, there are a few barriers such as the bouncing barrier, fragmentation barrier and radial drift barrier that

prevent dust grains from growing (Brauer et al., 2008; Zsom et al., 2010; Birnstiel et al., 2010), but some "lucky" particles step over these barriers and become sufficiently massive to accrete particles for further growth (Windmark et al., 2012). The typical born size of planetesimals is as large as > 100 km, inferred from the modern SFD of asteroids (Morbidelli et al., 2009).

Planetesimals formed in the different regions of the protoplanetary disk gathered somehow in the location of the modern asteroid belt, as speculated from the diversity of the spectra types of asteroids. Several mechanisms have been proposed for such dynamic mixing, such as the "grand tack" model (Walsh et al., 2011; Raymond et al., 2014; Deienno et al., 2019) and low-mass asteroid belt model (Raymond 2017; Izidoro et al., 2022).

In the "grand tack" model, initial S-type asteroids formed within Jupiter and C-type asteroids formed beyond the ancient Saturn. Jupiter migrated inward to 1.5 au due to its interaction with the disk, scattering S-type asteroids outward. During this process, Saturn grew and migrated inward to a mean motion resonance. Then the Jupiter-Saturn pair started to move outwards, scattering back some S-type and C-type asteroids. This process will deplete 99.7% mass of the initial asteroid belt objects, explaining the low mass of the current asteroid belt. The distribution of the orbital eccentricity and the inclination of the giant planets' migration are consistent with excited current ones.

In the scenario of an initial low-mass asteroid belt model, planets form in narrow rings, and the asteroids are implanted from both the terrestrial planet-forming and giant planet regions after gas depletion (Bottke et al., 2006; Raymond and Izidoro, 2017a,b). The narrow dust ring was observed in HL Tau's disk. In the model, planetesimals are scattered by planetary embryos to the current asteroid belt, and are subsequently damped by Kozai resonance in the mean motion resonance with Jupiter or scattering by pass-by embryos.

Around 60-100 Myr after gas depletion (Avdellidou et al., 2024), the asteroid belt is likely affected by the orbital instability of giant planets driven by their interaction with a massive disk of planetesimals located from a few au beyond the original orbit of Neptune to about ~ 30 au. This is also called "Nice model" as it was proposed and developed by researchers in Nice, France. In the process of the outer migration of icy planets, some outer planetesimals in the outer belt are scattered into the asteroid belt, explaining the existence of D-type and P-type asteroids.

After the giant planet instabilities, the asteroid belt evolves mainly under collisions, planetary interactions such as mean motion resonance and secular resonance, and thermal effects (Morbidelli et al., 2015). Destructive collisions shape the size frequency distribution into an equilibrium state called the collisional cascade, in which the rate

of removal for objects with an arbitrary size due to destructive impact equals the rate of generation for objects with that size due to the destruction of larger asteroids. Fresh collisional fragments could be responsible for Q-type asteroids (Binzel et al., 2004). Collisional fragments from the same parent body are called "asteroid families". The newly born family members are confined in an ellipse in the orbital element spaces (e.g. a - e space and a - i) and go through diffusion under the Yarkovsky effect (Bottke et al., 2001), which is a radiative force produced by the thermal radiation in the afternoon side of a spinning object that orbits around the Sun (Bottke Jr et al., 2006). Once the asteroid migrates across the resonance zone with giant planets, its eccentricity increases. Some of them could have close encounters with planets and be subsequently delivered to near-Earth asteroids (NEAs) (Farinella et al., 1998; Morbidelli and Vokrouhlický, 2003), which are considered to be the reason for the extinction of dinosaurs and still hold potential risks impacting our planet. The rotational evolution of small objects ($R < 50$ km) is dominated by the YORP effect, which is the radiative torque produced by the thermal radiation from the irregular surface of asteroids. Larger objects are mainly affected by mutual collisions. The YORP effect and collisions can either spin up or down the objects, although the preferred direction is not yet well understood (Vokrouhlický and Čapek, 2002).

This thesis deals with the last stage of evolution with a focus on the Yarkovsky and YORP effects, which will be given a more detailed introduction below.

1.3 YARKOVSKY EFFECT

The Yarkovsky effect is named after Ivan Osipovich Yarkovsky, a Polish engineer and scientist. He claimed that the planet could be accelerated by the recoil force caused by the hottest aether in the afternoon side, although the aether was proven not to exist later. Though his theories about the ether were mistaken, his concept of heat-driven acceleration was rediscovered in the 1950s by Opik and Radzievskii.

1.3.1 *Mechanism*

The Yarkovsky effect is composed of the diurnal component and the seasonal effect, which are caused by the spin and orbital motions, respectively.

DIURNAL EFFECT When a rotating asteroid absorbs sunlight, the surface heats up and re-radiates the energy later when it is facing away from the Sun. For prograde rotators (rotating in the same direction as their orbit), this leads to a net force that increases the semimajor axis of their orbit, causing them to slowly drift outward

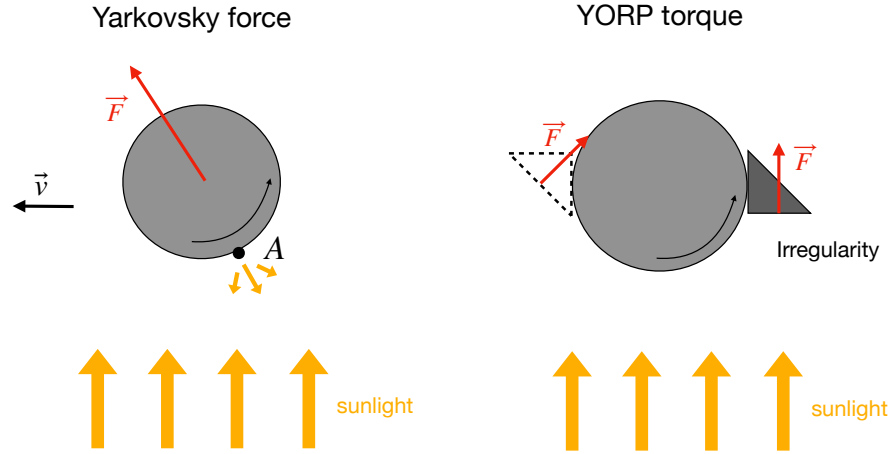


Figure 1.1: Schematics of the diurnal Yarkovsky and YORP effects where the radiative forces are denoted by the red arrows. Left: the asteroid is in the prograde rotation where its spin vector aligns with the orbital vector. The recoil force, represented by the hottest region in the afternoon side, accelerates the asteroid and therefore expands the orbit. Right: The irregularity of the asteroid is represented by the solid triangle. The dashed triangle denotes the orientation after half of the spin period. The radiative torque on the triangle over the spin period cannot cancel by itself and leads to a net torque that secularly modifies the rotation.

from the Sun. In contrast, retrograde rotators (rotating in the opposite direction) experience an inward drift as the thermal re-radiation decelerates their orbit. The illustration is shown in Fig. 1.1.

SEASONAL EFFECT The seasonal effect arises because different hemispheres of the asteroid are illuminated at different times during its orbit. When the asteroid is closest to the Sun, the illuminated hemisphere absorbs more heat and later re-emits it, causing a net force that affects the orbit's semimajor axis. Unlike the diurnal effect, the seasonal effect is always directed inward, causing a decrease in the semimajor axis regardless of the asteroid's rotation direction.

The Yarkovsky effect is affected by several factors such as the size, thermal inertia, spin rate and obliquity. The steps of solving the induced orbital drift rate are listed below.

HEAT CONDUCTION EQUATIONS The temperature T for the surface and the layer beneath is governed by

$$\frac{\partial T}{\partial t} = \frac{\kappa}{C\rho} \frac{\partial^2 T}{\partial z^2}, \quad (1.4)$$

with two boundary conditions,

$$\kappa \frac{\partial T}{\partial z} \Big|_{z=0} = E(t) - e\sigma T^4 \Big|_{z=0}, \quad (1.5)$$

$$\kappa \frac{\partial T}{\partial z} \Big|_{z \rightarrow \infty} = 0, \quad (1.6)$$

where t is the time, κ is the thermal conductivity, C is the specific heat capacity, ρ is the bulk density of the asteroid, e is the emissivity and σ is the Stefan-Boltzmann constant. These equations can be solved by the numerical approach or the analytical approach (with several assumptions) with details shown in Chapter 5 and 6.

RADIATIVE FORCE The radiative force for a surface element dS is

$$d\vec{f} = -\frac{2e\sigma}{3c} T^4 dS \vec{n} \quad (1.7)$$

with c being the light speed and \vec{n} is the normal vector of the surface element dS . The total force of the whole body is

$$\vec{F} = -\frac{2e\sigma}{3c} \int T^4 \vec{n} dS. \quad (1.8)$$

ORBITAL DRIFT RATE The secular orbital drift is caused by the transverse component of the force \vec{F} . Assuming a circular orbit, the orbital drift rate is

$$\dot{a} = \frac{2\vec{F} \cdot \vec{v}}{m\dot{n}}. \quad (1.9)$$

Here m and \dot{n} are the mass and the mean motion rate of the objects, respectively. For a spherical object, the solution is

$$\dot{a}_d = \frac{8 \cos \epsilon \Phi (1 - A) \pi r^2}{9\dot{n}} \frac{\Theta_\omega}{mc} \frac{1}{2 + 2\Theta_\omega + \Theta_\omega^2} \quad (1.10)$$

for the diurnal component and

$$\dot{a}_s = -\frac{4 \sin^2 \epsilon \Phi (1 - A) \pi r^2}{9\dot{n}} \frac{\Theta_n}{mc} \frac{1}{2 + 2\Theta_n + \Theta_n^2} \quad (1.11)$$

for the seasonal component. The Yarkovsky effect is exceedingly small, producing an orbital drifting rate of 10^{-5} au/Myr for km-sized objects in the main belt.

1.3.2 Detection

This tiny force can cause measurable changes in an asteroid's orbit over the long term. Detecting this effect requires precise tracking of an asteroid's position over extended periods, often through a combination of optical observations and radar ranging.

The first definitive detection of the Yarkovsky effect was made for the near-Earth asteroid (6489) Golevka (Chesley et al., 2003). This detection was possible due to radar observations made in 1991, 1995, and 2003, which allowed scientists to measure a deviation in Golevka's orbit from what was predicted by gravitational forces alone. The difference in the asteroid's position—about 15 kilometers—could be explained by the Yarkovsky effect.

Since then, more asteroids (~ 100) have shown evidence of Yarkovsky-induced drift (Vokrouhlický et al., 2015). To quantify the Yarkovsky effect on an asteroid, astronomers typically introduce a parameter A_2 , which represents the non-gravitational transverse acceleration. In cases where the Yarkovsky effect is detected, it becomes possible to infer additional properties about the asteroid, such as its density, thermal conductivity, and spin state, as revealed above.

1.3.3 *Application*

DELIVERY OF ASTEROIDS FROM THE MAIN BELT TO NEAR-EARTH SPACE One of the most critical applications of the Yarkovsky effect within the asteroid belt is its ability to deliver asteroids from the main belt into resonances that can push them toward near-Earth space. When an asteroid's semimajor axis changes due to this effect, it can eventually reach a mean-motion resonance or secular resonance with one of the giant planets, particularly Jupiter or Saturn. Once an asteroid enters one of these resonances, its orbit can become chaotic, increasing the probability of close encounters with terrestrial planets and ejection from the main belt, becoming a near-Earth object (NEO). This process is a major source of NEOs, which has been confirmed by the consistency of the simulation with the observed excess of retrograde rotators in NEAs.

ASTEROID FAMILIES Asteroid families are groups of asteroids that have formed from the fragmentation of a larger parent body. The Yarkovsky effect is responsible for spreading the members of an asteroid family over time, particularly in terms of their semimajor axes. After the initial collisional event that creates an asteroid family, the smallest fragments experience the strongest Yarkovsky drift, which causes them to spread more rapidly than the larger bodies. This dispersing effect, decreasing with the size, forms a near V-shape distribution in the diagram of $1/D$ versus a , with the center around the parent body and the slope of the edge denoting the family age (Vokrouhlický et al., 2006). A few old asteroid families have been identified using this method (Delbo' et al., 2017).

1.3.4 *Unsolved Issues*

While the Yarkovsky effect is well described by the equations shown above and has many successful applications on main-belt asteroids, there are a few unsolved issues.

CHAOTIC ROTATION STATE While idealized models often assume that asteroids are in principal axis rotation, some asteroids, especially those with slow spin rates, are in non-principal axis rotation, namely tumbling. This tumbling motion, which can not be described by a single period, introduces additional complexities in analytical and numerical calculation (Vokrouhlicky et al., 2015).

BINARY ASTEROIDS The Yarkovsky effect on a binary asteroid was not well understood although it was realized about twenty years ago. The problem will be addressed in Chapters 2 and 3.

STOCHASTIC BEHAVIOR The Yarkovsky effect depends on the asteroid's rotational state, which however undergoes a random walk due to collisions and YORP. Therefore, the Yarkovsky effect should also behave stochastically. This problem has not been addressed completely, but the situation has been improved as will be discussed in Chapter 5 and 6.

1.4 YORP EFFECT AND ROTATIONAL EVOLUTION

The Yarkovsky–O'Keefe–Radzievskii–Paddack (YORP) effect is introduced by David Rubincam (Rubincam, 2000), named after four important contributors to the concepts behind. Ivan Yarkovsky proposed the radiative force described in the last section, Vladimir Radzievskii proposed the force could lead to a torque when considering variations in albedo, Stephen Paddack, along with John O'Keefe, stated that the irregular shape is an important factor and the induced torque could apply to small asymmetric dust. The YORP effect became an important theoretical concept for asteroids by the early 2000s, advanced by David Rubincam.

1.4.1 *Mechanism*

The modern view of the YORP effect is the net radiative torque produced by the emitted thermal photons from the irregular surface, over the characteristic period (e.g. the orbital period and the spin period for asteroids), as illustrated in Fig. 1.1. A common confusion is that the YORP torque is produced by the incident solar photons. This was proved not to exert a net torque after averaging over the orbit (Breiter et al., 2007).

The YORP torque is composed of two components: the spin component that modifies the spin rate and the obliquity component that modifies the obliquity. The object is usually assumed to be in the principal axis rotation (e.g. rotation around its shortest or longest axis). The spin component does not depend on the thermal inertia, a parameter measuring the delay between the photon absorption and emission in the thermal wavelengths. On the contrary, the obliquity component depends on the thermal inertia. The YORP theory predicts that asteroids could spin up or down with equal probabilities in the case of non-zero thermal inertia and will prefer to spin down in the case of zero thermal inertia (Vokrouhlický and Čapek, 2002; Čapek and Vokrouhlický, 2004). However, this has not yet been demonstrated by statistical results from observation. In addition, according to the theory, the YORP effect drives asteroids towards asymptotic obliquities related to the shape of individual asteroids, with the most common asymptotic obliquities being 0° , 90° and 180° .

The procedures to calculate the YORP torque are listed below.

HEAT CONDUCTION EQUATION This is the same as described in Sec. 1.3.1.

RADIATIVE TORQUE The radiative force $d\vec{f}$ is calculated the same as described in Sec. 1.3.1. Then induced radiative torque of the whole body is

$$\vec{T}_{\text{YORP}} = -\frac{2\epsilon\sigma}{3c} \int T^4 \vec{n} \times \vec{r} dS. \quad (1.12)$$

Here \vec{r} is the position vector of the surface element dS . The torque is then required to be averaged over the spin period and orbital period. Symmetric shapes like spheres or ellipsoids are proven to result in a zero YORP torque. Therefore, the essence of the YORP effect is the irregular shape of the object, which requires accessing the YORP torque by the numerical approach

$$\vec{T}_{\text{YORP}} = -\frac{2\epsilon\sigma}{3c} \sum T_i^4 \vec{n}_i \times \vec{r}_i \Delta S_i. \quad (1.13)$$

More details will be shown in Chapter 5 and 6. Normally the timescale for the YORP torque (i.e. the time to change the same angular momentum as the initial one) is

$$\tau_{\text{YORP}} \simeq 1 \text{ Myr} \left(\frac{R}{1 \text{ km}} \right)^2 \left(\frac{8 \text{ h}}{P} \right) \left(\frac{a_h}{1 \text{ au}} \right)^2. \quad (1.14)$$

However, we should note this timescale is estimated with the assumption of a constant shape, which actually evolves over time. The YORP effect not only depends on the global shape, but is also subject to the fine surface structure. The effect YORP timescale is yet unknown

due to the frequent change of the YORP torque over the collisional history.

While the normal YORP effect focuses primarily on how an asteroid's overall shape causes asymmetric absorption and re-radiation of sunlight, the tangential YORP (TYORP) effect introduces an additional layer of complexity by considering how solar radiation interacts with small surface features like boulders, ridges, and slopes. The TYORP effect arises from heat conduction across boulders. The heat conduction between the eastern and western sides of the boulder in the morning is larger than that in the afternoon, leading to a weaker thermal emission. Therefore, the afternoon-illuminated side of the boulder will dominate, leading to a positive net radiative torque.

The TYORP effect could be used to study the effect of roughness on the total YORP torque (Golubov and Krugly, 2012). However, the shadow and self-heating effect induced by the surface roughness is also proven important but not included in the TYORP effect (Golubov and Lipatova, 2022). In Chapter 5 and 6, I develop a semi-analytical method to account for this crater-induced YORP (CYORP) effect.

1.4.2 *Detection*

The first observational evidence of the YORP effect came from monitoring asteroid spin rates over time. One of the earliest successful detections was made with the asteroid (54509) YORP (Taylor et al., 2007; Lowry et al., 2007), named after the phenomenon itself. In a series of radar observations conducted between 2001 and 2007, astronomers observed a clear acceleration in its spin rate, consistent with the predictions of theoretical YORP models, both in trend and order of magnitude.

More recent detections of the YORP effect have been made possible by advances in observational techniques and computational modeling. To date, there have been 12 confirmed YORP detections and 2 possible cases (Ďurech et al., 2024). However, an intriguing and puzzling observation is that, despite theoretical predictions suggesting equal probability for spin-up or spin-down, all detected cases thus far have been instances of spin-up.

1.4.3 *Application*

The YORP effect has several key applications in asteroid dynamics and evolution.

OBLIQUITY DISTRIBUTION Asteroids are observed to have a preferred spin vector alignment near 0° and 180° , except for those captured in spin-orbit resonances with giant planets (Vokrouhlický et al.,

2003; Hanuš et al., 2013). This distribution is consistent with the predictions of the YORP effect.

SPIN RATE DISTRIBUTION Asteroids exhibit an excess of fast rotators (with periods near 2.2 hours) and slow rotators (with periods longer than one day). The fast rotators are believed to result from YORP-induced spin-up and subsequent redistribution. However, the presence of slow rotators has not been fully explained by existing theories. Moreover, recent Gaia data have revealed a gap in the period-diameter distribution of main belt asteroids, separating slow rotators from faster ones. Chapter 4 provides a plausible explanation for these mysteries by applying the YORP theory.

TUMBLER DISTRIBUTION Some asteroids exhibit non-principal axis rotations, often attributed to YORP-induced spin-down. Their distribution follows a power law in the period-diameter diagram (Pravec et al., 2005). Although this distribution has not been well explained by previous theories, Chapter 4 explains their distribution by adapting the YORP theory.

SURFACE AND SHAPE EVOLUTION As the YORP effect alters an asteroid's spin rate, it can lead to surface mass movement due to increasing centrifugal forces. This process is believed to contribute to the formation of the "top-shaped" asteroids (Keller et al., 2010; Walsh et al., 2012).

BINARY ASTEROID FORMATION Binary asteroids in the main belt are thought to form through either YORP-induced rotational disruption of small objects (typically less than 10 km in diameter) or collisional disruption of larger objects (Walsh et al., 2008).

1.4.4 *Unsolved Issues*

Unlike the Yarkovsky effect, the YORP mechanism remains poorly understood, primarily due to its sensitivity to an asteroid's global shape and fine surface structures (Breiter et al., 2009; Statler, 2009).

INCONSISTENCY BETWEEN OBSERVED AND THEORETICAL YORP TORQUE Observations report that nearly 100% of detected YORP torques are positive, whereas theoretical predictions suggest only about 50% should be positive (Čapek and Vokrouhlický, 2004; Ďurech et al., 2024). One possible explanation is the contribution of positive TYORP, but the magnitude of this torque and its role in explaining slow rotators remains unclear. Additionally, observational biases may arise from the fact that most detections are of fast rotators, which are more likely to be spinning up toward the spin barrier. Although challeng-

ing, future observations of YORP torques in slow rotators may shed new light on this discrepancy.

CHAOTIC ROTATION STATES The YORP effect on tumbling asteroids is still not well understood. A few studies suggest that tumblers may evolve into stable states where their period and obliquity become fixed (Vokrouhlický et al., 2007a; Breiter and Murawiecka, 2015). However, these studies neglect the role of thermal inertia, which can influence the spin components of tumbling asteroids. Solving this chaotic problem numerically would be computationally expensive. Chapter 4 will explore constraints on this issue through model fitting and observational data.

PRECISE MODELING Due to our limited understanding of how microscopic structures affect the YORP effect, it remains difficult to calculate a precise YORP torque for real asteroids (Breiter et al., 2009). Theoretical models fail to converge as resolution increases. Chapters 5 and 6 aim to address these challenges and enhance our understanding of the YORP effect.

STOCHASTIC BEHAVIOR YORP torques are frequently reset by collisions that create impact craters, leading to a random walk in the spin rate and obliquity of asteroids (Bottke et al., 2015). This long-term stochastic behavior is not well understood, largely because of the complexities in modeling the changes caused by collisions. Chapters 5 and 6 will delve deeper into this issue, aiming to advance our comprehension of these stochastic processes.

Part II

YARKOVSKY EFFECT AND ORBITAL
EVOLUTION

BINARY YARKOVSKY EFFECT ON THE SECONDARY ASTEROID

The Yarkovsky effect on the binary asteroid system was not well understood. It was first realized to have perturbation and secular effects on the Earth-satellite LAGEOS in 1980s. Several authors advanced the theory and extended its application to the binary asteroid and planetary-ring systems (Rubincam, 1982; Milani et al., 1987; Farinella and Vokrouhlický, 1996; Métris et al., 1997; Vokrouhlický et al., 2005; Rubincam, 2006; Vokrouhlický et al., 2007b; Rubincam, 2014). However, this effect was not correctly interpreted and therefore its importance was not recognized.

This chapter explores the Yarkovsky effect on the secondary asteroid (the smaller component in a binary asteroid system) and its implications for long-term evolution. The Binary Yarkovsky effect can be divided into two sub-effects: the planet-Yarkovsky effect and the eclipse-Yarkovsky effect. The former, caused by planetary radiation, is well understood, while the latter, resulting from eclipse-induced perturbations, remains less explored. This chapter demonstrates that the eclipse-Yarkovsky effect dominates in low-inclination cases ¹, whereas the planet-Yarkovsky effect is more significant at higher inclinations.

In this chapter:

- I summarize the principles of the eclipse-Yarkovsky effect, which moves the orbit toward the synchronous state.
- I provide an analytical formula for the Binary Yarkovsky effect, verified by numerical simulations.
- I propose that the Binary Yarkovsky effect could be the primary driver behind the synchronous state of most discovered binary asteroids.
- I discuss its potential influence on the long-term evolutionary paths of binary asteroids.
- I present predicted orbital drift rates for relevant binary asteroids, offering potential tests for future observations.

This paper was published in the peer-reviewed journal *The Astrophysical Journal Letters*.

Author contributions: W.H. Zhou proposed the idea, conducted the analytical analysis and wrote the paper. D. Vokrouhlicky contributed

¹ Inclination refers to the angle between the spin vector and the mutual orbital vector of the secondary asteroid.

to the completion of the idea and the analytical analysis. K. Masanori conducted the numerical verification. H. Agrusa, P. Pravec, M. Delbo, P. Michel contributed to the discussion and the writing of the paper.



The Yarkovsky Effect on the Long-term Evolution of Binary Asteroids

Wen-Han Zhou (周文翰)¹, David Vokrouhlický², Masanori Kanamaru³, Harrison Agrusa¹, Petr Pravec⁴,
Marco Delbo¹, and Patrick Michel^{1,5}

¹ Université Côte d'Azur, Observatoire de la Côte d'Azur, CNRS, Laboratoire Lagrange, Nice, France

² Astronomical Institute, Charles University, V Holešovičkách 2, CZ 18000, Prague 8, Czech Republic

³ Department of Earth and Planetary Science, School of Science, the University of Tokyo, Japan

⁴ Astronomical Institute, Astronomical Institute of Czech Academy, Ondřejov, CZ-25165, Czech Republic

⁵ The University of Tokyo, Department of Systems Innovation, School of Engineering, Tokyo, Japan

Received 2024 April 18; revised 2024 May 16; accepted 2024 May 22; published 2024 June 4

Abstract

We explore the Yarkovsky effect on small binary asteroids. While significant attention has been given to the binary YORP effect, the Yarkovsky effect is often overlooked. We develop an analytical model for the binary Yarkovsky effect, considering both the Yarkovsky–Schach and planetary Yarkovsky components, and verify it against thermophysical numerical simulations. We find that the Yarkovsky force could change the mutual orbit when the asteroid's spin period is unequal to the orbital period. Our analysis predicts new evolutionary paths for binaries. For a prograde asynchronous secondary, the Yarkovsky force will migrate the satellite toward the location of the synchronous orbit on ~ 100 kyr timescales, which could be faster than other synchronization processes such as YORP and tides. For retrograde secondaries, the Yarkovsky force always migrates the secondary outward, which could produce asteroid pairs with opposite spin poles. Satellites spinning faster than the Roche limit orbit period (e.g., from ~ 4 hr to ~ 10 hr) will migrate inward until they disrupt, reshape, or form a contact binary. We also predict a short-lived equilibrium state for asynchronous secondaries where the Yarkovsky force is balanced by tides. We provide calculations of the Yarkovsky-induced drift rate for known asynchronous binaries. If the NASA DART impact broke Dimorphos from synchronous rotation, we predict that Dimorphos's orbit will shrink by $\dot{a} \sim 7$ cm yr⁻¹, which can be measured by the Hera mission. We also speculate that the Yarkovsky force may have synchronized the Dinkinesh–Selam system after a possible merger of Selam's two lobes.

Unified Astronomy Thesaurus concepts: Asteroids (72); Planetary rings (1254); Solar system (1528)

1. Introduction

Binary asteroids are found throughout the solar system at a wide range of size scales. Their formation mechanisms are also diverse. Kilometer-sized systems are generally thought to form by rotational disruption of the primary resulting from radiative torques (e.g., Walsh et al. 2008), large main-belt systems are thought to form by collisions (e.g., Michel et al. 2001; Durda et al. 2004), while binaries in the Kuiper Belt are thought to be primordial, forming directly from the streaming instability (e.g., Nesvorný et al. 2010). This study primarily focuses on \sim kilometer-sized binaries found among both the near-Earth asteroids (NEAs) and main-belt asteroids (MBAs). These systems are small and close enough to the Sun that radiation forces play an important role in their long-term evolution. Understanding their long-term dynamics is crucial to trace back their evolution and estimate their lifetime, which also provides information on the physical properties and geologic structures of asteroids.

It is widely accepted that the long-term dynamics of binaries are dominated by tides and the binary YORP (BYORP) effect, which is a radiative torque that modifies the orbit of the secondary asteroid (Čuk & Burns 2005; Vokrouhlický et al. 2015). Tidal dissipation can drive the secondary either outward or inward, depending on whether

the secondary's mean motion is slower or faster than the primary's spin (Murray & Dermott 1999). The primaries of binary NEAs typically have short rotation periods, in the range of 2.2–4.5 hr (Walsh & Jacobson 2015), which is likely due to the formation of the system by rotational failure (Pravec & Harris 2007). For simplicity, we assume the primary's spin rate always exceeds the secondary's mean motion and that tides will consequently drive the secondary outward. For small eccentricities, the time evolution of the binary semimajor axis can be written as (Murray & Dermott 1999)

$$\dot{a}_t = 3 \frac{k_p m_s}{Q_p m_p} \left(\frac{r_p}{a} \right)^5 n a. \quad (1)$$

Here k_p , Q_p , and m_p are the tidal Love number, quality factor, and mass of the primary, while n , a , and m_s are the mean motion, semimajor axis, and mass of the secondary, respectively. Throughout this manuscript, the subscript “p” denotes the primary, while the subscript “s” denotes the secondary. The nomenclature and symbols are given in Table 2.

While \dot{a}_t decreases dramatically with the semimajor axis ($\dot{a}_t \propto a^{-11/2}$), the drift rate caused by the BYORP effect becomes greater with the increasing semimajor axis (Čuk & Burns 2005; Jacobson & Scheeres 2011; Vokrouhlický et al.

2015). The averaged semimajor axis drift rate under BYORP is

$$\dot{a}_B = \frac{2f_B \mathcal{F}}{n}. \quad (2)$$

Here, f_B is the dimensionless BYORP coefficient that can be positive or negative, depending on the shape and surface morphology of the secondary.⁶ The calculated absolute value of f_B for polyhedron asteroid models shows a large range from 10^{-4} to 10^{-1} (Steinberg et al. 2011) with a typical value of 10^{-3} (Jacobson & Scheeres 2011). The nominal radiation pressure per unit mass \mathcal{F} is defined as

$$\mathcal{F} = \frac{\Phi(1-A)\pi r_s^2}{m_s c}, \quad (3)$$

where $\Phi = 1364 (a_h/\text{au})^{-2} \text{ W m}^{-2}$ is the solar flux, A is the Bond albedo, and c is the speed of light. Here a_h is the heliocentric orbital semimajor axis of the binary system. The BYORP effect could drive the secondary either outward to an unstable orbit, where external gravitational perturbations would finally destroy the binary system (Ćuk 2007), or inward until the secondary gets tidally disrupted or the BYORP effect is balanced by the tidal effect (Jacobson & Scheeres 2011). The theoretical timescale of the BYORP effect for NEAs is short (e.g., $\leq 10^5$ yr; Ćuk & Burns 2005; Ćuk 2007) compared to their dynamical lifetime (e.g., $\sim 10^7$ yr; Gladman et al. 2000), indicating that the observed binary asteroids are either very young or old enough, if they reached a BYORP–tide equilibrium. However, available measurements suggest that binary systems are evolving at much lower rates than predicted by BYORP. The binary asteroid system 1996 FG₃ is observed to have a semimajor axis drift of $-0.07 \pm 0.34 \text{ cm yr}^{-1}$ (Scheirich et al. 2015), which is much lower than the predicted values of 2.3 cm yr^{-1} (Scheirich et al. 2015) or 7 cm yr^{-1} (McMahon & Scheeres 2010) based on the secondary shape model. Similarly, based on an available shape model of the secondary, the binary system 1999 KW₄ has been estimated to have a BYORP drift rate of 6.98 cm yr^{-1} (McMahon & Scheeres 2010) or 8.53 cm yr^{-1} (Scheirich et al. 2021), while observations of the mutual orbit report an outward drift rate of 1.2 cm yr^{-1} corresponding to $f_B \sim 0.00157$ if tides are neglected (Scheirich et al. 2021). The two orbital solutions for the binary system 2001 SL₉ have drift rates of \dot{a} of $-2.8 \pm 0.2 \text{ cm yr}^{-1}$ or $-5.1 \pm 0.2 \text{ cm yr}^{-1}$ corresponding to $f_B = 0.006$ or 0.01 , respectively (Scheirich et al. 2021). Since there is no available shape model for the secondary in 2001 SL₉, a theoretical value of f_B cannot be derived. The observation data of the Didymos–Dimorphos system before the DART impact show a small drifting rate of $-0.08 \pm 0.02 \text{ cm yr}^{-1}$ (Scheirich & Pravec 2022; Naidu et al. 2024; Scheirich et al. 2024).

Several mechanisms have been proposed for weakening the BYORP effect. The BYORP torque can be weakened, or even removed, by either the nonsynchronous state of the satellite (Ćuk & Burns 2005) or its nonprincipal axis rotation (Quillen et al. 2022). Another possibility is a rotational state referred to as the “barrel instability” (Jacobson et al. 2021), in which the

satellite rolls about its longest axis during its orbital motion and its longest axis remains approximately aligned toward the primary (Agrusa et al. 2021). A recent study also suggests that the BYORP coefficient can be reduced by an order of magnitude for satellites like Dimorphos, the secondary of the binary asteroid Didymos, which has an overall “smooth” shape made up of boulders that are all significantly smaller than the size of the body (Ćuk 2023).

In this work, we investigate the Yarkovsky effect that has been largely overlooked in the context of the long-term evolution of binary asteroids. The Yarkovsky effect, which is the radiation force raised on the afternoon side of a rotating object, has been well studied for single asteroids (Vokrouhlický 1998, 1999; Bottke et al. 2006; Vokrouhlický et al. 2015). However, its impact on binary asteroids remains less explored. The Yarkovsky effect on a binary consists of two components: the Yarkovsky–Schach (YS) effect and the planetary Yarkovsky effect. The YS effect is caused by (1) elimination of the satellite irradiation by sunlight when it is located in the primary shadow and (2) the related asymmetric thermal cooling and heating of the secondary after it enters and exits the shadow (in fact, there is also a similar effect on the primary related by the shadow of the secondary, but this produces smaller dynamical perturbation). The YS effect has been studied for Earth satellites (Rubincam 1982, 1987; Milani et al. 1988; Farinella & Vokrouhlický 1996), space debris (Murawiecka & Lemaître 2018), and Saturn’s rings (Rubincam 2006; Vokrouhlický et al. 2007). This effect was noticed for binary asteroids too (Vokrouhlický et al. 2005a) but has not been studied in detail yet. The planetary Yarkovsky effect is simply the Yarkovsky effect caused by the primary’s radiation instead of the Sun (Rubincam 2006; Vokrouhlický et al. 2007).

In this Letter, we describe the binary Yarkovsky effect in Section 2 and discuss its implications on the long-term evolution of binary systems in Section 3. The main results are summarized in Section 4.

2. Theory

2.1. Analytical Model

When the secondary enters the shadow of the primary, its surface temperature drops, leading to a reduced Yarkovsky force. After the secondary exits the shadow of the primary, its temperature increases, restoring the Yarkovsky force level before entering the shadow. However, these two processes are not exactly balanced, resulting in a net perturbation over the orbit that leads to a secular change of a . This is the basis of the YS effect, whose concept is displayed in Figure 1. The necessary condition for the YS effect to operate is therefore that the secondary enters the shadow of the primary. This constrains the inclination i between the orbital plane defined by the secondary motion about the primary and the orbital plane of the binary barycenter about the Sun, $i < r_p/a$, implying that the satellite crosses the shadow in every orbit about the primary. A nonzero inclination could weaken the YS effect as the time fraction in the shadow decreases with the inclination (Murawiecka & Lemaître 2018). However, a larger inclination $i > r_p/a$ will result in only a fraction of the heliocentric orbit where the secondary can undergo an eclipse and therefore lead to a weakened YS effect. In fact, binary systems that have been discovered tend to exhibit a preferred inclination of approximately 0° or 180° (Pravec et al. 2012). Since the YORP effect

⁶ In the literature, the BYORP coefficient is often referred to as B , but we denote it as f_B to maintain consistency with other coefficients in this Letter.

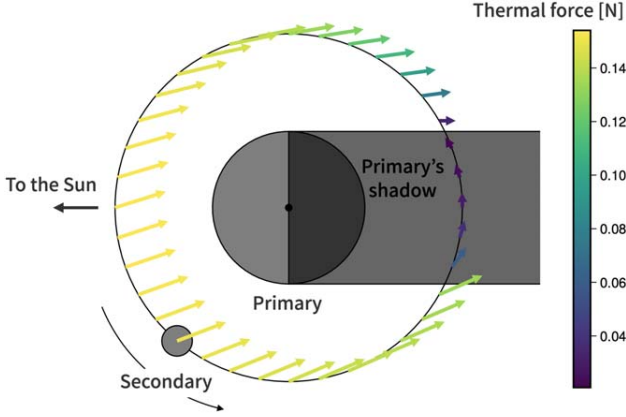


Figure 1. The principle of the YS effect. A binary system consists of a larger primary and a smaller secondary (satellite). The relative orbit is assumed circular, and the satellite has zero obliquity and a rotation synchronous with the motion about the primary; both periods are much smaller than the period of the binary heliocentric motion, such that during one satellite orbit about the primary, the Sun is assumed fixed and in the orbital plane of the satellite. The color-coded arrows attached to the satellite represent its thermal acceleration due to solar irradiation (see also the side bar); the tilt away from the opposite direction to the Sun is due to the satellite thermal inertia. The specific values were computed using the numerical model and binary parameters from Section 2.3. In the absence of the satellite passage through the primary’s shadow, the thermal acceleration would be constant. The orbit-averaged effect on the satellite distance from the primary would be zero. The essence of the YS effect is due to the satellite crossing the primary’s shadow. The interrupted solar irradiation results in the satellite cooling such that the thermal acceleration drops and tilts. Upon leaving the shadow, the satellite heats, slowly regaining the thermal state at the subsolar configuration. The net budget of the transverse component of the thermal acceleration may be nonzero, depending on the satellite rotation rate and obliquity, resulting in a secular change of its distance from the primary.

drives the primary’s obliquity to 0° or 180° (Rubincam 2000), the optimum condition $i < r_p/a$ is usually easily satisfied for small binaries if they form via YORP-driven spin-up and mass shedding followed by reaccumulation in the equatorial plane of the primary (Walsh et al. 2008; Pravec et al. 2012; Agrusa et al. 2024). For simplicity, in the following, we take $i = 0^\circ$. We first develop a simple analytical YS effect model, and later in this section, we justify it by comparison with the results of a numerical simulation.

There is also a “mirror” YS effect related to the satellite shadow that perturbs the thermal state of the primary. In principle, the corresponding drift rate of the satellite semimajor axis \dot{a} may be described by a similar approach used for the core YS effect on the satellite. While algebraic complications would arise due to primary’s larger size than the satellite’s cross section, it is conceivable that the primary-driven YS component would be a factor of $\sim (r_s/r_p)^2$ smaller than the secondary-driven YS effect. As our ambition is to provide a simple and introductory analytical estimate of the YS effect, we neglect the thermal acceleration of the primary at this moment.

Returning to the analytical formulation of the YS effect for the satellite, we assume that both the primary and the secondary have a spherical shape with radii r_p and r_s , respectively (nonsphericity of both components may result in corrections, which are typically lower than the aimed accuracy of our simple analytical model). The heliocentric orbit of the barycenter and the relative orbit of the two components in the binary are both assumed to be circular. We denote the semimajor axis of the secondary orbit about the primary by a , the corresponding mean motion by n , and the spin rate of the

secondary by ω . We introduce the frequency ratio $m = |\omega/(n - n_h)| \simeq |\omega/n|$, where n_h is the heliocentric mean motion of the binary system. In this work, we assume $n_h \ll n$; thus, $n - n_h \simeq n$ in the denominator of m . We assume the secondary is in principal axis rotation. Complex rotational states such as a tumbling state or the so-called barrel instability are left for future investigation.

The complete mathematical solution of the YS effect for a small satellite orbiting a large primary is given in Vokrouhlický et al. (2007; a ring particle about Saturn, in their context). The semimajor axis drift rate of the secondary due to the YS effect has a generic form:

$$\dot{a}_{YS} = \frac{2f_{YS}\mathcal{F}}{n}. \quad (4)$$

The dimensionless coefficient f_{YS} is called the YS coefficient in this work and depends on the physical properties of the binary system, such as the mutual orbital period, the sizes of the two bodies composing the binary, and the thermal properties. In fact, f_{YS} is the sum of the diurnal component and the seasonal component,

$$f_{YS} = f_{YS,d} + f_{YS,s}, \quad (5)$$

where

$$f_{YS,d} = \frac{4c_1}{9} \left[V(z_{m-1}) \cos^4 \frac{\varepsilon}{2} - V(z_{m+1}) \sin^4 \frac{\varepsilon}{2} \right], \quad (6)$$

$$f_{YS,s} = -\frac{2c_1}{9} V(z_1) \sin^2 \varepsilon. \quad (7)$$

Here $z_{m\pm 1} = \sqrt{-i(m \pm 1)} r_s/l_n$ ($i = \sqrt{-1}$), $c_1 \simeq r_p/\pi a$ expresses the orbital fraction spent by the satellite in the primary’s shadow, and $V(z)$ is a real-value function defined by

$$V(z) = \text{Im} \left(1 + \chi \frac{z}{j_1(z)} \frac{dj_1(z)}{dz} \right)^{-1}, \quad (8)$$

with $j_1(z)$ denoting the spherical Bessel function of the first kind and order 1,

$$j_1(z) = \frac{\sin z}{z^2} - \frac{\cos z}{z}. \quad (9)$$

The thermal penetration depth l_n at the satellite mean-motion frequency n is given by $l_n = \sqrt{K_s/(\rho_s C_s n)}$, where K_s is the thermal conductivity, C_s is the heat capacity, and ρ_s is the surface density of the satellite. The variable χ is defined as

$$\chi = \frac{K_s}{\sqrt{2} r_s \epsilon \sigma T_{\text{sub}}^3 c_0^{3/4}}, \quad (10)$$

with $c_0 = 1 - c_1$, the subsolar temperature T_{sub} defined by $\epsilon \sigma T_{\text{sub}}^4 = (1 - A)\Phi$, ϵ the thermal emissivity, and σ the Stefan–Boltzmann constant. Alternatively, the $V(z)$ function can be expressed using a real argument $x = \sqrt{2i} z$,

$$V(z) = \frac{E(x) \sin \delta(x)}{1 + \chi} = \frac{1}{1 + \chi} \frac{B(x)C(x) - A(x)D(x)}{C^2(x) + D^2(x)}. \quad (11)$$

The expressions for functions A , B , C , and D are derived in Vokrouhlický (1998) and are also provided in Appendix B.

Apart from the eclipse-induced YS effect, the radiation from the primary to the secondary would cause a so-called

“planetary” Yarkovsky effect (Rubincam 2006; Vokrouhlický et al. 2007), which replaces the solar radiation with the thermal radiation of the primary in the Yarkovsky effect. Its resulting semimajor axis drift rate can be expressed as

$$\dot{a}_{pY} = \frac{2f_{pY} \mathcal{F}_{pY}}{n}, \quad (12)$$

where

$$f_{pY} \simeq -\frac{f_{YS}}{c_1}, \quad (13)$$

$$\mathcal{F}_{pY} \simeq \mathcal{F} \left(\frac{r_p}{2a} \right)^2. \quad (14)$$

Equation (14) results from the fact that the radiation flux from the primary is smaller than the solar radiation flux by a factor of $(r_p/2a)^2$. It is important that the planetary Yarkovsky effect does not require the eclipse condition and therefore works for high-inclination cases. Noticing that $c_1 \simeq r_p/\pi a$, we have

$$\dot{a}_{pY} = -a_{YS} \frac{\pi r_p}{4a}, \quad (15)$$

showing that the planetary Yarkovsky effect is an opposite effect to the YS effect. Considering $r_p/a < 1$, the YS coefficient not only dominates over the planetary Yarkovsky effect but also becomes progressively stronger relative to it as the binary semimajor increases.

Combining the eclipse-induced YS effect (Equation (4)) and the planetary Yarkovsky effect (Equation (15)), we obtain the total Yarkovsky effect on the binary asteroid:

$$\dot{a}_Y = \dot{a}_{YS} + \dot{a}_{pY} = \dot{a}_{YS} \left(1 - \frac{\pi r_p}{4a} \right). \quad (16)$$

For the sake of simplicity, we introduce a combined Yarkovsky coefficient,

$$f_Y = f_{YS} \left(1 - \frac{\pi r_p}{4a} \right), \quad (17)$$

such that the total Yarkovsky effect has a generic form:

$$\dot{a}_Y = \frac{2f_Y \mathcal{F}}{n}. \quad (18)$$

2.2. Discussion

The sign of the Yarkovsky-induced drift rate \dot{a}_Y is the same as the Yarkovsky coefficient f_Y , while the latter is a complicated function that depends on the properties of the binary system (see Equations (6) and (7)). Roughly said, for prograde secondaries ($\varepsilon < 90^\circ$), the Yarkovsky effect tends to drive the secondary toward the synchronous orbit a_{syn} determined by $n = \omega$, while for retrograde secondaries ($\varepsilon > 90^\circ$), the Yarkovsky effect always drives the secondary outward until it leaves the system. The Yarkovsky coefficient f_Y could have a simpler form in the fast spin regime ($\omega \gg n$) or in the slow spin regime ($\omega \ll n$), as discussed in Appendix C.

For the purpose of an illustration, we consider a binary system on a heliocentric circular orbit and $a_h = 1$ au. We set $r_p = 1000$ m, $r_s = 200$ m, and the physical parameters $K_p = K_s = 0.1$ W m⁻¹ K⁻¹, $C_p = C_s = 550$ J K⁻¹ kg⁻¹, and $\rho_p = \rho_s = 2000$ kg m⁻³. The semimajor axis a of the binary components is fixed at 2650 m, which corresponds to an orbital

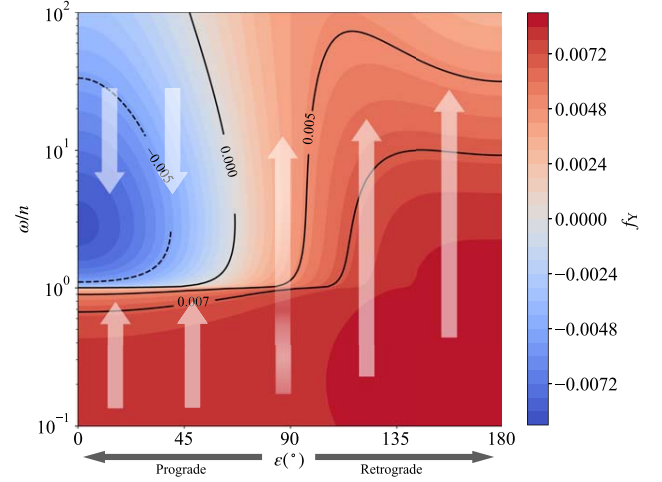


Figure 2. The Yarkovsky coefficient, f_Y , as a function of m and ε , where $m = \omega/n$ is the ratio of the spin frequency to the orbital frequency and ε is the angle between the spin vector and the orbital vector. The sign of f_Y is the same as the sign of \dot{a}_Y , and $f_Y = 0.005$ corresponds to $\dot{a} = 1.4$ cm yr⁻¹ for this system. The direction of the white arrows denotes the evolution direction under the Yarkovsky effect. For small values of ε , the Yarkovsky effect drives m toward 1; otherwise, the satellite is driven away from the primary.

period of 10 hr. As a result, different values of m are obtained solely by changing the spin frequency ω . We also set the obliquity ε as a free parameter. Figure 2 shows the Yarkovsky coefficient f_Y as a function of m and ε . Clearly, the Yarkovsky effect drives the secondary orbit to evolve toward the synchronous state ($m = 1$) for prograde rotators but always pushes the retrograde rotators outward. In the blue zone, the Yarkovsky effect maximizes at a spin period of ~ 3 hr, corresponding to the thermal parameter value $\Theta_\omega \sim \sqrt{2}$; here $\Theta_\omega = \Gamma \sqrt{\omega} / (\varepsilon \sigma T_{sub}^3)$ with the surface thermal inertia $\Gamma = \sqrt{K_s C_s \rho_s}$.

In the most common case seen for the observed binary systems, namely, $\varepsilon \sim 0^\circ$, the Yarkovsky coefficient simplifies (with only the diurnal component contributing)

$$f_{YS} = \frac{4c_1}{9} V(z_{m-1}). \quad (19)$$

We introduce the relative angular frequency $\Delta = \omega - n$ such that $z_{m-1} = \sqrt{-1} r_s / l_\Delta$, where l_Δ is defined as

$$l_\Delta = \sqrt{\frac{K_s}{\rho_s C_s |\Delta|}} = 2 \text{ cm} \left(\frac{|\Delta|}{2 \times 10^{-4} \text{ rad s}^{-1}} \right)^{-1/2} \quad (20)$$

(we use the above-given physical parameters of the satellite surface). In the case of large bodies $r_s \gg l_\Delta$, readily fulfilled in the cases of interest, we can further apply the approximate expression for the $V(z_{m-1})$ function,

$$V(z_{m-1}) = -\frac{\Theta_\Delta}{2 + 2\Theta_\Delta + \Theta_\Delta^2} \text{Sign}(\omega - n), \quad (21)$$

with the thermal parameter Θ_Δ defined as

$$\Theta_\Delta = \frac{\Gamma \sqrt{|\Delta|}}{\varepsilon \sigma T_{sub}^3}. \quad (22)$$

Note that f_Y does not depend on the size of the secondary when $r_s \gg l_\Delta$. In the regime of $r_s < l_\Delta$, f_Y gets smaller when r_s decreases. The Yarkovsky coefficient f_Y depends on the

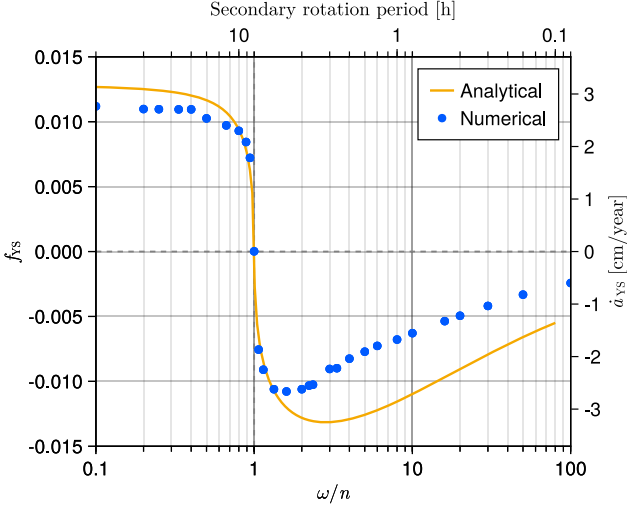


Figure 3. The YS coefficient f_{YS} as a function of the ratio of the spin velocity to the mean motion, ω/n . The blue dots show the numerical results of the zero-obliquity case compared with the analytical solution (orange). The secondary x -axis and y -axis indicate the corresponding rotation period and semimajor axis drift for the given binary system.

semimajor axis following $f_Y \propto r_p(1 - \pi r_p/4a)/a$, considering a constant Δ . As the secondary asteroid is always outside the Roche limit ($a \gtrsim 1.5r_p$), f_Y decreases with a .

2.3. Comparison with Numerical Simulation

To validate our analytical solution, we compare our results with numerical solutions. We performed thermophysical simulations using the `AsteroidThermoPhysicalModels.jl` library, one of the functionalities of the asteroid dynamical simulator `Astroshaper` (<https://github.com/Astroshaper>). This package was originally developed to predict the YORP effect on asteroid 162173 Ryugu, a target asteroid of Japan's Hayabusa2 spacecraft (Kanamaru et al. 2021). The thermophysical model, originally formulated for a single asteroid, has been generalized to include all relevant thermal effects in a binary system. Most importantly, we account for the mutual shadowing between the binary components.

For comparison with the analytical solution, we numerically evaluated the YS coefficients f_{YS} for different orbit and spin periods of the secondary. We consider a binary asteroid with the same parameters as Section 2.2. The binary at 1 au heliocentric distance has been given zero eccentricity (both the heliocentric and mutual orbits). The spherical binary components were approximated using a triangulated model with 2562 vertices and 5120 facets for both the primary and the secondary. The obliquity of the secondary's spin pole is set to be $\varepsilon = 0^\circ$.

We performed thermophysical simulations for 100 thermal cycles to reach converged values of f_{YS} , with the least common multiple of the secondary's orbit period and the spin period as one cycle. The orbital period of the satellite was fixed at 8 hr, and the rotation period was varied to simulate cases of different ω/n . The radiation flux between the primary and the secondary was hereby ignored to save computational time. At each time step, we calculated the temperature distribution of the asteroids and the thermally induced force on each surface facet, as described in Rozitis & Green (2012). The thermal force in an

asteroid-fixed frame was then transformed into an inertial frame to calculate the acceleration on the secondary. The effective YS coefficients f_{YS} are plotted in Figure 3 as a function of the ratio of the spin velocity to the mean motion, ω/n . The numerical results are in reasonable agreement with the analytical solution (Equation (21)), given its simplicity, providing its justification. A complete parameter survey by the numerical thermophysical model will be presented in future work.

3. Implications

3.1. Synchronization of the Secondary Component

The majority of the binary asteroid systems are observed to have a synchronized secondary. Simulation of rotational disruption of asteroids shows that the secondary could be born either asynchronous or synchronous due to the frequent reshaping near the Roche limit (Agrusa et al. 2024). Currently, there are two known mechanisms for the synchronization of the secondary asteroid: the tidal effect and the YORP effect. Both of these effects synchronize the secondary by changing the rotation of the secondary until it gets tidally locked. The tidal bulge raised on the secondary by the primary causes a torque that tends to remove the difference between the spin frequency and orbital frequency. The estimate of the characteristic timescale related to the tidal torque makes use of (Murray & Dermott 1999)

$$\dot{\omega} = \frac{5\pi G \rho_p^2 r_p^6}{r_s^5 a \rho_s} \left(\frac{r_s}{a}\right)^5 \frac{k_s}{Q}, \quad (23)$$

with $k_s = 0.038 G \rho_s^2 r_s^2 / \mu$ (Burns & Safronov 1973; Murray & Dermott 1999; Quillen et al. 2022) assuming a monolithic structure. While we note that k_s/Q is a more fundamental parameter for the tidal effect, we use the parameter μQ for ease of comparison with previous work. However, it is important to note that the expression of the tidal Love number k_2 for rubble piles is still under debate and poorly constrained (Burns & Safronov 1973; Yoder 1982; Jacobson & Scheeres 2011; Taylor & Margot 2011; DellaGiustina et al. 2024). The timescale $\tau_{t,\text{spin}} \simeq \omega/\dot{\omega}$ reads

$$\begin{aligned} \tau_{t,\text{spin}} &= \frac{\omega Q \rho_s}{5\pi k_2 G \rho_p^2} \left(\frac{a}{r_p}\right)^6 \\ &\simeq 10 \text{ Myr} \left(\frac{8.7 \text{ hr}}{P_s}\right) \left(\frac{a}{r_p}\right)^6 \left(\frac{r_s}{0.2 \text{ km}}\right)^{-2} \left(\frac{\mu Q}{10^{11} \text{ Pa}}\right), \end{aligned} \quad (24)$$

where $P_s = 2\pi/\omega$ is the satellite rotation period. The value of μQ , which varies by a few orders of magnitude in the literature (Burns & Safronov 1973; Goldreich & Sari 2009; Efroimsky 2015; Caudal 2023; Pou & Nimmo 2024), is still uncertain for rubble piles, and its dependence on the size is also poorly known.

The radiative torque due to the irregular shape, namely, the YORP torque, can spin the secondary up or down. The direction of the YORP torque, which depends on the shape and rotation state, is still poorly understood. The timescale of the YORP effect is (Rubincam 2000; Bottke et al. 2006; Marzari et al. 2020)

$$\tau_{\text{YORP}} \simeq 42 \text{ kyr} \left(\frac{r_s}{0.2 \text{ km}}\right)^2 \left(\frac{8 \text{ hr}}{P}\right) \left(\frac{a_h}{1 \text{ au}}\right)^2. \quad (25)$$

It is obvious that the YORP timescale is much shorter than the tidal timescale, implying that the YORP effect could be the major mechanism for the synchronization of the secondary asteroid. However, there are two issues. First, the YORP effect may be highly sensitive to the fine-scale surface irregularities (Breiter et al. 2009; Statler 2009; Cotto-Figueroa et al. 2015). In most cases, this information is beyond the resolution of the available observations. As a result, predicting even the instantaneous YORP value may be very difficult (this is the reason why the presently achieved YORP detections are often smaller than theoretically expected; see the latest compilation in the discussion section of Āurech et al. 2024). From a long-term perspective, the movement of boulders (Golubov & Krugly 2012) and formation of impact craters (Zhou et al. 2022; Zhou & Michel 2024) could modify or even reverse the direction of the YORP torque. Building on the YORP’s shape sensitivity, Bottke et al. (2015) introduced the “stochastic YORP” concept and showed that it overall weakens the long-term effects of nominal YORP. Second, theoretically, the YORP torque has an equal probability of taking a positive or negative sign. Therefore, we would expect that half of the secondaries are asynchronous due to the wrong direction of the YORP torque (i.e., opposite to $n - \omega$), which is inconsistent with the observed dominating synchronous population with tight orbits (e.g., $a < 2.2r_p$ or $P_{\text{orb}} < 20$ hr; see Pravec et al. 2016). Asynchronous secondaries occur more frequently in wide orbits compared to tighter ones (Pravec et al. 2016), implying a correlation to some mechanism that influences orbital configurations.

While there is no clear answer for the dominating mechanism of synchronization of the secondary, we find that the Yarkovsky effect also drives the prograde rotators toward the synchronous orbit (Section 2). Here, we estimate the timescale for the Yarkovsky effect to synchronize the orbit:

$$\tau_Y = \frac{a}{\dot{a}_Y} = \frac{am}{2f_Y \mathcal{F}} \simeq 160 \text{kyr} \left(\frac{r_p}{1 \text{ km}} \right)^2 \left(\frac{r_s}{0.2 \text{ km}} \right) \left(\frac{a/r_p}{2.5} \right)^{1/2} \left(\frac{0.005}{f_{Y,0}} \right) \left(\frac{a_h}{1 \text{ au}} \right)^2, \quad (26)$$

where $f_{Y,0}$ is the Yarkovsky coefficient at $a = 2.5r_p$. The Yarkovsky effect synchronizes the secondary by principally modifying its orbit, while the tidal and the YORP effects change its spin rate. Compared to the YORP timescale (Equation (25)), Equation (26) suggests that the Yarkovsky effect could operate more efficiently than the stochastic YORP for relatively large objects. The Yarkovsky could also dominate over the tidal effect unless the satellite is close in or large or the value μQ is smaller than assumed. Therefore, we propose that the Yarkovsky effect could be—at least in some small binaries—the major mechanism to synchronize the secondary. Let us give two examples of interest, namely, the Didymos–Dimorphos and Dinkinesh–Selam systems.

By abruptly reducing the binary orbit period, the NASA DART impact may have broken Dimorphos from synchronous rotation. Due to the oblate shape of Dimorphos (Daly et al. 2023), the spin–orbit coupling could be very weak, and instead of Dimorphos’s long axis librating about the postimpact synchronous state, it could be circulating (Richardson et al. 2023). If this is the case, we can estimate

the present Yarkovsky drift rate. By setting the orbital period to be 11.37 hr and the spin period to 12 hr, we obtained an estimate of $\dot{a} \sim 7.6 \text{ cm yr}^{-1}$, which could be examined by the subsequent space mission ESA Hera that will launch in 2024 October to visit Didymos in fall 2026 (Michel et al. 2022). However, we note that this possibility is only one of many possible Dimorphos postimpact spin states, including tumbling (Agrusa et al. 2021; Richardson et al. 2023). The Yarkovsky effect does not vanish for tumbling objects (not even in the strong tumbling regime such as the long-axis mode). For a weak tumbling regime (short-axis mode), the Yarkovsky effect could be acceptably well represented using a traditional formulation (with rotation about the principal axis of the inertia tensor) and assuming (i) a spin axis oriented along the rotational angular momentum, (ii) a rotation period close to the precession period, and (iii) the shape given by the convex hull swept during the tumbling cycle (Vokrouhlický et al. 2015). There are many examples of tumbling NEAs, such as 99942 Apophis (Pravec et al. 2005, 2014; Vokrouhlický et al. 2015; Del Vigna et al. 2018; Pérez-Hernández & Benet 2022) and 4179 Toutatis (Vokrouhlický et al. 2005b; Chesley et al. 2015; Del Vigna et al. 2018), for which the Yarkovsky signal was firmly detected, pretty much as expected and within the expected range of the nontumbling state. Thus, we suspect that the rule of the Yarkovsky effect would still be valid for tumbling components in a binary system, while a more thorough investigation is required for confirmation in the future. There is some observational evidence indicating that Dimorphos may be in some excited tumbling state (Pravec et al. 2024), where the satellite’s longest axis is approximately tidally locked to the direction toward the primary. Given its on average synchronous rotation, the Yarkovsky effect could be weak or even shut off in this case, but a more detailed analysis of this interesting system is needed.

In the latter case, the Dinkinesh–Selam binary recently discovered by the Lucy mission (Levison et al. 2024), the secondary asteroid Selam appears to be synchronous with a wide orbit at $a/r_p \simeq 9$. Selam is likely a contact binary, possibly formed by the merger of two satellites. If this is the case, Selam was unlikely to be in synchronous rotation following a merger, requiring some synchronization mechanism to explain its present spin state. The timescale for the tidal despinning could be as long as ~ 3 Gyr according to Equation (24), due to the wide orbit. However, the typical collisional lifetime of asteroids the size of Dinkinesh (0.8 km in diameter; Levison et al. 2024) is about 0.3 Gyr (Bottke et al. 2005). Since this lifetime is much smaller than the tidal despinning timescale, it is therefore unlikely that Selam was synchronized by the tidal effect, while the Yarkovsky effect can synchronize the orbit quickly. We found that the Yarkovsky timescale could be ~ 1 Myr by setting $r_p = 720$ m, $r_s = 277$ m, $a = 3.1$ km, $\rho_p = \rho_s = 2.4 \text{ g cm}^{-3}$, $a_h = 2.19$ au, and $e_h = 0.11$. Therefore, we propose that the Yarkovsky effect could be the main reason for its current synchronous state.

3.2. Long-term Evolution of Binary Asteroids

Let us now consider the possible evolutionary pathways of small binary systems in general terms, extending the canonical view (with tides and BYORP operating) by the Yarkovsky effect. Assume the parent body of the binary is disrupted either by

rotational fission or a catastrophic collision. The resulting fragments that are bound to the parent body accumulate to form a satellite, which can be either in synchronous or asynchronous rotation (Agrusa et al. 2024). The synchronous secondary evolves under the tidal and BYORP effects, resulting in a final state at the tide–BYORP equilibrium location (given that the BYORP torque is negative) or in a migration outward until it leaves the system or becomes chaotic (if the BYORP torque is positive) (Ćuk 2007; Ćuk & Nesvorný 2010; Jacobson & Scheeres 2011; Jacobson et al. 2014). Assuming a_{B-t} is the location of the BYORP–tide equilibrium, where $\dot{a}_B = -\dot{a}_t$, secondaries with a large BYORP coefficient f_B such that $a_{B-t} < a_{\text{Roche}}$ will cross the Roche limit and get tidally disrupted (Ćuk & Nesvorný 2010).

If the secondary is born asynchronous or perturbed into such a rotation state, it will evolve under the joint effect of tides and the Yarkovsky effect. If it happens to be in a spin–orbit resonance, BYORP is also active (Jacobson et al. 2014). For retrograde rotators, both tides and the Yarkovsky effect expand the secondary’s semimajor axis until it is lost, forming an asteroid pair. The timescale for this process is $\min(\tau_t, \tau_Y) \lesssim \tau_Y$, considering that the strength of tides declines rapidly with the semimajor axis. In this case, the two components of the asteroid pair have opposite spin poles, different from asteroid pairs produced by rotational fission (Pravec & Scheirich 2010; Pravec et al. 2019) or BYORP (Ćuk 2007). For prograde rotators, the Yarkovsky effect will shrink the orbit if the secondary spins faster than the mean motion. If the secondary has a spin period P shorter than the orbital period at the Roche limit P_{Roche} , which is given by

$$P_{\text{Roche}} = 2\pi \sqrt{\frac{3}{4\pi G \rho_p}} \left(\frac{a_{\text{Roche}}}{r_p} \right)^{3/2} \simeq 4.3 \text{ hr} \left(\frac{a_{\text{Roche}}}{1.5r_p} \right)^{3/2}, \quad (27)$$

then the secondary will migrate to this point and undergo significant reshaping or even tidal disruption. The typical Roche radius is given as $\sim 1.5 r_p$ (Holsapple & Michel 2006), assuming the binary components have equal density. The traditional hydrostatic Roche radius is roughly $2.46 r_p$, corresponding to an orbital period of ~ 9 hr. The distribution of orbital periods of known binary systems shows a cutoff at 11 hr (Pravec et al. 2006). More recently confirmed binaries have confined the cutoff orbital period to 10.5 hr, suggesting that the Roche radius could be $2.7 r_p$ for rubble piles with a weak structure or low density if the cutoff in the orbital period distribution is caused by tidal disruption. If the secondary has sufficient material strength (e.g., small monoliths), it is also possible that it would continue migrating inward and form a contact binary. Note that this process requires the Yarkovsky effect to overcome the outward torque due to tides. The semimajor axis a_{Y-t} , where tides balance the Yarkovsky effect, can be obtained by equating Equations (1)–(18):

$$a_{Y-t} = 0.84 r_p \left(\frac{r_s}{0.2 \text{ km}} \right)^{4/7} \left(\frac{0.005}{f_Y} \right)^{1/7} \left(\frac{10^{11} \text{ Pa}}{\mu Q} \right)^{1/7}. \quad (28)$$

This implies that the Yarkovsky effect easily overcomes tides for small binaries unless the tidal effect is much stronger than assumed. Changing f_Y to f_B makes the above equation for a_{B-t} . Considering the uncertainty of the tidal effect, we assume that a_{B-t} and a_{Y-t} could be located either inside or outside the a_{Roche} . If $a_{Y-t} > a_{\text{Roche}}$, the secondary will be stopped outside the Roche

limit and be in a Yarkovsky–tide equilibrium state. However, this state can only last for a YORP timescale or a tidal despinning timescale, as the YORP torque or tides change the spin to shut off the Yarkovsky effect. For rotators with $P > P_{\text{Roche}}$, the Yarkovsky effect will move the secondary toward the synchronous orbit a_{syn} , except in the special case where the Yarkovsky effect is negative and balanced by tides, leading to a temporary Yarkovsky–tide equilibrium state at a_{Y-t} .

To summarize, we provide some predictions on the secondary dynamical state based on the Yarkovsky effect: (1) retrograde secondaries should be relatively far from the primaries; (2) some asteroid pairs could have opposite spin directions if they are formed by the Yarkovsky effect; (3) secondaries with a period shorter than the orbital period at the Roche radius, ranging from ~ 4 to ~ 10 hr, should be destroyed in a Yarkovsky timescale (~ 0.1 Myr), otherwise they should be in a Yarkovsky–tide equilibrium (asynchronous) that lasts for a YORP timescale; and (4) secondaries with a period longer than the Roche orbital period should become synchronous after a Yarkovsky timescale.

3.3. Predicted Orbital Drift Rates of Real Binary Asteroids

As of now, there are 66 binary asteroid systems with documented secondary spin periods (Pravec & Harris 2007; Warner et al. 2009; Pravec et al. 2012, 2016; Monteiro et al. 2023). Among these, five are known to exhibit spin periods that are different from their orbital periods to date. While there are other potentially asynchronous binary systems, their information is either undetermined or incomplete (Pravec et al. 2016). Consequently, we computed the theoretical Yarkovsky drift rates for these five asynchronous binary asteroids for future tests.

It is important to note that the Yarkovsky effect remains applicable to those binary systems with $n = \omega$, provided their obliquity is nonzero. However, due to insufficient data on the spin vectors, the information regarding the axial tilt of real asteroids remains ambiguous. Here our focus is limited to asteroids with $n \neq \omega$, for which BYORP does not work. We estimated the Yarkovsky effect for these bodies in the limiting cases $\varepsilon = 0^\circ$ and 180° . The result is shown in Table 1. We notice that there are a few asteroid binaries (e.g., Esclangona, Arlon) with a large separation, although their spin periods are much smaller than the orbital periods ($m \ll 1$). This large separation was explained as a result of the BYORP-induced expansion and subsequent desynchronization (Jacobson et al. 2014). We found that the Yarkovsky effect could also expand the mutual orbit, if the secondaries have obliquities around or larger than 90° , which is left for future observational tests. The Yarkovsky effect decreases with increasing separation, not only because of the decreasing time fraction in the shadow over a mutual orbit (i.e., c_1 in Equations (6) and (7)) but also due to the challenges in maintaining the shadow condition over the heliocentric orbit. For a distant satellite, the inclination of its orbit about the primary should be confined in a narrower interval of values than for close satellites. Accounting for the potential nonexistence of the shadow in a relatively high-inclination heliocentric orbit, the c_1 should be revised as the time fraction that the secondary spends in the shadow over a heliocentric orbit.⁷ Therefore, thorough orbital modeling is crucial for assessing the Yarkovsky drift rates for distant satellites. The predictions provided by Table 1 are based on the

⁷ This reduces to $c_1 \simeq r_p/\pi a$ when $i = 0$.

Table 1
The Yarkovsky Effect Predicted for Known Asynchronous Binaries

| Name | a_h (au) | e_h | r_p (km) | r_s/r_p | a/r_p | P_{orb} (hr) | P_s (hr) | $f_Y (\times 10^{-3})$ | \dot{a}_Y (cm yr $^{-1}$) |
|-------------------|------------|-------|------------|-----------|---------|-----------------------|------------|------------------------|------------------------------|
| (1509) Esclangona | 1.866 | 0.032 | 4.25 | 0.33 | 49.2 | 768 | 6.6422 | $-0.54/+0.41$ | $-0.52/+0.39$ |
| (2486) Metsahovi | 2.269 | 0.08 | 4 | 0.30 | 18.3 | 172.6 | 2.64 | $-0.97/+1.0$ | $-0.17/+0.17$ |
| (2623) Zech | 2.255 | 0.234 | 3.4 | 0.29 | 14.1 | 117.2 | 18.718 | $-2.0/+1.7$ | $-0.29/+0.25$ |
| (32039) 2000 JO23 | 2.223 | 0.283 | 1.3 | 0.65 | 33.1 | 360 | 11.09 | $-0.81/+0.67$ | $-0.45/+0.37$ |
| (311066) 2004 DC | 1.634 | 0.400 | 0.15 | 0.20 | 4.6 | 23 | 7 | $-5.3/+4.6$ | $-10.2/+9.0$ |

Note. The orbital period of the binary components relative to each other is $P_{\text{orb}} = 2\pi/n$, while the rotation period of the secondary is $P_s = 2\pi/\omega$. The Yarkovsky coefficient f_Y and the drift rate \dot{a}_Y are calculated for an obliquity equal to $0^\circ/180^\circ$. The thermal parameters are assumed to be the same as those used in Section 2.2. It is important to note that for the distant satellites, the Yarkovsky effect could be diminished (see Section 3.3).

simplest situations and therefore only give the upper limits of Yarkovsky drift rates.

There are also some binaries (e.g., 1994 CC, 2001 SN263, 2004 DC, etc.) with large heliocentric eccentricities; therefore, they may also suffer from strong planetary perturbations that modify the mutual orbit and the spin state. Since the Yarkovsky effect is much more deterministic than the BYORP effect once the rotational state is known, our hypotheses can be easily examined by future observations.

4. Conclusions

The Yarkovsky effect is the radiative force acting on a rotating object with nonzero thermal inertia, gradually altering its orbit over the long term. In this work, we investigate the Yarkovsky effect on a binary asteroid system. The binary Yarkovsky effect, manifesting primarily on the secondary asteroid, comprises two main components: the YS effect and the planetary Yarkovsky effect. The former is the net Yarkovsky force averaged over the mutual orbital period due to the eclipse caused by the primary on the secondary. As a result of the eclipse condition, the YS effect is only significant for low-inclination binary asteroids (e.g., $i < r_p/a$), which are common in both the NEA and MBA populations. The planetary Yarkovsky effect is simply produced by the radiation from the primary asteroid instead of the Sun. For low-inclination asteroids, the YS effect dominates over the planetary Yarkovsky effect. The direction of the binary Yarkovsky effect depends on the obliquity and the difference between the spin rate and the mean motion of the secondary, while the magnitude depends on the thermal and orbital properties of the binary system. In general, the binary Yarkovsky effect moves the secondary to make the mean motion match the spin rate on a timescale of ~ 0.1 Myr.

We found that for prograde-rotating secondaries, the Yarkovsky effect can synchronize the secondary (i.e., $\omega = n$) by orbit modification on a timescale much shorter than tidal despinning, except for large or close-in secondaries. On the other hand, the YORP effect could be more efficient for synchronization of small secondaries. This is because of its timescale depending on $\sim r_s^2$ rather than $\sim r_s$ for the Yarkovsky effect. This brings us new insights about the mechanism of the synchronization of binary asteroids and the underlying reason why the majority of binary asteroids are found to be in synchronous states. Our calculations also predict that the secondary asteroids with spin periods shorter than the orbital period around the Roche limit (e.g., from ~ 4 to ~ 10 hr) will fall into the Roche limit quickly driven by the Yarkovsky effect and then get tidally disrupted, reshaped, or accreted on the

primary. In addition, some asynchronous binaries might be in the Yarkovsky–tide equilibrium state where the orbit does not drift, but such a state may be quickly broken by the YORP effect or tides. For retrograde secondaries, the Yarkovsky effect would drive them outward until they leave the binary system due to planetary perturbations or collisions, producing asteroid pairs. In this scenario, the two components of the asteroid pair would exhibit opposite spin directions.

We also calculated the Yarkovsky-caused drift rate for known asynchronous binaries, listed in Table 1 for future observational tests. Some of the asynchronous binary asteroids have wide mutual orbits, which could be the result of the Yarkovsky effect on retrograde secondaries. We found that the synchronization of the Dinkinesh–Selam system discovered by the Lucy spacecraft could be due to the Yarkovsky effect, considering that tides are weak for such a distant secondary. In addition, we calculated the possible Yarkovsky effect on the Didymos–Dimorphos system in its state following the impact of the NASA DART mission, which might have perturbed it into an asynchronous state. The Yarkovsky coefficient f_Y is around 0.0067, and the resulting semimajor axis drift rate is $\dot{a} \simeq 7.6$ cm yr $^{-1}$. This could be examined by in situ observation conducted by the space mission ESA Hera during its rendezvous with Didymos in late 2026.

Acknowledgments

We thank Miroslav Brož and Jay McMahon for useful discussions and the referee whose comments helped to improve the submitted manuscript. We acknowledge support from the Université Côte d’Azur. W.-H.Z. would like to acknowledge the funding support from the Chinese Scholarship Council (No. 202110320014). The work of D.V. and P.P. was partially supported by the Czech Science Foundation (grant 23-04946S). M.K. acknowledges the funding support by the JSPS KAKENHI No. JP22J00435/JP22KJ0728 and MEXT Promotion of Distinctive Joint Research Center Program grant No. JPMXP0622717003/JPMXP0723830458. H.A. was supported by the French government through the UCA J.E.D.I. Investments in the Future project managed by the National Research Agency (ANR) with the reference number ANR-15-IDEX-01. P.M. acknowledges funding support from the French space agency (CNES) and the European Space Agency (ESA).

Appendix A Nomenclature

The symbols used in this Letter are listed in Table 2.

Table 2
Notation Used throughout This Letter

| Symbols | | Subscripts | |
|---------------|---------------------------------------|------------|--|
| a | Semimajor axis of a mutual orbit | p | Primary component of a binary asteroid |
| k | Love number | s | Secondary component of a binary asteroid |
| n | Mean motion | h | Heliocentric parameter |
| Q | Quality factor | B | BYORP |
| r | Radius | Y | Yarkovsky |
| f | Dimensionless coefficient | YS | Yarkovsky–Schach |
| A | Bond albedo | pY | Planetary Yarkovsky |
| ρ | Density | Y-t | Yarkovsky–tide equilibrium |
| μ | Rigidity | B-t | BYORP–tide equilibrium |
| i | Inclination | Roche | Roche limit |
| ε | Obliquity | | |
| ω | Spin rate of the secondary | | |
| τ | Timescale | | |
| Θ | Thermal parameter | | |
| Γ | Thermal inertia | | |
| \mathcal{F} | Nominal radiative force per unit mass | | |

Appendix B Functions $A(x)$, $B(x)$, $C(x)$, and $D(x)$

The functions $A(x)$, $B(x)$, $C(x)$, and $D(x)$, useful to express the $V(z)$ in real notation (Equation (11)), are given by (e.g., Vokrouhlický 1998, 1999)

$$A(x) = -(x + 2) - e^x[(x - 2)\cos x - x \sin x], \quad (\text{B1})$$

$$B(x) = -x - e^x[x \cos x + (x - 2)\sin x], \quad (\text{B2})$$

$$a(x) = 3(x + 2) + e^x[3(x - 2)\cos x + x(x - 3)\sin x], \quad (\text{B3})$$

$$b(x) = x(x + 3) - e^x[x(x - 3)\cos x - 3(x - 2)\sin x], \quad (\text{B4})$$

with $C(x) = A(x) + \chi a(x)/(1 + \chi)$ and $D(x) = B(x) + \chi b(x)/(1 + \chi)$.

Appendix C Special Cases for f_Y

The formula of the Yarkovsky coefficient f_Y can be simplified in some special cases. In the fast spin regime, where $\omega \gg n$ such that $m \gg 1$, $V(z_{m+1}) \simeq V(z_{m-1}) \simeq V(z_m)$ and $z_m = \sqrt{-im} r_s/l_n$. In this case, one could replace the penetration depth l_n of the thermal wave at mean-motion frequency n with a penetration depth $l_d = l_n/\sqrt{m}$ of the thermal wave at rotation frequency, thence $z_m = \sqrt{-i} r_s/l_d$. Since $\cos^4(\varepsilon/2) - \sin^4(\varepsilon/2) = \cos \varepsilon$, we obtain a simpler form of Equation (6) reading

$$f_{Y,S,d} = \frac{4c_1}{9} V(z_m) \cos \varepsilon. \quad (\text{C1})$$

This equation resembles the classic Yarkovsky effect for a single asteroid orbiting around the Sun but is multiplied by

$-c_1$. Therefore, the Yarkovsky is maximized when the spin thermal parameter $\Theta_\omega \sim \sqrt{2}$, which is defined as

$$\Theta_\omega = \frac{\Gamma \sqrt{\omega}}{\varepsilon \sigma T_{\text{sub}}^3} \sim \sqrt{2} \left(\frac{\Gamma}{200 \text{ J m}^{-2} \text{ K}^{-1} \text{ s}^{-1/2}} \right) \times \left(\frac{P_s}{3 \text{ hr}} \right)^{-1/2} \left(\frac{a_n}{1 \text{ au}} \right)^{3/2}. \quad (\text{C2})$$

It is obvious that when $\varepsilon = 0^\circ$, there is only the diurnal component left, leading to the inward migration of the secondary asteroid and the decrease of m (since n becomes larger).

In the slow spin regime, where $\omega \ll n$ such that $m \sim 0$, we have $V(z_{m+1}) \simeq -V(z_{m-1}) \simeq V(z_1)$ and $z_1 = \sqrt{-i} r_s/l_n$. Therefore,

$$f_{Y,S,d} = -\frac{4c_1}{9} V(z) \left(1 - \frac{1}{2} \sin^2 \varepsilon \right). \quad (\text{C3})$$

Interestingly, when combined with the seasonal component, we get the total YS coefficient f_{YS} ,

$$f_{YS} = -\frac{4c_1}{9} V(z_1), \quad (\text{C4})$$

that is independent of the obliquity ε . Here, $f_{YS} > 0$, which leads to an outward migration and increasing m (since n becomes smaller).

In the synchronous regime where $m = 1$, considering $V(z_0) \rightarrow 0$, we obtain

$$f_{Y,S,d} = \frac{4c_1}{9} V(z_{-2}) \sin^4 \frac{\varepsilon}{2}, \quad (\text{C5})$$

and $f_{Y,S,s}$ remains the same. This will result in a zero Yarkovsky effect given that $\varepsilon = 0^\circ$. For the case of $\varepsilon \neq 0^\circ$, the Yarkovsky effect always transfers a positive angular momentum, driving the secondary outward.

ORCID iDs

Wen-Han Zhou (周文翰)  <https://orcid.org/0000-0003-4229-8936>
David Vokrouhlický  <https://orcid.org/0000-0002-6034-5452>
Masanori Kanamaru  <https://orcid.org/0000-0002-2533-3077>
Harrison Agrusa  <https://orcid.org/0000-0002-3544-298X>
Petr Pravec  <https://orcid.org/0000-0001-8434-9776>
Marco Delbo  <https://orcid.org/0000-0002-8963-2404>
Patrick Michel  <https://orcid.org/0000-0002-0884-1993>

References

- Agrusa, H. F., Gkolias, I., Tsiganis, K., et al. 2021, *Icar*, **370**, 114624
Agrusa, H. F., Zhang, Y., Richardson, D. C., et al. 2024, *PSJ*, **5**, 54
Botke, W. F., Durda, D. D., Nesvorný, D., et al. 2005, *Icar*, **175**, 111
Botke, W. F., Vokrouhlický, D., Rubincam, D. P., & Nesvorný, D. 2006, *AREPS*, **34**, 157
Botke, W. F., Vokrouhlický, D., Walsh, K. J., et al. 2015, *Icar*, **247**, 191
Breiter, S., Bartczak, P., Czekaj, M., Oczujda, B., & Vokrouhlický, D. 2009, *A&A*, **507**, 1073
Burns, J. A., & Safronov, V. S. 1973, *MNRAS*, **165**, 403
Caudal, G. 2023, *Icar*, **402**, 115606
Chesley, S., Farnocchia, D., Pravec, P., & Vokrouhlický, D. 2015, *IAUGA*, **29**, 2248872
Cotto-Figueroa, D., Statler, T. S., Richardson, D. C., & Tanga, P. 2015, *ApJ*, **803**, 25
Ćuk, M. 2007, *ApJL*, **659**, L57

- Čuk, M. 2023, AAS/Division of Dynamical Astronomy Meeting, [55, 501.01](#)
- Čuk, M., & Burns, J. A. 2005, [Icar, 176, 418](#)
- Čuk, M., Jacobson, S. A., & Walsh, K. J. 2021, [PSJ, 2, 231](#)
- Čuk, M., & Nesvorný, D. 2010, [Icar, 207, 732](#)
- Daly, R. T., Ernst, C. M., Barnouin, O. S., et al. 2023, [Natur, 616, 443](#)
- Del Vigna, A., Faggioli, L., Milani, A., et al. 2018, [A&A, 617, A61](#)
- DellaGiustina, D. N., Ballouz, R. L., Walsh, K. J., et al. 2024, [MNRAS, 528, 6568](#)
- Durda, D. D., Bottke, W. F., Enke, B. L., et al. 2004, [Icar, 170, 243](#)
- Đurech, J., Vokrouhlický, D., Pravec, P., et al. 2024, [A&A, 682, A93](#)
- Efroimsky, M. 2015, [AJ, 150, 98](#)
- Farinella, P., & Vokrouhlický, D. 1996, [P&SS, 44, 1551](#)
- Gladman, B., Michel, P., & Froeschlé, C. 2000, [Icar, 146, 176](#)
- Goldreich, P., & Sari, R. 2009, [ApJ, 691, 54](#)
- Golubov, O., & Krugly, Y. N. 2012, [ApJL, 752, L11](#)
- Holsapple, K. A., & Michel, P. 2006, [Icar, 183, 331](#)
- Jacobson, S. A., & Scheeres, D. J. 2011, [ApJL, 736, L19](#)
- Jacobson, S. A., Scheeres, D. J., & McMahon, J. 2014, [ApJ, 780, 60](#)
- Kanamaru, M., Sasaki, S., Morota, T., et al. 2021, [JGRE, 126, e06863](#)
- Levison, H., et al. 2024, [Natur, 629, 1015](#)
- Marzari, F., Rossi, A., Golubov, O., & Scheeres, D. J. 2020, [AJ, 160, 128](#)
- McMahon, J., & Scheeres, D. 2010, [Icar, 209, 494](#)
- Michel, P., Benz, W., Tanga, P., & Richardson, D. C. 2001, [Sci, 294, 1696](#)
- Michel, P., Küppers, M., Bagatin, A. C., et al. 2022, [PSJ, 3, 160](#)
- Milani, A., Nobili, A. M., & Farinella, P. 1988, [AN, 309, 38](#)
- Monteiro, F., Lazzaro, D., Rondón, E., et al. 2023, [Icar, 390, 115297](#)
- Murawiecka, M., & Lemaître, A. 2018, [AdSpR, 61, 935](#)
- Murray, C. D., & Dermott, S. F. 1999, *Solar System Dynamics* (Cambridge: Cambridge Univ. Press)
- Naidu, S. P., Chesley, S. R., Moskovitz, N., et al. 2024, [PSJ, 5, 74](#)
- Nesvorný, D., Youdin, A. N., & Richardson, D. C. 2010, [AJ, 140, 785](#)
- Pérez-Hernández, J. A., & Benet, L. 2022, [ComEE, 3, 10](#)
- Pou, L., & Nimmo, F. 2024, [Icar, 411, 115919](#)
- Pravec, P., Fatka, P., Vokrouhlický, D., et al. 2019, [Icar, 333, 429](#)
- Pravec, P., & Harris, A. W. 2007, [Icar, 190, 250](#)
- Pravec, P., Harris, A. W., Scheirich, P., et al. 2005, [Icar, 173, 108](#)
- Pravec, P., & Scheirich, P. 2010, AAS/Division for Planetary Sciences Meeting Abstracts, [42, 13.13](#)
- Pravec, P., Scheirich, P., Ďurech, J., et al. 2014, [Icar, 233, 48](#)
- Pravec, P., Scheirich, P., Kušnirák, P., et al. 2006, [Icar, 181, 63](#)
- Pravec, P., Scheirich, P., Kušnirák, P., et al. 2016, [Icar, 267, 267](#)
- Pravec, P., Scheirich, P., Meyer, A., et al. 2024, [Icar, 418, 116138](#)
- Pravec, P., Scheirich, P., Vokrouhlický, D., et al. 2012, [Icar, 218, 125](#)
- Quillen, A. C., LaBarca, A., & Chen, Y. 2022, [Icar, 374, 114826](#)
- Richardson, D., Agrusa, H., Barbee, B., et al. 2023, LPI Contribution, [2851, 2040](#)
- Rozitis, B., & Green, S. F. 2012, [MNRAS, 423, 367](#)
- Rubincam, D. P. 1982, [CeMec, 26, 361](#)
- Rubincam, D. P. 1987, [JGR, 92, 1287](#)
- Rubincam, D. P. 2000, [Icar, 148, 2](#)
- Rubincam, D. P. 2006, [Icar, 184, 532](#)
- Scheirich, P., & Pravec, P. 2022, [PSJ, 3, 163](#)
- Scheirich, P., Pravec, P., Jacobson, S. A., et al. 2015, [Icar, 245, 56](#)
- Scheirich, P., Pravec, P., Kušnirák, P., et al. 2021, [Icar, 360, 114321](#)
- Scheirich, P., Pravec, P., Meyer, A. J., et al. 2024, [PSJ, 5, 17](#)
- Statler, T. S. 2009, [Icar, 202, 502](#)
- Steinberg, E., & Sari, R. 2011, [AJ, 141, 55](#)
- Taylor, P. A., & Margot, J.-L. 2011, [Icar, 212, 661](#)
- Vokrouhlický, D. 1998, [A&A, 335, 1093](#)
- Vokrouhlický, D. 1999, [A&A, 344, 362](#)
- Vokrouhlický, D., Bottke, W. F., Chesley, S. R., Scheeres, D. J., & Statler, T. S. 2015, in *Asteroids IV*, ed. P. Michel, F. E. DeMeo, & W. F. Bottke (Tucson, AZ: Univ. of Arizona Press), [509](#)
- Vokrouhlický, D., Čapek, D., Chesley, S. R., & Ostro, S. J. 2005a, [Icar, 179, 128](#)
- Vokrouhlický, D., Čapek, D., Chesley, S. R., & Ostro, S. J. 2005b, [Icar, 173, 166](#)
- Vokrouhlický, D., Farnocchia, D., Čapek, D., et al. 2015, [Icar, 252, 277](#)
- Vokrouhlický, D., Nesvorný, D., Dones, L., & Bottke, W. F. 2007, [A&A, 471, 717](#)
- Walsh, K. J., & Jacobson, S. A. 2015, in *Asteroids IV*, ed. P. Michel, F. E. DeMeo, & W. F. Bottke (Tucson, AZ: Univ. of Arizona Press), [375](#)
- Walsh, K. J., Richardson, D. C., & Michel, P. 2008, [Natur, 454, 188](#)
- Warner, B. D., Harris, A. W., & Pravec, P. 2009, [Icar, 202, 134](#)
- Yoder, C. F. 1982, [Icar, 49, 327](#)
- Zhou, W.-H., & Michel, P. 2024, [A&A, 682, A130](#)
- Zhou, W.-H., Zhang, Y., Yan, X., & Michel, P. 2022, [A&A, 668, A70](#)

BINARY YARKOVSKY EFFECT ON THE PRIMARY ASTEROID

Following Chapter 2, this chapter investigates the Binary Yarkovsky effect on the primary asteroid in a binary system. The analysis is more complex for the primary asteroid, as it undergoes partial, rather than full, eclipses like the secondary. This may introduce non-linear effects. The significance of this scenario is particularly evident when the secondary is synchronous, which is the most common configuration for discovered binary asteroids.

In this Chapter:


- I present a modified formula for the primary asteroid, by fitting an empirical parameter with numerical results.
- I establish a unified framework for radiative effects in binary asteroid systems.
- I propose that singly synchronous binaries¹ tend to experience orbital shrinkage due to the combined effects of the Binary Yarkovsky and Binary YORP forces.
- I estimate the orbital drift rates caused by the Binary Yarkovsky effect for singly synchronous binary asteroids for future tests.

This paper was accepted by the peer-reviewed journal *Astronomy & Astrophysics Letters*.

¹ Singly synchronous binaries refer to systems in which the secondary asteroid is synchronous.

LETTER TO THE EDITOR

The binary Yarkovsky effect on the primary asteroid with applications to singly synchronous binary asteroids

Wen-Han Zhou^{*} 

Université Côte d'Azur, Observatoire de la Côte d'Azur, CNRS, Laboratoire Lagrange, 96 Bd de l'Observatoire, Nice 06304, France

Received 6 September 2024 / Accepted 16 November 2024

ABSTRACT

Context. The binary Yarkovsky effect on the secondary asteroid (BYS) was recently discovered to influence binary asteroid systems by pushing the secondary asteroid towards a synchronous orbit on a short timescale. However, the binary Yarkovsky effect on the primary (BYP) remains less understood, partly due to non-linear effects from partial eclipses, but could have significant implications for singly synchronous binaries.

Aims. We aim to obtain an empirical formula for the BYP and estimate its induced orbital drifting rates for real binary asteroids.

Methods. We solved the radiation forces numerically. By fitting the numerical results, we find an empirical modified solution to estimate the effective BYP: the traditional BYP formula multiplied by $(r_s/r_p)^{(\alpha-1)}$, which accounts for the partial eclipse.

Results. We confirm that the BYP pushes the primary towards a synchronous orbit where its spin equals the mean motion. Numerical results indicate that the parameter α is relatively insensitive to the ratio of the spin rate to the mean motion and decreases slightly with increasing thermal inertia. For small binary systems with a typical thermal inertia of 200 tiu , α is approximately 1.7. The BYP is found to affect the mutual orbit of singly synchronous binaries with a timescale typically an order of magnitude longer than that of the BYS. Drift rates induced by the BYP for known small binary asteroids (primary radius < 1 km) range from -0.001 to -1 cm yr^{-1} . A comparative analysis with observed orbital drift rates shows agreement for pre-impact Didymos and 1996 FG₃ but discrepancies for 2001 SL₉ and 1999 KW₄, suggesting complex dynamics in these systems involving the BYP, the binary Yarkovsky-O'Keefe-Radzievskii-Paddack (BYORP) effect, and tides.

Conclusions. The BYP is changing the mutual orbits of most discovered binary asteroids. We suggest that the BYP should be considered along with BYORP and tidal effects when studying binary systems' long-term dynamics.

Key words. minor planets, asteroids: general – planets and satellites: general

1. Introduction

Binary asteroids are estimated to account for approximately 15% of the asteroid population (Margot et al. 2015; Virkki et al. 2022; Minker & Carry 2023; Liberato et al. 2024). The dynamical lifetime of near-Earth asteroids and the collisional lifetime of main-belt asteroids are typically comparable to or longer than 10 million years (Farinella et al. 1998; Gladman et al. 2000). Understanding the long-term dynamics of binary asteroids is crucial for unravelling their evolutionary paths to their current configurations and deciphering their history.

In classical theory, the tidal effect and the binary Yarkovsky-O'Keefe-Radzievskii-Paddack (BYORP) effect governs the long-term evolution of binary asteroid systems (Čuk & Burns 2005; Čuk 2007; Čuk & Nesvorný 2010; Jacobson & Scheeres 2011; Jacobson et al. 2014). The tidal effect results from energy dissipation due to deformation, which drives the spin of the object towards a synchronous state and moves the orbit out of a synchronous state (Murray & Dermott 1999). A synchronous state occurs when the spin period equals the mutual orbital period. The BYORP effect is a net radiative force with a random direction and magnitude averaged over a period and is caused by anisotropic radiation from the asteroid's irregular shape (Čuk & Burns 2005).

However, some aspects are not satisfactorily explained by classical theory. The tidal synchronization timescale for small binaries is considerably long (e.g. ~ 10 Myr) unless a small tidal parameter, Q/k , is assumed, where k is the Love number and Q is the quality factor (Murray & Dermott 1999; Čuk & Burns 2005; Quillen et al. 2022; Zhou et al. 2024). The Yarkovsky-O'Keefe-Radzievskii-Paddack (YORP) effect predicts that half of secondaries are synchronous and the other half asynchronous; however, in reality the vast majority of known binaries (i.e., $\sim 90\%$) are singly synchronous where only the secondary is synchronous, like the Earth-Moon system (Zhou et al. 2024). Furthermore, four binary asteroids (namely the 1996 FG₃, 1999 KW₄, 2001 SL₉, and Didymos systems) have been detected with secular mutual orbital drifts. BYORP and tidal effects could potentially explain these drift rates, but refinements to shape models and tidal parameters are needed (Scheirich et al. 2015, 2021, 2024; Scheirich & Pravec 2022; Naidu et al. 2024; Cueva et al. 2024; Richardson et al. 2024). This suggests that additional factors may be influencing the long-term dynamics of binary asteroids.

Recently, Zhou et al. (2024) revisited the Yarkovsky effect on binary asteroid systems, building on pioneering work related to Earth's satellites and planetary rings (Rubincam 1982, 2006, 2014; Milani et al. 1987; Farinella & Vokrouhlický 1996; Métris et al. 1997; Vokrouhlický et al. 2005, 2007). The

* Corresponding author; wenhan.zhou@oca.eu

binary Yarkovsky effect arises from eclipse-induced thermal perturbations and thermal radiation from the other component in the system. By reorganizing the solution provided by Vokrouhlický et al. (2007), Zhou et al. (2024) found that the binary Yarkovsky effect on a secondary asteroid with a low inclination can drive the mutual orbit towards a synchronous state. The typical timescale for this synchronization process is approximately 0.1 Myr, which can be shorter than the timescales associated with tidal effects and the YORP effect. Thus, it has been proposed that the binary Yarkovsky effect may account for the synchronous state observed in the majority of known binary asteroids (Zhou et al. 2024). The binary Yarkovsky effect ceases to operate on the secondary once it enters a synchronous state.

However, there should also be a mirror binary Yarkovsky effect on the primary asteroid (hereafter the BYP) similar to the binary Yarkovsky effect on the secondary asteroid (BYS). The BYP is expected to continue modifying the mutual orbit after the BYS is inactive for the synchronized secondary, suggesting that most observed binary asteroids (~90%) should be influenced by the BYP in addition to tidal effects and the BYORP effect. Preliminary estimates indicate that the orbital drift rate caused by the BYP is weaker than that of the BYS, by roughly a factor of $(r_s/r_p)^2$, where r_s is the radius of the secondary and r_p is the radius of the primary. However, because the primary experiences only a partial eclipse due to the smaller size of the secondary, unknown non-linear effects may be at play.

This study explores the behaviours of the BYP and its influence on singly synchronous binary asteroids and evaluates its typical strength using numerical methods. This paper is organized as follows: Section 2 overviews the mechanism and main equations of the binary Yarkovsky effect; Sect. 3 describes the numerical method used in this work to investigate the BYP; Sect. 4 discusses the numerical result, develops the empirical approximate formula for the BYP, and presents the estimated orbit drift rates of known synchronous binaries due to the BYP.

2. Analytical consideration

In this paper, subscripts ‘s’ and ‘p’ denote parameters related to the secondary and primary, respectively. According to Zhou et al. (2024), for binary asteroids with aligned spin vectors, mutual orbital vectors, and heliocentric orbits, the BYS-induced orbital drift rate is

$$\dot{a}_{\text{BY},s} = \frac{2f_{\text{BY},s}\mathcal{F}_s}{n}, \quad (1)$$

with

$$f_{\text{BY},s} = f_{\text{YS},s} \left(1 - \frac{\pi r_p}{4a}\right). \quad (2)$$

Here f_{BY} and f_{YS} are the binary Yarkovsky coefficient and the Yarkovsky-Schach (YS) coefficient, respectively. The n is the mean motion, and the a is the semi-major axis of the mutual orbit. The nominal radiation pressure per unit mass, \mathcal{F} , is defined as

$$\mathcal{F} = \frac{\Phi(1-A)\pi r^2}{mc}. \quad (3)$$

The coefficient f_{YS} is a complicated function of the physical properties of the components. However, in the limit that the size of the binary components is larger than a few centimetres, which is true in the context of binary asteroids, f_{YS} can be approximated as

$$f_{\text{YS},s} = \frac{4r_p}{9\pi a} \frac{\Theta_s}{2 + 2\Theta_s + \Theta_s^2} \text{Sign}(n - \omega_s). \quad (4)$$

Here ω is the spin rate, and $r_p/\pi a$ accounts for the time fraction of the eclipse. The thermal parameter, Θ_s , is defined as

$$\Theta_s = \frac{\Gamma \sqrt{|\Delta|}}{\epsilon \sigma T_{\text{sub}}^3}. \quad (5)$$

Here Γ is the thermal inertia, $\Delta_s = \omega_s - n$ is the relative frequency, ϵ is the emissivity, $\sigma = 5.67 \times 10^{-8} \text{ W m}^{-2} \text{ K}^{-4}$ is the Stefan-Boltzmann constant, and $T_{\text{sub}} = ((1-A)\Phi/\epsilon\sigma)^{1/4}$ is the subsolar temperature.

The total binary Yarkovsky effect is the combined contribution of both the primary and secondary asteroids. For the primary component, in principle, there is a mirror effect to the secondary. The formula for the primary can be obtained by simply replacing the subscript ‘s’ with ‘p’ in Eqs. (1) and (4), which gives

$$f_{\text{YS},p} = \frac{4r_s}{9\pi a} \frac{\Theta_p}{2 + 2\Theta_p + \Theta_p^2} \text{Sign}(n - \omega_p). \quad (6)$$

However, due to the complexity of the geometry of the shadow cast on the primary component by the secondary component, this may not be accurate. In the derivation of Eq. (4), we assumed that the entire body stops receiving sunlight once its mass centre enters the shadow region, for the sake of simplifying the calculation. This assumption is reasonable for the secondary but not for the primary component since only a portion of the primary enters the eclipse at any given time (similar to a solar eclipse on Earth caused by the Moon). This partial eclipse reduces the strength of the YS effect, which heavily depends on the shadow; because of its induced non-linearity, a numerical approach is required to solve it.

This study ignores the planetary Yarkovsky (pY) effect on the primary, which is caused by the radiation from the secondary asteroid, as it is expected to be minimal. It would only induce a correction factor of $(1 - \pi r_s/4a) \sim 1$ for the overall effect for the primary.

3. Numerical model

The radiation force of a surface element is $\propto \sigma T^4 S$, where T denotes the temperature and S denotes the surface area. Thus, to obtain the radiation force, we need to obtain the surface temperature of the shape model.

An irregular shape could produce the BYORP torque (Čuk & Burns 2005). To eliminate the influence of the BYORP effect, we chose a spherical shape model approximated by a polyhedron with 1280 triangulated facets as the shape model. This symmetric shape model introduces a BYORP-induced error of only 10^{-6} to f_{YS} , which is negligible compared to $f_{\text{YS}} \sim 10^{-3}$.

The temperature, T , of the surface and the layer beneath is governed by

$$\frac{\partial T}{\partial t} = \frac{\kappa}{C\rho} \frac{\partial^2 T}{\partial z^2}, \quad (7)$$

with two boundary conditions,

$$\kappa \frac{\partial T}{\partial z} \Big|_{z=0} = E(t) - \epsilon \sigma T^4 \Big|_{z=0}, \quad (8)$$

$$\kappa \frac{\partial T}{\partial z} \Big|_{z \rightarrow \infty} = 0, \quad (9)$$

where t is the time, κ is the thermal conductivity, C is the specific heat capacity, ρ is the bulk density of the asteroid, and ϵ is the emissivity. In this study we set $\kappa = 0.1 \text{ W m}^{-1} \text{ K}^{-1}$,

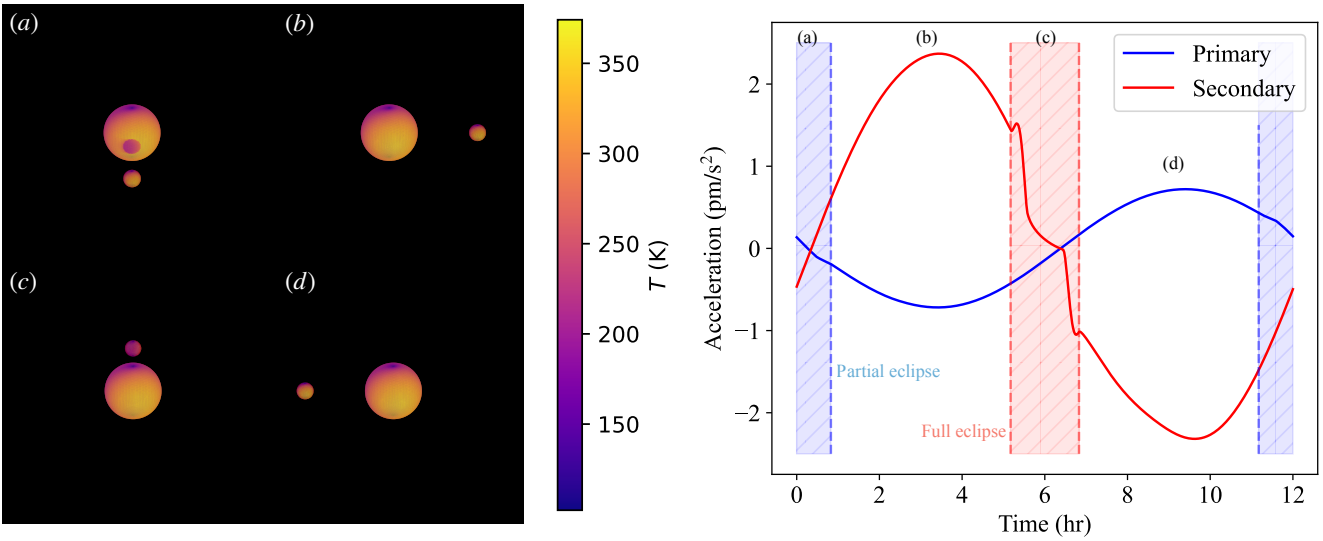


Fig. 1. Left: Snapshots of the temperature field of the binary asteroids. Diagrams (a)–(d) illustrate the anti-clockwise orbit of the secondary asteroid around the primary. Both the primary and secondary have spin rates of 3 hours. The other properties of the binary system are detailed in Sect. 4.1. In phase (a) the primary is partially eclipsed by the secondary, while in phase (c) the primary fully eclipses the secondary. Right: Tangential accelerations due to thermal forces for the primary (blue) and secondary (red). The eclipse periods are represented by shaded areas.

$C = 550 \text{ J K}^{-1} \text{ kg}^{-1}$, and $\rho = 2000 \text{ kg m}^{-3}$ for both the primary and secondary components by default. This gives a thermal inertia $\Gamma = \sqrt{C\rho\kappa} \sim 330 \text{ tiu} [\text{J m}^{-2} \text{ K}^{-1} \text{ s}^{-1/2}]$, which is close to the measured mean value of $\sim 200 \text{ tiu}$ for kilometre-sized near-Earth objects (NEOs; Delbo' et al. 2007). According to in situ measurements, asteroids Ryugu and Bennu have thermal inertia values of $225 \pm 45 \text{ tiu}$ (Shimaki et al. 2020) and $350 \pm 20 \text{ tiu}$ (DellaGiustina et al. 2019), respectively. The one-dimensional heat conduction equation (Eq. (7)) is sufficient for our problem since our interests lie in binary asteroid systems whose components are much larger than the thermal penetration depth; the latter is approximately a few centimetres. A full three-dimensional heat conduction equation is needed when investigating small (sub-centimetre-scale) dust.

We solved the temperature $T_{i,j,k}$ at a depth of $(j-1)\delta z$ below the i -th facet at the k -th time step using the numerical scheme described in Zhou & Michel (2024). The thermal equilibrium state, where the intake energy equals the released energy of the system, is usually established after ~ 50 mutual orbits unless the thermal inertia is considerably high (e.g. $> 1000 \text{ tiu}$). A snapshot of our simulation is shown in Fig. 1. With the surface temperature, one can obtain the radiation force in the k -th timestep for the whole body via

$$\mathbf{F}_k = -\frac{2\epsilon\sigma}{3c} \sum_i T_{i,0,k}^4 S_i \mathbf{n}_i, \quad (10)$$

where S_i and \mathbf{n}_i are the area and the normal vector of the i -th surface element, respectively. The tangential component of the force, which is the source of the Yarkovsky effect, in the k -th timestep is then easily obtained as $\mathbf{F}_k \cdot \mathbf{v}_k / v_k$, assuming a circular orbit. The YS coefficient is calculated as

$$f_{\text{YS}} = \frac{1}{k_{\text{max}}} \sum_k \frac{\mathbf{F}_k \cdot \mathbf{v}_k \cdot c}{v_k \Phi (1-A) \sum_i S_i}, \quad (11)$$

with A , the albedo of the asteroid, being ~ 0.1 . The mutual heating between the primary and the secondary was ignored due to its minimal contribution to the overall effect on the primary.

4. Results and implications

We investigate the YS coefficient as a function of the frequency ratio, ω_p/n , in Sect. 4.1 and propose an empirical modified formula for BYP in Sect. 4.2. Finally, we discuss the implications of the BYP on the long-term evolution of binary asteroids and estimate its magnitude for known synchronous binary asteroids in Sect. 4.3.

For simplicity, we assumed the spin vector of the primary asteroid aligns with the mutual orbit vector and considered the mutual orbit to be co-planar with the heliocentric orbit, given the low inclinations (i.e. $i < 30^\circ$) observed in real binary asteroids (Pravec et al. 2012). Low inclinations are likely common as these systems are believed to form via YORP-driven spin-up and mass shedding followed by re-accumulation in the equatorial plane of the primary (Walsh et al. 2008; Pravec et al. 2012; Zhang et al. 2021; Agrusa et al. 2024). We note that this assumption leads to an upper limit for our estimated Yarkovsky effect. The dependence of the BYS and BYP on non-zero inclinations is discussed in Appendix A.

4.1. Synchronization of the mutual orbit

We considered a typical small binary asteroid system on a heliocentric circular orbit with a heliocentric semi-major axis $a_h = 1 \text{ au}$. We set the semi-major axis of the mutual $a \approx 3.1r_p$ to keep the orbital period $P = 12 \text{ h}$. By varying the spin periods of the primary and the secondary, we obtain the YS coefficient as a function of the frequency ratio, ω_p/n , which can be easily translated to Δ_s via Eq. (4) and Δ_p via Eq. (6).

Figure 2 shows the YS coefficient, $f_{\text{YS},p}$, for the primary, obtained from the numerical model and the simple analytical model, as a function of the frequency ratio, ω_p/n . The Yarkovsky force has the same sign as the YS coefficient. The YS coefficient is positive when ω_p/n is smaller than 1, indicating the mutual orbit will expand under the Yarkovsky force. On the other hand, when ω_p/n is larger than 1, the YS coefficient is negative, implying a shrinking orbit. The Yarkovsky force vanishes when the primary is in a synchronous state, $\omega_p = n$. Therefore, we

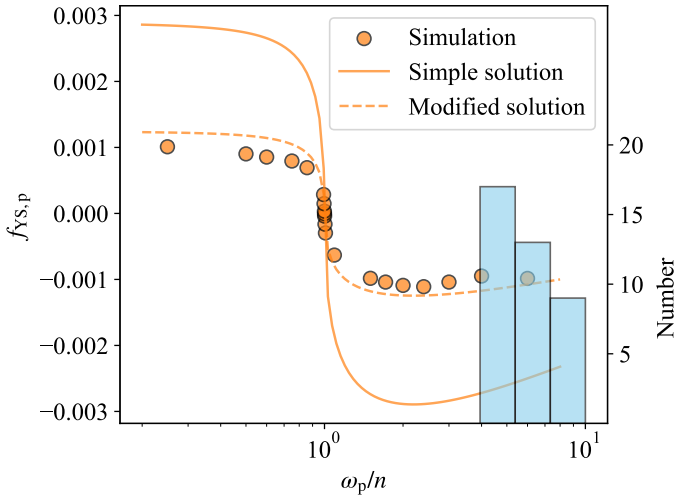


Fig. 2. YS coefficient for the primary as a function of the ratio of spin velocity to mean motion. The primary asteroid has a radius of 1 km, and the secondary has a radius of 0.3 km. Gold circles represent the numerical results. The solid gold curve shows the simple analytical solution from Eq. (6), while the dashed gold curve shows the modified solution from Eq. (12) with $\alpha = 1.7$. The ω_p/n distribution of confirmed binary asteroids is depicted in the blue histogram, which is truncated at 10.

conclude that the BYP pushed the mutual orbit towards the synchronous orbit of the primary component.

However, we observe that the magnitude of the numerical results deviates slightly from the analytical results, which may be due to the partial eclipse on the primary, as discussed in the following section.

4.2. Empirical formula for the primary

Ideally, the ratio of $f_{YS,p}$ to $f_{YS,s}$ should be proportional to r_s/r_p . However, due to the non-linear effect produced by the partial eclipse stated above, the YS coefficient for the primary, assuming the same physical properties as the secondary except the size, is affected by a non-linear dependence on r_s . As a result, the ratio of $f_{YS,p}$ to $f_{YS,s}$ is better described as

$$\tilde{f}_{YS,p} = \left(\frac{r_s}{r_p}\right)^\alpha f_{YS,s} = \left(\frac{r_s}{r_p}\right)^{\alpha-1} f_{YS,p}, \quad (12)$$

where $f_{YS,s}$ and $f_{YS,p}$ can be obtained from Eqs. (4) and (6), respectively.

We searched the best-fit α for the numerical results by minimizing the sum of the squares of the difference between simulation results and the fitted values, as shown in the left panel in Fig. 3. The right panel of Fig. 3 shows the values of α under different frequency ratios, ω/n , and thermal inertia. We find that α is insensitive to ω/n but shows a clear decreasing trend with increasing thermal inertia. The values of α are 1.81 ± 0.05 , 1.77 ± 0.05 , 1.75 ± 0.05 , 1.70 ± 0.04 , and 1.65 ± 0.03 for $\Gamma = 100, 200, 300, 500$, and 1000 tui [$\text{J m}^{-2} \text{s}^{-1/2} \text{K}^{-1}$], respectively. One-kilometre-sized objects typically have a thermal inertia of around 300 tui (Delbo' et al. 2007), as seen in Didymos (Rivkin et al. 2023; Rozitis et al. 2024). Once α was determined, we obtained the modified $f_{YS,p}$ solution. An example of the modified $f_{YS,p}$ solution with $\alpha = 1.7$ is shown in Fig. 2 (dashed gold curve). It fits the simulation much better than the simple solution with $\alpha = 1$.

4.3. Implications

We have demonstrated that the BYP moves the primary asteroid towards a synchronous orbit, albeit on a longer timescale than the BYS. Together with the BYS (Zhou et al. 2024) and the BYORP effect (Ćuk & Burns 2005), this forms a unified description of radiative forces acting on binary asteroid systems, as summarized in Table 1: For an asynchronous component, the binary Yarkovsky effect is at play; for a synchronous component with an asymmetric shape, the binary YORP effect is dominant; and for a synchronous component with a symmetric shape, there is no significant secular radiative effect.

Based on this framework, we summarize the primary dynamics for different types of binary asteroids as follows. For synchronous binaries where both components are asynchronous, the BYS, the BYP, and tidal effects are all active. The BYS dominates over the BYP and, with the assistance of tidal effects, drives the secondary component towards a synchronous state. The synchronization timescale for a binary asteroid system with a primary radius of approximately 1 km is roughly 0.1 million years (Zhou et al. 2024). For larger objects, the tidal effect predominates over the BYS. The YORP effect may also contribute to synchronization, though its stochastic nature is not yet well constrained (Statler 2009; Golubov & Krugly 2012; Bottke et al. 2015; Zhou et al. 2022).

For singly synchronous binaries where the secondary is synchronous, which is the most common type of known binary asteroids, BYP, BYORP (acting on the secondary), and tidal effects are all active. The BYP is expected to shrink the orbit of most binary asteroids given that the majority of primary asteroids in the main belt or in near-Earth orbit rotate rapidly, close to the spin limit of 2.2 hours (Walsh & Jacobson 2015). The timescale of the BYP is typically an order of magnitude longer than that of the BYS and depends on the size ratio of the two components. The BYORP effect is predicted to act on a timescale ranging from 0.01 to 10 million years with a random direction and depends on factors such as shape (Ćuk & Burns 2005; McMahon & Scheeres 2010; Steinberg 2011; Jacobson & Scheeres 2011), surface roughness (Ćuk et al. 2024), and rotational state (Quillen et al. 2022).

For doubly synchronous binaries (i.e. both components are synchronous), the BYORP effect acts on both components. Tidal effects also become significant in eccentric orbits (Wisdom 2008; Goldberg & Batygin 2024) or for librating objects (Scheeres 2009; Jacobson et al. 2014).

While the magnitude of the BYORP effect remains largely uncertain due to the unconstrained shape and fine surface structures of most asteroids, the BYP can be estimated quickly using the formula in this work (see Eq. (12)). We have estimated the YS coefficients and orbital drift rates for known synchronous binary asteroids with detected spin periods and orbital periods (Pravec & Harris 2007; Warner et al. 2009; Pravec et al. 2012, 2016; Monteiro et al. 2023). As an order-of-magnitude approximation, we assumed spherical binaries that have relatively low inclinations, which ensures that these binaries experience eclipses during each mutual orbit. This assumption is appropriate for most binary asteroids (Pravec et al. 2012). The binary Yarkovsky effect is expected to be insensitive to shape, except in cases of extreme irregularity, which is unrealistic for binary asteroids. These bodies are expected to have relatively regular shapes following rotational disruption. All of these binary asteroids shrink the mutual orbit under the BYP due to their faster spin relative to the mean motion (see also the histogram in Fig. 2).

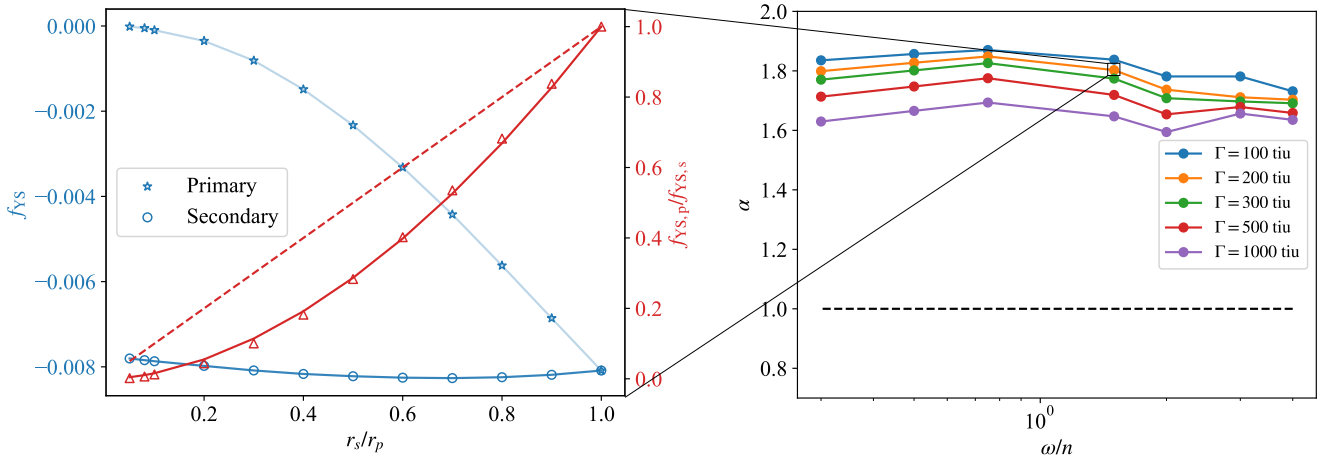


Fig. 3. Left: YS coefficient as a function of the secondary-to-primary size ratio. The primary asteroid has a radius of 1 km. The orbital period is 12 hours, and the spin periods of both components are 8 hours. The ratio of the primary-to-secondary YS coefficient is indicated by red triangles. The solid red line represents the best-fit curve: $f_{YS,p}/f_{YS,s} = (r_s/r_p)^{1.80}$. The dashed red line shows the theoretical formula without accounting for the non-linear effect of partial eclipses: $f_{YS,p}/f_{YS,s} = (r_s/r_p)$. Right: Value of α as a function of the frequency ratio and thermal inertia. The dashed black line represents the theoretical value, excluding the non-linear effects of partial eclipses. For a typical small binary system with $\Gamma \sim 200$ tiu and a primary spin period of approximately three hours, α is around 1.8.

Table 1. Radiative effects on the object in a binary system.

| Shape | Orbit | |
|------------|-------------|------------------|
| | Synchronous | Asynchronous |
| Symmetric | Null | Binary Yarkovsky |
| Asymmetric | Binary YORP | Binary Yarkovsky |

Notes. The binary Yarkovsky effect includes the pY effect and the YS (eclipse-induced) effect.

Figure 4 shows that for the known small binary asteroids, the absolute value of $f_{YS,p}$ ranges from 10^{-4} to a few $\times 10^{-3}$ and the BYP-induced orbital drifting rate from -0.001 cm yr $^{-1}$ to -1 cm yr $^{-1}$. For comparison, the typical BYORP coefficient is $\sim 10^{-3}$ (McMahon & Scheeres 2010; Jacobson & Scheeres 2011) and decreases with reduced relative surface roughness (Ćuk et al. 2024). There is a clear trend that larger and colder binary asteroids have smaller values of $f_{YS,p}$ and \dot{a} (located towards the left and bottom of the plot). Thermal inertia influences these results in a complex manner. Generally, within the range of 100–500 tiu, as thermal inertia increases, the Yarkovsky effect decreases for more distant objects (e.g. middle and outer main belt objects), while it strengthens for closer objects (e.g. NEOs and inner main belt objects).

We compared our results with four binary asteroids that have observed orbital migration. The estimated binary Yarkovsky effect versus observed values are as follows: -0.05 versus -0.08 ± 0.02 cm yr $^{-1}$ (Scheirich & Pravec 2022; Scheirich et al. 2024; Naidu et al. 2024) for pre-impact Didymos, -0.079 versus -0.07 ± 0.34 cm yr $^{-1}$ (Scheirich et al. 2015) for 1996 FG₃, -0.13 versus -2.8 ± 0.2 cm yr $^{-1}$ (Scheirich et al. 2021) for 2001 SL₉, and -0.19 versus 1.2 cm yr $^{-1}$ (Scheirich et al. 2021) for 1999 KW₄. For pre-impact Didymos and 1996 FG₃, the BYP predicts orbital drift rates close to the observed values. However, for asteroid 2001 SL₉, our estimated BYP-induced orbital drift rate is an order of magnitude lower than the observed value. Furthermore, the outward drift of 1999 KW₄ cannot be explained by the BYP alone, suggesting the presence of additional mechanisms,

such as a strong tidal effect, a BYORP effect on a synchronous secondary, or the BYS on an asynchronous secondary. Further observational data are needed to better understand the complex long-term dynamics of binary asteroids.

In Vokrouhlický et al. (2005)’s pioneering work on the Yarkovsky effect in binary asteroids, simulations of asteroid 2000 DP₁₀₇ showed that the mean transverse acceleration of the mutual orbital motion is $\sim -6 \times 10^{-15}$ m s $^{-2}$ assuming $K = 0.1$ W m $^{-1}$ K $^{-1}$, $C = 800$ J kg $^{-1}$ K $^{-1}$, and $\rho = 1.7$ g cm $^{-3}$ for both components. This translates to an orbital drift rate of about $\dot{a} \sim -0.85$ cm yr $^{-1}$. In their simulation, the primary and secondary are both spherical polyhedral shape models with the assumption of a synchronous secondary. Therefore, their results reflect the BYP. Our theoretical estimate of -0.27 cm yr $^{-1}$ is consistent in both sign and order of magnitude with the previous simulation result despite some deviation that may arise from the system’s eccentricity.

5. Conclusion

This work, together with our previous work on the BYS (Zhou et al. 2024), completes the basic theoretical framework of the binary Yarkovsky effect. The BYP is shown to modify the mutual orbit after the secondary asteroid reaches synchronization. The timescale of the BYP is generally an order of magnitude longer than that of the BYS and depends on the size ratio between the secondary and primary.

We propose an empirical modified formula to estimate the BYP: applying the traditional binary Yarkovsky formula (Eq. (6)) and then multiplying it by $(r_s/r_p)^{(\alpha-1)}$ (see Eq. (12)). Our numerical results indicate that α is relatively insensitive to the frequency ratio, ω/n , but decreases with increasing thermal inertia. For a typical small binary asteroid system with $\Gamma = 200$ tiu, the best-fit value for α is approximately 1.7. We summarize the primary mechanisms for binary asteroid systems as follows: the BYS and tidal effects are active for asynchronous binaries, while BYS, BYORP, and tidal effects operate in singly synchronous binaries, which are the most commonly observed binary asteroids.

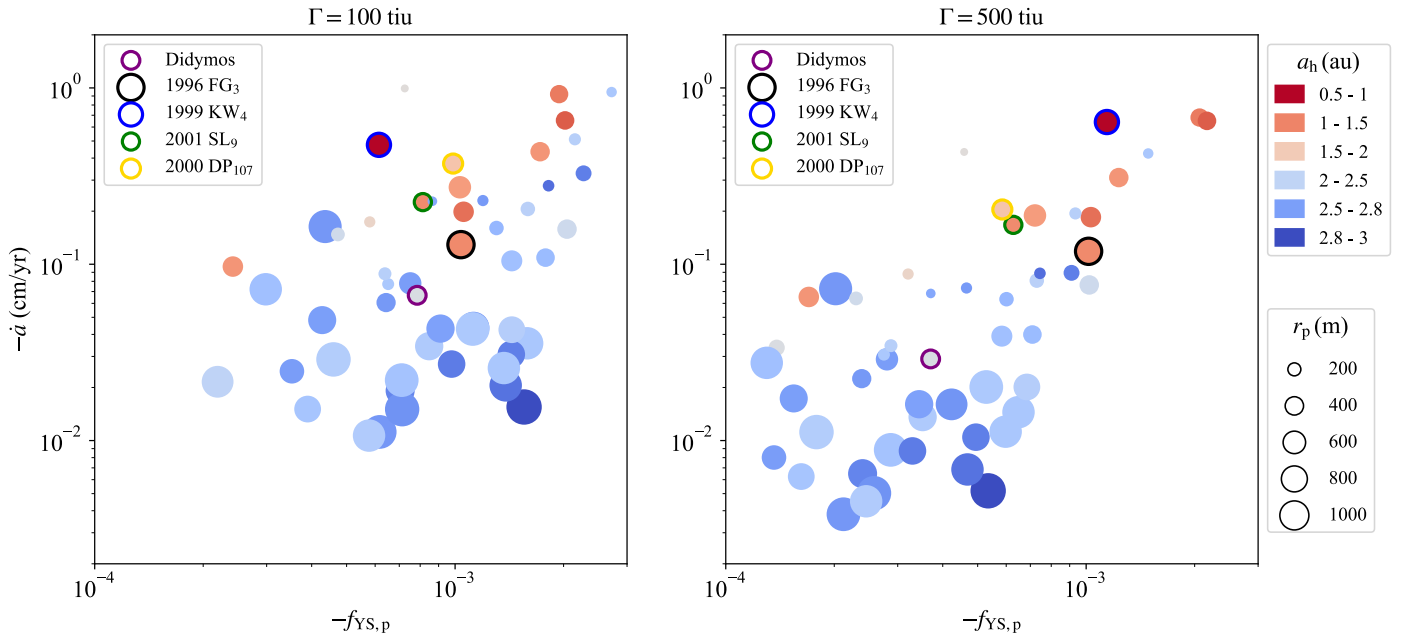


Fig. 4. YS coefficient and YS-induced orbital drift rate for confirmed small binary asteroids, assuming thermal inertia of 100 tiu (left) and 500 tiu (right). The colours indicate the heliocentric semi-major axis, with bluer colours representing greater distances from the Sun. The size of each circle corresponds to the size of the primary asteroid. As thermal inertia increases, blue dots tend to move downwards and red dots upwards, although the outcome is a complex function of thermal inertia.

We estimated BYP-induced drift rates for known small binary asteroids with primary radii $r_p < 1$ km. These drift rates range from -0.001 to -1 cm yr^{-1} . For middle and outer main belt objects, the BYP tends to decrease with increasing thermal inertia, whereas for NEOs and inner main belt objects, the BYP increases with increasing thermal inertia.

We compared our results with the observed orbital drift rates of four binary systems. Our findings are consistent with the pre-impact Didymos and 1996 FG₃ systems but show discrepancies for the 2001 SL₉ and 1999 KW₄ systems. We suggest that a complicated model involving BYP, BYORP, and tidal effects is required to fully understand the long-term dynamics of binary systems.

Acknowledgements. I thank the referee for the constructive suggestions. I thank David Vokrouhlický for his valuable suggestions. I am also grateful to Patrick Michel and Seiji Sugita for their support of this research. I would like to acknowledge the mobility aid from the Université Côte d’Azur and funding support from the Chinese Scholarship Council (No. 202110320014).

References

Agrusa, H. F., Zhang, Y., Richardson, D. C., et al. 2024, *Planet. Sci. J.*, **5**, 54
 Bottke, W. F., Vokrouhlický, D., Walsh, K. J., et al. 2015, *Icarus*, **247**, 191
 Cueva, R. H., McMahon, J. W., Meyer, A. J., et al. 2024, *Planet. Sci. J.*, **5**, 48
 Čuk, M. 2007, *ApJ*, **659**, L57
 Čuk, M., & Burns, J. A. 2005, *Icarus*, **176**, 418
 Čuk, M., & Nesvorný, D. 2010, *Icarus*, **207**, 732
 Čuk, M., Agrusa, H., Cueva, R. H., et al. 2024, *Planet. Sci. J.*, **5**, 166
 Delbo’, M., dell’Oro, A., Harris, A. W., Mottola, S., & Mueller, M. 2007, *Icarus*, **190**, 236
 DellaGiustina, D., Emery, J., Golish, D., et al. 2019, *Nat. Astron.*, **3**, 341
 Farinella, P., & Vokrouhlický, D. 1996, *Planet. Space Sci.*, **44**, 1551
 Farinella, P., Vokrouhlický, D., & Hartmann, W. K. 1998, *Icarus*, **132**, 378
 Gladman, B., Michel, P., & Froeschlé, C. 2000, *Icarus*, **146**, 176
 Goldberg, M., & Batygin, K. 2024, *Icarus*, **413**, 116014
 Golubov, O., & Krugly, Y. N. 2012, *ApJ*, **752**, L11
 Jacobson, S. A., & Scheeres, D. J. 2011, *ApJL*, **736**, L19
 Jacobson, S. A., Scheeres, D. J., & McMahon, J. 2014, *ApJ*, **780**, 60
 Liberato, L., Tanga, P., Mary, D., et al. 2024, *A&A*, **688**, A50

Margot, J. L., Pravec, P., Taylor, P., Carry, B., & Jacobson, S. 2015, *Asteroids IV* (University of Arizona Press), 355
 McMahon, J., & Scheeres, D. 2010, *Icarus*, **209**, 494
 Métris, G., Vokrouhlický, D., Ries, J. C., & Eanes, R. J. 1997, *J. Geophys. Res.*, **102**, 2711
 Milani, A., Nobili, A. M., & Farinella, P. 1987, *Non-gravitational Perturbations and Satellite Geodesy* (CRC Press)
 Minker, K., & Carry, B. 2023, *A&A*, **672**, A48
 Monteiro, F., Lazzaro, D., Rondón, E., et al. 2023, *Icarus*, **390**, 115297
 Murray, C. D., & Dermott, S. F. 1999, *Solar System Dynamics* (Cambridge university press)
 Naidu, S. P., Chesley, S. R., Moskovitz, N., et al. 2024, *Planet. Sci. J.*, **5**, 74
 Pravec, P., & Harris, A. W. 2007, *Icarus*, **190**, 250
 Pravec, P., Scheirich, P., Vokrouhlický, D., et al. 2012, *Icarus*, **218**, 125
 Pravec, P., Scheirich, P., Kušnirák, P., et al. 2016, *Icarus*, **267**, 267
 Quillen, A. C., LaBarca, A., & Chen, Y. 2022, *Icarus*, **374**, 114826
 Richardson, D. C., Agrusa, H. F., Barbee, B., et al. 2024, *Planet. Sci. J.*, **5**, 182
 Rivkin, A. S., Thomas, C. A., Wong, I., et al. 2023, *Planet. Sci. J.*, **4**, 214
 Rozitis, B., Green, S. F., Jackson, S. L., et al. 2024, *Planet. Sci. J.*, **5**, 66
 Rubincam, D. P. 1982, *Celest. Mech.*, **26**, 361
 Rubincam, D. P. 2006, *Icarus*, **184**, 532
 Rubincam, D. P. 2014, *Icarus*, **239**, 96
 Scheeres, D. J. 2009, *Celest. Mech. Dyn. Astron.*, **104**, 103
 Scheirich, P., & Pravec, P. 2022, *Planet. Sci. J.*, **3**, 163
 Scheirich, P., Pravec, P., Jacobson, S. A., et al. 2015, *Icarus*, **245**, 56
 Scheirich, P., Pravec, P., Kušnirák, P., et al. 2021, *Icarus*, **360**, 114321
 Scheirich, P., Pravec, P., Meyer, A. J., et al. 2024, *Planet. Sci. J.*, **5**, 17
 Shimaki, Y., Senshu, H., Sakatani, N., et al. 2020, *Icarus*, **348**, 113835
 Statler, T. S. 2009, *Icarus*, **202**, 502
 Steinberg, E., et al. 2011, *AJ*, **141**, 55
 Virkki, A. K., Marshall, S. E., Venditti, F. C. F., et al. 2022, *Planet. Sci. J.*, **3**, 222
 Vokrouhlický, D., Čapek, D., Chesley, S. R., & Ostro, S. J. 2005, *Icarus*, **179**, 128
 Vokrouhlický, D., Nesvorný, D., Dones, L., & Bottke, W. F. 2007, *A&A*, **471**, 717
 Walsh, K. J., & Jacobson, S. A. 2015, *Asteroids IV* (University of Arizona Press), 375
 Walsh, K. J., Richardson, D. C., & Michel, P. 2008, *Nature*, **454**, 188
 Warner, B. D., Harris, A. W., & Pravec, P. 2009, *Icarus*, **202**, 134
 Wisdom, J. 2008, *Icarus*, **193**, 637
 Zhang, Y., Michel, P., Richardson, D. C., et al. 2021, *Icarus*, **362**, 114433
 Zhou, W.-H., & Michel, P. 2024, *A&A*, **682**, A130
 Zhou, W.-H., Zhang, Y., Yan, X., & Michel, P. 2022, *A&A*, **668**, A70
 Zhou, W.-H., Vokrouhlický, D., Kanamaru, M., et al. 2024, *ApJ*, **968**, L3

Appendix A: Discussion on non-zero inclination cases

The inclination i is defined as the angle between the vectors of the mutual orbit and the heliocentric orbit. A non-zero inclination complicates the thermal perturbation caused by the shadow. We offer an estimate of the non-zero inclination and justify the importance of BYP on real binary asteroids. A comprehensive numerical investigation on how a non-zero inclination affects both BYS and BYP is out of the scope of this paper and is left for future study due to its complexity. Our following simple estimation is based on the principle that the strength of the YS effect is generally proportional to the solar flux loss due to the shadow. We will use an inclination-dependent factor f_i to describe the ratio of the YS effect for a non-zero inclination relative to the case with zero inclination.

To begin, we considered how inclination influences the YS effect on the secondary. When the inclination is non-zero, the shadow cast by the secondary on the primary no longer remains fixed at the equator but oscillates around it, reaching a maximum altitude, β . Because the primary is approximately spherical, the duration it experiences shadowing is roughly proportional to $\cos\beta$, leading to a weakening factor of

$$f_{i,s} = \cos\beta. \quad (\text{A.1})$$

The parameter β can be estimated via simple geometry,

$$\sin\beta = \frac{a \tan i}{r_p}. \quad (\text{A.2})$$

A $\sin\beta < 1$ naturally necessitates a low inclination, $i < \arctan(r_p/a) \simeq r_p/a$, for the occurrence of the shadow.

The case for the primary would be a bit different. The shadow cast by the secondary on the primary is above the equator rather than at the equator when the inclination is not zero. These high-altitude areas affected by the shadow have lower temperatures than the equator, as the total incident solar energy decreases by a factor of $\cos\beta$. Consequently, the overall YS effect would be reduced by a factor of

$$f_{i,p} = \cos^2\beta. \quad (\text{A.3})$$

Recall that the binary Yarkovsky effect also includes the pY effect in addition to the YS effect. The strength of pY effect is approximated by the YS coefficient multiplied by $-\pi r_p/a$ for the secondary and $-\pi r_s/a$ for the primary. Therefore, compared to Eq. 2, the total binary Yarkovsky coefficient becomes more complicated for non-zero inclination cases:

$$f_{\text{BY},s} = \left(\cos\beta - \frac{\pi r_p}{4a} \right) f_{\text{YS},s} \quad (\text{A.4})$$

for the secondary and

$$f_{\text{BY},p} = \left(\cos^2\beta - \frac{\pi r_s}{4a} \right) f_{\text{YS},p} \quad (\text{A.5})$$

for the primary. We note that the typical values for $f_{\text{YS},s}$ and $f_{\text{YS},p}$ are 0.01 (Zhou et al. 2024) and 0.001 (Fig. 2), respectively.

Figure A.1 shows the value of the binary Yarkovsky coefficient as a function of inclination, described by Eqs. A.4 and A.5. It is seen that YS decreases with the inclination and vanishes with a critical inclination, within which the eclipse always occurs during a mutual orbit. In contrast, the pY effect remains independent of inclination, as it is driven by radiation from the companion object within the binary system. There is a specific

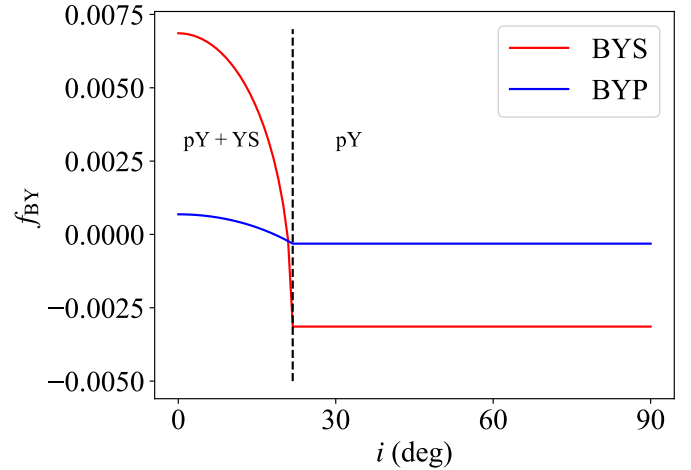


Fig. A.1. Binary Yarkovsky coefficient as a function of the inclination for the secondary (red) and the primary (blue). The dashed black line is the critical inclination (i.e. $\arctan(r_p/a)$), within which the eclipse always occurs during a mutual orbit. The values of parameters to calculate f_{BY} (Eqs. A.4 and A.5) are set as follows: $a/r_p = 2.5$, $f_{\text{BY},s} = 0.01$ and $f_{\text{BY},p} = 0.001$. In this figure, a positive value of f_{BY} represents the migration direction towards the synchronous orbit and a negative value denotes the opposite direction to the synchronous orbit.

inclination at which pY cancels out YS, resulting in the disappearance of the binary Yarkovsky effect.

When the inclination is low and YS dominates, the binary Yarkovsky effect tends to synchronize the orbit. Conversely, at high inclinations where pY is dominant, the effect causes desynchronization. The assumption of zero inclination in the main text maximizes the binary Yarkovsky effect and ensures mutual orbital synchronization. Although the strength of the binary Yarkovsky effect diminishes with increasing inclination, it does not change by more than an order of magnitude except near the critical inclination (i.e. $\arctan(r_p/a)$), justifying the importance of the binary Yarkovsky effect for most of the binary asteroids.

We note that a more detailed numerical investigation of the role of the inclination is required in the future, especially considering the non-zero obliquities that complicate the problem significantly.

Part III

YORP EFFECT AND ROTATIONAL EVOLUTION

A ROTATIONAL EVOLUTION MODEL EXPLAINING THE OBSERVED SPIN DISTRIBUTION

There are three mysteries regarding the slowly rotating asteroids in the main belt:

- Excess of slow rotators. The overabundance of asteroids rotating slowly was realized about 40 years ago. Collisions typically produce a Maxwell distribution in the spin rate and the classic YORP theory produces a uniform distribution. The existing theory cannot explain the excess of slow rotators.
- Gap. Recent Gaia observation reveals a visible gap in the period-diameter distribution of asteroids, which separates the slow rotators from faster rotators. Classic theory only predicts smooth distributions without any kind of gap.
- Tumbler distribution. The distribution of tumbling asteroids in the period-diameter is not well explained.

This chapter attempted to solve the above three problems by constructing a novel comprehensive rotation evolution model and fitting it to Gaia observation. The attached paper is in press on the journal *Nature Astronomy*.

Author Contributions: W.H. Zhou led the project. W.H. Zhou proposed the model, derived the formula, carried out the numerical simulations, analyzed the results, and led the writing of the paper. M. Delbo and W.H. Zhou initiated the collaboration. W.C. Wang, Y. Wang, and W.H. Zhou led the gap identification using machine learning. M. Delbo and P. Michel contributed to writing the manuscript. J. Āurech and J. Hanuř provided the asteroid data based on Gaia observations. All authors collaborated on the interpretation of the results.

Confined tumbling state as the origin of the excess of slowly rotating asteroids

Wen-Han Zhou^{1*}, Patrick Michel^{1,2}, Marco Delbo¹, Wenchao Wang³,
Bonny Y. Wang⁴, Josef Ďurech⁵, Josef Hanuš⁵

¹Laboratoire Lagrange, Observatoire de la Côte d'Azur, Université Côte
d'Azur, Nice, France.

²Department of Systems Innovation, University of Tokyo, Tokyo, 10587,
Japan.

³Department of Physics, University of Hong Kong, Hong Kong, China.

⁴Center for Computational Astrophysics, Flatiron Institute, New York, USA.

⁵Charles University, Faculty of Mathematics and Physics, Institute of
Astronomy, V Holešovičkách 2, 180 00 Prague, Czech Republic.

*Corresponding author(s). E-mail(s): wenhan.zhou@oca.eu;

Abstract

The rotational distribution of asteroids as a function of their size is used as a diagnostic of their physical properties and evolution. Recent photometric surveys from the Gaia mission, allowing observation of long (e.g. $\gtrsim 24$ h) period asteroids, found an excessive group of slow rotators and a gap separating them from faster rotators, which is unexplained by current theories. Here we developed an asteroid rotational evolution model capable of reproducing the observed distribution. We suggest that this distribution is regulated by the competition between collisions and internal friction dampening of "tumbler" -asteroids with unstable rotation vectors, and that the slow rotator group is mainly populated by tumblers. We constrain the product of the rigidity and quality factor, which relates to the body's viscosity, to $\mu Q \sim 4 \times 10^9$ Pa. This number, two orders of magnitude smaller than the one assumed for monolithic boulders, implies that rubble pile asteroids could have a porous structure or a thick regolith layer, and undergo stronger tidal effects.

27 1 Introduction

28 It was initially assumed that asteroid rotation distribution had to take a Maxwellian form,
29 peaking at about four revolutions per day as the result of the collision-induced random distri-
30 bution of their spin vectors in three-dimensional velocity space [1]. However, as observations
31 progressed, an excess of fast rotators near the spin barrier (2.2 hours) [2, 3] and of slow
32 rotators was noted for small asteroids [2–9]. The excess of fast rotators has been modeled
33 [3] as due to spin up until the spin barrier by the Yarkovsky–O’Keefe–Radzievskii–Paddack
34 (YORP) effect, which is a thermal torque influencing asteroids’ rotation rates over a long term
35 [10, 11]. The YORP effect has indeed been observed for eleven asteroids [12–15].

36 On the other hand, the abnormal excess of slow rotators is not captured by the prevail-
37 ing model involving the YORP effect and collisions [3]. Prior studies have modeled this
38 excess empirically, either by artificially reducing the spin acceleration by a factor of 2 [3]
39 or ceasing the rotation [16] beyond a certain period, or assigning a spin rate where lower
40 rates are more probable [17]. Yet, these methods do not rest upon a solid physical founda-
41 tion. Moreover, recent observations [18] reveal an obvious drop in the number density in
42 specific size-dependent periods, forming a visible “gap” that separates the slow rotators from
43 the faster rotators (Fig. 1).

44 Another puzzle relates to the asteroids in non-principal rotation states, termed “tumblers”
45 [19]. Observation shows that nearly all observed tumblers are distributed in the slow rotation
46 zone [19, 20]. The distribution of these tumblers is constrained by a transition line fitting
47 a power-law on period-diameter diagram [19–21], which coincidentally matches the newly
48 discovered “gap” (Fig. 1). A plausible explanation for the distribution of tumblers is still
49 lacking [21], especially for its correlation with the visible gap in the spin distribution of
50 asteroids.

51 2 Mechanism

52 2.1 Formation of the slow rotators and gap

We constructed a self-consistent rotational evolution model that takes into account collisional
excitation, internal friction damping, and the YORP effect on tumblers (see details in Meth-
ods). In this model, the tumbling motion can be initiated either by the YORP torque spinning
down the asteroid to a quasi-static rotational state [22], or by sub-catastrophic collision, the
latter occurring on a timescale:

$$\tau_{\text{col}} = \tau_{\text{col},0} \left(\frac{D}{1 \text{ km}} \right)^{(4\alpha-10)/3} \left(\frac{P}{8 \text{ h}} \right)^{(1-\alpha)/3}. \quad (1)$$

Here $\tau_{\text{col},0} = 113$ Myrs is determined by the collisional frequency of main belt asteroids
(Methods) and $\alpha = 3.2$ is the power index of the size distribution of main belt asteroids
[17]. In our simulation, we do not take into account the evolution of α (otherwise $\alpha \leq 3.2$
[23] since most of asteroids were born big [24]), because the spin distribution reaches an
equilibrium state on a relatively short timescale (~ 300 Myrs) compared to the time scales
of the evolution of the size-frequency distribution. The timescale above is shorter when the
asteroid rotates slower, indicating that tumbling is more easily triggered for slow rotators. The

tumbling motion can be damped to the principal-axis rotation by internal energy dissipation on a timescale:

$$\tau_{\text{damp}} = \tau_{\text{damp},0} \left(\frac{D}{1 \text{ km}} \right)^{-2} \left(\frac{P}{8 \text{ h}} \right)^3, \quad (2)$$

53 where $\tau_{\text{damp},0}$ depends on the viscosity (Methods). Here, the period P is the main lightcurve
 54 period, closely associated with the total angular momentum [21], which is conserved during
 55 the damping process.

56 These slow tumblers could evolve into a principal-axis rotation, a stable tumbling state
 57 with a fixed period, or a completely chaotic state (the nutation angle reaches 90°) [25],
 58 depending on the initial orientation and the asteroid shape. In a completely chaotic state,
 59 the YORP effect could be ineffective, since the radiation torque can be averaged out over
 60 a long term if its direction is random. The same logic is used to justify the absence of the
 61 binary YORP effect in non-synchronous asteroid binary system [26]. Therefore, we reason-
 62 ably assume that a tumbler has a probability p_{fix} to maintain its period. In the long-term
 63 evolution, the YORP torque is reset numerous times after collisions due to the crater-induced
 64 YORP effect [16, 27, 28] given the extreme sensitivity of YORP to small-scale topography
 65 [29]. As a result, the tumblers experience random interchanges between the tumbling states
 66 both with or without a fixed period. Therefore, the expected value of the YORP torque equals
 67 the standard YORP torque multiplied by a “weaken factor” $f_{\text{weaken}} = 1 - p_{\text{fix}}$ which is smaller
 68 than 1 (Methods).

69 As a result of a weakened YORP torque, these tumblers evolve slowly in the long-period
 70 region (Fig. 2), forming a concentrated group (Fig. 3). The terminal spin distribution of our
 71 simulation is shown in Fig. 1. The animation for the spin evolution can be found in Sup-
 72 plementary Video 1. Therefore, our results suggest that the slowly evolving tumblers are
 73 the origin of the excess of slow rotators. We compare our simulation result with the spin
 74 distribution for small asteroids between 3 km and 15 km reported by previous research
 75 [3](Supplementary Fig. 8) and constrain $f_{\text{weaken}} \sim 0.1$, assuming the YORP torque has equal
 76 probability of spinning up or down as indicated by the theoretical study [30]. Fitting the frac-
 77 tion of slow rotators in Gaia data gives $f_{\text{weaken}} \sim 0.1$ (Methods). Our model predicts that most
 78 slow rotators are tumbling, consistent with observation data [20, 21].

79 2.2 Location of the gap and its implications

The distribution of tumblers is constrained by the transition line where the collisional excita-
 tion of tumbling balances the internal energy damping. The transition line can be obtained by
 equating Eq. 1 to Eq. 2:

$$P = 8 \text{ h} \left(\frac{\tau_{\text{col},0}}{\tau_{\text{damp},0}} \right)^{3/(8+\alpha)} \left(\frac{D}{1 \text{ km}} \right)^\beta, \quad (3)$$

80 with $\beta = (4\alpha - 4)/(8 + \alpha)$. In the zone below this line, the excitation from collisions is dom-
 81 inant over damping, leading to the creation of numerous slowly rotating tumblers. However,
 82 we note that this transition line is not equivalent to the gap line but should be slightly lower
 83 than the gap line, as the tumblers may undergo minor diffusion during damping. Consider-
 84 ing $\alpha = 3.2$ [17], the slope of the transition line (Eq. 3) becomes $\beta \simeq 0.785$. The rarity
 85 of observed tumblers above the gap is consistent with our prediction, that is, the damping
 86 timescale above the gap is shorter than the excitation timescale. There is an outlier, asteroid

87 1994 XF₁, which is tumbling but located well above the gap [31], suggesting a recent col-
 88 lision event. Our calculations estimate that the most recent sub-catastrophic collision could
 89 have occurred less than four thousand years ago. This timescale is comparable to that of space
 90 weathering [32], highlighting this asteroid as a potential candidate for future spectral obser-
 91 vations. More observations could be performed for asteroids with yet unmeasured rotation
 92 states in the long-period zone in order to further test our hypothesis that the large majority of
 93 them are tumblers.

The observed gap in the period-diameter diagram (Fig. 1,3), which separates the slow rota-
 tors from faster rotators, is the boundary of these slow tumblers. We used a semi-supervised
 machine-learning method to locate the gap of the observation data from Gaia (see Meth-
 ods section: Identification of the gap by a semi-supervised machine-learning method), which
 gives

$$P = P_0 \left(\frac{D}{1 \text{ km}} \right)^{\beta_0} . \quad (4)$$

94 with $P_0 = 13.38 \text{ h}$ and $\beta_0 = 0.783$ for the observed gap. This is closely aligned with the
 95 predicted slope (i.e. 0.785) of the distribution of tumblers.

96 In our model, the location of the gap and the transition line depends on the parameter
 97 $\tau_{\text{damp},0}$, which is proportional to the ratio of the quality factor and Love number Q/k_2 . In
 98 the literature, the Love number is commonly assumed to be inversely proportional to the
 99 asteroid rigidity μ , although rigidity plays only a marginal role in dissipation, as compared to
 100 viscosity. A high k_2 means the body is easily deformed and a low Q value signifies that the
 101 body is relatively good at dissipating tidal energy and is not highly elastic [33]. This provides
 102 invaluable information on the asteroid's internal structure and composition (e.g., the layered
 103 structure and the thickness of the regolith [34]). Furthermore, it is often associated with the
 104 tidal response of a celestial body, affecting the long-term evolution of the rotation and orbit
 105 of a binary system (e.g. binary asteroids [35], Earth-Moon system [33]). However, due to
 106 the lack of seismic data or in-situ detection of tidal effects by space missions to asteroids,
 107 the value of Q/k_2 is poorly constrained despite, its importance in our understanding of the
 108 physical properties and evolution of asteroids. Our model offers a novel approach to constrain
 109 Q/k_2 by fitting the gap in the observed period-diameter distribution diagram of asteroids. We
 110 assume μQ as a constant for our considered size range (1-50 km). By fitting the gap in the
 111 simulation results to that in Gaia data (Fig. 4), our best-fit model suggests $\mu Q \sim 4 \times 10^9 \text{ Pa}$, or
 112 equivalently $Q/k_2 \sim 5 \times 10^8 (D/\text{km})^{-2}$, which produces a gap with the parameters $P_0 = 13 \pm 1 \text{ h}$
 113 and $\beta_0 = 0.78 \pm 0.06$. This leads to $\tau_{\text{damp},0} \sim 0.4 \text{ Myr}$ in Eq. 2. Our obtained value of μQ is
 114 much smaller than usually assumed $> 10^{11} \text{ Pa}$ [21, 25, 36] for monolithic boulders or 10^{13} Pa
 115 for cold less-porous solid minerals, indicating that rubble piles are weaker (e.g. have a high
 116 porosity or a thick regolith layer [34]) and more susceptible to the tidal effect than previously
 117 assumed. This leads to a faster evolution [33] and a larger equilibrium separation of binary
 118 asteroids [37].

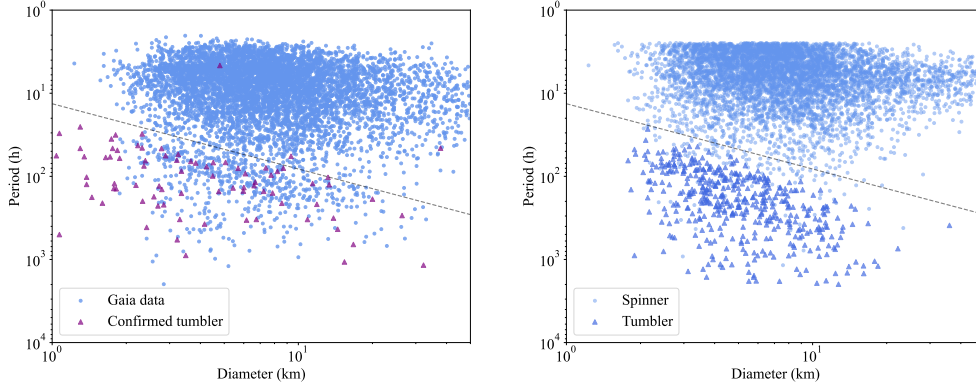


Fig. 1 Period-diameter distribution from **a**, Gaia observation [18] and **b**, simulation. The grey line represents a fitted line identifying the gap (Eq. 4). **a**. The data for the tumblers come from Asteroid Lightcurve Data Base (LCDB) [38]. **b**. This simulation adopts $\mu Q = 4 \times 10^9$ Pa, $f_{\text{weaken}} = 0.1$, and 50% positive YORP torques.

119 3 Methods

120 3.1 Identification of the gap by a semi-supervised machine-learning 121 method

122 To identify the location of the gap from a statistical perspective, we use a semi-supervised
123 machine-learning method to classify asteroid data into two groups and obtain the boundary
124 line (the gap) that separates them. For a set of data, we performed pseudo labeling by manu-
125 ally defining a grey zone as a starting reference zone for the model to locate the line, and label
126 the data above the grey region as class I, and those below as class II, as shown in Supple-
127 mentary Fig. 5. We use these well-classified data to fit a gap, using the linear Support Vector
128 Machine (SVM) model [39], which aims at finding the maximum distance between the gap
129 and two groups by using stochastic descent to converge on the solution. Expressed in the log
130 scale, the gap is described by a line with the slope (k) and the intercept (b) with $k = \beta$ and
131 $b = \log P_0$. We train the model by using the following semi-supervised approach:

- 132 1. Initialize the configuration of the gap line in log-scale: $k = 0.6$, $b = 1.2$. The y-distance
133 of the gap is 0.4. The initial values are reasonably chosen by observation. The principle of
134 choosing the values is to make sure the type of the asteroids above the gap is different from
135 the type below the gap. We leave the data points inside the grey area as unclassified data.
- 136 2. Use the manually classified data to train the linear SVC model and get the parameters of
137 the model. The parameters include k and b .
- 138 3. Use the new values of k and b obtained from the previous step to re-label the data points.
139 Similarly, the new k and b represent another gap and we label the data above the gap as
140 class I, the data below the gap as class II and leave data inside the gap as unclassified.
- 141 4. Redo step 2 by re-training the model until the gap gets converged, i.e., the values of k and
142 b have little variations during each iteration.

143 We apply the above semi-supervised machine-learning method to both the observation
144 and our simulation data. As the gap between slow rotators and fast rotators is clearly observed

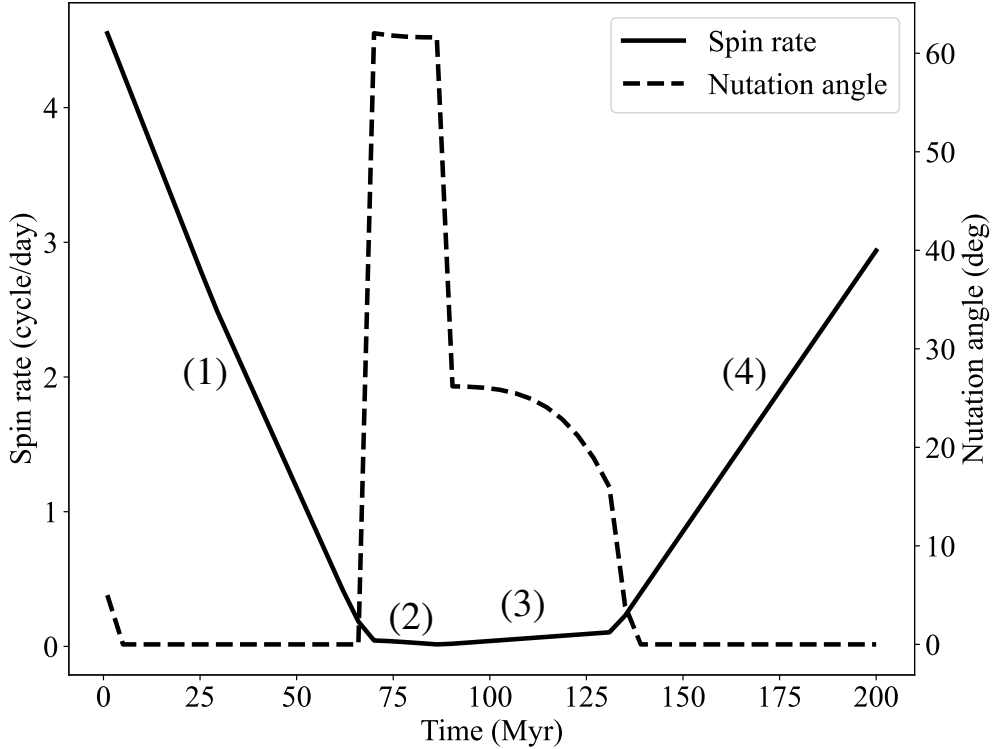


Fig. 2 Rotational evolution of a synthetic asteroid over 200 Myr. The spin rate and nutation angle are denoted by the solid and dashed lines, respectively. This asteroid follows such a typical sequence: (1) it spins down, under the YORP effect, until it goes through a sub-catastrophic collision; (2) subsequently, the tumbling motion is triggered and it spins down at a slower rate than before due to a weak YORP effect until a new tumbling state is triggered; (3) then it starts to spin up at a slow rate until the tumbling is damped; (4) it spins up at a normal YORP acceleration until getting disrupted. It can be seen that the time fraction of lifetime in the slow region for asteroids is relatively high compared to that in the faster region, resulting in a larger number density of asteroid population in the slow region.

145 in Gaia data for the first time [18], we use the Gaia data reported by Āurech and Hanuř
 146 [18] as the primary source of observation asteroids. All selected asteroids are main-belt
 147 asteroids, with semimajor axes ranging from 1.85 to 3.97 au. The converged solution is
 148 $P_0 = 13.38$ hours and $\beta = 0.783$, as shown in Supplementary Fig. 5. The obtained $\beta = 0.783$
 149 for Gaia data closely matches the theoretical value 0.785. We run 100 Monte Carlo simulations
 150 on the rotational evolution model for each μQ , and then input the simulation results of
 151 the period-diameter distribution to the machine-learning model to identify the gap. The gap
 152 parameters obtained in simulations are shown in Fig. 4. However, we should note that due to
 153 the data quality and the systematic uncertainty of the SVM model, results might vary, result-
 154 ing from specific parameters in the machine-learning model—such as the gap width or the
 155 initial value of k . We also use unsupervised clustering methods including but not limited to
 156 K-Means, Density-based spatial clustering of applications with noise (DBSCAN) and spec-
 157 tral clustering, as well as the geometric data analysis mentioned in Contardo et al. [40]. In our
 158 experiments, unsupervised methods are more sensitive to their hyper-parameters and would

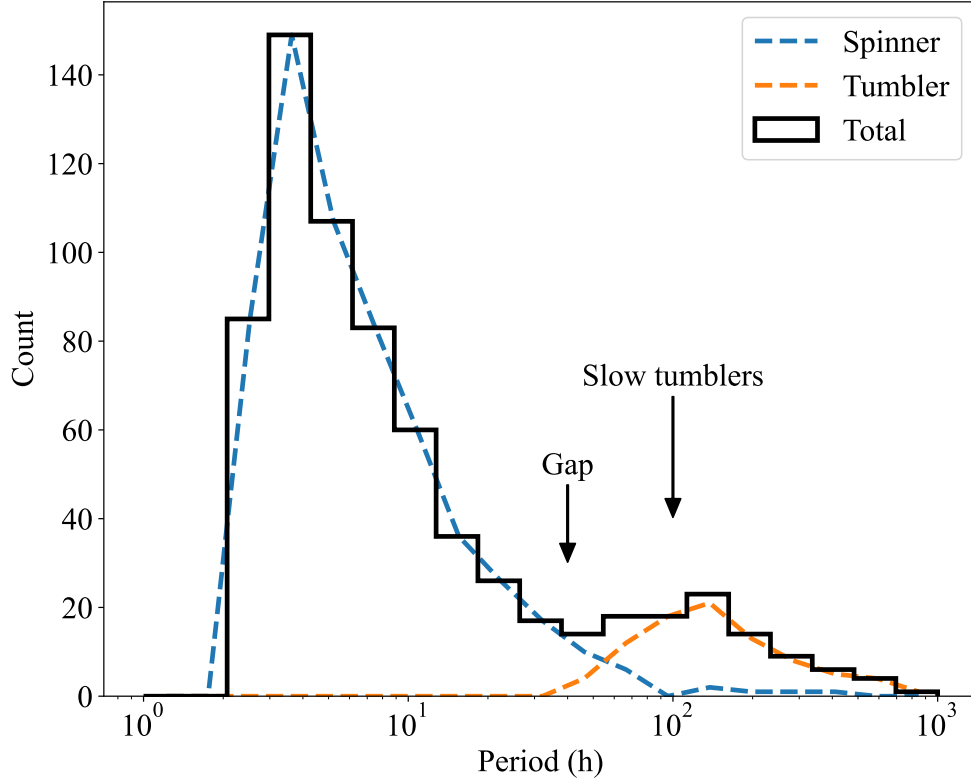


Fig. 3 Bimodal period distribution for simulated asteroids between 3 km and 4 km as an example showing the location of the gap. The group of fast rotators is dominated by pure spinners while the group of slow rotators is dominated by tumblers. A distinct gap clearly separates the two groups. The peak of the distribution of slow tumblers is described by Eq. 3.

159 introduce considerable uncertainty if they were forced to identify a single gap. An example of
 160 DBSCAN method with different min samples is shown in Supplementary Fig. 6. In general,
 161 these unsupervised methods do not yield converging results for our problem. Animations of
 162 the iteration process with different initial conditions are presented in Supplementary Videos
 163 2 and 3.

164 **3.2 Rotational evolution model**

165 The long-term rotational dynamics of asteroids are mainly dominated by the YORP effect,
 166 which is a radiative torque caused by radiation from the irregular asteroid surface, and sub-
 167 catastrophic collisions. Both collisions and the YORP effect can transfer positive or negative
 168 angular momentum, leading to spin-up or spin-down of asteroids. Comparing the collision
 169 timescale with the YORP timescale, it is obvious that the YORP effect dominates over colli-
 170 sions unless the asteroid enters an extremely slow rotation. The term "YORP cycle" is used
 171 to describe the process by which the asteroid evolves into an end-state where its rotation state

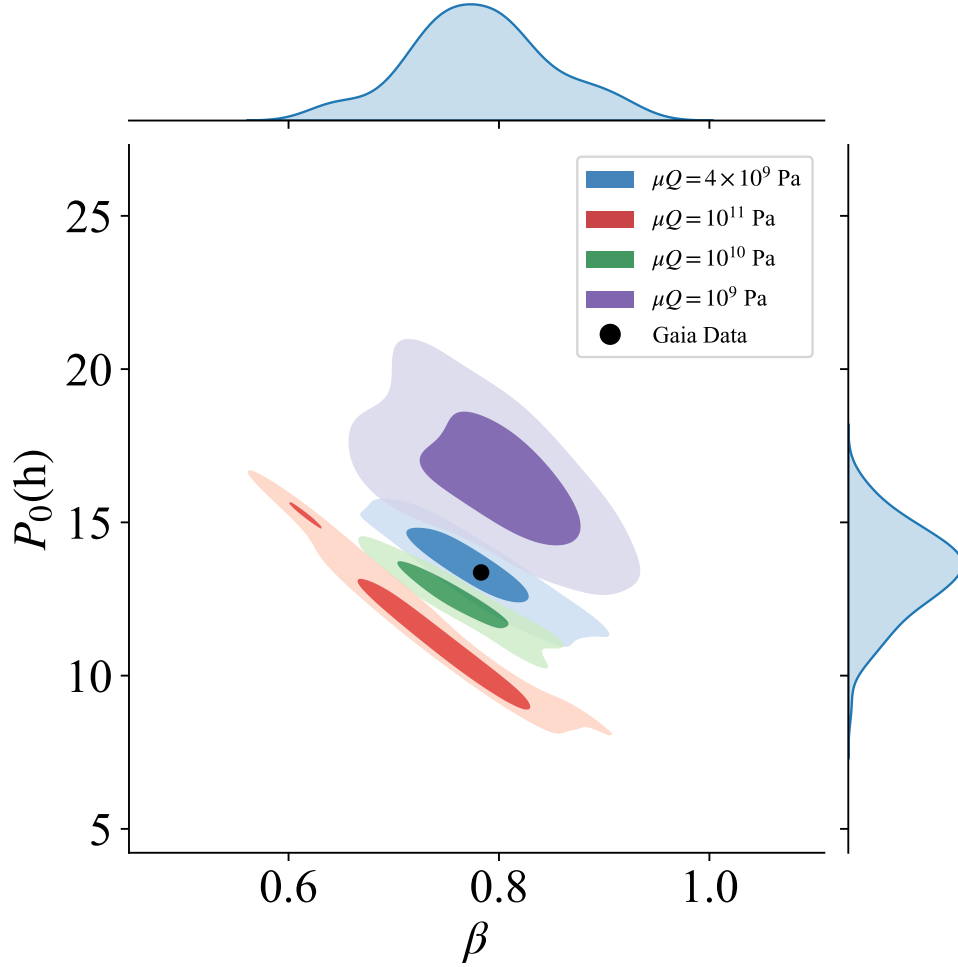


Fig. 4 Probability density distribution of the gap parameters P_0 and β (see Eq. 4) for our simulation results with different μQ (colored). The Gaia data is represented by the black dot. The parameters μ and Q are obtained by the semi-supervised machine learning method (Methods). We run 100 Monte Carlo simulations of rotational evolution for $\mu Q = 10^9$, 4×10^9 , 10^{10} and 10^{11} Pa. The commonly assumed value μQ for the damping of tumbling is 10^{11} Pa [21]. The two levels of the contours of the simulation results represent the 30% and 68.27% (1σ) probability of the data to lie below the contour. The curves (blue) on the marginal axes represent the density distribution of the parameter β and P_0 in the case of $\mu Q = 4 \times 10^9$ Pa.

172 needs resetting under the YORP effect [16]. One YORP cycle is terminated when (1) the spin
 173 rate exceeds the rotational disruption limit $\omega = \sqrt{4\pi G\rho/3} \sim 2.2$ hours; (2) a sub-catastrophic
 174 collision occurs; and (3) the spin rate decreases to zero.

175 These three cases yield distinct outcomes (Table 1). In the first case, the asteroid is
 176 assumed to be reshaped or divided into fragments. The spin rate should be reset, as well as the
 177 YORP torque since it is sensitive to the surface topology [27, 29]. We consider the new object

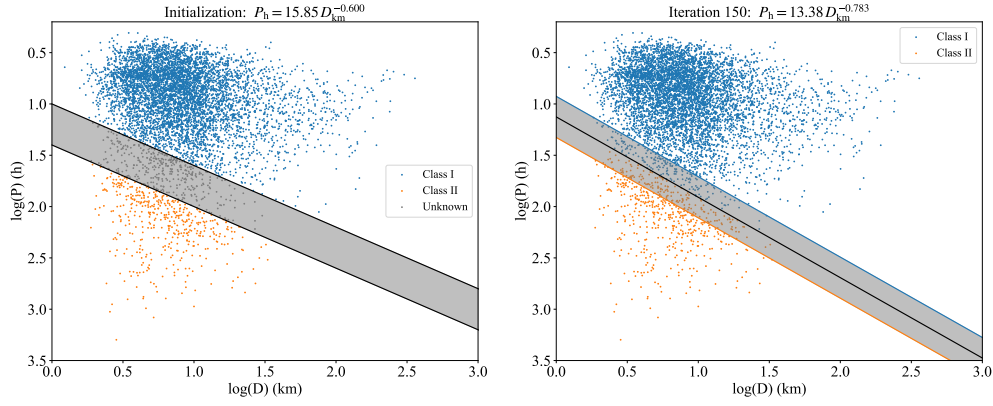


Fig. 5 Identification of the gap. **a.** The gap is initialized manually with a shaded area. The dots above and below the shaded area are classified as fast rotators (class I) and slow rotators (class II), respectively, while the dots in the shaded area are unclassified. The y-distance of the shaded area is 0.4. **b.** The converged result for the gap is shown after 150 iterations (Methods).

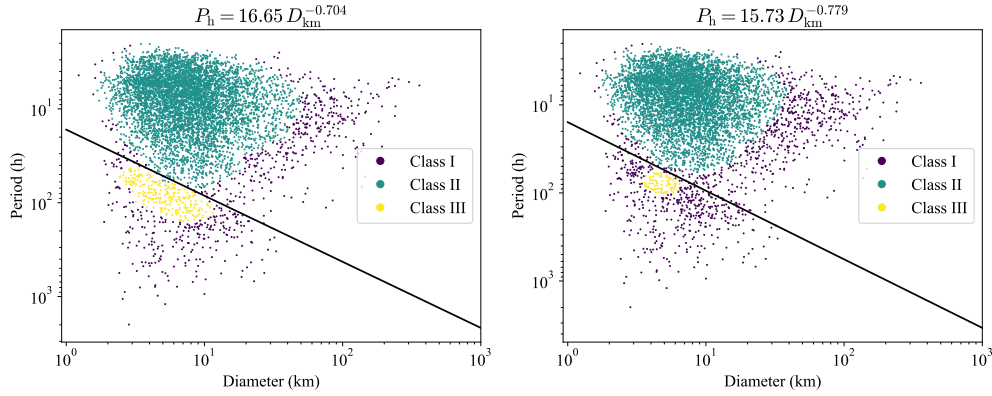


Fig. 6 Classification by the DBSCAN method with min sample number of **a**, 40 and **b**, 50,

178 to maintain a pure spin state, as the rotational disruption chiefly alters the angular momen-
 179 tum along the major principal axis. Moreover, the process of reshaping or uniting the rubble
 180 piles rapidly dissipates energy to realign the asteroid. Thus, the nutation angle, which gauges
 181 the degree of tumbling, remains nearly zero. In the second case, a sub-catastrophic collision
 182 induces the spin rate to renew with a random increment and the obliquity to reset randomly.
 183 Since a collision lacks a preferred direction of incidence, it imparts an angular momentum
 184 with equal probability to all directions, thereby instigating tumbling. In the third case, the
 185 asteroid spins down to a quasi-static rotational state, triggering a tumbling state due to the
 186 YORP effect or collisions. In our model, the initial spin rate distribution follows a Maxwell
 187 distribution with the peak at 8 hours, the minimum at 2000 hours, and the maximum at 2.2

188 hours. In fact, the initial condition does not affect significantly the spin distribution at equi-
 189 librium. We generate as many test particles as asteroids in the Gaia sample with the same
 190 sizes and orbital elements and run the simulation for 400 Myrs. The spin distribution arrives
 191 at equilibrium after around 300 Myrs.

192 3.3 Sub-catastrophic collisions

Sub-catastrophic collisions transfer angular momentum to asteroids, modifying the spin rate and potentially triggering tumbling. We follow the route of Farinella et al. [41] to calculate the characteristic collision timescale at which an asteroid's rotational state is reset. To transfer the angular momentum that is comparable to that of the target asteroid with the angular speed ω_{targ} and radius r_{targ} , the radius of the impactor is

$$r_{\text{imp}} \sim \left(\frac{\omega_{\text{targ}} r_{\text{targ}}}{v_{\text{imp}}} \right)^{1/3} r_{\text{targ}}, \quad (5)$$

where $v_{\text{imp}} \sim 5.8$ km/s is the average impact speed between asteroids [42]. The collision timescale for such a collision can be estimated as

$$\tau_{\text{col}} = \frac{1}{P_i N_{r>r_{\text{imp}}} (r_{\text{imp}} + r_{\text{targ}})^2}. \quad (6)$$

Here $P_i \sim 2.85 \times 10^{-18}$ km⁻² yr⁻¹ is the intrinsic collisional probability [42], and $N_{r>r_{\text{imp}}}$ is the number of the asteroid that has a larger radius than r_{imp} :

$$N_{r>r_{\text{imp}}} = N_0 \left(\frac{r_{\text{imp}}}{r_0} \right)^{1-\alpha} \quad (7)$$

with $-\alpha$ being the power index of the size-frequency distribution (SFD) of asteroids. Substituting Eq. (5) and Eq. (7) into Eq. (6), we can obtain

$$\tau_{\text{col}} \simeq \frac{f_{\text{col}}}{P_i N_0} \left(\frac{1}{v_{\text{imp}} r_0^3} \right)^{(\alpha-1)/3} \omega_{\text{targ}}^{(\alpha-1)/3} r_{\text{targ}}^{(4\alpha-10)/3} \quad (8)$$

where f_{col} is a dimensionless coefficient related to the shape of asteroids, the impact angle and the density ratio of the impactor to the target. The general form of the collision timescale we use in our simulation is

$$\tau_{\text{col}} = \tau_{\text{col},0} \left(\frac{D}{1 \text{ km}} \right)^{(4\alpha-10)/3} \left(\frac{P}{8 \text{ h}} \right)^{(1-\alpha)/3}. \quad (9)$$

Applying $f_{\text{col}} \simeq 0.83$, $\alpha = 3.5$, $r_0 = 1$ km and $N_0 = 3.5 \times 10^5$ for a rough estimate, Farinella et al. [41] obtain $\tau_{\text{col},0} = 50.8$ Myrs. With an update to f_{col} by Farinella and Vokrouhlický [43], the hereafter studies utilise $\tau_{\text{col},0} = 228.8$ Myrs. Bottke et al. [23] show the wavy characteristics of the size distribution of asteroids, in particular, the decreasing slope in the small size

end. To account the slightly shallower distribution in the size range (0.1, 1) km, Holsapple [17] uses $N_0 = 6.1 \times 10^5$ and $\alpha = 3.2$ and obtains $\tau_{\text{col},0} = 113$ Myrs. In this study, we follow the size distribution fitted by Holsapple [17]. In our numerical code, when the evolution time reaches τ_{col} , the spin rate ω receives an increment $\Delta\omega$ due to a random collision:

$$\Delta\omega = (\sqrt{2 + 2\cos\gamma} - 1)\omega \quad (10)$$

193 where γ is the random angle between the projectile angular momentum and the target angular
 194 momentum, uniformly distributed from 0° to 360° . After such a sub-catastrophic collision,
 195 the nutation angle is set to be a random number between 0° and 90° , denoting a tumbling
 196 state. We also reset the YORP coefficient, since the YORP torque is shown to be sensitive to
 197 the change of fine surface structures (e.g. boulders and craters) [27, 29, 44].

198 3.4 YORP effect

The YORP effect is a radiative torque produced by the recoil force of the emitted photons from the asteroid. The asteroid could spin up or spin down under the YORP effect. In our model, the asteroid is initially assigned with a YORP torque, which can be expressed as [45–48]

$$T_{\text{YORP},z} = \delta_{\text{YORP}} f_{\text{YORP}} \frac{\Phi R^3}{c} \left(\cos 2\epsilon + \frac{1}{3} \right) \quad (11)$$

$$T_{\text{YORP},\epsilon} = -f_{\text{YORP}} \frac{2\Phi R^3}{3c} \sin 2\epsilon. \quad (12)$$

199 Here $T_{\text{YORP},z}$ and $T_{\text{YORP},\epsilon}$ are the YORP torque components that modify the spin rate and the
 200 obliquity, respectively. The obliquity ϵ ranges from 0° to 90° . Here Φ is the mean flux of solar
 201 radiation at the asteroid’s orbit, R is the asteroid radius and c is the light speed.

202 The dimensionless YORP coefficient f_{YORP} is highly sensitive to the shape of asteroids.
 203 The probability distribution of f_{YORP} is commonly modeled as either a normal distribution
 204 [49–51] or an exponential law [47]. In our study, we adopt a half-normal distribution to
 205 ensure f_{YORP} remains positive, setting the standard deviation at 0.005, which is a typical
 206 value [27, 48]. This simple YORP model leads asymptotically asteroid obliquity to either 0°
 207 or 180° , consistent with observations on asteroid obliquities [11], although simulations show
 208 the asymptotic obliquity could be also 90° for some asteroids [52]. We introduce the param-
 209 eter δ_{YORP} , which can take values of 1 or -1, to control the sign of $T_{\text{YORP},z}$. A positive δ_{YORP}
 210 signifies a spin-up torque, while a negative value indicates a spin-down torque. For asteroids
 211 with an unrealistic zero thermal inertia, simulations suggest a tendency to spin down [52, 53].
 212 Conversely, for realistic asteroids with non-zero thermal inertia, the YORP effect appears to
 213 equally drive spin-up or spin-down [30]. To date, eleven confirmed YORP detections all show
 214 increasing spin rates [15], a finding that contradicts theoretical predictions and remains unex-
 215 plained. Possible observational biases include: (1) all detections are for near-Earth objects
 216 (NEOs), primarily retrograde rotators from the ν_6 resonance in the main belt; (2) all detec-
 217 tions are for fast rotators, which are more likely to be spinning up towards to the spin barrier.
 218 In the literature, δ_{YORP} is typically assumed to be equally likely to be positive or negative [48–
 219 51, 54]. We maintain this assumption in our primary analysis but also explore scenarios with

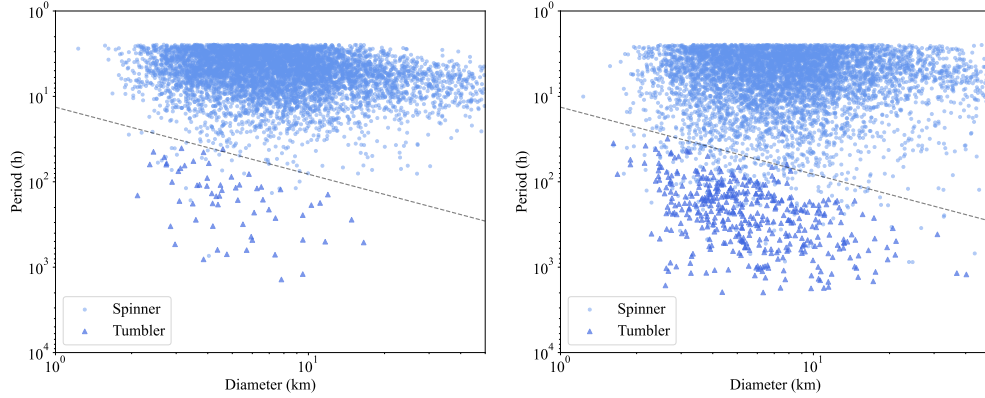


Fig. 7 Results for **a**, 90% positive YORP torques and **b**, 90% negative YORP torques.

220 a preference for either positive or negative δ_{YORP} . Two extreme cases, which may not be real-
 221 istic but are helpful for a quick grasp of the idea, are shown in Supplementary Fig. 7 where
 222 δ_{YORP} has 90% probability to be 1 or -1. Generally, an increased likelihood of positive YORP
 223 torque leads to a reduction in the population of slow rotators, aligning with expectations.
 224 Observations, however, poorly constrain the proportion of slow rotators, as one can see from
 225 inconsistencies between data derived predominantly from an asteroid family [3] and data from
 226 Gaia observation on main belt asteroids [18]. Consequently, this study does not endeavor to
 227 refine the parameters that define the fraction of slow rotators but rather focuses on examining
 228 the gap feature and the distribution of tumbling asteroids. Fortunately, the preference to spin
 229 up or down does not affect the location of the gap and the distribution of tumbling asteroids.

230 The YORP coefficient is reset when the asteroid goes through a rotational disruption (i.e.
 231 the spin rate exceeds the limit corresponding to a period of 2.2 hours), or experiences a sub-
 232 catastrophic collision, after which the surface is largely deformed, leading to a change on the
 233 YORP torque [29]. If the asteroid spins down to a quasi-static rotation, the tumbling motion
 234 could be easily triggered by the YORP torque or collisions. In our model, we assign a nuta-
 235 tion angle of 45° to the asteroid if the period becomes longer than 1000 hours to denote the
 236 tumbling motion. The understanding of the YORP effect on a tumbling asteroid is still largely
 237 limited due to the shape-sensitivity of the YORP torque and the sometimes chaotic nature of
 238 tumbling motion [22, 55–57]. Breiter and Murawiecka [25] demonstrate that the combined
 239 impact of the YORP effect and the damping on tumblers might produce a stable tumbling
 240 motion with a fixed period, or can evolve into a completely chaotic tumbling motion when
 241 the nutation angle arrives 90° [25]. In the latter case, the YORP effect might be ineffective
 242 since the radiation torque can be averaged out over a long term if the direction of the radi-
 243 ative torque is random. The same logic is used to justify the absence of the binary YORP effect
 244 in non-synchronous asteroid binary systems [26]. Therefore, a tumbling asteroid has a prob-
 245 ability p_{fix} of maintaining its angular momentum under the complex coupling effects of the
 246 YORP torque and internal energy dissipation. The high sensitivity of p_{fix} to the initial rota-
 247 tion state and the shape of asteroids, makes it hard to obtain a typical value of p_{fix} theoret-
 248 ically, especially considering that the above studies have ignored the thermal inertia.

In our model, the probability p_{fix} can be translated into a "weaken" factor of the YORP effect f_{weaken} in the simulation of long-term rotational evolution of asteroids by

$$f_{\text{weaken}} = 1 - p_{\text{fix}}, \quad (13)$$

so that the expected value of the YORP torque is

$$T_{\text{YORP}}' = f_{\text{weaken}} T_{\text{YORP}}. \quad (14)$$

249 The rationale behind this is explained as follows: since the YORP torque is sensitive to the
 250 surface deformation [29], the YORP torque can be reset from time to time [16] by the crater-
 251 induced YORP (CYORP) torque [27, 28]. With every reset of the YORP torque, the tumbler
 252 has a probability of p_{fix} to fix the period (invalidate the YORP torque), the expected value of
 253 the YORP torque over a long term can be simply estimated as $(1 - p_{\text{fix}})T_{\text{YORP}}$, given that the
 254 simulation time t (\sim hundreds of Myrs) is much larger than the reset timescale $\tau_{\text{reset}} (\leq 1 \text{ Myr})$
 255 [16, 27]. In fact, the YORP effect that accounts for the random reset by the CYORP torque is
 256 referred to as the "stochastic YORP" effect [16], which reduces the efficiency of the YORP
 257 torque [16, 27]. However, this effect makes no difference in the equilibrium spin distribution,
 258 because it works for all asteroids, indicating that it only affects the evolution rate. For the
 259 sake of simplicity, we choose to overlook this effect, especially considering the absence of a
 260 comprehensive model for the stochastic YORP effect [27].

261 It is possible to constrain the value of f_{weaken} by observations, taking advantage of the
 262 fact that f_{weaken} directly influences the number of slow rotators. A greater f_{weaken} introduces
 263 a larger fraction of slow rotators. In case the Gaia observation has a bias against fast aster-
 264 oids, we utilize the histogram provided by Pravec, P. and others [3] (see their Fig. 2) of the
 265 spin distribution of 268 small main-belt and Hungaria asteroids with the diameter range 3–15
 266 km, which was considered as the best estimate of the rotation rate distribution of small aster-
 267 oids [16]. $\sim 30\%$ of the asteroids in Pravec, P. and others [3] belong to two asteroid families,
 268 i.e., the Hungaria and Phocaea families. Family member asteroids are thought to share the
 269 same age. Thus they are more suitable with agreeing with our synthetic asteroids that evolve
 270 concurrently in our simulations, compared to a general sample e.g. from Gaia data, the lat-
 271 ter potentially suffering from a bias against the detection of low-lightcurve-amplitude fast
 272 rotators. We vary the value of f_{weaken} in our simulation and compare the resulting spin distri-
 273 bution of asteroids in the same size range with that in [3]. The most consistent result is shown
 274 in Supplementary Fig. 8, indicating $f_{\text{weaken}} \sim 0.1$. Compared to ground-observation, Gaia is
 275 less biased for slow rotators, while fast rotators might be more biased. By fitting the fraction
 276 of slow rotators ($\omega < 1 \text{ cycle/day}$), we fit $f_{\text{weaken}} \sim 0.12$. In the result presented in Fig. 1, we
 277 adopted $f_{\text{weaken}} = 0.1$.

278 We note that the unknown preference of the YORP torque to be positive or negative
 279 also affects the histogram, as shown in Supplementary Fig. 7. The parameter f_{weaken} may
 280 be smaller than 0.1 if the YORP torque favors positivity. Consequently, the constraints on
 281 f_{weaken} become complicated due to inconsistent information from different observations and
 282 unknown chaotic behaviors of the YORP torque. However, fortunately, the value of f_{weaken} ,
 283 given $f_{\text{weaken}} < 1$, does not change the position and the slope of the gap in the slow-rotating
 284 region and the distribution of tumblers. A more precise constraint on the parameter f_{weaken}

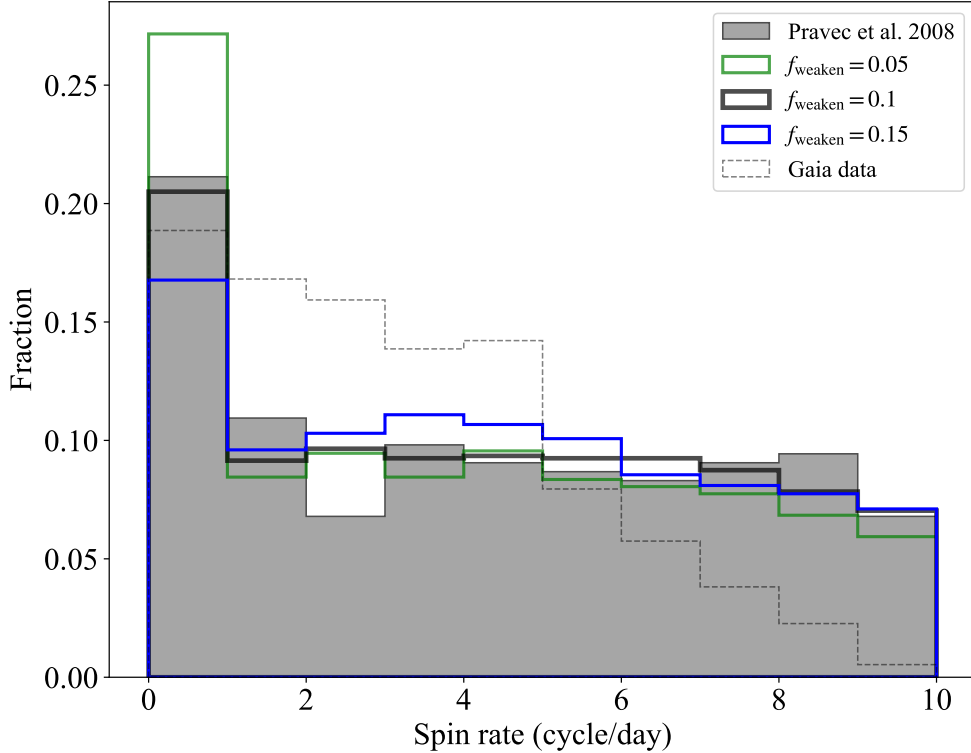


Fig. 8 Comparison of the spin rate distribution of asteroids (3-15 km) from Pravec, P. and others [3] and Āurech and Hanuř [18] with our model results assuming $f_{\text{weaken}} = 0.05, 0.1$ and 0.2 . As f_{weaken} decreases, the fraction of the slow rotators increases. Our findings indicate that $f_{\text{weak}} = 0.1$ provides the best match to observation data by Pravec, P. and others [3], especially for the slow rotators with $\omega < 1$ cycle/day. The less consistency in the group of faster asteroids with Gaia data could arise from systematic issues in the Gaia dataset. Compared to ground-based observations, Gaia might exhibit a greater bias against fast rotators (the expected excess of fast rotators isn't evident), while the slow rotators are less biased. In fact, focusing only on the fraction of slow rotators ($\omega < 1$ cycle/day), we fit $f_{\text{weaken}} \sim 0.12$ for Gaia data, which is close to the result fit from Pravec, P. and others [3].

285 may be deferred for future investigations, provided that unbiased observations demonstrate
 286 agreement with the histogram in the spin rate distribution.

287 3.5 Internal energy dissipation

Due to the internal friction, a tumbling object will finally evolve into a pure spin state around the major principal axis. The damping rate of asteroids is usually estimated by using an empirical quality factor Q whose inverse measures the energy lost per precession period, and the Love number k_2 describes the tumbling-caused deformation. In the classical theory [58], k_2 is translated into the rigidity μ for a homogeneous elastic body:

$$k_2 \simeq \frac{\pi G \rho^2 D^2}{19\mu}, \quad (15)$$

leading to the commonly used “ μQ ” prescription. The damping timescale is generally expressed as

$$\tau_{\text{damp}} \simeq \frac{\mu Q}{\rho R^2 \omega^3} A = \tau_{\text{damp},0} \left(\frac{D}{1 \text{ km}} \right)^{-2} \left(\frac{P}{8 \text{ h}} \right)^3, \quad (16)$$

where A is a dimensionless shape factor. The uncertainty of this estimate comes from the quality factor Q , which is usually set to be 100 but never actually measured for rubble pile asteroids [21, 58]. The value of the shape factor A is suggested to be 18 in Breiter’s model [21, 59], although its value varies by two orders of magnitude in the older literature [58–63]. The nominal timescale is

$$\tau_{\text{damp},0} \simeq 1.1 \text{ Myrs} \left(\frac{\mu Q}{10^{10} \text{ Pa}} \right) \left(\frac{2 \text{ g cm}^{-3}}{\rho} \right) \quad (17)$$

288 While rubble piles have shear rigidity [35], dissipation and the damping rate are not very
 289 sensitive to its value. Recent studies have demonstrated that it is the viscosity that predomi-
 290 nantly defines the efficiency of friction [64–66]. An accurate approach to the problem should
 291 be based on a rheological equation including the viscosity as a key parameter. This treatment
 292 would render a frequency dependence of the quality factor.

However, the viscosity of asteroids is still unknown and more complex rheologies may be needed [65, 66]. For convenient comparison with previous studies, we utilize the classic Q/k_2 method with the μQ prescription in this work. We assume μQ as a constant for the size range of our interest (1–50 km), although μQ could vary with the size [35] or the frequency [67]. In our model, the nutation angle θ evolves as

$$\dot{\theta} = 1/\tau_{\text{damp}} \quad (18)$$

293 for the sake of simplicity, although $\dot{\theta}$ should be a complex function of θ [59, 62]. Each time
 294 the asteroid is excited to tumble under the YORP effect or a collision, the nutation angle is
 295 reset to a random number between 0° and 180° for simplicity, considering the probability
 296 distribution of the nutation angle reset by a sub-catastrophic collision is unknown.

297 Our best fit model suggests that $\mu Q \sim 4 \times 10^9 \text{ Pa}$ (see Fig. 4), which is equivalent to $Q/k_2 \sim$
 298 $5 \times 10^8 (D/\text{km})^{-2}$. The results with $\mu Q \sim 10^{11} \text{ Pa}$ and 10^9 Pa are shown in Supplementary
 299 Fig. 9. It can be seen that the usually assumed $\mu Q \sim 10^{11} \text{ Pa}$ yields a gap above the observed
 300 gap, as a result of a weak damping effect. Conversely, a $\mu Q \sim 10^9 \text{ Pa}$ creates a gap lower than
 301 the observed one, according to diagnosis by our semi-supervised machine learning method.

302 **Data availability.** For the observation data, the code is available at [https://github.com/WH-](https://github.com/WH-Zhou/Zhou-2024-Gap-Finder)
 303 [Zhou/Zhou-2024-Gap-Finder](https://github.com/WH-Zhou/Zhou-2024-Gap-Finder).

304 **Code availability.** For the gap identification, the code is available at
 305 <https://github.com/WH-Zhou/Zhou-2024-Gap-Finder>.

306 **Acknowledgments.** We are grateful for the constructive suggestions from reviewers. W.H.
 307 Zhou would like to acknowledge the funding support from the Chinese Scholarship Council
 308 (No. 202110320014). P. Michel acknowledges funding support from the French space agency
 309 CNES and from the European Union’s Horizon 2020 research. The work of J. Ďurech and J.
 310 Hanuš was supported by the grant 23-04946S of the Czech Science Foundation.

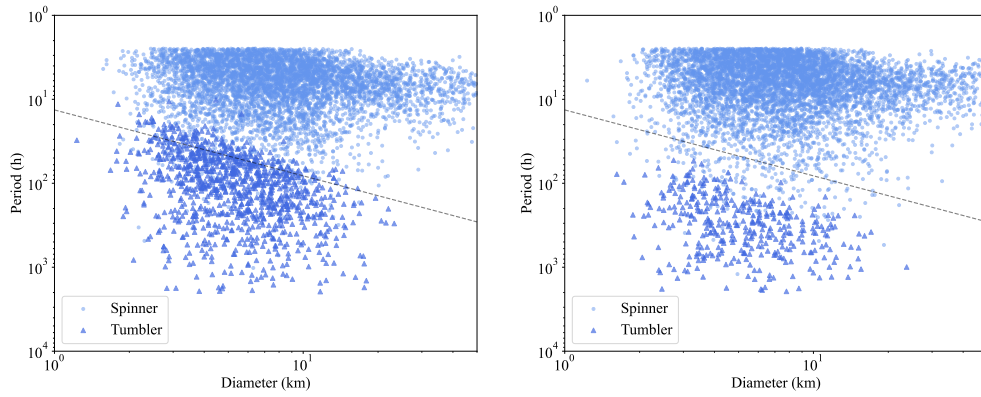


Fig. 9 Period-diameter distribution of the simulation results with **a**, $\mu Q \sim 10^{11}$ Pa and **b**, 10^9 Pa. The dashed line is the gap identified for Gaia data.

311 **Author contributions.** W.H.Zhou led the project. W.H.Zhou proposed the model, derived
 312 the formula, carried out the numerical simulations, analyzed the results, and led the writ-
 313 ing of the paper. M.Delbo and W.H.Zhou initiated the collaboration. W.C.Wang, Y.Wang,
 314 and W.H.Zhou led the gap identification using machine learning. M.Delbo and P.Michel con-
 315 tributed to writing the manuscript. J.Ďurech and J.Hanuš provided the asteroid data based on
 316 Gaia observations. All authors collaborated on the interpretation of the results.

317 **Competing interest.** Authors declare that they have no competing interests.

Table 1 Outcomes of YORP-cycle endstates.

| Events | Spin rate | Obliquity | YORP torque | Rotation mode |
|------------------------------------|-----------|-----------|----------------------|---------------|
| Rotational disruption ¹ | Reset | Remain | Reset | Pure spin |
| Quasi-static rotation | Remain | Remain | Reverse and weakened | Tumbling |
| Sub-catastrophic collision | Reset | Reset | Reset and weakened | Tumbling |

¹This applies to the larger remnant; disruption can also mean mass shedding.

318 **Tables.**

319 **References**

- 320 [1] Harris, A.W., Burns, J.A.: Asteroid rotation: I. tabulation and analysis of rates, pole
 321 positions and shapes. *Icarus* 40(1), 115–144 (1979)
- 322 [2] Pravec, P., Harris, A.W.: Fast and slow rotation of asteroids. *Icarus* 148(1), 12–20 (2000)
- 323 [3] Pravec, P. and others: Spin rate distribution of small asteroids. *Icarus* 197(2), 497–504
 324 (2008) <https://doi.org/10.1016/j.icarus.2008.05.012>

- 325 [4] Farinella, P., Paolicchi, P., Zappala, V.: Analysis of the spin rate distribution of asteroids.
326 Astron. Astrophys., vol. 104, no. 1, Dec. 1981, p. 159-165. Research supported by the
327 Consiglio Nazionale delle Ricerche. 104, 159–165 (1981)
- 328 [5] Dermott, S.F., Harris, A.W., Murray, C.D.: Asteroid rotation rates. *Icarus* 57(1), 14–34
329 (1984)
- 330 [6] Binzel, R.P., Farinella, P., Zappala, V., Cellino, A.: Asteroid rotation rates: distributions
331 and statistics. *Asteroids II*, 416–441 (1989)
- 332 [7] Fulchignoni, M., Barucci, M., Di Martino, M., Dotto, E.: On the evolution of the asteroid
333 spin. *Astron. Astrophys.* 299, 929 (1995)
- 334 [8] Harris, A.W.: On the slow rotation of asteroids. *Icarus* 156(1), 184–190 (2002)
- 335 [9] Pál, A., *et al.*: Solar system objects observed with tess—first data release: Bright main-
336 belt and trojan asteroids from the southern survey. *Astrophys. J. Suppl. Ser.* 247(1), 26
337 (2020)
- 338 [10] Rubincam, D.P.: Radiative spin-up and spin-down of small asteroids. *Icarus* 148(1),
339 2–11 (2000)
- 340 [11] Vokrouhlický, D., Nesvorný, D., Bottke, W.F.: The vector alignments of asteroid spins
341 by thermal torques. *Nature* 425(6954), 147–151 (2003)
- 342 [12] Lowry, S.C., *et al.*: Direct detection of the asteroidal yorp effect. *Science* 316(5822),
343 272–274 (2007)
- 344 [13] Taylor, P.A., *et al.*: Spin rate of asteroid (54509) 2000 ph5 increasing due to the yorp
345 effect. *Science* 316(5822), 274–277 (2007)
- 346 [14] Ďurech, J., Vokrouhlický, D., Pravec, P., Krugly, Y.N., Kim, M.-J., Polishook, D.,
347 Ayvazian, V., Bonev, T., Choi, Y.-J., Datashvili, D., *et al.*: Rotation acceleration of aster-
348 oids (10115) 1992 sk,(1685) toro, and (1620) geographos due to the yorp effect. *Astron.*
349 *Astrophys.* 657, 5 (2022)
- 350 [15] Ďurech, J., *et al.*: Secular change in the spin states of asteroids due to radiation and
351 gravitation torques. New detections and updates of the YORP effect. *Astron. Astrophys.*,
352 682, 93 (2024) <https://doi.org/10.1051/0004-6361/202348350> [arXiv:2312.05157](https://arxiv.org/abs/2312.05157) [astro-
353 ph.EP]
- 354 [16] Bottke, W.F., Vokrouhlický, D., Walsh, K.J., Delbo, M., Michel, P., Lauretta, D.S.,
355 Campins, H., Connolly Jr, H.C., Scheeres, D.J., Chelsey, S.R.: In search of the source
356 of asteroid (101955) bennu: Applications of the stochastic yorp model. *Icarus* 247,
357 191–217 (2015)
- 358 [17] Holsapple, K.A.: Main belt asteroid collision histories: Cratering, ejecta, erosion, catas-
359 trophic dispersions, spins, binaries, tops, and wobblers. *Planet Space Sci.* 219, 105529

- 360 (2022)
- 361 [18] Ďurech, J., Hanuš, J.: Reconstruction of asteroid spin states from gaia dr3 photometry.
362 *Astron. Astrophys.* 675, 24 (2023)
- 363 [19] Harris, A.W.: Tumbling asteroids. *Icarus* 107(1), 209–211 (1994)
- 364 [20] Pravec, P., *et al.*: Tumbling asteroids. *Icarus* 173(1), 108–131 (2005)
- 365 [21] Pravec, P.e.a.: The tumbling spin state of (99942) apophis. *Icarus* 233, 48–60 (2014)
- 366 [22] Vokrouhlický, D., Breiter, S., Nesvorný, D., Bottke, W.: Generalized yorp evolution:
367 Onset of tumbling and new asymptotic states. *Icarus* 191(2), 636–650 (2007)
- 368 [23] Bottke, W.F., *et al.*: The fossilized size distribution of the main asteroid belt. *Icarus*
369 175(1), 111–140 (2005)
- 370 [24] Morbidelli, A., Bottke, W.F., Nesvorný, D., Levison, H.F.: Asteroids were born big.
371 *Icarus* 204(2), 558–573 (2009)
- 372 [25] Breiter, S., Murawiecka, M.: Tumbling asteroid rotation with the yorp torque and
373 inelastic energy dissipation. *Mon. Not. R. Astron. Soc.* 449(3), 2489–2497 (2015)
- 374 [26] Čuk, M., Burns, J.A.: Effects of thermal radiation on the dynamics of binary neas. *Icarus*
375 176(2), 418–431 (2005)
- 376 [27] Zhou, W.-H., Zhang, Y., Yan, X., Michel, P.: The crater-induced YORP effect.
377 *Astron. Astrophys.*, 668, 70 (2022) <https://doi.org/10.1051/0004-6361/202244386>
378 [arXiv:2210.15802](https://arxiv.org/abs/2210.15802) [astro-ph.EP]
- 379 [28] Zhou, W.-H., Michel, P.: A semi-analytical thermal model for craters with application
380 to the crater-induced YORP effect. *Astron. Astrophys.*, 682, 130 (2024) [https://doi.org/](https://doi.org/10.1051/0004-6361/202346970)
381 [10.1051/0004-6361/202346970](https://doi.org/10.1051/0004-6361/202346970)
- 382 [29] Statler, T.S.: Extreme sensitivity of the yorp effect to small-scale topography. *Icarus*
383 202(2), 502–513 (2009)
- 384 [30] Čapek, D., Vokrouhlický, D.: The YORP effect with finite thermal conductivity. *Icarus*
385 172(2), 526–536 (2004) <https://doi.org/10.1016/j.icarus.2004.07.003>
- 386 [31] Oey, J., Williams, H., Groom, R., Pray, D., Benishek, V.: Lightcurve Analysis of Binary
387 and Potential Binary Asteroids in 2015. *Minor Planet Bulletin* 44(3), 193–199 (2017)
- 388 [32] Matsumoto, T., Hasegawa, S., Nakao, S., Sakai, M., Yurimoto, H.: Population character-
389 istics of submicrometer-sized craters on regolith particles from asteroid Itokawa. *Icarus*
390 303, 22–33 (2018) <https://doi.org/10.1016/j.icarus.2017.12.017>
- 391 [33] Murray, C.D., Dermott, S.F.: *Solar System Dynamics*. Cambridge university press,

- 392 Cambridge, UK (1999)
- 393 [34] Nishiyama, G., *et al.*: Simulation of seismic wave propagation on asteroid ryugu induced
 394 by the impact experiment of the hayabusa2 mission: Limited mass transport by low yield
 395 strength of porous regolith. *J. Geophys. Res. Planets* 126(2), 2020–006594 (2021)
- 396 [35] Goldreich, P., Sari, R.: Tidal evolution of rubble piles. *Astrophys. J.* 691(1), 54 (2009)
- 397 [36] C., F.W., *et al.*: The tumbling rotational state of 1i/‘oumuamua. *Nat. Astron.* 2(5), 383–
 398 386 (2018)
- 399 [37] Jacobson, S.A., Scheeres, D.J.: Long-term stable equilibria for synchronous binary
 400 asteroids. *Astrophys. J. Lett.* 736(1), 19 (2011)
- 401 [38] Warner, B.D., Harris, A.W., Pravec, P.: The asteroid lightcurve database. *Icarus* 202(1),
 402 134–146 (2009)
- 403 [39] Cortes, C., Vapnik, V.: Support-vector networks. *Machine learning* 20, 273–297 (1995)
- 404 [40] Contardo, G., Hogg, D.W., Hunt, J.A.S., Peek, J.E.G., Chen, Y.-C.: The Emptiness
 405 Inside: Finding Gaps, Valleys, and Lacunae with Geometric Data Analysis. *Astron. J.*
 406 164(5), 226 (2022) <https://doi.org/10.3847/1538-3881/ac961e> [arXiv:2201.10674](https://arxiv.org/abs/2201.10674) [astro-
 407 ph.IM]
- 408 [41] Farinella, P., Vokrouhlický, D., Hartmann, W.K.: Meteorite delivery via yarkovsky
 409 orbital drift. *Icarus* 132(2), 378–387 (1998)
- 410 [42] Bottke Jr, W.F., Nolan, M.C., Greenberg, R., Kolvoord, R.A.: Velocity distributions
 411 among colliding asteroids. *Icarus* 107(2), 255–268 (1994)
- 412 [43] Farinella, P., Vokrouhlický, D.: Semimajor Axis Mobility of Asteroidal Fragments.
 413 *Science* 283, 1507 (1999) <https://doi.org/10.1126/science.283.5407.1507>
- 414 [44] Golubov, O., Krugly, Y.N.: Tangential component of the yorp effect. *Astrophys. J. Lett.*
 415 752(1), 11 (2012)
- 416 [45] Nesvorný, D., Vokrouhlický, D.: Analytic Theory of the YORP Effect for Near-
 417 Spherical Objects. *Astron. J.* 134(5), 1750 (2007) <https://doi.org/10.1086/521651>
- 418 [46] Mysen, E.: Dynamical effects of thermal emission on asteroids. *Mon. Not. R. Astron.*
 419 *Soc.* 383(1), 50–53 (2008) <https://doi.org/10.1111/j.1745-3933.2007.00405.x>
- 420 [47] Golubov, O., Scheeres, D.J.: Systematic structure and sinks in the yorp effect. *Astron. J.*
 421 157(3), 105 (2019)
- 422 [48] Marzari, F., Rossi, A., Golubov, O., Scheeres, D.J.: Evolution of an Asteroid Family
 423 under YORP, Yarkovsky, and Collisions. *Astron. J.* 160(3), 128 (2020) [https://doi.org/](https://doi.org/10.3847/1538-3881/aba7be)
 424 [10.3847/1538-3881/aba7be](https://doi.org/10.3847/1538-3881/aba7be) [arXiv:2009.00392](https://arxiv.org/abs/2009.00392) [astro-ph.EP]

- 425 [49] Rossi, A., Marzari, F., Scheeres, D.J.: Computing the effects of YORP on the spin rate
426 distribution of the NEO population. *Icarus* 202(1), 95–103 (2009) [https://doi.org/10.](https://doi.org/10.1016/j.icarus.2009.02.030)
427 [1016/j.icarus.2009.02.030](https://doi.org/10.1016/j.icarus.2009.02.030)
- 428 [50] Marzari, F., Rossi, A., Scheeres, D.J.: Combined effect of YORP and collisions on the
429 rotation rate of small Main Belt asteroids. *Icarus* 214(2), 622–631 (2011) [https://doi.](https://doi.org/10.1016/j.icarus.2011.05.033)
430 [org/10.1016/j.icarus.2011.05.033](https://doi.org/10.1016/j.icarus.2011.05.033)
- 431 [51] Jacobson, S.A., Marzari, F., Rossi, A., Scheeres, D.J., Davis, D.R.: Effect of rota-
432 tional disruption on the size-frequency distribution of the Main Belt asteroid population.
433 *Mon. Not. R. Astron. Soc.* 439, 95–99 (2014) [https://doi.org/10.1093/mnras/](https://doi.org/10.1093/mnras/slu006)
434 [arXiv:1401.1813](https://doi.org/10.1093/mnras/slu006) [astro-ph.EP]
- 435 [52] Vokrouhlický, D., Čapek, D.: YORP-Induced Long-Term Evolution of the Spin State of
436 Small Asteroids and Meteoroids: Rubincam’s Approximation. *Icarus* 159(2), 449–467
437 (2002) <https://doi.org/10.1006/icar.2002.6918>
- 438 [53] Zhou, W.H.: ‘Oumuamua’s Rotation with the Mechanical Torque Produced by Inter-
439 stellar Medium. *Astron. J.* 899(1), 42 (2020) <https://doi.org/10.3847/1538-4357/ab9f3e>
440 [arXiv:1911.12228](https://doi.org/10.3847/1538-4357/ab9f3e) [astro-ph.EP]
- 441 [54] Hanuš, J., Ďurech, J., Brož, M., Warner, B.D., Pilcher, F., Stephens, R., Oey, J.,
442 Bernasconi, L., Casulli, S., Behrend, R., Polishook, D., Henych, T., Lehký, M., Yoshida,
443 F., Ito, T.: A study of asteroid pole-latitude distribution based on an extended set of
444 shape models derived by the lightcurve inversion method. *Astron. Astrophys.*, 530, 134
445 (2011) <https://doi.org/10.1051/0004-6361/201116738> [arXiv:1104.4114](https://doi.org/10.1051/0004-6361/201116738) [astro-ph.EP]
- 446 [55] Cicalo, S., Scheeres, D.: Averaged rotational dynamics of an asteroid in tumbling
447 rotation under the yorp torque. *Celest. Mech. Dyn. Astron.* 106, 301–337 (2010)
- 448 [56] Breiter, S., Rožek, A., Vokrouhlický, D.: Yarkovsky–o’keefe–radzievskii–paddack
449 effect on tumbling objects. *Mon. Not. R. Astron. Soc.* 417(4), 2478–2499 (2011)
- 450 [57] Vokrouhlický, D., Bottke, W.F., Chesley, S.R., Scheeres, D.J., Statler, T.S.: The
451 yarkovsky and yorp effects. *arXiv preprint arXiv:1502.01249* (2015)
- 452 [58] Burns, J.A., Safronov, V.S.: Asteroid nutation angles. *Mon. Not. R. Astron. Soc.* 165,
453 403 (1973) <https://doi.org/10.1093/mnras/165.4.403>
- 454 [59] Breiter, S., Rožek, A., Vokrouhlický, D.: Stress field and spin axis relaxation for inelastic
455 triaxial ellipsoids. *Mon. Not. R. Astron. Soc.* 427(1), 755–769 (2012)
- 456 [60] Efroimsky, M., Lazarian, A.: Inelastic dissipation in wobbling asteroids and comets.
457 *Mon. Not. R. Astron. Soc.* 311(2), 269–278 (2000)
- 458 [61] Molina, A., Moreno, F., Martínez-López, F.: Energy dissipation by internal stresses in
459 a free-rotating symmetric ellipsoid: Application to comet p/halley. *Astron. Astrophys.*

- 460 398(3), 809–817 (2003)
- 461 [62] Sharma, I., Burns, J.A., Hui, C.-Y.: Nutational damping times in solids of revolution.
462 Mon. Not. R. Astron. Soc. 359(1), 79–92 (2005)
- 463 [63] Caudal, G.: Tidal dissipation within an elongated asteroid with satellite, and application
464 to asteroid (216) kleopatra. Icarus 402, 115606 (2023)
- 465 [64] Efroimsky, M.: Tidal evolution of asteroidal binaries. ruled by viscosity. ignorant of
466 rigidity. Astron. J. 150(4), 98 (2015)
- 467 [65] Frouard, J., Efroimsky, M.: Precession relaxation of viscoelastic oblate rotators. Mon.
468 Not. R. Astron. Soc. 473(1), 728–746 (2018)
- 469 [66] Kwiecinski, J.A.: Relaxation of viscoelastic tumblers with application to 1i/2017
470 ('oumuamua) and 4179 toutatis. Mon. Not. R. Astron. Soc. 497(1), 19–36 (2020)
- 471 [67] Nimmo, F., Matsuyama, I.: Tidal dissipation in rubble-pile asteroids. Icarus 321, 715–
472 721 (2019) <https://doi.org/10.1016/j.icarus.2018.12.012>

CRATER-INDUCED YORP EFFECT WITH ZERO THERMAL INERTIA

The YORP effect is sensitive to the convex and concave structures on the surface, which could be represented by boulders and craters, respectively. Understanding how these structures affect YORP is crucial to precisely calculating the YORP torque and its random-walk evolution due to the morphological alteration during the collisional history.

This chapter develops a semi-analytical method to calculate the crater-induced YORP (CYORP) torque produced by a crater, assuming zero thermal inertia. By investigating CYORP's dependence on the properties of the crater and asteroid, we found the typical size for the crater to modify the total YORP torque is one-tenth of the asteroid size, which leads to a YORP reset timescale of 0.4 Myr. This paper was published in the peer-reviewed journal *Astronomy & Astrophysics*.

Author Contributions: W.H. Zhou led the project. W.H. Zhou proposed the model, derived the formula, carried out the numerical simulations, analyzed the results, and led the writing of the paper. Y. Zhang, X. Yan and P. Michel collaborated on the interpretation of the results.

The crater-induced YORP effect

Wen-Han Zhou^{1,2}, Yun Zhang³, Xiaoran Yan^{1,4}, and Patrick Michel¹

¹ Université Côte d'Azur, Observatoire de la Côte d'Azur, CNRS, Laboratoire Lagrange, 96 Bd de l'Observatoire, 06300 Nice, France

e-mail: wenhan.zhou@oca.eu

² Origin Space Co. Ltd., Kechuang Road, Nanjing, 212415 Jiangsu, PR China

³ Department of Aerospace Engineering, University of Maryland, College Park, MD, 20742, USA

⁴ Department of Aerospace Engineering, Tsinghua University, 30 Shuangqing Road, 100190 Beijing, PR China

Received 30 June 2022 / Accepted 13 October 2022

ABSTRACT

Context. The Yarkovsky–O'Keefe–Radzievskii–Paddack (YORP) effect plays an important role in the rotational properties and evolution of asteroids. While the YORP effect induced by the macroscopic shape of the asteroid and by the presence of surface boulders has been well studied, no investigation has been performed yet regarding how craters with given properties influence this effect.

Aims. We introduce and estimate the crater-induced YORP effect (CYORP), which arises from the concave structure of the crater, to investigate the magnitude of the resulting torques as a function of varying properties of the crater and the asteroid by a semi-analytical method.

Methods. By using a simple spherical shape model of the crater and assuming zero thermal inertia, we calculated the total YORP torque due to the crater, which was averaged over the spin and orbital motions of the asteroid, accounting for self-sheltering and self-sheltering effects.

Results. The general form of the CYORP torque can be expressed in terms of the crater radius R_0 and the asteroid radius R_{ast} : $\langle T_{\text{CYORP}} \rangle \sim WR_0^2 R_{\text{ast}} \Phi / c$, where W is an efficiency factor. We find that the typical values of W are about 0.04 and 0.025 for the spin and obliquity component, respectively, which indicates that the CYORP can be comparable to the normal YORP torque when the size of the crater is about one-tenth of the size of the asteroid, or equivalently when the crater/roughness covers one-tenth of the asteroid surface. Although the torque decreases with the crater size R_0 as $\sim R_0^2$, the combined contribution of all small craters can become non-negligible due to their large number when the commonly used power-law crater size distribution is considered. The CYORP torque of small concave structures, usually considered as surface roughness, is essential to the accurate calculation of the complete YORP torque. Under the CYORP effect that is produced by collisions, asteroids go through a random walk in spin rate and obliquity, with a YORP reset timescale typically of 0.4 Myr. This has strong implications for the rotational evolution and orbital evolution of asteroids.

Conclusions. Craters and roughness on asteroid surfaces, which correspond to concave structures, can influence the YORP torques and therefore the rotational properties and evolution of asteroids. We suggest that the CYORP effect should be considered in the future investigation of the YORP effect on asteroids.

Key words. minor planets, asteroids: general

1. Introduction

The Yarkovsky–O'Keefe–Radzievskii–Paddack (YORP) effect, which is a thermal torque produced by surface emission, has a strong influence on the rotational state and evolution of asteroids (Rubincam 2000; Vokrouhlický & Čapek 2002; Bottke Jr et al. 2006). It can either increase or decrease the spin rate and can also change the spin obliquity of an asteroid on timescales that also depend on physical and dynamical properties of the considered asteroid (e.g., Čapek & Vokrouhlický 2004; Scheeres & Gaskell 2008; Statler 2009; Rozitis & Green 2012). Although a slow process in general, it could be directly measured by ground-based observations (e.g., Āurech et al. 2018). Moreover, it provides an explanation for some observed properties, such as the preferred orientation of the spin axis of members of the Koronis asteroid family (Vokrouhlický et al. 2003), as well as some asteroid shapes, such as the top shapes of primaries of small binary systems (e.g., Walsh et al. 2008), and possibly the shapes of the asteroids Bennu and Ryugu (although another explanation has been proposed for these particular cases; Michel et al. 2020).

In particular, to be at the origin of top-shaped asteroids, the YORP effect needs to cause an increase in spin rate on a

continuous basis or in a trend that allows the shape to evolve in a spinning top on a timescale that makes it possible. However, it was found that small changes in the surface topography of an asteroid can strongly influence the YORP effect outcome (Statler 2009), for instance, causing a spin down rather than a spin up, which could alter a systematic increase in the rotation rate and potentially make it difficult to achieve a top shape. Therefore, it is crucial to assess the effect of surface topography on the total YORP torque.

The current YORP model reads

$$T_{\text{YORP}} = T_{\text{NYORP}} + T_{\text{TYORP}}, \quad (1)$$

where T_{NYORP} stands for the YORP effect on the whole asteroid, and T_{TYORP} stands for the tangential YORP effect, which describes the YORP effect related to the presence of boulders and surface roughness (Golubov & Krugly 2012; Golubov et al. 2014; Golubov 2017).

Here, we consider another surface characteristic that has not been considered so far and that might also influence the evolution of an asteroid rotation state under the YORP effect. Images sent by space missions showed us that asteroid surfaces are populated with craters, whose distribution and properties can differ from

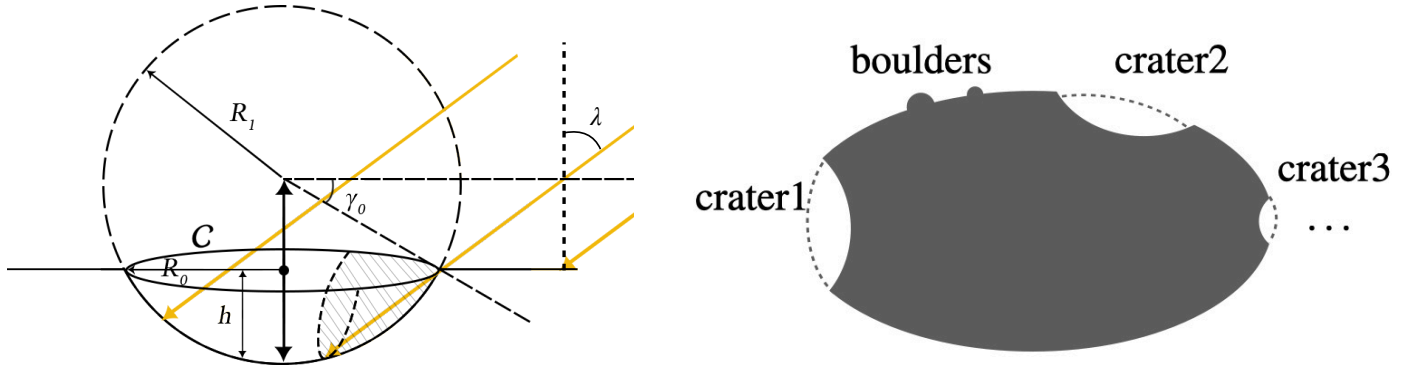


Fig. 1. Simple crater model (*left panel*) and features in the asteroid that affect the total YORP torque (*right panel*). In the *left panel*, the yellow arrow represents the light coming from the direction of the Sun, and the shadow region is shaded in gray. Parameters h and R_0 are the depth and radius of the crater, respectively. The edge circle of the crater on the ground level is denoted by C . The angle between the sunlight and ground normal is denoted by λ_0 . The *right panel* shows the boulders and craters on the surface of asteroids that could contribute to the total YORP effect.

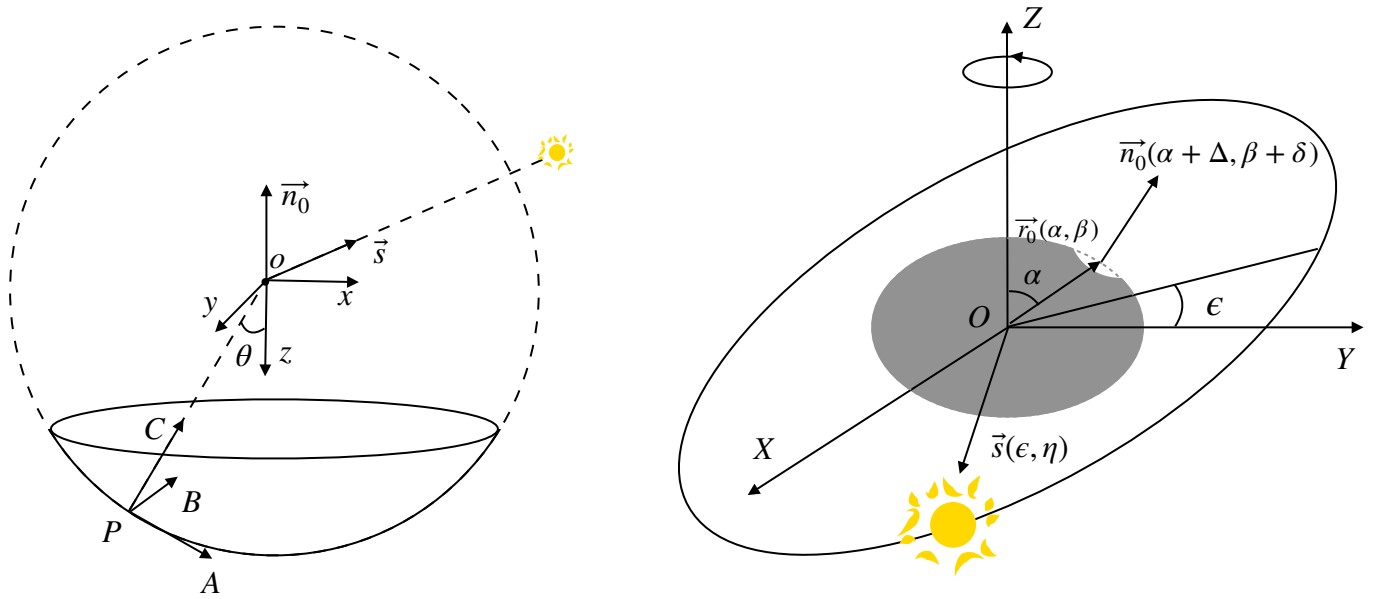


Fig. 2. Three coordinate systems in this paper: coordinate system $oxyz$ for calculating the illuminated domain in the crater, $PABC$ for calculating the effective recoil force of an arbitrary surface element, and $OXYZ$ for averaging the YORP torque over the spin and orbital motion.

one object to the next (see, e.g., [Marchi et al. 2015](#), for a review), depending on its age, its response to impacts, and other possible processes, such as surface motions that can erase small features or boulder armoring that can prevent a crater from forming (e.g., [Bierhaus et al. 2022](#); [Daly et al. 2022](#)). Nevertheless, craters are an important and systematic characteristic of asteroid surfaces that may have some influence on the YORP effect because this effect is sensitive to the fine topography ([Statler 2009](#)).

For the first time, we propose here the concept of the crater-induced YORP (called CYORP hereafter) and show that CYORP may contribute to the total YORP torque as well, which adds a “CYORP” term into Eq. (1),

$$\mathbf{T}_{\text{YORP}} = \mathbf{T}_{\text{NYORP}} + \mathbf{T}_{\text{TYORP}} + \mathbf{T}_{\text{CYORP}}, \quad (2)$$

where

$$\mathbf{T}_{\text{CYORP, total}} = \sum_i \mathbf{T}_{\text{CYORP, } i} \quad (3)$$

as a summation for a whole set of craters or concave structures on the asteroid (see Fig. 1). The CYORP torque is the difference

between the torque caused by the crater and the torque by the ground before the birth of the crater,

$$\mathbf{T}_{\text{CYORP}} = \mathbf{T}_{\text{crater}} - \mathbf{T}_{\text{ground}}. \quad (4)$$

Here $\mathbf{T}_{\text{ground}}$ is the normal YORP torque of the ground before the birth of the crater (see Fig. 1), which can be expressed as

$$\mathbf{T}_{\text{ground}} = \pi R_0^2 \frac{2\Phi}{3c} \cos \lambda \mathbf{r}_0 \times \mathbf{n}_0, \quad (5)$$

where R_0 is the radius of the crater, Φ is the solar flux on the asteroid, c is the speed of light, λ is the incident angle of the light, and \mathbf{r}_0 and \mathbf{n}_0 are the position vector and unit normal vector of the crater, respectively (see Fig. 2).

The CYORP torque arises due to the concave structure of the crater. The vertical wall of the crater induces a force tangential to the surface, and the curvature of the crater induces a normal force component that is different from the force that is produced by the ground without the crater. Thus, the force that leads to the CYORP torque comprises of both the tangential and normal components. The self-sheltering and self-heating effects because

of concavity influence the total torque; this is also considered in this work. In general, T_{CYORP} takes the form of the following scaling rule with the radius of the crater R_0 and of the asteroid R_{ast} :

$$T_{\text{CYORP}} = W \frac{\Phi}{c} R_0^2 R_{\text{ast}}, \quad (6)$$

where W is a function of the properties of the crater and the asteroid (the detailed derivation of this equation is presented in Sect. 2). As a general rule, T_{CYORP} is thus proportional to the square of the crater radius and to the asteroid radius. Based on this scaling relation, we developed a semi-analytic method that can be applied to the calculation of the CYORP effect, and it provides a basic understanding of the relative influence of each parameter. The derived CYORP torque can be applied both for craters and for any concave structures on the surface of an asteroid, although a modification accounting for the geometry is needed.

We focus here on one crater and vary its properties to determine how they influence the YORP effect. As a first step, we assume zero thermal inertia (Rubincam's approximation; see Rubincam 2000), which can be applied to asteroids with low thermal conductivity or slow rotation. Rubincam's approximation is suitable for calculating the spin component of the YORP torque. The model including the thermal inertia of the asteroid will be the topic of a next study. In the following, we present our calculation of the crater-induced YORP torque in Sect. 2, accounting for the crater shape and other related thermophysical processes. Section 3 presents results for various asteroid properties and locations of the crater. In Sect. 4 we give the typical value of the CYORP torque (Sect. 4.1), which could be used to estimate the order of magnitude, and we analyze the applicability of the CYORP effect to the complete YORP torque and to the spin evolution of asteroids (Sect. 4.2). In Sect. 5 we summarize the main results and draw the conclusion.

2. Calculation of the crater-induced YORP torque

2.1. Shape model for the crater

We considered a simple shape model for the crater, which is represented by a full or part of a semi-sphere with a radius R_1 and depth h (see Fig. 1). In this way, the size and the shape of the crater can be determined by two parameters R_1 and γ_0 , where

$$\sin \gamma_0 = \frac{R_1 - h}{R_1}. \quad (7)$$

We considered a coordinate system (x, y, z) with the origin located at the sphere center (see Fig. 2). The unit vectors e_x , e_y , and e_z were chosen so that e_z lay along the symmetry axis of the spherical crater and e_x lay in the plane of e_z and the unit solar position vector s . Vector e_y follows the right-hand rule. Equivalently, e_y and e_z are defined as

$$\begin{aligned} e_y &= e_z \times s, \\ e_x &= e_y \times e_z. \end{aligned} \quad (8)$$

In this coordinate system (see Fig. 2), the crater can be defined as

$$\mathcal{Z} := \{(x, y, z) \in \mathbb{R}^3 | x^2 + y^2 + z^2 = R_1^2, z \geq R_1 \sin \gamma_0\}. \quad (9)$$

Applying

$$\begin{cases} x = r \sin \theta \cos \phi \\ y = r \sin \theta \sin \phi \\ x = r \cos \theta, \end{cases} \quad (10)$$

the crater is equivalently

$$\mathcal{Z} := \{(x, y, z) \in \mathbb{R}^3 | r = R_1, \theta \in (0, \pi/2 - \gamma_0), \phi \in (0, 2\pi)\}. \quad (11)$$

The widely used parameter depth-diameter ratio translates as

$$\frac{h}{D_0} = \frac{1 - \sin \gamma_0}{2 \cos \gamma_0}, \quad (12)$$

where $D_0 = 2R_0$ is the diameter of the crater.

2.2. Shadowing effect

For a concave geometry such as a crater, the influence of self-shadowing plays a significant role for the YORP effect. There are three consequences of self-shadowing. (1) The crater is sheltered by itself, that is, the fraction in the shadow of the crater does not receive the photons from direct solar radiation. (2) The effective angular momentum transfer that occurs in a surface element is affected by the neighboring topology because the radiated photons can be reabsorbed by the shelter. As a result, the effective recoil force (and the YORP torque) is different from that in the case of a nonsheltered environment. (3) The radiation caused by secondary illumination from the crater itself, which is ignored in this work for simplicity. As we show in Sect. 3, the first effect of shadowing contributes to the net YORP torque of a crater, and the second effect weakens the YORP torque.

2.2.1. Illuminated area

The unit vector directed toward the Sun from the crater s' represents the direction of the parallel sunlight. When we consider that the size of a typical asteroid R_{ast} (on the order of some kilometers) is much smaller than the distance from the Sun d (on the order of one au), the unit vector pointing from the center of the asteroid to the Sun is $s \approx s'$. In the following context, we use s to denote the position of the Sun relative to both the asteroid and the crater.

The unit position vector of the Sun in the coordinate system (x, y, z) can be expressed as

$$s = \sin \lambda e_x - \cos \lambda e_z, \quad (13)$$

where λ is the incident angle of the light. To determine the region that is exposed to sunlight, we need to find the expression function of the boundary of the illuminated region. First, we define the edge of the crater at the ground level, which is a circle as

$$C := \{(x, y, z) | x^2 + y^2 = R_1^2 \cos^2 \gamma_0, z = R_1 \sin \gamma_0\}. \quad (14)$$

The boundary is the projection of the upmost circle C_1 of the crater on the crater \mathcal{Z} along the light. The boundary can be obtained by solving the intersection of the crater \mathcal{Z} and an elliptic cylinder, which contains C_1 and along s . When an arbitrary point in the circle C_1 is (x', y', z') , the elliptic cylinder is

$$\begin{cases} x'^2 + y'^2 = R_1^2 \cos^2 \gamma_0 \\ z' = 0 \\ \frac{x - x'}{\sin \lambda} = \frac{z - z'}{-\cos \lambda} \\ y = y'. \end{cases} \quad (15)$$

After reduction, the expression of this elliptic cylinder is

$$(x + z \tan \lambda)^2 + y^2 = R_1^2. \quad (16)$$

Combining this with the expression of the crater (Eq. (9)) and applying $x = R_1 \sin \theta \sin \phi$, $y = R_1 \sin \theta \cos \phi$ and $z = R_1 \cos \theta$, we obtain the expression of the intersection curve,

$$\cos \phi = \frac{\cos 2\lambda \cos \theta + \sin \gamma_0}{\sin 2\lambda \sin \theta}. \quad (17)$$

Because $0 < \phi < 2\pi$, given a polar angle θ , Eq. (17) has two solutions (if a solution exists) ϕ_1 and ϕ_2 , for ϕ with $\phi_1 + \phi_2 = 2\pi$, in which we assume $\phi_1 < \phi_2$ for further analysis. The illuminated region is represented by

$$\mathcal{W} := \left\{ (x, y, z) \in \mathcal{Z} \mid \cos \phi < \frac{\cos 2\lambda \cos \theta + \sin \gamma_0}{\sin 2\lambda \sin \theta} \right\}. \quad (18)$$

It is not guaranteed that Eq. (17) has a solution because the right side of the equation can be larger than 1. Depending on the incident angle of the light λ , there are three illumination modes, given an incident angle of light λ as follows:

- (1) The whole crater is illuminated $\iff \lambda < \gamma_0$. In this case, $\mathcal{W} = \mathcal{Z}$.
- (2) Two sides of the crater (e.g., east and west) are illuminated $\iff \gamma_0 < \lambda < \pi/4 + \gamma_0/2$. In this case, $\mathcal{W} = \{(x, y, z) \in \mathcal{Z} \mid \theta \in (0, \pi/2 - 2\lambda + \gamma_0), \phi \in (0, 2\pi) \text{ or } \theta \in (\pi/2 - 2\lambda + \gamma_0, \pi/2 - \gamma_0), \phi \in (\phi_1, \phi_2)\}$.
- (3) One side of the crater is illuminated $\iff \pi/4 + \gamma_0/2 < \lambda < \pi/2$. In this case, $\mathcal{W} = \{(x, y, z) \in \mathcal{Z} \mid \theta \in (2\lambda - \gamma_0 - \pi/2, \pi/2 - \gamma_0), \phi \in (\phi_1, \phi_2)\}$.

We refer to Appendix A for the details of the above mathematical description of these three illumination modes, or a self-examination may be made through plane geometry in Fig. 1. Although the different illumination modes are based on Eq. (18), they refer to different integration domains. Expressing them explicitly helps solve the thermal recoil force of the crater (see Eq. (31) in Sect. 2.2.2), as the crater could go through all these modes during a rotational period.

2.2.2. Self-heating

The surface of asteroids experiences three types of forces, which are caused by absorbed, scattered, and reemitted photons, respectively. The torque produced by absorbed photons is proven to average out after integrating over the spin and orbital periods for any asteroid shapes. Therefore, this type of force does not contribute to the YORP torque of the whole asteroid (Nesvorný & Vokrouhlický 2008). Both the recoil forces produced by scattered and reemitted photons depend on the light scattering law. We assumed the simple and most widely used Lambert scattering law, in which the light is emitted in all directions with an intensity proportional to the cosine of the angle between the light direction and the normal vector of the surface. For concave configurations such as a crater, we should consider the self-heating effect, which arises because some of the photons may be re-absorbed by the nearby shelter, which prevents them from contributing to the effective recoil force (Statler 2009; Yan & Li 2019). The reemission of the obscuring parts, which might make a difference for a concave structure (Rozitis & Green 2013), is ignored in this work for its complexity and will be studied in the future.

We consider a reference frame with the origin at the point P located at the polar angle θ (see Fig. 2). The orthogonal basis is represented by three unit vectors:

$$\begin{aligned} \mathbf{e}_C &= \mathbf{n} \\ \mathbf{e}_B &= \mathbf{e}_C \times \mathbf{e}_z \\ \mathbf{e}_A &= \mathbf{e}_B \times \mathbf{e}_C. \end{aligned} \quad (19)$$

Here \mathbf{n} is the normal vector of the surface element. An arbitrary vector of the light ray that is emitted through a solid angle $d\Omega$ can be expressed by the polar angle μ and the azimuth angle ν in this reference frame. According to Lambert's scattering law, the recoil force on the surface element dS that is located at the latitude of θ can be expressed as

$$\mathbf{f} = - \int_{\mathcal{H}} \frac{\Phi}{c} \cos \mu \begin{pmatrix} \sin \mu \cos \nu \\ \sin \mu \sin \nu \\ \cos \mu \end{pmatrix} d\Omega. \quad (20)$$

Here \mathcal{H} is the region on the sky in which the light ray is not reabsorbed. In the spherical coordinate system, the boundary of \mathcal{H} is the intersection curve of an elliptic cone and the unit sphere, both of which are centered at the origin. This elliptic cone must contain the upmost circle (C in Fig. 1). When an arbitrary point in C is (x', y', z') , the elliptic cone expressed by (x, y, z) is

$$\begin{cases} y'^2 + [(x' - x_0) \cos \theta - (z' - z_0) \sin \theta]^2 = \cos^2 \gamma_0 \\ (x' - x_0) \sin \theta + (z' - z_0) \cos \theta = 0 \\ \frac{x}{x'} = \frac{y}{y'} = \frac{z}{z'} \end{cases}. \quad (21)$$

Here $(x_0, 0, z_0) = (\sin \gamma_0 \sin \theta, 0, 1 - \sin \gamma_0 \cos \theta)$ is the center of the circle C in the coordinate system (a, b, c) . Combining this with the unit sphere, which is

$$\begin{cases} x = \sin \mu \cos \nu \\ y = \sin \mu \sin \nu \\ z = \cos \mu, \end{cases} \quad (22)$$

we obtain the function of the boundary of the illuminated sky:

$$\cos \nu = - \frac{\cos 2\mu \cos \theta + \sin \gamma_0}{\sin 2\mu \sin \theta}. \quad (23)$$

Here we assume that the solutions of this equation for ν are ν_1 and ν_2 with $\nu_1 < \nu_2$. Thus, the region \mathcal{H} is

$$\mathcal{H} = \left\{ (x, y, z) \in \mathbb{R}^3 \mid \mu \in (0, \pi/2), \cos \nu < - \frac{\cos 2\mu \cos \theta + \sin \gamma_0}{\sin 2\mu \sin \theta} \right\}. \quad (24)$$

It can be also expressed as

$$\mathcal{H} = \left\{ (x, y, z) \in \mathbb{R}^3 \mid \nu \in (0, 2\pi), \mu \in \left(\frac{\pi + \gamma_0 - \gamma_1}{2}, \pi \right) \right\}, \quad (25)$$

where

$$\gamma_1 = \arctan \left(\frac{1}{\tan \theta \cos \nu} \right) \in (0, \pi). \quad (26)$$

Therefore, the recoil force of the surface element that is located at the latitude θ is

$$\mathbf{f} = - \int_{\mathcal{H}} \frac{\Phi}{c} \cos \mu \begin{pmatrix} \sin \mu \cos \nu \\ \sin \mu \sin \nu \\ \cos \mu \end{pmatrix} \sin \mu d\nu d\mu = \begin{pmatrix} f'_1(\theta) \\ 0 \\ f'_3(\theta) \end{pmatrix}. \quad (27)$$

Here $f'_1(\theta)$ and $f'_3(\theta)$ are functions of the latitude θ of the surface element, resulting from ν_1 and ν_2 . The second component cancels out because the integral of $\sin \nu$ over either (ν_1, ν_2) or $(0, 2\pi)$ is zero. Given $\mathbf{e}_C = \mathbf{n}$ and $\mathbf{e}_A = \mathbf{n} / \tan \theta + \mathbf{e}_z / \sin \theta$ (see Eq. (19)), we have

$$\mathbf{f} = f_1(\theta)\mathbf{n} + f_3(\theta)\mathbf{e}_z, \quad (28)$$

with

$$\begin{aligned} f_1(\theta) &= f'_3(\theta) + \frac{f'_1(\theta)}{\tan \theta}, \\ f_3(\theta) &= \frac{f'_3(\theta)}{\sin \theta}. \end{aligned} \quad (29)$$

2.3. Integral of the recoil force

The total recoil force of the crater can be obtained by integrating the recoil force (Sect. 2.2.2) over the illuminated region (Sect. 2.2.1),

$$\mathbf{F} = \int_{\mathcal{W}} \mathbf{f} dS = \int_{\mathcal{W}} f_1(\theta)\mathbf{n} + f_3(\theta)\mathbf{e}_z \sin \theta d\phi d\theta. \quad (30)$$

Because $\mathbf{n} = -\sin \theta \cos \phi \mathbf{e}_x - \sin \theta \sin \phi \mathbf{e}_y - \cos \theta \mathbf{e}_z$, in the coordinate system (x, y, z) , we have

$$\mathbf{F} = \int_{\mathcal{W}} \sin \theta \begin{pmatrix} -f_1(\theta) \sin \theta \cos \phi \\ -f_1(\theta) \sin \theta \sin \phi \\ -f_1(\theta) \cos \theta + f_3(\theta) \end{pmatrix} d\phi d\theta = \begin{pmatrix} F_1(\lambda) \\ 0 \\ F_3(\lambda) \end{pmatrix}. \quad (31)$$

The y -component vanishes due to the symmetry of the integral domain on ϕ (see Eq. (18)). The tangential component and the normal component of the recoil force both exist, and not only one of them as in TYORP or NYORP.

2.4. Averaged YORP torque

The radiative torque is expressed as

$$\mathbf{T}_{\text{crater}} = \int_{\mathcal{W}} \mathbf{r}' \times \mathbf{f} dS. \quad (32)$$

Here $\mathbf{r}' = \mathbf{r}_0 + \mathbf{r}$ is the position vector from the mass center of the asteroid to the surface element dS on the crater, where \mathbf{r}_0 denotes the position vector of the sphere center of the crater, and \mathbf{r} denotes the vector from the sphere center to the surface element. Because $\mathbf{r} \times \mathbf{f} \sim \mathbf{n} \times \mathbf{n} = 0$ and $r \ll r_0$, Eq. (32) can be simplified as

$$\mathbf{T}_{\text{crater}} = \int_{\mathcal{W}} \mathbf{r}_0 \times \mathbf{f} dS = \mathbf{r}_0 \times \mathbf{F} = F_1(\lambda)\mathbf{r}_0 \times \mathbf{e}_x + F_3(\lambda)\mathbf{r}_0 \times \mathbf{e}_z. \quad (33)$$

When we substitute $\mathbf{e}_x = s / \sin \lambda + \mathbf{e}_z / \tan \lambda$ into Eq. (33), the total torque becomes

$$\mathbf{T}_{\text{crater}} = \frac{F_1(\lambda)}{\sin \lambda} \mathbf{r}_0 \times \mathbf{s} - \left(\frac{F_1(\lambda)}{\tan \lambda} + F_3(\lambda) \right) \mathbf{r}_0 \times \mathbf{n}_0. \quad (34)$$

Plugging Eqs. (5) and (34) into Eq. (4), we obtain

$$\mathbf{T}_{\text{CYORP}} = \frac{F_1(\lambda)}{\sin \lambda} \mathbf{r}_0 \times \mathbf{s} - \left(\frac{F_1(\lambda)}{\tan \lambda} + F_3(\lambda) + \pi R_0^2 \frac{2\Phi}{3c} \cos \lambda \right) \mathbf{r}_0 \times \mathbf{n}_0. \quad (35)$$

In order to understand this CYORP effect on the secular spin evolution of an asteroid, we need to average it over its dynamic timescale. It is well known that the timescale of the YORP effect is much longer than the orbital period and spin period, therefore it is useful to calculate the average YORP torque over the orbital period and the spin period. In general, the spin period (some hours) is much shorter than the orbital periods (some years), so that the integral over the orbital motion and that over the spin motion can be treated separately.

We consider an inertia reference frame (XYZ) with the origin O at the asteroid center (see Fig. 2). The axis OZ is the spin axis of the asteroid, and the OXY plane is the equatorial plane. The position vector of the crater \mathbf{r}_0 is

$$\mathbf{r}_0 = r_0(\sin \alpha \cos \beta, \sin \alpha \sin \beta, \cos \alpha), \quad (36)$$

where r_0 is the distance from the crater to the mass center of the asteroid. The unit normal vector \mathbf{n}_0 of the ground can be expressed as

$$\mathbf{n}_0 = (\sin(\alpha + \Delta) \cos(\beta + \delta), \sin(\alpha + \Delta) \sin(\beta + \delta), \cos(\alpha + \Delta)) = -\mathbf{e}_z, \quad (37)$$

where the independent variables δ and Δ denote deviations of the normal vector from the position vector, which is determined by the geometry of the asteroid. The unit solar vector \mathbf{s} is

$$\mathbf{s} = (\cos \eta, \cos \epsilon \sin \eta, \sin \epsilon \sin \eta), \quad (38)$$

where η is the angle of orbital motion. The vector \mathbf{e}_x can be expressed as a function of \mathbf{s} and \mathbf{e}_z according to Eq. (13). Therefore, the averaged CYORP torque is

$$\langle \mathbf{T}_{\text{CYORP}} \rangle = \frac{1}{4\pi^2} \int_0^{2\pi} \int_0^{2\pi} \mathbf{T}_{\text{CYORP}} H(\mathbf{s} \cdot \mathbf{n}_0) d\beta d\eta. \quad (39)$$

Here H is the Heaviside step function, which is defined as

$$H(x) := \begin{cases} 1, & x > 0 \\ 0, & x \leq 0. \end{cases} \quad (40)$$

The average CYORP torque turns out to be a function of γ_0 , α , ϵ , δ and Δ , where

- γ_0 describes the depth-diameter ratio of the crater (see Fig. 1),
- α is the latitude of the crater,
- ϵ is the obliquity of the asteroid,
- Δ and δ describes the deviation of the normal vector \mathbf{n}_0 from the position vector \mathbf{r}_0 (see Eq. (37)), which is determined by the macroscopic geometry of the asteroid.

The dependence of the CYORP effect on these parameters is exposed in the next section.

3. Results

In general, the averaged CYORP torque has the form

$$\langle \mathbf{T}_{\text{CYORP}} \rangle_z = W_z(\gamma_0, \alpha, \epsilon, \Delta, \delta) \frac{\Phi}{c} R_0^2 R_{\text{ast}}, \quad (41)$$

$$\langle \mathbf{T}_{\text{CYORP}} \rangle_\epsilon = W_\epsilon(\gamma_0, \alpha, \epsilon, \Delta, \delta) \frac{\Phi}{c} R_0^2 R_{\text{ast}}, \quad (42)$$

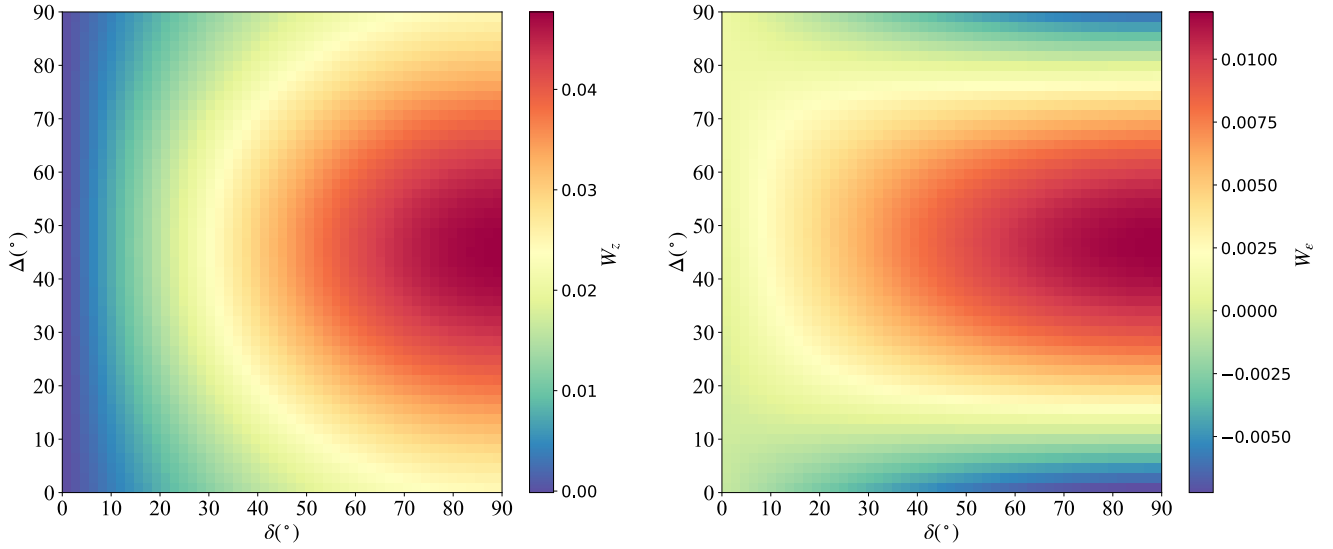


Fig. 3. Map of the dimensionless parameter W scaled by color from blue (low) to red (high) as a function of δ and Δ (which are related to the asymmetry of the asteroid; see Sect. 3.1). The spin component W_z is shown in the left panel, and the obliquity component W_ϵ is shown in the right panel. Here both α and ϵ are set to be $\pi/4$.

where the W function can be obtained from Eq. (39). Here $\langle T_{\text{CYORP}} \rangle_z$ and $\langle T_{\text{CYORP}} \rangle_\epsilon$ are equivalent to the Z and Y components of the CYORP torque, denoting the spin and obliquity torques, respectively. In the following analysis, we present the values of W_z and W_ϵ in different cases to show how the CYORP torque varies with the parameters.

3.1. Asteroid shape

The asteroid shape affects the relation between \mathbf{r}_0 and \mathbf{n}_0 . For example, a spherical asteroid has $\mathbf{r}_0/r_0 = \mathbf{n}_0$, while a prolate asteroid does not. The relation between \mathbf{r}_0 and \mathbf{n}_0 translates into Δ and δ (see Eqs. (36) and (37)) in our calculation. Figure 3 shows the values of the dimensionless parameter W in terms of δ and Δ , where $\alpha = \epsilon = \pi/4$. We demonstrate that for Z -axis symmetric asteroids, which is equivalent to $\delta = 0$, the CYORP torque disappears due to the antisymmetry of the torque function over the integral domain. However, for nonsymmetric asteroids ($\delta \neq 0$), the CYORP torque includes both the spin and obliquity components.

3.1.1. Z -axis symmetric asteroid

Here, we call a Z -axis symmetric asteroid an asteroid that has a surface of revolution around the z -axis (major principal axis)¹. Some well-known examples are top-shape asteroids and symmetric ellipsoid asteroids with an axis ratio 1:1: c_l ($c_l > 0$). A Z -axis symmetric asteroid has $\delta = 0$ everywhere on its surface, as demonstrated in Appendix B. Given $\delta = 0$, we substitute Eqs. (36) and (37) into Eq. (35), leading to

$$\mathbf{T}_{\text{CYORP}} = \frac{F_1(\lambda)}{\sin \lambda} \begin{pmatrix} \sin \eta \sin \alpha \sin \beta \sin \epsilon - \sin \eta \cos \alpha \cos \epsilon \\ \cos \eta \cos \alpha - \sin \eta \sin \alpha \cos \beta \sin \epsilon \\ \sin \eta \sin \alpha \cos \beta \cos \epsilon - \cos \eta \sin \alpha \sin \beta \end{pmatrix} + \left(\frac{F_1(\lambda)}{\tan \lambda} + F_3(\lambda) + \pi R_1^2 \frac{2\Phi}{3c} \cos \lambda \right) \begin{pmatrix} \sin \beta \sin \Delta \\ \cos \beta \sin \Delta \\ 0 \end{pmatrix}, \quad (43)$$

¹ Cross sections perpendicular to the Z -axis are circular.

where

$$\begin{aligned} \cos \lambda &= \mathbf{n}_0 \cdot \mathbf{s} \\ &= \cos \eta \sin(\alpha + \Delta) \cos \beta + \sin \eta \sin(\alpha + \Delta) \sin \beta \cos \epsilon \\ &\quad + \sin \eta \cos(\alpha + \Delta) \sin \epsilon. \end{aligned} \quad (44)$$

The secular CYORP torque is calculated by averaging $T_{\text{CYORP}} H(\cos \lambda)$ over the spin angle ζ and orbital angle η according to Eq. (39).

Interestingly, after averaging, the obliquity component (Y component) and the spin component (Z component) vanish because they are antisymmetric in the interval domain $\beta \in (0, 2\pi)$ and $\eta \in (0, 2\pi)$. This becomes clear in the example of the domain $\beta \in (0, \pi)$ and $\eta \in (0, \pi)$. Because $\sin(\pi - x) = \sin x$ and $\cos(\pi - x) = -\cos x$, for any point pair (ζ, η) , we can find that another point pair $(\pi - \zeta, \pi - \eta)$ exists for which the Y -axis and Z -axis components of $T_{\text{CYORP}} H(\cos \lambda)$ have the same absolute value but the opposite sign; this is shown by investigating Eqs. (43) and (44). The Y -axis and Z -axis components of T_{CYORP} change sign, but λ does not change at all. In the domain $\zeta \in (0, \pi)$ and $\eta \in (0, \pi)$, the average function is therefore antisymmetric about $(\pi/2, \pi/2)$ for Y -axis and Z -axis components, which leads to the fact that the average is 0. Other antisymmetric points in the whole domain are $(\pi/2, 3\pi/2)$, $(3\pi/2, \pi/2)$, and $(3\pi/2, 3\pi/2)$. Therefore, there is no spin and obliquity component of the CYORP torque left for Z -axis symmetric asteroids ($\delta = 0$). This antisymmetric property does not occur in the X -axis component of $\langle T_{\text{CYORP}} \rangle$, which changes the precession angle of the asteroid. Although Nature knows no perfectly Z -axis symmetric asteroid, this analysis implies that the torque would be severely weakened for a nearly Z -axis symmetric asteroid (small δ), which is also shown in Fig. 3. However, this antisymmetry of T_{CYORP} is only valid when Rubincam's approximation (zero thermal inertia) is applied and would be broken in the case of nonzero thermal inertia, for which the spin and obliquity components still exist (see Sect. 3.4).

3.1.2. Asymmetric asteroid

A perfectly Z -axis symmetric asteroid does not exist in Nature, for which even the normal YORP effect vanishes

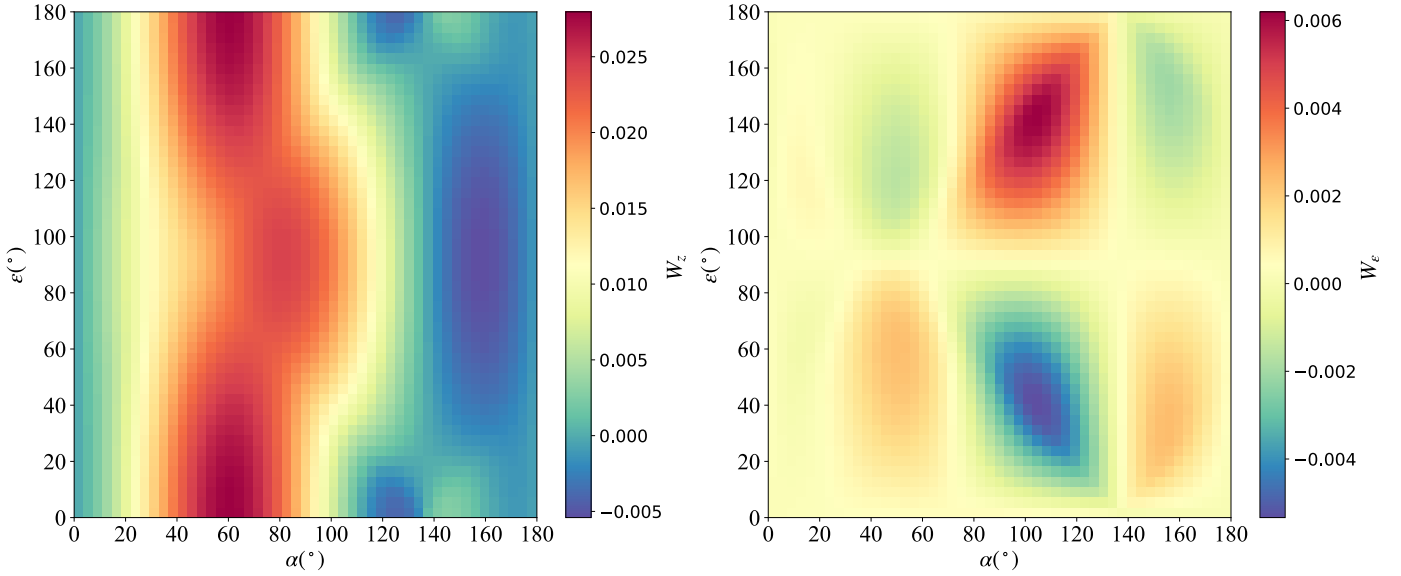


Fig. 4. Map of the dimensionless parameter W , which varies with the latitude of the crater α and the obliquity of the asteroid ϵ , scaled by color from blue (low) to red (high). The spin component W_z is shown in the *left panel*, and the obliquity component W_ϵ is shown in the *right panel*. Here both δ and Δ are set to be $\pi/4$.

(Breiter et al. 2007). We therefore investigated how the CYORP effect depends on the asymmetry of the asteroid. For an asteroid without a perfectly symmetric shape, the position vector \mathbf{r}_0 and the normal vector \mathbf{n}_0 are not always aligned in the same longitude ($\delta \neq 0$). We already know (Sect. 3.1.1) that when $\delta = 0$, the CYORP torque only has the obliquity component. In this section, we investigate how δ affects the CYORP effect in the imperfectly symmetric case. We also investigate the effect of Δ . For simplicity, we fixed other parameters by setting the crater shape parameter $\gamma_0 = 0.2$, the latitude $\alpha = \pi/4$, and the obliquity $\epsilon = \pi/4$.

Figure 3 shows that the spin component starts from 0 and grows with increasing δ to a magnitude comparable to the obliquity component. Thus, in the case of $\delta \neq 0$, which is more common in real craters on asteroids, the CYORP torque has a non-negligible spin component that changes the spin rate of the asteroid in the long term.

3.2. Crater latitude α and asteroid obliquity ϵ

In order to determine how W varies with the crater latitude and the obliquity, we need to keep other variables constant. Figure 4 shows the W map with a crater latitude $\alpha \in (0, \pi)$ and an asteroid obliquity $\epsilon \in (0, \pi)$ when δ and Δ are set to be $\pi/4$. The latitude of large craters can cause their shape to depart from the semi-sphere model used in our study (Fujiwara et al. 1993; Daly et al. 2020b). The effect of more complex geometries is left for future studies.

3.3. Crater depth-diameter ratio

The above results assume that the depth-diameter ratio h/D_0 of the crater is ~ 0.16 , while real craters on asteroids exhibit wide ranges of this ratio. Figure 5 shows the recoil forces (Eq. (31)) caused by craters with different depth-diameter ratios. Moreover, for the tangential component of the recoil force, the self-sheltering effect is negligible in shallow craters (low h/D_0), while for the normal component, the self-heating effect cannot be ignored even in shallow craters.

3.4. Thermal inertia

The inclusion of nonzero thermal inertia increases the complexity of the problem and requires a numerical method to obtain a precise solution, which is beyond the scope of this paper. However, we can reasonably modify the total force of the crater in order to mimic the thermal lag effect due to nonzero thermal inertia. We assumed that the Sun rises from the east and sets in the west from the view of a crater on the asteroid. The west part of the crater is illuminated in the morning and the east part is illuminated in the evening. The YORP torque arises from the temperature difference between the west and east parts. However, the temperature difference in the morning should be different from that in the evening as a result of the thermal inertia. In the morning, the crater just experienced a dark night, while in the evening, the crater has been sunlit for the whole day. This means that the temperature of the crater is *not* symmetric in the daytime, which will induce a nonzero y component of the total recoil force \mathbf{F} in Eq. (31),

$$\mathbf{F}_2(\lambda) \neq 0. \quad (45)$$

Although we are currently unable to obtain the precise solution of $\mathbf{F}_2(\lambda)$, we can at least examine whether it has an effect on the CYORP torque by simply performing the transformation $F_1(\lambda) \rightarrow F_1(\lambda)/\sqrt{2}$ and $F_2(\lambda) \rightarrow F_1(\lambda)/\sqrt{2}$. Here a hidden assumption is that $F_1(\lambda)$ and $F_2(\lambda)$ are on the same order of magnitude. This transformation does not give a direct estimate of the considered thermal inertia, and it is used here only to account for the effect of nonzero thermal inertia. In future work, we will directly estimate the consequences of given values of thermal inertia on CYORP.

Figure 6 shows the values obtained for W_z and W_ϵ when $\delta = \Delta = 0$. With nonzero thermal inertia, the spin and obliquity components arise for some sets of (α, ϵ) , while they are always zero without thermal inertia due to $\delta = 0$, which has already been proven in Sect. 3.1.1. Therefore, we infer that the nonzero thermal inertia of the asteroid can induce a nonzero spin component of the CYORP torque for Z -axis symmetric asteroids, and should

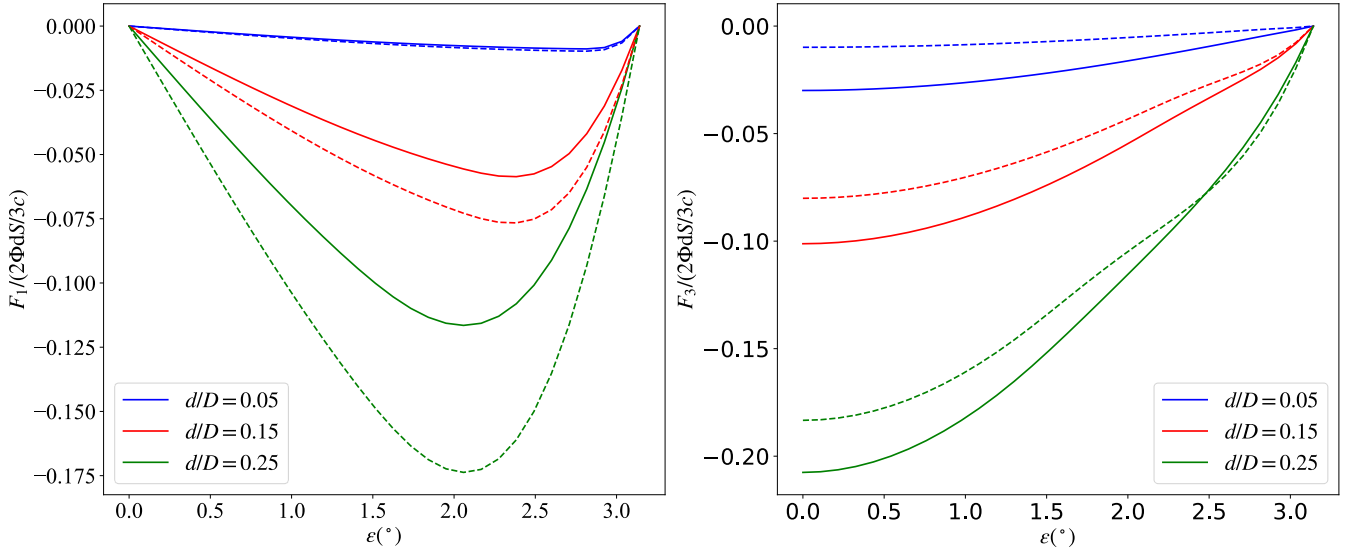


Fig. 5. Recoil forces for craters with different h/D_0 . The results considering the self-heating effect are shown by solid lines, and the results obtained without the self-heating effect are shown by dashed lines. The *left panel* denotes the tangential component of the recoil force, and the *right panel* denotes the normal component.

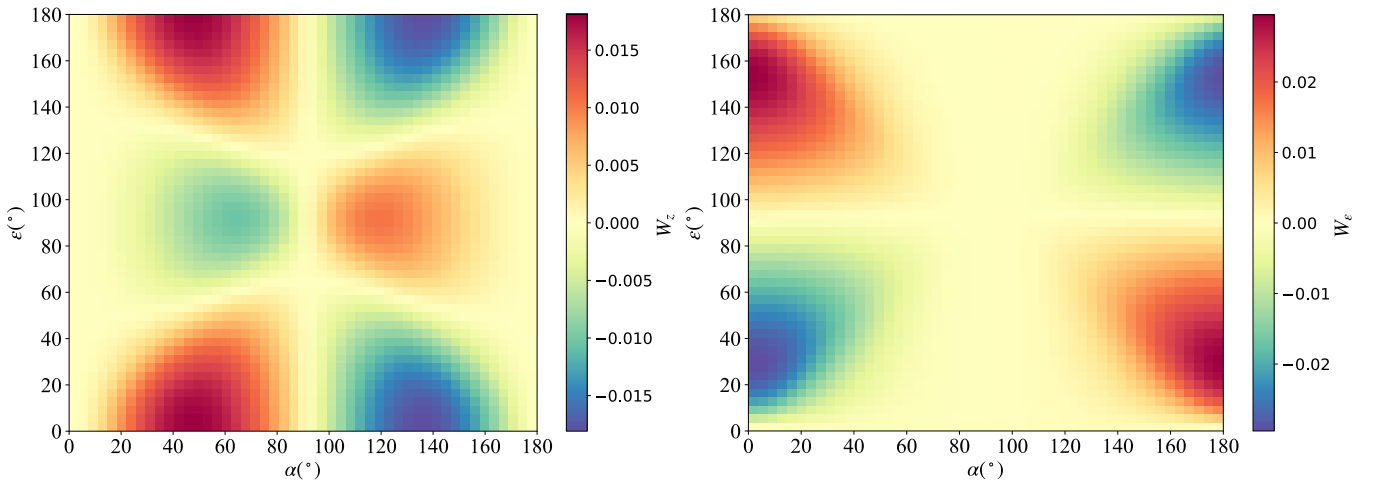


Fig. 6. Color map of the dimensionless parameters W_z (*left panel*) and W_ϵ (*right panel*) accounting for nonzero thermal inertia. The variables δ and Δ are set to zero. Here a nonzero value of W_z and W_ϵ arises, while the values are zero throughout the map in the regime of zero-thermal inertia, as proven in Sect. 3.1.1.

affect the behavior of the CYORP torque; this will be studied in future works.

4. Discussion and implications

4.1. Order of magnitude

In order to understand the effectiveness of the CYORP torque better, it is useful to compare it with the two torques in the current YORP model: the normal YORP (NYORP) torque, which is caused by the global asymmetry of the asteroid, and the tangential YORP (TYORP) torque, which results from the temperature difference of two sides of boulders. To a first approximation, the normal YORP torque for an asteroid can be simply expressed as

$$\langle T_{\text{NYORP},z} \rangle \sim C_z \frac{\Phi}{c} R_{\text{ast}}^3 \cos \left(2\epsilon + \frac{1}{3} \right), \quad (46)$$

$$\langle T_{\text{NYORP},\epsilon} \rangle \sim C_\epsilon \frac{\Phi}{c} R_{\text{ast}}^3 \sin 2\epsilon. \quad (47)$$

Here C_z and C_ϵ are dimensionless YORP coefficients of the spin component and obliquity component, respectively. Golubov & Scheeres (2019) computed the normal YORP torques for type I, II, III, and IV asteroids² from the sources of photometric observations, radar measurements, and in situ observations. For type I and II asteroids, the number distribution of C_z peaks around 0.005, while for type III and IV asteroids, the peak is located at $C_z < 0.001$. Here we took $C_z = 0.005$ for the following comparison. It was shown that an approximate correlation between these two coefficients is given by $C_\epsilon/C_z \sim 2/3$ (Golubov & Scheeres 2019; Marzari et al. 2020).

The tangential YORP torque for one boulder, which is dominated by the spin component, is (Golubov & Krugly 2012)

$$\langle T_{\text{TYORP},b} \rangle = C_{\text{T},b} S R_{\text{ast}} \frac{\Phi}{c}, \quad (48)$$

² Asteroids are categorized into types I, II, III, and IV according to the behavior of the YORP torque curve (Vokrouhlický & Čapek 2002).

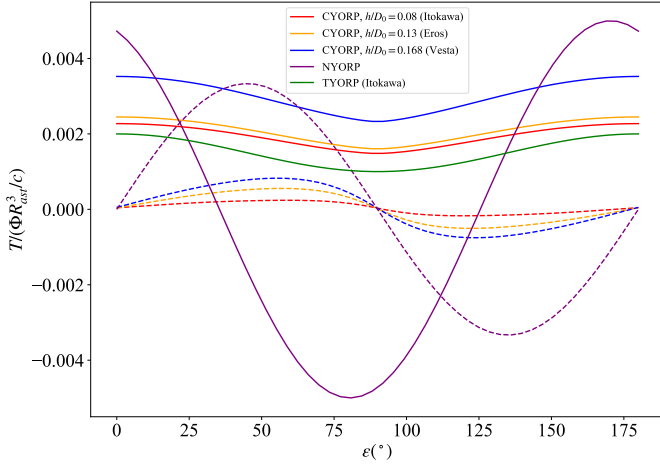


Fig. 7. Comparison between the CYORP, TYORP, and NYORP torques, which are shown in different colors. The solid curve denotes the spin component, and the dashed curve denotes the obliquity component.

where S is the projection area of the boulder on the ground base. The parameter $C_{T,b}$ measures the efficiency of the torque, depending on the thermal parameter and the shape model (Golubov 2017). For a spherical boulder, $C_{T,b} \sim 0.002$, while for a wall, $C_{T,b} \sim 0.01$. The numerical simulation by Ševeček et al. (2015) on a polyhedron model of the boulder found $C_{T,b} \sim 0.001$. When all the boulders on asteroid Itokawa were considered, the total TYORP torque was (Golubov & Scheeres 2019)

$$\langle T_{TYORP} \rangle \sim C_T \frac{\Phi}{c} R_{ast}^3 \exp\left(-\frac{(\ln \Theta - \ln \Theta_0)}{\Gamma^2}\right) (\cos^2 \epsilon + 1). \quad (49)$$

For spherical boulders, $\Gamma = 1.518$ and $\ln \Theta_0 = 0.58$. The coefficient C_T depends on the roughness of the surface and on the shape of the asteroid. For asteroid (25143) Itokawa, the value of C_T was estimated as 0.0008 ± 0.0005 (Ševeček et al. 2015; Marzari et al. 2020).

The general form for the CYORP torque of one crater is similar to Eq. (48),

$$\langle T_{CYORP} \rangle = W \frac{\Phi}{c} R_0^2 R_{ast}. \quad (50)$$

When $\delta = \Delta = \alpha = \pi/4$, W_z is about 0.04 and W_ϵ is about 0.025. Comparing Eqs. (50) to (48), we find that the CYORP torque is one order of magnitude stronger than the TYORP torque for a crater and a boulder (spherical model) of the same size.

In Figure 7 we compare the CYORP torque for a single crater to the NYORP and TYORP torques for the whole asteroid as functions of the obliquity ϵ . Here parameters and the magnitude of the TYORP (e.g., the size distribution and the thermal parameter of boulders) follow the research performed on asteroid Itokawa (Ševeček et al. 2015). The TYORP torque differs from one asteroid to the next because the morphology of asteroids differs (Kanamaru et al. 2021). For the CYORP torque, other parameters apart from the obliquity were set to be constant as $\delta = \Delta = \alpha = \pi/4$ and $R_0/R_{ast} = 1/3$. We considered three crater depth-diameter ratios, $h/D_0 = 0.08, 0.13, \text{ and } 0.168$, as examples, which are the mean values for asteroids Itokawa, Eros, and Vesta, respectively (Hirata et al. 2009; Robinson et al. 2002; Vincent et al. 2014). In these cases, the values of W_z are 0.04, 0.028, and 0.025, respectively, while W_ϵ is much smaller. For a deep crater with $h/D_0 = 0.168$, the CYORP torque for a single

crater is comparable to the NYORP torque. CYORP decreases with decreasing depth-diameter ratio, but even for a shallow crater with a depth-diameter ratio ~ 0.08 , the CYORP torque is stronger than the total TYORP torque for the whole asteroid.

Although we assumed a large crater with a size one-third of the size of the asteroid to calculate the CYORP torque, large craters like this exist on real asteroids (e.g., asteroids Itokawa and Ryugu, Hirata et al. 2009; Noguchi et al. 2021). According to Hirata et al. (2009), the largest three craters on Itokawa are 134 m ($h/D_0 \sim 0.11$), 128 m ($h/D_0 \sim 0.12$), and 117 m ($h/D_0 \sim 0.15$). Considering that the mean diameter of asteroid Itokawa is ~ 313 m, the value of R_0/R_{ast} set to one-third is reasonable for real asteroids and appropriate for asteroid Itokawa. It might be twice the total torque or cancel the NYORP torque, depending on whether the sign of the CYORP torque is opposite to that of the TYORP torque. In Fig. 7, the CYORP torque is positive all over the obliquity, which is not the same for all cases, however, leading to the change in sign of the total YORP torque in some obliquities when the CYORP torque is added to the NYORP torque. Therefore, we show that the CYORP effect might be the main complement to the NYORP effect in addition to the TYORP effect. Especially when the thermal inertia of the asteroid is extremely low, the TYORP effect vanishes, so that the CYORP effect might be the only complement to the NYORP effect.

The CYORP torque for a smaller crater decreases as the CYORP torque scales as $\sim R_0^2$, which, however, does not mean that the contribution of small craters to the total CYORP torque is negligible. On the contrary, small craters could even give rise to a more significant CYORP torque than that produced by large craters because there are many small craters. This is analyzed in more detail in the next section as this section focuses on the order of magnitude of the CYORP torque of a single crater.

4.2. Applicability

The CYORP effect, which is induced by concave structures on an asteroid surface, is expected to have widespread applications in the rotational dynamics of asteroids. It contributes to the accurate calculation of the complete YORP torque by providing a systematical assessment of the YORP torques from large-scale (craters) and small-scale (roughness) concave structures over a huge parameter space (Sect. 4.2.1). In addition, the CYORP effect is linked to the collision history of asteroids, whose surfaces are modified by impact craters. The spin rate and obliquity are expected to go through a random walk under the CYORP effect. This has strong implications on the rotational and orbital evolutions of asteroids (Sect. 4.2.2).

4.2.1. Calculation of the total YORP torque

Recently, in situ observations by spacecraft provided high-resolution images of asteroids and measurements of their physical properties (e.g., Hirata et al. 2009; Daly et al. 2020a), which enabled investigating the YORP effect with a high-resolution shape model of the considered asteroid (Kanamaru et al. 2021; Roberts et al. 2021). With high-resolution images, the thermally induced torque of craters whose sizes are above the image resolutions can be well represented by the NYORP torque, but we still miss the consideration of small craters or concave structures that are below the image resolution.

As we highlight in Sect. 4.1, the CYORP torque produced by small craters and not by large craters might be the main contributor to the total CYORP effect. The cumulative size distribution

of craters is typically represented by a power law of the form

$$N(R \geq R_0) \propto R_0^{-p} \quad (51)$$

(e.g., $p \sim 3$ for asteroid Itokawa; Hirata et al. 2009). The total CYORP torque of craters is simply the sum of torques due to all the craters (see Eq. (3)), which reads

$$T_{\text{CYORP, total}} \geq N(R \geq R_0) \cdot W \frac{\Phi}{c} R_0^2 R_{\text{ast}}^2 \propto W \frac{\Phi}{c} R_0^{2-p} R_{\text{ast}}. \quad (52)$$

In the case of $p > 2$, the total CYORP torque is dominated by small craters because it scales as R_0^{2-p} . Some of the CYORP torques may cancel out due to the opposite signs of the torques over different latitudes. However, because the torque curve is not antisymmetric over the latitude (see Fig. 4), it is still possible that there are enough torques of one sign to keep the net value of the torque from all craters on the same order of magnitude as the equivalent torque from a single large crater. Essentially, the CYORP torque depends on the total area of the craters on the surface. For example, 100 craters, each covering an area of 1 m^2 , are equivalent for the CYORP torque to one single crater covering an area of 100 m^2 .

The concept of a ‘‘crater’’ in this paper can be extended to any concave structure as we do not use other properties of craters than the shape. It is hard to confine a characteristic size range of the CYORP effect because it works for all sizes in principle. Therefore, even though the resolution of the shape model might seem high from in situ observations (e.g., 80 cm in the shape model of Bennu; Barnouin et al. 2019), it may still not be high enough to resolve the small surface structures that could nevertheless induce a considerably strong CYORP torque. This poses challenges to the precise measurement of the total YORP torque. The definition of a very small crater is vague, and to compute YORP torques, the term ‘‘roughness’’ may be more appropriate. In this sense, the CYORP effect resulting from small-scale concave structures serves the same purpose as the YORP effect from surface roughness (Rozitis & Green 2012). Rozitis & Green (2012) showed with numerical simulations that the surface roughness mainly dampens the total YORP effect, while our result based on a semi-analytical method shows that the CYORP effect may either enhance or weaken the YORP torque, depending on many factors (see Figs. 3, 4, and 6). Furthermore, by using a semi-analytical method, which is much faster to run over the whole parameter space, we performed a systematic investigation of how the CYORP effect depends on the properties of the craters and the asteroid. The CYORP effect resulting from the roughness on a surface provides a potential explanation for the inconsistency of the YORP model that have been encountered so far with the measurement in the case of asteroid Itokawa, even though high-resolution shape models were used (Vokrouhlický et al. 2004; Scheeres et al. 2007; Lowry et al. 2014; Breiter et al. 2009; Ševeček et al. 2015). Therefore, applying the CYORP effect to the measurement of the YORP torque caused by the surface roughness, together with the TYORP effect (Golubov & Lipatova 2022), would be an effective way to improve the estimated accuracy of the YORP effect. In addition, the CYORP effect can also be applied to estimating the YORP torque when it is too expensive to compute the total YORP torque on a precise shape model or when detailed information of an asteroid is unavailable.

The resolution of the OSIRIS-REx mission is $\sim 80 \text{ cm}$ (see Daly et al. 2020a). This leads to a shape model with more than three million facets, which makes it computationally demanding and time-consuming to calculate the complete

YORP torque, however. It is impractical to apply such a complicated shape model to an analysis of the YORP effect under different rotational and orbital conditions (e.g., for building a statistical database of the YORP torques). The computational expense increases the difficulty of fully investigating the rotational evolution of a particular asteroid or of an asteroid family. Moreover, precise shape models are not available for most asteroids, of which high-resolution images are lacking. Therefore, a simplified but still accurate YORP model is needed, to which the CYORP effect might contribute. The CYORP torque, together with the TYORP torque, might be interpreted as estimation errors to the NYORP torque through a lack of necessary information on the asteroid,

$$T_{\text{YORP}} = T_{\text{NYORP}} + \sigma_{\text{TYORP}} + \sigma_{\text{CYORP}}. \quad (53)$$

Here σ_{TYORP} and σ_{CYORP} are the uncertainties caused by all boulders and craters, respectively. Although we do not fully understand the precise magnitude of σ_{TYORP} and σ_{CYORP} at the current stage, with more information on asteroid surfaces (e.g., the size distribution of boulders and craters) and further explorations of TYORP and CYORP effects, we would be able to estimate the YORP torque from limited information (e.g., a low-resolution shape model derived from photometric observations).

The existence of σ_{CYORP} might explain the different distributions of the YORP torques from photometric shape models and from radar shape models that were found by previous simulations (Marzari et al. 2020). Because shape models derived from the photometry are usually convex, which means that the information on craters is lost, while those from radar data could be concave, the different distribution of the YORP torques in these two groups might be caused by the CYORP effect in the second group. In addition, to simulate the YORP effect on synthetic pseudo-asteroid shape models, shape models including concave structures (e.g., Devogele et al. 2015) would be more appropriate to account for the CYORP effect.

4.2.2. Influence on spin evolution

The CYORP torque measures the torque difference of a crater and the ground before the occurrence of the crater (see Eq. (4)). As the crater is produced by a collision event, the CYORP torque naturally computes the change in YORP torque before and after a collision by its definition. Each collision event produces a CYORP torque, resulting in a random walk of the YORP torque over the collisional history, which affects the spin evolution of the asteroid. Therefore, by applying the CYORP effect to an asteroid, we might be able to trace back its spin evolution assuming the crater age is known, although other factors (e.g., the boulder distribution) should be considered together. In this way, the CYORP effect builds a bridge between spin evolution and collisional history.

We consider a crater with a radius R_0 on an asteroid with a radius R_{ast} . The size of the impactor has a relation to the crater size

$$R_{\text{imp}} = R_0 / f_c, \quad (54)$$

where the factor f_c is determined by a crater scaling law (Holsapple 1993; Bottke et al. 2020). The timescale of such an impact is

$$\tau_{\text{imp}} = \frac{1}{P_i \pi R_{\text{ast}}^2 N(R > R_{\text{imp}})}. \quad (55)$$

Here $P_1 = 2.85 \times 10^{-18} \text{ km}^{-2} \text{ yr}^{-1}$ is the intrinsic collision probability. The number of impactors that are larger than R_{imp} can be calculated by a simple power law (Holsapple 2022),

$$N(R > R_{\text{imp}}) = C_R \left(\frac{R_{\text{imp}}}{1 \text{ km}} \right)^{-b_R} \quad (56)$$

with $C_R = 6 \times 10^5$ and $b_R = 2.2$. When the total area of craters reaches one-tenth of the asteroid surface area (equivalent to a crater with the size one-third of the asteroid radius), the YORP torque is reset by the CYORP torque, as shown in Sect. 4.1. Therefore, the critical number of impacts that can reset the YORP torque is

$$N_0 \simeq R_{\text{ast}}^2 / 10R_0^2. \quad (57)$$

Now we are able to derive the timescale for a reset of the YORP torque,

$$\begin{aligned} \tau_{\text{YORP,reset}} &= N_0 \tau_{\text{imp}} \\ &= \frac{R_{\text{ast}}^2 (R_0 / f_C 1 \text{ km})^{b_R}}{10R_0^2 C_R P_i \pi R_{\text{ast}}^2} \\ &= \frac{1}{10\pi C_R P_i f_C^{b_R}} \frac{R_0^{b_R-2}}{(1 \text{ km})^{b_R}}. \end{aligned} \quad (58)$$

The dependence of the $\tau_{\text{YORP,reset}}$ on the crater size R_0 is weak, and the YORP reset effect does not depend on the asteroid size R_{ast} . When we substitute $f_C \sim 100$ as was found from the small carry-on impactor (SCI) experiment of the mission Hayabusa2 on asteroid Ryugu (Arakawa et al. 2020), we obtain

$$\tau_{\text{YORP,reset}} \sim 0.4 \left(\frac{f_C}{100} \right)^{-b_R} \left(\frac{R_0}{100 \text{ m}} \right)^{b_R-2} \text{ Myr}. \quad (59)$$

Equation (59) is a rough estimate because the factor f_C and the power index b_R should be functions of the asteroid size. The timescale (~ 0.4 Myr) for reorientation caused by the CYORP effect is much shorter than the typical timescale of spin axis reorientation by collisions (~ 1 Gyr for a 1 km radius object; see Athanasopoulos et al. 2022). This indicates that the CYORP effect may play an important role in the spin evolution of a single asteroid or asteroid families, while in current models, the change of the YORP torque caused by a collision event, as well as other resurfacing activities (e.g., regolith movement Miyamoto et al. 2007; Cheng et al. 2021), is lacking (Marzari et al. 2011; Holsapple et al. 2020; Holsapple 2022).

In addition, the CYORP effect could be applied to rotational disruption models (Jacobson et al. 2014) to determine the lifetime of an asteroid; here a more comprehensive knowledge of the outcomes of rotational failure is also needed (Zhang et al. 2018). Furthermore, the Yarkovsky effect, which is a radiative force that slowly changes the orbits of asteroids (Vokrouhlický 1998; Vokrouhlický et al. 2000; Bottke Jr et al. 2001), highly depends on the spin obliquity, which can be altered by the CYORP torque. Thus, the CYORP effect could play an important role in the long-term orbital dynamics of asteroid families, and it might, for example, modify the V-shape evolution of asteroid families (Vokrouhlický et al. 2006; Nesvorný et al. 2015; Delbo' et al. 2017; Bolin et al. 2018).

Therefore, the CYORP effect is a mechanism that is crucial for understanding the spin evolution and even the orbital evolution of asteroids. To include the CYORP effect in a Monte Carlo

simulation of the spin evolution and the orbital evolution of asteroids, we need a complete sample of all possible outcomes of the CYORP torque, which depends on the properties of craters and asteroids. At the current stage, this would not be possible because we ignored the effects of thermal inertia and of secondary illumination of the crater here, which may also be important and will be investigated in the next work.

5. Conclusions

We first proposed and examined the significance of the crater-induced YORP (CYORP) torque by developing a semi-analytical method. This method speeds up the computation and allows us to study the functional dependence of the CYORP on the properties of the crater and the asteroid.

CYORP arises from the torque difference produced by a crater and the ground without the crater. The assumption of zero thermal conductivity (Rubincam's approximation) and a simple semi-sphere model of craters were implemented. We find that the CYORP torque includes the spin and obliquity components, the values of which depend on the diameter-depth ratio, latitude and normal vector of the crater, and the obliquity and thermal inertia of the asteroid.

We gave a general form of the CYORP torque as $T_{\text{CYORP}} \sim W\Phi R_0^2 R_{\text{ast}}/c$ (see Eqs. (41) and (42)) and estimated the typical value of the dimensionless CYORP coefficient $W_z \sim 0.04$, $W_\epsilon \sim 0.01$ for a deep crater and $W_z \sim 0.025$, $W_\epsilon \sim 0.005$ for a shallow crater. We showed that the CYORP torque is one order of magnitude stronger than the TYORP torque for a crater and a boulder of the same size. A crater with a radius of one-third of the asteroid radius (as found on asteroid Itokawa) will produce a CYORP torque that is comparable to the NYORP torque and stronger than the TYORP torque for the whole asteroid. Craters or roughness that cover one-tenth of the asteroid surface have the same effect. Unlike the necessary presence of thermal inertia for a nonzero value of the TYORP torque, CYORP exists without thermal inertia, which implies that for fast-spinning asteroids or asteroids with low thermal conductivity, the YORP effect will be dominated by NYORP and CYORP effects.

Although CYORP decreases with the size of the crater as R_0^2 , the large number of small craters may mean that the CYORP torques that are due to all small craters are non-negligible. It is the total area covered by concave structures that matters, which implies that the CYORP effect caused by the surface roughness would be crucial for the complete YORP torque (see Sect. 4.2.1). Previous research demonstrated the YORP sensitivity to surface roughness by a numerical method (Rozitis & Green 2012). Our work performed a systematic investigation of the YORP torque of the concave structure, which could be applied in surface roughness, over a much larger parameter space by a semi-analytical method. This lies the foundation for the accurate prediction of the YORP torque on a real asteroid. The CYORP effect provides a potential reason why the modeled YORP torque so far was unable to match the measured value in the case of asteroid Itokawa (Breiter et al. 2009) even though high-resolution shape models were applied. The CYORP effect might also explain the difference of the YORP torques between photometric-shape models, which is convex, and radar-shape models, which contain concave structure (Marzari et al. 2020). However, at the current stage, it is unclear whether the CYORP torque is dominated by large concave structures (e.g., craters) or small ones (e.g., roughness).

Moreover, because an asteroid experiences numerous impacts that lead to the production of craters during its evolution

(Bottke et al. 2020), the resulting CYORP torques may cause a random walk of the spin rate and obliquity of the asteroid, which may either slow down or even prevent the YORP spin-up from occurring, deferring the formation of top shapes and binary systems based on this process (Walsh & Jacobson 2015). Our estimation showed that the timescale for reorientation of an asteroid caused by the CYORP effect is ~ 0.4 Myr with a weak dependence on the asteroid size (see Sect. 4.2.2), which is much shorter than the timescale caused by collisions. This is a rough estimate, and a more complete CYORP model with nonzero thermal inertia and the secondary illumination effect is needed to build a statistic sample pool covering all possible outcomes of the CYORP torque under different conditions. The CYORP effect can have strong implications on the spin evolution and also on the orbital evolution (through the Yarkovsky effect), which will be assessed in a future work. Overall, we suggest that the CYORP effect should be incorporated into future research of the YORP effect.

Acknowledgements. We acknowledge support from the Université Côte d'Azur. Wen-Han Zhou would like to acknowledge the funding support from the Origin Space Company and the Chinese Scholarship Council (No. 202110320014). Xiaoran Yan acknowledges the funding support from the Chinese Scholarship Council (No. 202006210258). Patrick Michel acknowledges funding support from the French space agency CNES and from the European Union's Horizon 2020 research and innovation program under grant agreement No. 870377 (project NEO-MAPP). We are thankful to Bin Ren, Liangliang Yu, Masanori Kanamaru and Yue Wang for useful discussions.

References

- Arakawa, M., Saiki, T., Wada, K., et al. 2020, *Science*, **368**, 67
- Athanasopoulos, D., Hanuš, J., Avdellidou, C., et al. 2022 *A&A*, **666**, A116
- Barnouin, O., Daly, M., Palmer, E., et al. 2019, *Nat. Geosci.*, **12**, 247
- Bierhaus, E. B., Trang, D., Daly, R. T., et al. 2022, *LPI Contrib.*, **2678**, 1317
- Bolin, B. T., Morbidelli, A., & Walsh, K. J. 2018, *A&A*, **611**, A82
- Bottke Jr, W. F., Vokrouhlický, D., Brož, M., Nesvorný, D., & Morbidelli, A. 2001, *Science*, **294**, 1693
- Bottke Jr, W. F., Vokrouhlický, D., Rubincam, D. P., & Nesvorný, D. 2006, *Annu. Rev. Earth Planet. Sci.*, **34**, 157
- Bottke, W. F., Vokrouhlický, D., Ballouz, R. L., et al. 2020, *AJ*, **160**, 14
- Breiter, S., Michalska, H., Vokrouhlický, D., & Borczyk, W. 2007, *A&A*, **471**, 345
- Breiter, S., Bartzak, P., Czekaj, M., Oczujda, B., & Vokrouhlický, D. 2009, *A&A*, **507**, 1073
- Čapek, D., & Vokrouhlický, D. 2004, *Icarus*, **172**, 526
- Cheng, B., Yu, Y., Asphaug, E., et al. 2021, *Nat. Astron.*, **5**, 134
- Daly, M., Barnouin, O., Seabrook, J., et al. 2020a, *Sci. Adv.*, **6**, eabd3649
- Daly, R. T., Bierhaus, E. B., Barnouin, O. S., et al. 2020b, *Geophys. Res. Lett.*, **47**, e89672
- Daly, R. T., Barnouin, O. S., Bierhaus, E. B., et al. 2022, *Icarus*, **384**, 115058
- Delbo', M., Walsh, K., Bolin, B., Avdellidou, C., & Morbidelli, A. 2017, *Science*, **357**, 1026
- Devegele, M., Rivet, J.-P., Tanga, P., et al. 2015, *MNRAS*, **453**, 2232
- Đurech, J., Vokrouhlický, D., Pravec, P., et al. 2018, *A&A*, **609**, A86
- Fujiwara, A., Kadono, T., & Nakamura, A. 1993, *Icarus*, **105**, 345
- Golubov, O. 2017, *AJ*, **154**, 238
- Golubov, O., & Krugly, Y. N. 2012, *AJ*, **752**, L11
- Golubov, O., & Lipatova, V. 2022, *A&A*, **666**, A146
- Golubov, O., & Scheeres, D. J. 2019, *AJ*, **157**, 105
- Golubov, O., Scheeres, D., & Krugly, Y. N. 2014, *ApJ*, **794**, 22
- Hirata, N., Barnouin-Jha, O. S., Honda, C., et al. 2009, *Icarus*, **200**, 486
- Holsapple, K. A. 1993, *Ann. Rev. Earth Planet. Sci.*, **21**, 333
- Holsapple, K. A. 2020, *ApJ*, submitted [arXiv:2012.15300]
- Holsapple, K. A. 2022, *Planet. Space Sci.*, **219**, 105529
- Jacobson, S. A., Marzari, F., Rossi, A., Scheeres, D. J., & Davis, D. R. 2014, *MNRAS*, **439**, L95
- Kanamaru, M., Sasaki, S., Morota, T., et al. 2021, *J. Geophys. Res. Planets*, **126**, e2021JE006863
- Lowry, S., Weissman, P., Duddy, S., et al. 2014, *A&A*, **562**, A48
- Marchi, S., Chapman, C. R., Barnouin, O. S., Richardson, J. E., & Vincent, J. B. 2015, in *Asteroids IV* (Tucson: University of Arizona Press), 725
- Marzari, F., Rossi, A., & Scheeres, D. J. 2011, *Icarus*, **214**, 622
- Marzari, F., Rossi, A., Golubov, O., & Scheeres, D. J. 2020, *AJ*, **160**, 128
- Michel, P., Ballouz, R. L., Barnouin, O. S., et al. 2020, *Nat. Commun.*, **11**, 2655
- Miyamoto, H., Yano, H., Scheeres, D. J., et al. 2007, *Science*, **316**, 1011
- Nesvorný, D., & Vokrouhlický, D. 2008, *A&A*, **480**, 1
- Nesvorný, D., Brož, M., Carruba, V., et al. 2015, *Asteroids IV* (Tucson: University of Arizona Press), 29, 7
- Noguchi, R., Hirata, N., Hirata, N., et al. 2021, *Icarus*, **354**, 114016
- Roberts, J., Barnouin, O., Daly, M., et al. 2021, *Planet. Space Sci.*, **204**, 105268
- Robinson, M., Thomas, P., Veverka, J., Murchie, S., & Wilcox, B. 2002, *Meteor. Planet. Sci.*, **37**, 1651
- Rozitis, B., & Green, S. F. 2012, *MNRAS*, **423**, 367
- Rozitis, B., & Green, S. F. 2013, *MNRAS*, **433**, 603
- Rubincam, D. P. 2000, *Icarus*, **148**, 2
- Scheeres, D., & Gaskell, R. 2008, *Icarus*, **198**, 125
- Scheeres, D., Abe, M., Yoshikawa, M., et al. 2007, *Icarus*, **188**, 425
- Ševeček, P., Brož, M., Čapek, D., & Ďurech, J. 2015, *MNRAS*, **450**, 2104
- Statler, T. S. 2009, *Icarus*, **202**, 502
- Vincent, J.-B., Schenk, P., Nathues, A., et al. 2014, *Planet. Space Sci.*, **103**, 57
- Vokrouhlický, D. 1998, *A&A*, **335**, 1093
- Vokrouhlický, D., & Čapek, D. 2002, *Icarus*, **159**, 449
- Vokrouhlický, D., Milani, A., & Chesley, S. 2000, *Icarus*, **148**, 118
- Vokrouhlický, D., Nesvorný, D., & Bottke, W. F. 2003, *Nature*, **425**, 147
- Vokrouhlický, D., Čapek, D., Kaasalainen, M., & Ostro, S. 2004, *A&A*, **414**, L21
- Vokrouhlický, D., Brož, M., Bottke, W., Nesvorný, D., & Morbidelli, A. 2006, *Icarus*, **182**, 118
- Walsh, K. J., & Jacobson, S. A. 2015, in *Asteroids IV* (Tucson: University of Arizona Press), 375
- Walsh, K. J., Richardson, D. C., & Michel, P. 2008, *Nature*, **454**, 188
- Yan, X., & Li, J. 2019, *Scientia Sinica Physica, Mechanica & Astronomica*, **49**, 084511
- Zhang, Y., Richardson, D. C., Barnouin, O. S., et al. 2018, *ApJ*, **857**, 15

Appendix A: Integration domain for three illumination modes

There are three illumination modes for a crater according to different solutions of inequality: (1) full illumination; (2) two-side illumination; and (3) one-side illumination. These three illumination modes have different illuminated domains, which are all equivalent to inequality (18), however. Categorizing them is just for the sake of integration of the total recoil force (see Eq. (31)).

To obtain the illuminated area, we need to solve the inequality

$$\cos \phi < \frac{\cos 2\lambda \cos \theta + \sin \gamma_0}{\sin 2\lambda \sin \theta}. \quad (\text{A.1})$$

One obvious solution is when the right-hand side of the above inequality is larger than 1,

$$\frac{\cos 2\lambda \cos \theta + \sin \gamma_0}{\sin 2\lambda \sin \theta} > 1, \quad (\text{A.2})$$

we have

$$\cos(2\lambda + \theta) > \cos\left(\frac{\pi}{2} + \gamma_0\right). \quad (\text{A.3})$$

Noting that $2\lambda + \theta \in (2\lambda, 2\lambda + \pi/2 - \gamma_0)$, $\pi/2 + \gamma_0 \in (0, \pi)$, and the cosine function decreases in this domain, we can easily obtain the condition that inequality (A.2) always holds for all ϕ and θ , which is given by

$$\frac{\pi}{2} + \gamma_0 > 2\lambda + \frac{\pi}{2} - \gamma_0, \quad (\text{A.4})$$

which gives

$$\lambda < \gamma_0. \quad (\text{A.5})$$

Therefore, when $\lambda < \gamma_0$, inequality (18) holds for all θ and ϕ , which means that the crater is illuminated everywhere. This is illumination mode (1). In this case,

$$\mathcal{W} = \mathcal{Z}. \quad (\text{A.6})$$

When $\lambda > \gamma_0$, the inequality can hold for all ϕ when θ fulfills the requirement according to inequality (A.3)

$$\theta < \frac{\pi}{2} + \gamma_0 - 2\lambda. \quad (\text{A.7})$$

A hidden condition of the above inequality is $\pi/2 + \gamma_0 - 2\lambda > 0$. Therefore

$$\gamma_0 < \lambda < \frac{\pi}{4} + \frac{\gamma_0}{2}. \quad (\text{A.8})$$

This is illumination mode (2). In this mode, when $\theta > \frac{\pi}{2} + \gamma_0 - 2\lambda$, the solution of inequality (A.1) is $\phi_1 < \phi < \phi_2$. Therefore, illumination mode (2) can be described as

$$\begin{aligned} \mathcal{W} = \{(x, y, z) \in \mathcal{Z} | \theta \in (0, \frac{\pi}{2} - 2\lambda + \gamma_0), \phi \in (0, 2\pi) \\ \text{or } \theta \in (\frac{\pi}{2} - 2\lambda + \gamma_0, \frac{\pi}{2} - \gamma_0), \phi \in (\phi_1, \phi_2)\}. \end{aligned} \quad (\text{A.9})$$

For $\lambda > \pi/4 + \gamma_0/2$, the solution of inequality (A.1) is $\phi_1 < \phi < \phi_2$, but we have to ensure that the right-hand side is larger than -1,

$$\frac{\cos 2\lambda \cos \theta + \sin \gamma_0}{\sin 2\lambda \sin \theta} > -1, \quad (\text{A.10})$$

which yields

$$\theta < \frac{\pi}{2} + \gamma_0 - 2\lambda. \quad (\text{A.11})$$

Therefore, illumination mode (3) is equivalent to

$$\mathcal{W} = \{(x, y, z) \in \mathcal{Z} | \theta \in (2\lambda - \gamma_0 - \pi/2, \pi/2 - \gamma_0), \phi \in (\phi_1, \phi_2)\}. \quad (\text{A.12})$$

Appendix B: δ of Z-axis symmetric asteroids

The variable δ is the longitude difference between the position vector \mathbf{r}_0 and the normal vector \mathbf{n}_0 . We show below that when the shape of the asteroid is Z-axis symmetric, $\delta = 0$ is valid everywhere on the surface of the asteroid.

For an arbitrary Z-axis symmetric asteroid, the unit position vector of a point on the surface can be expressed by two independent variables ζ and k as

$$\mathbf{r}_0 = (k \cos \zeta, k \sin \zeta, p(k)), \quad (\text{B.1})$$

where $p(k)$ is a function of k , depending on the specific shape of the asteroid. If the asteroid is an unit sphere, for example, we have $p(k) = \pm \sqrt{1 - k^2}$. The unit normal vector is

$$\begin{aligned} \mathbf{n}_0 &= \frac{\partial \mathbf{r}_0}{\partial \zeta} \times \frac{\partial \mathbf{r}_0}{\partial k} \\ &= -\frac{dp/dk}{\sqrt{1 + (dp/dk)^2}} (\cos \zeta, \sin \zeta, -\frac{1}{dp/dk}). \end{aligned} \quad (\text{B.2})$$



By comparing Equation (B.1) and (B.2), we see that \mathbf{r}_0 and \mathbf{n}_0 share the same azimuth angle ζ . Therefore, for any point on a Z-axis symmetric asteroid, the difference between the azimuth angles of the position vector and the normal vector is zero, which means $\delta = 0$ in Equation (37).

CRATER-INDUCED YORP EFFECT WITH FINITE THERMAL INERTIA

Following Chapter 5, this chapter develops a semi-analytical method to calculate the temperature field of a crater and its CYORP torque, assuming non-zero thermal inertia. We confirm the uniformly distributed roughness will decrease the total YORP torque by a factor of 2-3. We found that non-zero thermal inertia will decrease the CYORP torque by a typical factor of 4, leading to a YORP-reset timescale close to 1 Myr. This work and the work in Chapter 5 complete the basic theory for CYORP in different thermal inertia limits. This paper was published in the peer-reviewed journal *Astronomy & Astrophysics*.

Author Contributions: W.H. Zhou led the project. W.H. Zhou proposed the model, derived the formula, carried out the numerical simulations, analyzed the results, and led the writing of the paper. P. Michel collaborated on the interpretation of the results.

A semi-analytical thermal model for craters with application to the crater-induced YORP effect

Wen-Han Zhou¹ , and Patrick Michel^{1,2} 

¹ Université Côte d'Azur, Observatoire de la Côte d'Azur, CNRS, Laboratoire Lagrange, 96 Bd de l'Observatoire, 06304 Nice, France
e-mail: wenhan.zhou@oca.eu

² University of Tokyo, Department of Systems Innovation, School of Engineering, Tokyo, Japan

Received 23 May 2023 / Accepted 4 December 2023

ABSTRACT

Context. The YORP effect is the thermal torque generated by radiation from the surface of an asteroid. The effect is sensitive to surface topology, including small-scale roughness, boulders, and craters.

Aims. The aim of this paper is to develop a computationally efficient semi-analytical model for the crater-induced YORP (CYORP) effect that can be used to investigate the functional dependence of this effect.

Methods. This study linearizes the thermal radiation term as a function of the temperature in the boundary condition of the heat conductivity, and obtains the temperature field in a crater over a rotational period in the form of a Fourier series, accounting for the effects of self-sheltering, self-radiation, and self-scattering. By comparison with a numerical model, we find that this semi-analytical model for the CYORP effect works well for $K > 0.1 \text{ W m}^{-1} \text{ K}^{-1}$. This semi-analytical model is computationally three-orders-of-magnitude more efficient than the numerical approach.

Results. We obtain the temperature field of a crater, accounting for the thermal inertia, crater shape, and crater location. We then find that the CYORP effect is negligible when the depth-to-diameter ratio is smaller than 0.05. In this case, it is reasonable to assume a convex shape for YORP calculations. Varying the thermal conductivity yields a consistent value of approximately 0.01 for the spin component of the CYORP coefficient, while the obliquity component is inversely related to thermal inertia, declining from 0.004 in basalt to 0.001 in metal. The CYORP spin component peaks at an obliquity of 0° , 90° , or 180° , while the obliquity component peaks at an obliquity of around 45° or 135° . For a z -axis symmetric shape, the CYORP spin component vanishes, while the obliquity component persists. Our model confirms that the total YORP torque is damped by a few tens of percent by uniformly distributed small-scale surface roughness. Furthermore, for the first time, we calculate the change in the YORP torque at each impact on the surface of an asteroid explicitly and compute the resulting stochastic spin evolution more precisely.

Conclusions. This study shows that the CYORP effect due to small-scale surface roughness and impact craters is significant during the history of asteroids. The semi-analytical method that we developed, which benefits from fast computation, offers new perspectives for future investigations of the YORP modeling of real asteroids and for the complete rotational and orbital evolution of asteroids accounting for collisions. Future research employing our CYORP model may explore the implications of space-varying roughness distribution, roughness in binary systems, and the development of a comprehensive rotational evolution model for asteroid groups.

Key words. minor planets, asteroids: general

1. Introduction

The Yarkovsky-O'Keefe-Radzievskii-Paddack (YORP) effect is a thermal torque that can alter the spin state of an asteroid over time (Rubincam 2000; Vokrouhlický & Čapek 2002; Vokrouhlický et al. 2015), and is caused by the asymmetric re-emission of solar radiation by the irregular surface of the asteroid, resulting in a net torque that can spin up or spin down the asteroid's rotation. The absorption of solar radiation makes no contributions to the YORP torque as it is averaged out over the spin and orbital periods for any asteroid shapes (Nesvorný & Vokrouhlický 2008). So far, 11 asteroids showing time-varying rotational periods have been detected (Lowry et al. 2007; Taylor et al. 2007; Ďurech et al. 2022; Tian et al. 2022).

The YORP effect has important implications for an asteroid's long-term rotational evolution. This effect can either spin down the asteroid to an extremely slow rotation, triggering a tumbling motion (Pravec et al. 2005), or spin up the asteroid to its rotation limit (e.g. rotational period of 2.2 h for rubble pile asteroids), leading to resurfacing (Sánchez & Scheeres 2020) and rotation

disruption (Scheeres 2007; Fatka et al. 2020; Veras & Scheeres 2020). YORP-induced rotational disruption is supported by the observed asteroid pairs (Vokrouhlický & Nesvorný 2008; Polishook 2014) and binary asteroids (Jacobson & Scheeres 2011; Delbo et al. 2011; Jacobson et al. 2013, 2016), including contact-binary asteroids (Rožek et al. 2019; Zegmott et al. 2021) and binary comets (Agarwal et al. 2020), which evolve under tidal effects and the binary YORP (BYORP) effect after the binary system is formed (Čuk & Burns 2005; Steinberg & Sari 2011). Further potential observational evidence is the abnormal spin distribution and the obliquity distribution of near-Earth asteroids (Vokrouhlický et al. 2003; Pravec et al. 2008; Rozitis & Green 2013b; Lupishko & Tielieusova 2014) and main belt asteroids (Lupishko et al. 2019), although a recent study points out that collisions might reproduce the observed distribution without the involvement of the YORP effect (Holsapple 2022). The YORP effect can influence the orbital evolution through the Yarkovsky effect, which is a thermal force that depends on the rotational state of the asteroid (Vokrouhlický et al. 2000; Bottke et al. 2006). Therefore, understanding the YORP effect

is important for correctly estimating the ages of asteroid families based on how much time is needed for the Yarkovsky effect to cause the observed orbital dispersion of their members from the original orbit following the disruption of their parent bodies (Vokrouhlický et al. 2006; Čuk et al. 2015; Carruba et al. 2014, 2015, 2016; Lowry et al. 2020; Marzari et al. 2020).

However, accurately calculating the YORP effect on a real asteroid remains a challenge, as it has been demonstrated to be highly sensitive to surface topology (Statler 2009; Breiter et al. 2009), such as uniform small-scale roughness (Rozitis & Green 2012), boulders (Golubov & Krugly 2012; Golubov et al. 2014, 2021; Ševeček et al. 2015; Golubov 2017; Golubov & Scheeres 2019; Golubov & Lipatova 2022), and craters (Zhou et al. 2022). Although the YORP torque caused by boulders and the tangential radiative force has been well studied, the YORP effect caused by concave structures has not yet been fully explored. More specifically, there are two kinds of concave structures on asteroid surfaces. The first one corresponds to craters, which result from impacts that an asteroid's surface undergoes during its history and which can cover a large size range and be distributed in various ways. The second corresponds to surface roughness, which corresponds to uniformly distributed small-scale concave features that originate from the continuous effect of various processes that take place at the surface, such as thermal fatigue and space weathering. In our study, we consider both craters and surface roughness. While a pioneering study by Rozitis & Green (2012) used numerical simulations to investigate the effect of roughness, the high computational expense of such simulations prevents a comprehensive exploration of the functional dependence of this effect and its application to the global spin evolution of asteroid populations.

In addition to the precise calculation of the complete YORP effect, the long-term evolution of asteroids needs to account for stochastic collisions that affect this evolution, because each collision introduces a YORP torque due to the resulting crater. Bottke et al. (2015) performed a first study of the YORP effect accounting for craters caused by collisions, finding strong implications in the age estimate of asteroid families. However, their introduction of the concept of the stochastic YORP effect due to collisions assumed an arbitrary reset timescale for the YORP cycle. In reality, this reset timescale depends on the actual occurrence of each impact causing a crater on the asteroid's surface and the resulting change in the YORP effect. In summary, collisions and the YORP and Yarkovsky effects are all coupled with each other in a way that is so far not well understood.

To account explicitly for the YORP torque caused by roughness and craters, Zhou et al. (2022) developed a semi-analytical model that is computationally efficient for the crater-induced YORP (CYORP) torque. The CYORP torque is defined as the torque difference between the crater and the flat ground:

$$\mathbf{T}_{\text{CYORP}} = \mathbf{T}_{\text{crater}} - \mathbf{T}_{\text{ground}}. \quad (1)$$

In general, it takes the form of the following scaling rule with the radius of the crater R_0 and of the asteroid radius R_{ast} :

$$\mathbf{T}_{\text{CYORP}} = W \frac{\Phi}{c} R_0^2 R_{\text{ast}}, \quad (2)$$

where Φ is the flux of solar radiation at the asteroid's semimajor axis, and W is the CYORP coefficient, which in turn depends on the obliquity and irregularity of the asteroid, and the depth-to-diameter ratio, location, thermal inertia, and albedo of the crater. As a first step, this model assumed a zero thermal conductivity.

Zhou et al. (2022) found that roughness or craters that cover 10% of the asteroid's surface area could produce a CYORP torque comparable to the normal YORP (NYORP) torque, which arises from the macroscopic shape, with ignorance of the fine surface structure. Based on this number, which assumes that all craters have a depth-to-diameter ratio of 0.16, the reset of the YORP torque by the CYORP torque could be as short as 0.4 Myr.

However, the effects of finite thermal conductivity, self-radiation, and self-scattering were not considered in Zhou et al. (2022). In the present paper, we propose a semi-analytical model that accounts for the effects of self-sheltering, self-radiation, self-scattering, and non-zero thermal conductivity. This new model allows a more general exploration of the functional dependence of the CYORP effect. Moreover, as this semi-analytical model is much more efficient than a purely numerical one, it can be used to study the combined influence of the YORP effect, collisions, and the Yarkovsky effect by incorporating the CYORP effect into the standard evolution model of asteroid families. We assume that the craters considered in this work are on a convex asteroid. It is possible to apply the model derived in this work to a moderately concave asteroid by approximating concave structures as craters, but this is beyond the scope of this paper.

In this paper, we describe our analytical model for the temperature field in a crater in Sect. 2. In Sect. 3, we introduce the numerical model that we developed to validate the analytical model. The main results are shown in Sects. 4 and 5. In Sect. 4, we analyse the effects of self-sheltering, self-radiation, and self-scattering of the crater, and in Sect. 5 we show the results of the calculation of the CYORP torque as a function of different variables. For the purpose of illustration, in Sect. 6 we provide an example of the analysis of CYORP considering a specific real asteroid shape and its surface roughness as well as the consequential rotational evolution. In Sect. 7, we summarise our main findings and draw conclusions.

2. Analytical model

2.1. Calculation of temperature distribution in a crater

2.1.1. Linearized analytical solution

The temperature u for the surface and the layer beneath is governed by

$$\frac{\partial u}{\partial t} = \frac{K}{C\rho} \frac{\partial^2 u}{\partial z^2}, \quad (3)$$

with two boundary conditions,

$$K \frac{\partial u}{\partial z} \Big|_{z=0} = F(t) - e\sigma u^4 \Big|_{z=0}, \quad (4)$$

$$K \frac{\partial u}{\partial z} \Big|_{z \rightarrow \infty} = 0, \quad (5)$$

and a periodic condition,

$$u|_{t=2\pi/\omega} = u|_{t=0}, \quad (6)$$

where t is the time, z is the depth of the crater, ω is the angular velocity, K is the thermal conductivity, C is the specific heat capacity, ρ is the bulk density of the asteroid, e is the emissivity, and σ is the Stefan-Boltzmann constant. In the following, we use the spin angle $\beta = \omega t$ to replace time for simplicity. The effect of the seasonal wave is marginal and is ignored in this work.

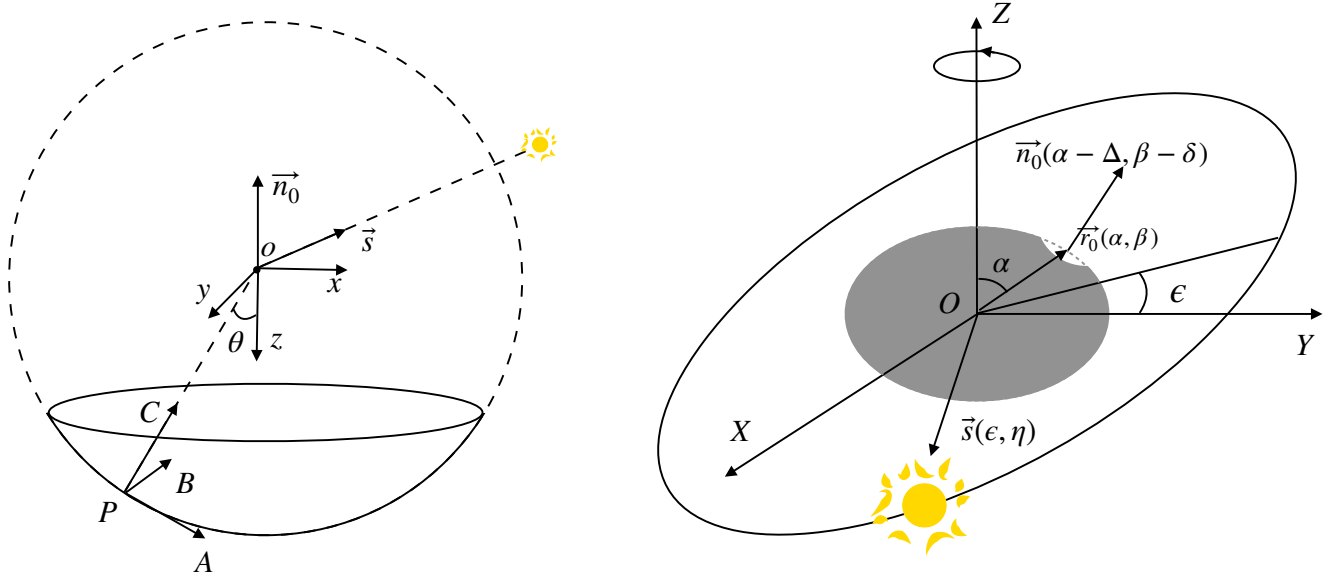


Fig. 1. Three coordinate systems in this paper: coordinate system $oxyz$ for calculating the illuminated domain in the crater, PABC for calculating the effective radiative force of an arbitrary surface element, and $OXYZ$ for averaging the YORP torque over the spin and orbital motion.

While the one-dimensional heat diffusion equation with the boundary condition of radiation has no complete analytical solution, it could be solved by linearizing the fourth power of the temperature, with the assumption that the temperature does not change significantly during a rotational period. For an arbitrary point in the hemispherical crater surface, the location of which is described by the polar angle θ and the azimuthal angle ϕ , the solution of the temperature is the real part of the expression

$$u(\theta, \phi, \beta) = u_0(\theta, \phi) + \sum_{n=1}^{\infty} u_n(\theta, \phi) e^{in\beta}, \quad (7)$$

with

$$u_0(\theta, \phi) = \left(\frac{F_0(\theta, \phi)}{e\sigma} \right)^{1/4}, \quad (8)$$

$$u_n(\theta, \phi) = \frac{F_n(\theta, \phi)}{4e\sigma u_0(\theta, \phi)^3} \frac{e^{iJ_n}}{\sqrt{2\Theta_n^2 + 2\Theta_n + 1}}, \quad (9)$$

where

$$l_n = \sqrt{\frac{n\omega}{2M}}, \quad (10)$$

$$\Theta_n = \frac{Kl_n}{4e\sigma u_0^3}, \quad (11)$$

$$\tan J_n = -\frac{\Theta_n}{\Theta_n + 1}, \quad (12)$$

with $M = K/\rho C$. The function F_n is the n th-order of the Fourier series of the absorbed radiation flux F , which is expressed as

$$F(\theta, \phi) = \sum_{n=0}^{\infty} F_n(\theta, \phi) e^{in\beta}. \quad (13)$$

We see that the only unknown variable is the absorbed radiation flux F . The absorbed radiation on a surface element contains

three parts: solar radiation $E(\theta, \phi, \beta)$, radiation from the crater itself $H(\theta, \phi, \beta)$, and the scattering flux from the crater $G(\theta, \phi, \beta)$, which leads us to

$$\begin{aligned} F(\theta, \phi) &= (1 - A)(E(\theta, \phi) + H(\theta, \phi) + G(\theta, \phi)) \\ &= (1 - A) \sum_{n=0}^{\infty} (E_n(\theta, \phi) + H_n(\theta, \phi) + G_n(\theta, \phi)) e^{in\beta}, \end{aligned} \quad (14)$$

where $E_n(\theta, \phi, \beta)$ and $H_n(\theta, \phi, \beta)$ denote the n th-order Fourier modes of $E(\theta, \phi, t)$ and $H(\theta, \phi, t)$, respectively. Here the albedo A is assumed to be 0.1 for these three flux components for the sake of simplicity, although the albedo at the thermal-infrared wavelengths is almost zero. Following Eqs. (8), (9), and (14), we obtain

$$u_0(\theta, \phi) = \left(\frac{(1 - A)(E_0(\theta, \phi) + H_0(\theta, \phi) + G_0(\theta, \phi))}{e\sigma} \right)^{1/4}, \quad (15)$$

$$u_n(\theta, \phi) = \frac{(1 - A)(E_n(\theta, \phi) + H_n(\theta, \phi) + G_n(\theta, \phi))}{4e\sigma u_0(\theta, \phi)^3} \frac{e^{iJ_n}}{\sqrt{2\Theta_n^2 + 2\Theta_n + 1}}. \quad (16)$$

Therefore, to solve the temperature $u(\theta, \phi, \beta)$, we need to obtain the Fourier series of $E(\theta, \phi, \beta)$, $H(\theta, \phi, \beta)$, and $G(\theta, \phi, \beta)$.

2.1.2. Coordinate systems

We use three coordinate systems to calculate the radiation and the force received by the crater, as shown in Fig. 1. The coordinate system $OXYZ$ is an inertial frame used to calculate the averaged YORP torque over the spin and orbital motion. Based on the axis OZ , we define the coordinate system $oxyz$ fixed with the crater to calculate the instant solar flux. Finally, based on the axis oz , we define the coordinate system PABC to calculate the self-sheltering effect of the crater. The self-sheltering effect for a point in the crater refers to the non-working moment of the photons reabsorbed by the shelter (i.e. the crater itself), which leads to the effective radiation force of the surface being tilted

relative to the surface normal with a modified magnitude. This self-sheltering effect on the point P depends on the geometry of the surrounding shelter. We adopt a simple sphere with a radius of R_1 to depict the crater shape.

In the coordinate system $OXYZ$, OZ points along the rotation axis and OXY is the equatorial plane. The axis OY is chosen such that the normal vector of the orbit plane lies in the plane OYZ . The axis OX follows the right-hand rule. There are three crucial vectors determining the CYORP torque expressed in polar coordinates in the coordinate system $OXYZ$: the crater position vector \mathbf{r}_0 (denoted by α and β), the crater normal vector \mathbf{n}_0 (described by α , β , δ , and Δ), and the solar position \mathbf{s} (described by ϵ and η), as shown in the right panel of Fig. 1. As the polar angle is between 0° and 180° by definition, we limit $0^\circ < \alpha < 180^\circ$ and $0^\circ < \alpha - \Delta < 180^\circ$ in our results.

The coordinate system $oxyz$ with the origin o located at the sphere centre is fixed with the crater in order to simplify the calculation of the solar flux on the crater. The axis oz points in the opposite direction to the surface normal vector \mathbf{n}_0 , which is also the symmetry axis of the spherical crater. The direction of axis oy is along $\mathbf{e}_{OZ} \times \mathbf{e}_{oz}$ and ox follows the right-hand rule. In this coordinate system, a crater with a depth of h can be defined as

$$\mathcal{Z} := \{(x, y, z) \in \mathbb{R}^3 | x^2 + y^2 + z^2 = R_1, z \geq R_1 \cos \theta_0\}, \quad (17)$$

with $\cos \theta_0 = (R_1 - h)/R_1$.

The coordinate system $PABC$ with the origin P at a chosen point on the crater is used to calculate the self-sheltering effect. The axis PC is along the direction of Po , PA points in the direction of $\mathbf{e}_{oz} \times \mathbf{e}_{PC}$, and PB follows the right-hand rule. In our code, the effective force felt by the point P is calculated first in the coordinate system $PABC$ for simplicity and this is then transformed to the coordinate system $oxyz$ by a rotation matrix.

2.1.3. Solar radiation E

In this section, we show how we derive the solar radiation received by an arbitrary point P in the crater, whose coordinates in $oxyz$ system are $\mathbf{r}_P = (\sin \theta \cos \phi, \sin \theta \sin \phi, \cos \theta)$. The unit position vector of the Sun in the coordinate system $OXYZ$ is described by

$$\mathbf{s}_{OXYZ} = (\cos \eta, \cos \epsilon \sin \eta, \sin \epsilon \sin \eta), \quad (18)$$

where ϵ is the obliquity and η is the angle of orbital motion. The transform matrix between the coordinate systems $oxyz$ and $OXYZ$ is set to

$$\mathcal{R} = \begin{pmatrix} \cos \alpha \cos \beta & \cos \alpha \sin \beta & -\sin \alpha \\ \sin \beta & -\cos \beta & 0 \\ -\cos \beta \sin \alpha & -\sin \alpha \sin \beta & -\cos \alpha \end{pmatrix}. \quad (19)$$

Therefore, the coordinates of the vector \mathbf{s} in the coordinate system $oxyz$ is

$$\mathbf{s}_{oxyz} = \begin{pmatrix} -\sin \alpha \sin \epsilon \sin \eta + \cos \alpha \cos \beta \cos \eta + \cos \alpha \sin \beta \cos \epsilon \sin \eta \\ \sin \beta \cos \eta - \cos \beta \cos \epsilon \sin \eta \\ -\sin \alpha \cos \beta \cos \eta - \sin \alpha \sin \beta \cos \epsilon \sin \eta - \cos \alpha \sin \epsilon \sin \eta \end{pmatrix}. \quad (20)$$

On the other hand, we can use the angle λ and ϕ' to represent \mathbf{s}_{oxyz} :

$$\mathbf{s}_{oxyz} = (\sin \lambda \cos \phi', \sin \lambda \sin \phi', -\cos \lambda), \quad (21)$$

such that

$$\cos \lambda = \sin \alpha \cos \beta \cos \eta + \sin \alpha \sin \beta \cos \epsilon \sin \eta + \cos \alpha \sin \epsilon \sin \eta, \quad (22)$$

and

$$\tan \phi' = \frac{\sin \alpha \sin \epsilon \sin \eta - \cos \alpha \cos \beta \cos \eta - \cos \alpha \sin \beta \cos \epsilon \sin \eta}{\sin \beta \cos \eta + \cos \beta \cos \epsilon \sin \eta}. \quad (23)$$

The absorbed radiation flux is

$$\begin{aligned} E(\theta, \phi) &= (1 - A)\Phi H(\cos \lambda)H(w)(-\mathbf{r}_P \cdot \mathbf{s}) \\ &= (1 - A)\Phi H(\cos \lambda)H(w) \cdot [m_1 \cos(\beta - \beta_1) + m_2] \end{aligned} \quad (24)$$

where

$$w = \cos 2\lambda \cos \theta + \sin \theta_0 - \sin 2\lambda \sin \theta \cos(\phi - \phi'), \quad (25)$$

$$\tan \beta_1 = \frac{(\sin \alpha \cos \theta - \cos \alpha \sin \theta \cos \phi) \cos \epsilon \sin \eta - \sin \theta \sin \phi \cos \eta}{(\sin \alpha \cos \theta - \cos \alpha \sin \theta \cos \phi) \cos \eta + \cos \epsilon \sin \eta \sin \theta \sin \phi}, \quad (26)$$

$$\begin{aligned} m_1 &= (\cos^2 \eta + \cos^2 \epsilon \sin^2 \eta)^{1/2} \\ &\quad \cdot (\cos^2 \theta \sin^2 \alpha - \frac{\cos \phi \sin 2\alpha \sin 2\theta}{2} \\ &\quad + (\cos^2 \alpha \cos^2 \phi + \sin^2 \phi) \sin^2 \theta)^{1/2}, \end{aligned} \quad (27)$$

$$m_2 = \cos \alpha \cos \theta \sin \epsilon \sin \eta + \cos \phi \sin \alpha \sin \epsilon \sin \eta \sin \theta. \quad (28)$$

Here, H is the Heaviside function defined by

$$H(x) := \begin{cases} 1, & x > 0 \\ 0, & \text{else.} \end{cases} \quad (29)$$

Using the substitution $\beta' = \beta - \beta_1$, the absorbed radiation flux has the form

$$E(\theta, \phi) = \begin{cases} (1 - A)\Phi(m_1 \cos \beta' + m_2), & \beta'_{\min} < \beta < \beta'_{\max} \\ 0, & \text{else.} \end{cases} \quad (30)$$

Expanding Eq. (30) in Fourier series, we obtain

$$E(\theta, \phi) = E_0 + \frac{(1 - A)\Phi}{\pi} \sum_{n=1}^{\infty} [C_n \cos(n\beta') + S_n \sin(n\beta')], \quad (31)$$

with

$$E_0 = \frac{(1 - A)\Phi}{2\pi} (m_1 \sin \beta + m_2 \beta) \Big|_{\beta'_{\min}}^{\beta'_{\max}}, \quad (32)$$

$$\begin{aligned} C_n &= \int_{\beta'}^{\beta'_{\min}} (m_1 \cos \beta'_{\max} + m_2) \cos(n\beta') d\beta' \\ &= \begin{cases} \left(\frac{m_1 \sin 2\beta' + 2m_1\beta'}{4} + m_2 \sin \beta' \right) \Big|_{\beta'_{\min}}^{\beta'_{\max}}, & n = 1 \\ \left(\frac{m_1 n \cos \beta' \sin n\beta' - m_1 \cos n\beta' \sin \beta'}{n^2 - 1} + \frac{m_2 \sin(n\beta')}{n} \right) \Big|_{\beta'_{\min}}^{\beta'_{\max}}, & n > 1, \end{cases} \end{aligned} \quad (33)$$

and

$$S_n = \int_{\beta'}^{\beta'_{\min}} (m_1 \cos \beta'_{\max} + m_2) \sin(n\beta') d\beta'$$

$$= \begin{cases} -\left(\frac{m_1 \cos \beta'^2}{2} + m_2 \cos \beta'\right) \Big|_{\beta'_{\min}}^{\beta'_{\max}}, & n = 1 \\ \left(\frac{m_1 n \cos \beta' \cos n\beta' + m_1 \sin \beta' \sin n\beta' - m_2 \cos n\beta'}{1 - n^2}\right) \Big|_{\beta'_{\min}}^{\beta'_{\max}}, & n > 1. \end{cases} \quad (34)$$

The n th coefficient of the Fourier series of $E(\theta, \phi)$ is

$$E_n = \sqrt{C_n^2 + S_n^2} \cdot e^{i\Phi_n}, \quad (35)$$

with

$$\tan \Phi_n = -\frac{S_n}{C_n}. \quad (36)$$

2.1.4. Self-heating effect

Due to the concave structure of the crater, the surface element in the crater also receives photons emitted by the crater itself, which is a process referred to as 'self-heating'. In this section, we derive the self-radiation H and the self-scattering G as a function of the position in the crater.

Let us consider a surface element dS_1 receiving the radiation from another surface element dS_2 . In the reference frame $oxyz$, the positions of dS_1 and dS_2 are

$$\mathbf{r}_1 = R_1(\sin \theta_1 \cos \phi_1, \sin \theta_1 \sin \phi_1, \cos \theta_1), \quad (37)$$

$$\mathbf{r}_2 = R_1(\sin \theta_2 \cos \phi_2, \sin \theta_2 \sin \phi_2, \cos \theta_2). \quad (38)$$

The displacement from dS_1 to dS_2 is

$$\mathbf{r}_{1,2} = \mathbf{r}_2 - \mathbf{r}_1. \quad (39)$$

The incident angle ζ_1 and the emission angle ζ_2 are defined as

$$\cos \zeta_1 = -\mathbf{r}_1 \cdot \mathbf{r}_{1,2} / R_1 r_{1,2}, \quad (40)$$

$$\cos \zeta_2 = \mathbf{r}_2 \cdot \mathbf{r}_{1,2} / R_1 r_{1,2}, \quad (41)$$

respectively. The radiation flux at the location of dS_1 produced by the thermal radiation of dS_2 is

$$H_{1,2} = \frac{e\sigma u_2^4}{\pi} \frac{\cos \zeta_1 \cos \zeta_2}{r_{1,2}^2} dS_2. \quad (42)$$

Substituting Eqs. (37)–(41) into Eq. (42), we obtain

$$H_{1,2} = \frac{e\sigma u_2^4}{4\pi R_1^2} dS_2. \quad (43)$$

For an arbitrary point, the radiation flux caused by the whole crater is

$$H(\theta, \phi) = \int_{\mathcal{Z}} \frac{e\sigma u(\theta', \phi')^4}{4\pi} \sin \theta' d\theta' d\phi', \quad (44)$$

where \mathcal{Z} is the crater surface, and is defined as

$$\mathcal{Z} := \{(x, y, z) \in \mathbb{R}^3 | r = R_1, \theta \in (0, \pi/2 - \theta_0), \phi \in (0, 2\pi)\}. \quad (45)$$

Similarly, we obtain the self-scattering term:

$$G(\theta, \phi) = \int_{\mathcal{Z}} \frac{AE(\theta', \phi')}{4\pi} \sin \theta' d\theta' d\phi'. \quad (46)$$

Therefore, both $H(\theta, \phi)$ and $G(\theta, \phi)$ can be expressed in terms of $u(\theta, \phi)$ and $E(\theta, \phi)$. As $E(\theta, \phi)$ is derived in Sect. 2.1.3, the only unknown variable is the temperature $u(\theta, \phi)$, the solution for which is discussed in the following section.

2.2. Solution for temperature

We obtained the Fourier series of the solar radiation flux (Sect. 2.1.3) and the radiation flux produced by the crater (Sect. 2.1.4), which allows us to return to Eq. (14) to solve the temperature distribution $u(\theta, \phi)$. We note that the self-radiation term H contains the unknown temperature distribution that is to be solved.

The Fourier coefficients of the temperature of the crater follow

$$\sigma u_0^4(\theta, \phi) = (1 - A)(E_0(\theta, \phi) + G_0(\theta, \phi) + H_0(\theta, \phi))$$

$$\sigma u_n(\theta, \phi) u_0^3(\theta, \phi) \frac{2\sqrt{2\Theta_n^2 + 2\Theta_n + 1}}{(1 - A)e^{iJ_n}} = E_n(\theta, \phi) + G_n(\theta, \phi) + H_n(\theta, \phi), \quad (47)$$

with

$$G_n(\theta, \phi) = \int_{\mathcal{Z}} \frac{AE_n(\theta', \phi')}{4\pi} \sin \theta' d\theta' d\phi',$$

$$H_0(\theta, \phi) = \int_{\mathcal{Z}} \frac{e\sigma u_0(\theta', \phi')^4}{4\pi} \sin \theta' d\theta' d\phi', \quad (48)$$

$$H_n(\theta, \phi) = \int_{\mathcal{Z}} \frac{e\sigma u_0(\theta', \phi')^3 u_n(\theta', \phi')}{\pi} \sin \theta' d\theta' d\phi'.$$

Here, terms G and H are the scattering flux and self-radiation flux, respectively.

2.2.1. Solution of a general form

Equation (47) have a general form:

$$f(\theta, \phi) = g(\theta, \phi) + C \int_{\mathcal{Z}} f(\theta', \phi') \sin \theta' d\theta' d\phi'. \quad (49)$$

By setting

$$k = \int_{\mathcal{Z}} f(\theta', \phi') \sin \theta' d\theta' d\phi', \quad (50)$$

we have

$$f(\theta, \phi) = g(\theta, \phi) + C \cdot k. \quad (51)$$

Substituting Eq. (51) into Eq. (50), we obtain

$$k = \int_{\mathcal{Z}} (g(\theta', \phi') + C \cdot k) \sin \theta' d\theta' d\phi'. \quad (52)$$

Rearranging Eq. (52), we find k is

$$k = \frac{\int_{\mathcal{Z}} g(\theta', \phi') \sin \theta' d\theta' d\phi'}{1 - C \int_{\mathcal{Z}} \sin \theta' d\theta' d\phi'}, \quad (53)$$

with which $f(\theta, \phi)$ is solved out by Eq. (51).

2.2.2. Solution for temperature

In the case of u_0 ,

$$f(\theta, \phi) = e\sigma u_0^4 / (1 - A), \quad (54)$$

$$g(\theta, \phi) = E_0(\theta, \phi) + G_0(\theta, \phi), \quad (55)$$

$$C = \frac{1}{4\pi}, \quad (56)$$

and in the case of u_n ,

$$f(\theta, \phi) = e\sigma u_0^3 u_n \frac{2\sqrt{2\Theta_n^2 + 2\Theta_n + 1}}{(1-A)e^{iJ_n}}, \quad (57)$$

$$g(\theta, \phi) = E_n(\theta, \phi) + G_n(\theta, \phi), \quad (58)$$

$$C = \frac{e^{iJ_n}}{2\pi\sqrt{2\Theta_n^2 + 2\Theta_n + 1}}. \quad (59)$$

2.3. The CYORP torque

The CYORP torque is defined as the YORP torque difference between the crater and the flat ground:

$$T_{\text{CYORP}} = T_{\text{crater}} - T_{\text{ground}}. \quad (60)$$

2.3.1. The YORP torque of the crater

The average radiative torque produced by the crater should be calculated in the inertial frame $OXYZ$:

$$\mathbf{T}_{\text{crater}} = \mathbf{r}_{0,OXYZ} \times \mathbf{f}_{OXYZ}. \quad (61)$$

Here, \mathbf{f}_{OXYZ} is the radiative force, and

$$\mathbf{f}_{OXYZ} = \int_{\mathcal{W}} \frac{e\sigma T(\theta, \phi)^4}{c} \mathbf{n}_f(\theta, \phi) dS, \quad (62)$$

where \mathbf{n}_f is the corrected force direction vector for each surface element. If there is no shelter around the surface element, \mathbf{n}_f is equal to the surface unit normal vector \mathbf{n}_0 . However, the surface element in a crater has a sky sheltered by other elements, resulting in the reabsorption of the emitted photons along the direction of the shelter.

For the surface element $dS(\theta, \phi)$, the radiative force is

$$\mathbf{f} = - \int_{\mathcal{H}} \frac{\Phi}{\pi c} \cos \theta' \begin{pmatrix} \sin \theta' \cos \phi' \\ \sin \theta' \sin \phi' \\ \cos \theta' \end{pmatrix} \sin \theta' d\theta' d\phi'. \quad (63)$$

Without sheltering (e.g. for convex asteroids), \mathcal{H} is replaced by the hemisphere (i.e. $\theta \in (0, \pi/2)$, $\phi \in (0, 2\pi)$). In this case, the force is reduced to $2\Phi\mathbf{n}_0/3c$.

2.3.2. The YORP torque of the flat portion of the surface

The absorbed radiation flux for a flat ground with the normal vector \mathbf{n}_0 is

$$E_{\text{ground}} = (1-A)\Phi H(\cos \lambda) \cos \lambda \\ = \begin{cases} (1-A)\Phi(m_1 \cos \beta' + m_2), & \beta'_{\min} < \beta' < \beta'_{\max} \\ 0, & \text{else.} \end{cases} \quad (64)$$

Here, $\beta' = \beta - \beta_1$, with

$$\tan \beta_1 = \frac{\sin \alpha \cos \epsilon \sin \eta}{\sin \alpha \cos \eta}, \quad (65)$$

$$m_1 = (\sin^2 \alpha (\cos^2 \eta + \cos^2 \epsilon \sin^2 \eta))^{1/2}, \quad (66)$$

$$m_2 = \cos \alpha \sin \epsilon \sin \eta, \quad (67)$$

and β_{\min} and β_{\max} are the negative and positive values of $\arccos(-m_2/m_1)$, respectively.

3. Numerical model for examination

In the above analytical method, we adopted the assumption of a ‘‘small’’ temperature variation during a rotation period, which allows us to linearize the biquadrate of the temperature (i.e. $u^4 \sim u_0^3 \sum u_n e^{\beta n i}$). This assumption is equivalent to a high value of the thermal parameter, which is defined as

$$\Gamma = \frac{\sqrt{C\rho\omega\kappa}}{(\epsilon\sigma)^{1/4}(1-A)^{3/4}\Phi^{3/4}}. \quad (68)$$

In the case of a low thermal parameter, the analytical model should be used with caution. To examine the appropriate range of the thermal inertia for which our analytical model is valid, we built a one-dimensional thermophysical numerical model to perform cross-validation.

3.1. Numerical model

We used a finite difference numerical method to solve Eq. (3) with the second-order Crank-Nicholson scheme:

$$c_n u_{i,j+1,k+1} - (2c_n + 1)u_{i,j,k+1} + c_n u_{i,j-1,k+1} = \\ -c_n u_{i,j+1,k} + (2c_n - 1)u_{i,j,k} - c_n u_{i,j-1,k}. \quad (69)$$

Here, $u_{i,j,k}$ represents the temperature at the depth of $(j-1)\delta z$ below the i th facet at the k th time step, where i , j , and k are integrals starting from 1 to i_{\max} , j_{\max} , and k_{\max} . The coefficient c_n is

$$c_n = \frac{a\delta t}{2(\delta x)^2}. \quad (70)$$

The value of c_n should be smaller than 0.5 for the convergence of the iteration.

The surface temperature is determined by the first boundary condition (Eq. (4)):

$$(1-A)(E_{i,k} + H_{i,k} + S_{i,k}) - \sigma u_{i,1,k+1}^4 = K \frac{u_{i,1,k+1} - u_{i,2,k}}{\delta z}, \quad (71)$$

which can be solved by a Newtonian-Raphson iterative method. The solar flux $E_{i,k}$ on the i th facet at the k th time step is

$$E_{i,k} = \begin{cases} \Phi_0 \mathbf{n}_i \cdot \mathbf{s}_k H(\mathbf{n}_i \cdot \mathbf{s}_k), & \text{unsheltered} \\ 0, & \text{sheltered,} \end{cases} \quad (72)$$

where Φ_0 is 1364 W m^{-2} at the distance of 1 au to the Sun. Here, \mathbf{n}_i is the normal vector of the i th facet and \mathbf{s}_k is the unit solar position vector at the k th time step. Whether or not the facet is sheltered is judged according to the projections of other facets on the plane of the i th facet along the solar position vector \mathbf{s}_k . The self-radiation term $H_{i,k}$ is the sum of radiation from other facets:

$$H_{i,k} = \sum_{i' \neq i} e\sigma u_{i',1,k}^4 \frac{-(\mathbf{n}_i \cdot \mathbf{r}_{i,i'}) (\mathbf{n}_{i'} \cdot \mathbf{r}_{i,i'})}{\pi r_{i,i'}^2} S_{i'}, \quad (73)$$

where $\mathbf{r}_{i,i'}$ is the vector from the centre of the i th facet to the centre of i' th facet, and $S_{i'}$ is the area of the i' th facet. The scattering term $S_{i,k}$ is given by

$$S_{i,k} = \sum_{i' \neq i} A E_{i'} \frac{-(\mathbf{n}_i \cdot \mathbf{r}_{i,i'}) (\mathbf{n}_{i'} \cdot \mathbf{r}_{i,i'})}{\pi r_{i,i'}^2} S_{i'}. \quad (74)$$

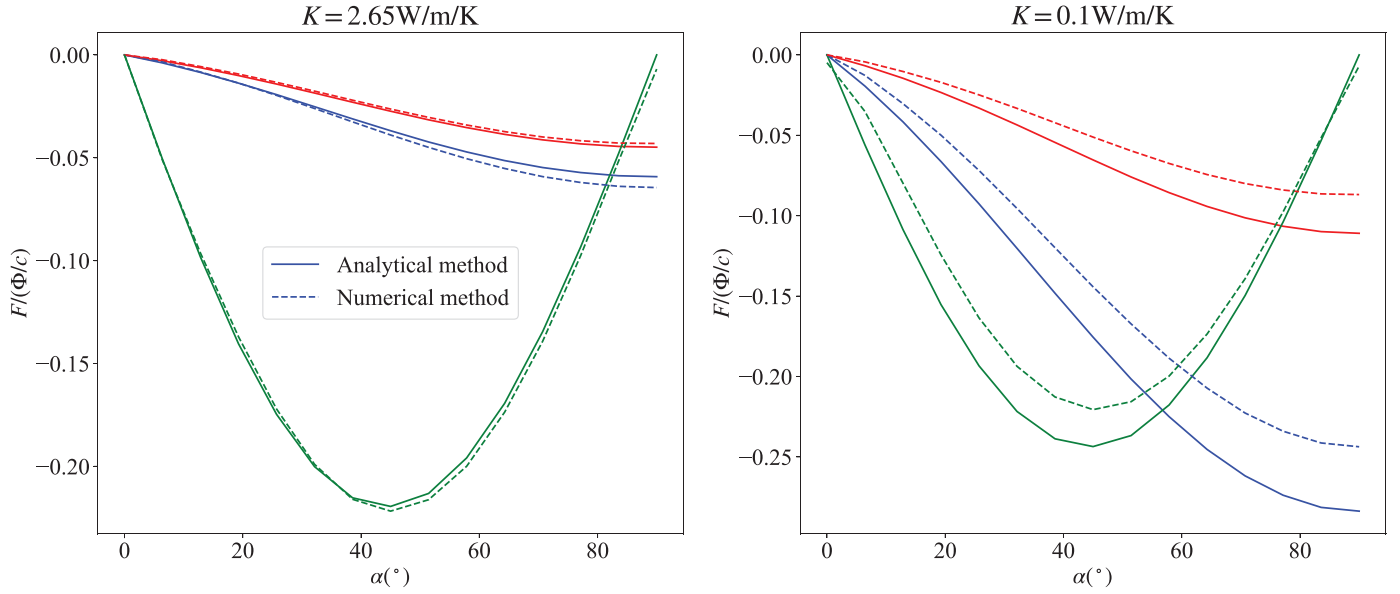


Fig. 2. Radiative force of the total crater averaged over a rotational period (8 h by default) obtained from the analytical method (solid lines) and the numerical method (dashed lines), as a function of the crater colatitude α for $K = 2.65 \text{ W m}^{-1} \text{ K}^{-1}$ (left panel) and $K = 0.1 \text{ W m}^{-1} \text{ K}^{-1}$ (right panel). The x , y , and z components of the radiative force are shown in blue, red, and green, respectively. The distance of the crater here is 1 au from the Sun.

The second boundary condition (Eq. (5)) translates into

$$u_{i,j_{\max},k+1} = u_{i,j_{\max}-1,k+1}. \quad (75)$$

Combining Eqs. (69), (71), and (75), we can obtain the solution for the temperature in the next time step $u_{i,j,k+1}$ based on the temperature in the current time step $u_{i,j,k}$. We adopted an initial temperature of $u_{i,j,0} = 280 \text{ K}$. The maximum depth is set to be a few thermal skin depths $\sqrt{K/C\rho\omega}$ and the total number of layers is set as $j_{\max} = 50$. In order to make sure that the surface temperature is in an equilibrium state, we set the total time as $k_{\max}\delta t \sim 20$ spin periods. We divided the considered crater into about 1000 facets and solve the temperature for each facet using the above method.

3.2. Comparison with the analytical model

The thermal parameters of asteroids can vary widely depending on their composition and structure. For example, the thermal conductivity of a porous material is much lower than that of a dense metal. The thermal conductivity of stony asteroids, which are made mostly of silicates, can range from about 0.1 W mK^{-1} to 1 W mK^{-1} , while the thermal conductivity of metallic asteroids is generally much higher, in the range of $20\text{--}50 \text{ W mK}^{-1}$. Asteroids that are composed of a mixture of rock and metal will have thermal conductivity values between those of pure rock and pure metal.

Here, we test three typical types of asteroid materials: regolith, solid basalt, and metal, whose properties are shown in Table 1. We calculate the radiative force of the total crater averaged over a rotational period (8 h by default), as a function of the colatitude of the crater. The craters in the test are placed at 1 au from the Sun. For simplicity, we set the obliquity to $\epsilon = 0$. The results computed from the analytical method and the numerical method are shown in Fig. 2. We can see that the analytical result is consistent with the numerical result to a high degree, while a large discrepancy shows up when the thermal conductivity

Table 1. Thermal parameter for three typical materials on asteroids, taken from Farinella et al. (1998).

| | ρ (kg m^{-3}) | K ($\text{W m}^{-1} \text{ K}^{-1}$) | C ($\text{J kg}^{-1} \text{ K}^{-1}$) |
|--------------|-------------------------------|--|---|
| Regolith | 1500 | 0.0015 | 680 |
| Solid basalt | 3500 | 2.65 | 680 |
| Solid iron | 8000 | 40 | 500 |

decreases to $0.1 \text{ W m}^{-1} \text{ K}^{-1}$. This coincides with our prerequisite of the application of our analytical method, which is that the temperature variation should be small. Therefore, our method is appropriate for solid basalt and metal materials.

Regarding regolith material, with a thermal conductivity of as low as $0.001 \text{ W m}^{-1} \text{ K}^{-1}$, we test the model described in Zhou et al. (2022), where zero thermal conductivity is assumed. The result is shown in Fig. 3, which indicates that this latter model works well for regolith materials. Therefore, for three materials representing asteroid surfaces, our two methods, namely the one in the present work and that described in Zhou et al. (2022), behave well in modelling the YORP effect.

4. Discussion on self-modification effects

For a concave structure, there are three self-modification effects: the self-sheltering, self-radiation, and self-scattering effect. The first one refers to the radiative force modification on the surface element due to the re-absorption of photons by the crater. The second and third ones refer to the temperature increase due to the emitted photons and scattered photons from the crater itself. Previous research shows that these self-modification effects could be important for the YORP torque of the crater (Statler 2009; Rozitis & Green 2012, 2013a), but a quantitative description is still lacking. For example, it is not clear how deep the crater needs to be so that these self-modification effects can no longer

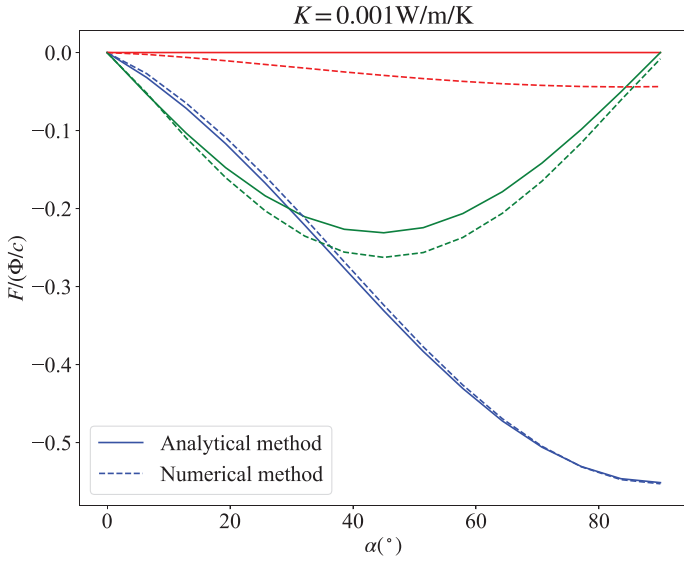


Fig. 3. Same as Fig. 2 but for $K = 0 \text{ W m}^{-1} \text{ K}^{-1}$ in the analytical model and $K = 0.001 \text{ W m}^{-1} \text{ K}^{-1}$ in the numerical model.

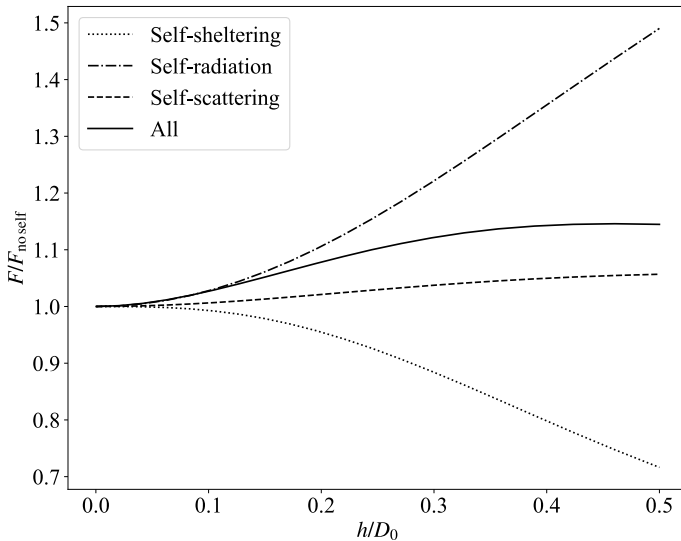


Fig. 4. Ratio of the radiative force including self-modification effects to that without self-modification effects, as a function of crater depth-to-diameter ratio and accounting for different self-modification effects.

be ignored. This is crucial to the validity of the commonly made assumption that the asteroid can be considered as a moderately convex shape with the craters being overlooked when evaluating the YORP torque. An essential metric in this respect is the depth-to-diameter ratio of the crater. We explore the radiative force (leading to the YORP torque) of a crater based on its depth-to-diameter ratio under varying conditions – one for each self-modification effect. Figure 4 shows our findings, situating the craters at the equator ($\alpha = \pi/2$) with a spin axis of zero-degree obliquity.

Our analysis reveals that both self-radiation and self-scattering amplify the force, raising the temperature by as much as 50% when the crater mirrors a hemisphere. In contrast, self-sheltering diminishes the force by up to 30%. Notably, the impact of self-scattering remains negligible for typical asteroid surface albedos ranging between 0.1 and 0.2. When integrating all self-modification effects, the radiative force increases by 15%.

Our result also shows that when the depth-to-diameter ratio $h/D_0 < 0.05$, the force increase is less than 1%. Therefore, for those shallow concave structures with $h/D_0 < 0.05$, no self-modification effects are needed in the YORP model for it to remain accurate. These can then be efficiently approximated as flat surfaces.

5. Analysis of the CYORP torque

As shown in a previous work (Zhou et al. 2022), the CYORP torque depends on many factors, including the depth-to-diameter ratio and location (or the colatitude α for example) of the crater as well as the obliquity and thermal parameter of the asteroid. In this section, we discuss the dependence of the CYORP torque on these factors. In the following, except for in Sect. 5.1, we assume the depth-to-diameter ratio to be ~ 0.16 .

5.1. Depth-to-diameter ratio

Asteroid craters exhibit a range of distinct features in size and shape, with diameters ranging from a few centimetres to several kilometres for large asteroids. These craters generally display bowl-shaped structures, containing central peaks and terraced walls when produced in the gravity regime. To simplify the modelling, a semi-sphere approximation is often used to represent the shape of craters.

According to the definition of CYORP torque, if the depth-to-diameter ratio reaches zero, the CYORP torque is zero (Eq. (60)). Figure 5 shows the CYORP torques generated by craters with various depth-to-diameter ratios. The parameters $\delta = \Delta = \pi/6$, $K = 2.65 \text{ W m}^{-1} \text{ K}^{-1}$, and $\alpha = \pi/2$ are used. Higher depth-to-diameter ratios correspond to larger spin components of the CYORP torque. A crater with $h/D_0 < 0.05$ produces an insignificant CYORP torque, which may be disregarded. Furthermore, the depth-to-diameter ratio also impacts the obliquity component, influencing both the torque magnitude and shape of the torque curve. For instance, when the depth-to-diameter ratio is low, the asymptotic obliquity is 90° , while for higher depth-to-diameter ratios, new asymptotic obliquities arise around 0° and 180° .

5.2. Crater latitude α and asteroid obliquity ϵ

Figure 6 displays the CYORP torque components as a function of the crater latitude and asteroid obliquity. The values of the parameters δ and Δ are set to a representative value of $\pi/4$. The spin component W_z exhibits symmetry about the axis $\epsilon = 90^\circ$, while the obliquity component W_ϵ is anti-symmetric. The minimum and maximum values of the torque occur when the obliquity is 0° or 90° , with the absolute value of these extrema reaching up to 0.02. The coefficient of the obliquity component of the CYORP torque is considerably smaller, with a maximum value of 0.004.

For comparison, the typical value of the normal YORP spin coefficient is 0.005 for type I/II and < 0.001 for type III/IV asteroids¹. The ratio of the CYORP torque to the normal YORP torque scales as

$$\frac{T_{\text{CYORP}}}{T_{\text{NYORP}}} = \frac{W_{\text{CYORP}} S_{\text{crater}}}{W_{\text{YORP}} S_{\text{asteroid}}}. \quad (76)$$

¹ See the definition by Vokrouhlický & Čapek (2002).

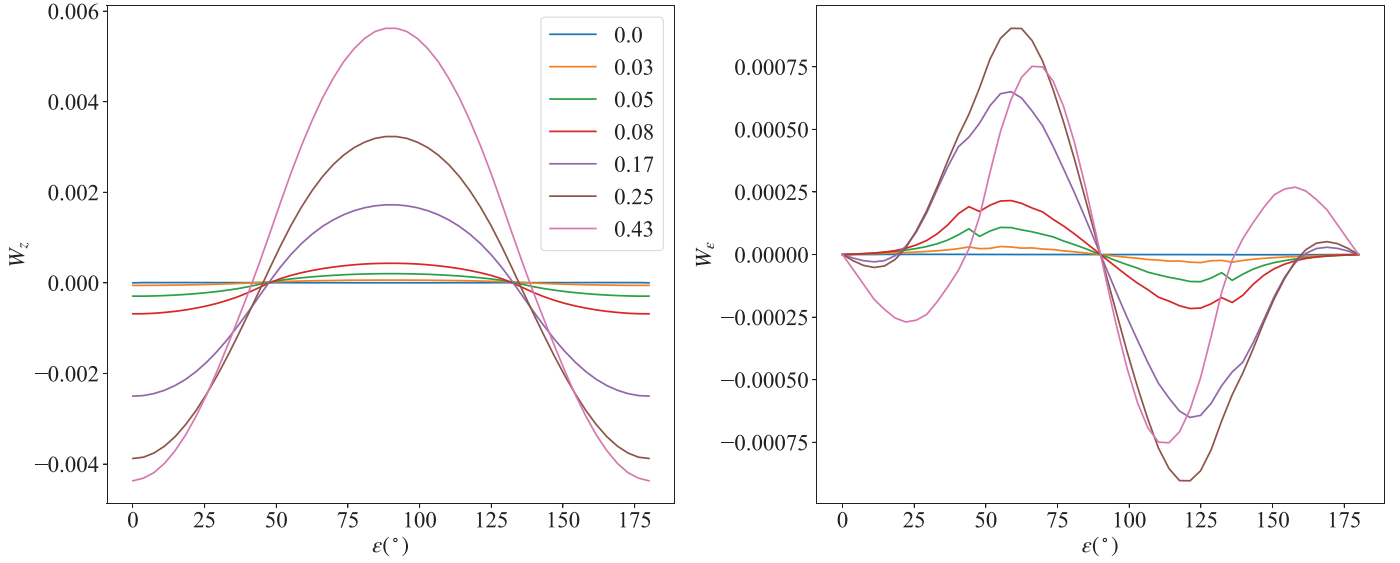


Fig. 5. Spin component (left panel) and the obliquity component (right panel) of the CYORP coefficient as a function of the asteroid obliquity ϵ , accounting for different depth-to-diameter ratios, which are denoted by different colours.

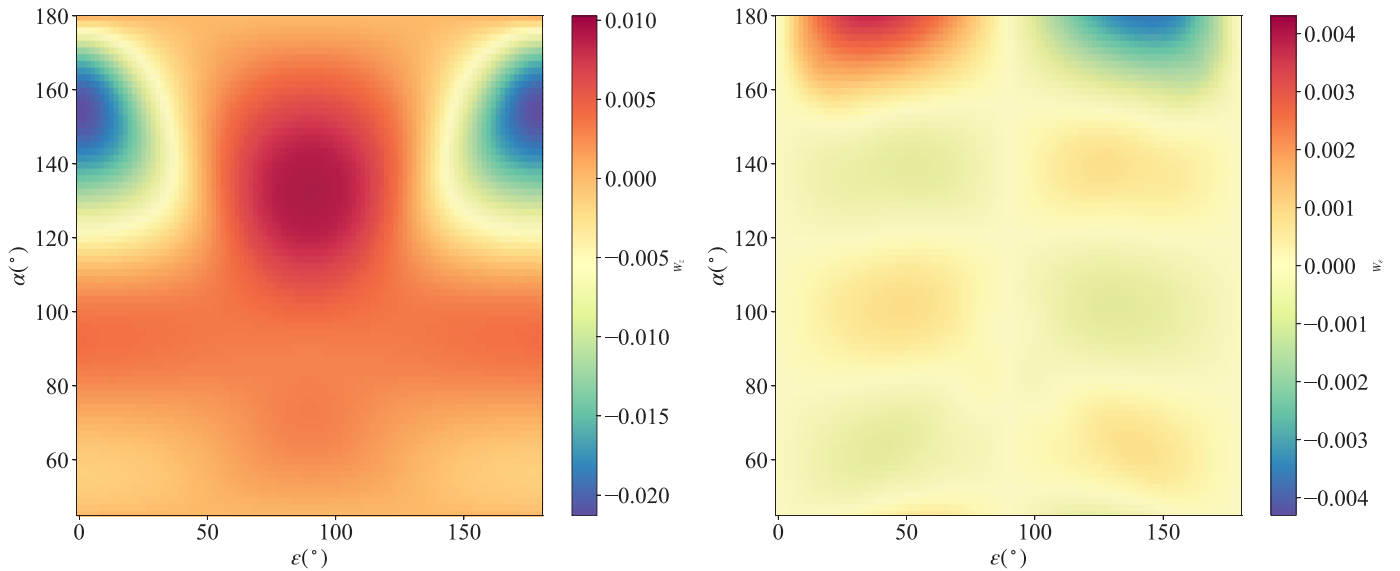


Fig. 6. Spin component (left panel) and the obliquity component (right panel) of the CYORP coefficient as a function of the asteroid obliquity ϵ and the crater colatitude $\alpha (> \Delta)$, for $K = 2.65 \text{ W m}^{-1} \text{ K}^{-1}$. Here, $d/D_0 = 0.16$ and $\delta = \Delta = \pi/4$.

Setting the ratio to 1, we find that the total area of concave structures needs to be as large as 1/4 and 1/20 of the asteroid surface area for type I/II and type III/IV asteroids, respectively.

5.3. Thermal parameter

When the asteroid rotates quickly and has high heat conductivity, a higher value of the thermal parameter arises, resulting in a smaller variation in temperature. To explore the role of the thermal parameter, we employ the same parameters as in Sect. 5.2, but with $K = 40 \text{ W m}^{-1} \text{ K}^{-1}$ for metal materials, and the resulting CYORP torques are depicted in Fig. 7. The comparison with Fig. 6 reveals that the spin component remains relatively unchanged, while the obliquity component displays significant variation. This observation aligns with the prior assertion that the thermal parameter mainly impacts the obliquity component

(Vokrouhlický & Čapek 2002). In the regime of high thermal conductivity, the obliquity component diminishes as the thermal conductivity increases.

5.4. Irregularity δ and Δ

The angular parameters δ and Δ are used to describe the irregularity of the asteroid, where $\delta = 0$ and $\Delta = 0$ correspond to a perfect sphere. We explore the CYORP torque as a function of δ and Δ with fixed asteroid obliquity and crater colatitude of $\pi/4$. The results are presented in Fig. 8. We can see that for the spin component, δ controls the torque magnitude while Δ controls the torque direction.

Zhou et al. (2022) demonstrates that the CYORP torque vanishes for $\delta = 0$. However, in the presence of finite thermal inertia, the obliquity component of the CYORP torque arises while

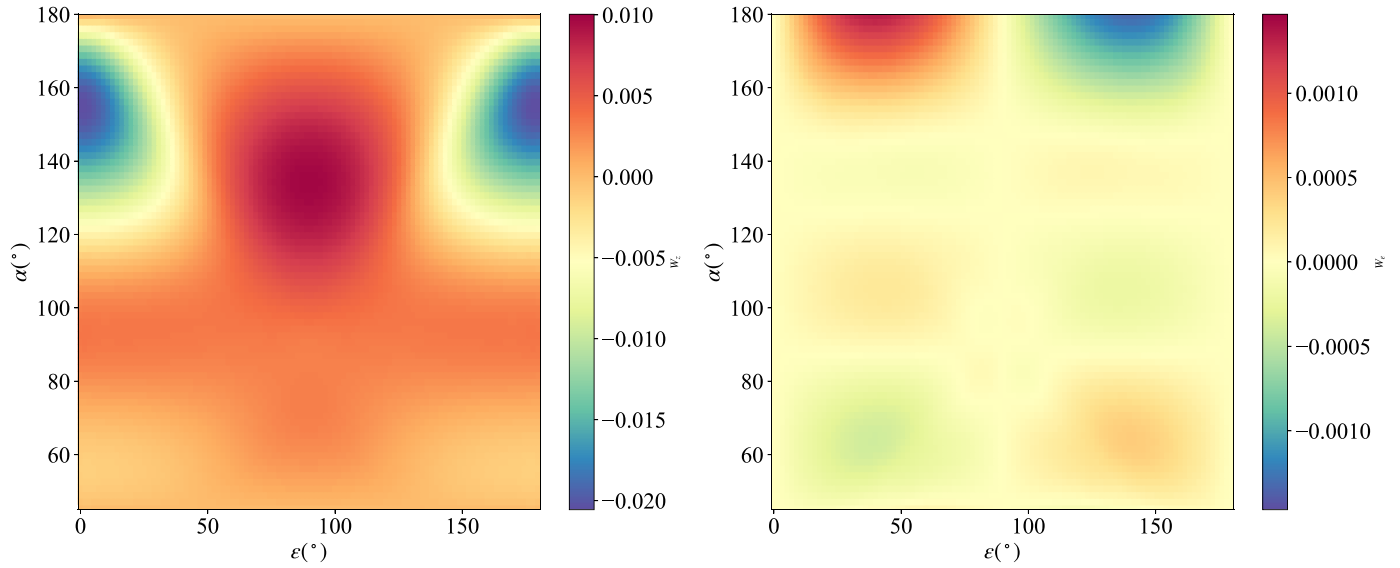


Fig. 7. Same as Fig. 6 but for $K = 40 \text{ W m}^{-1} \text{ K}^{-1}$.

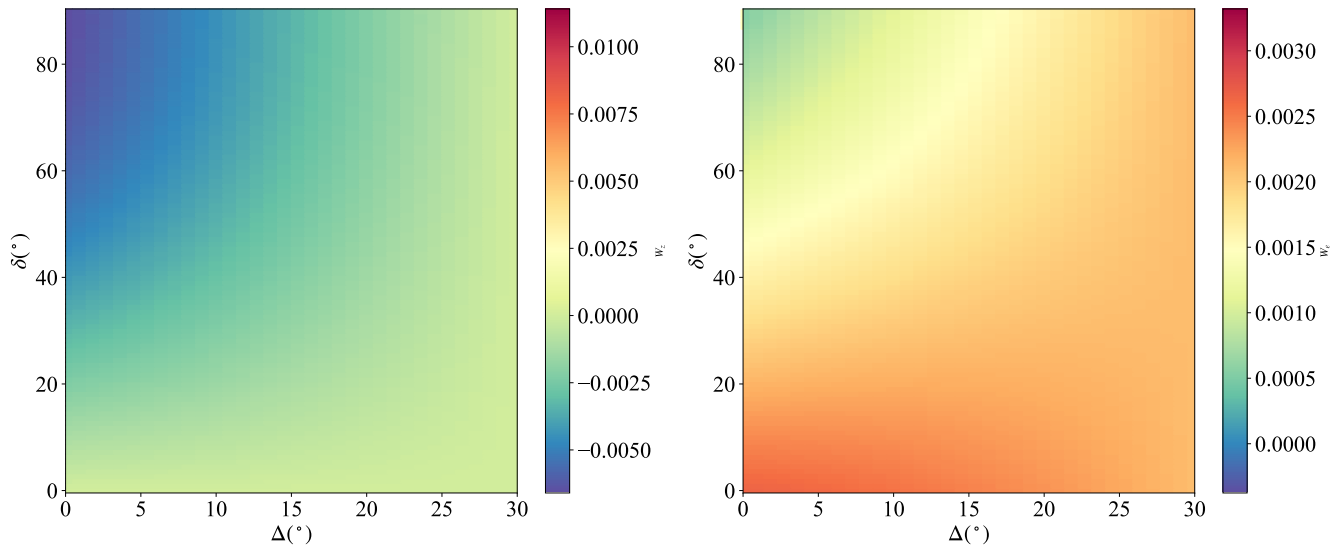


Fig. 8. Spin component (left panel) and the obliquity component (right panel) of the CYORP coefficient as a function of $\Delta (< \alpha)$ and δ , for $K = 2.65 \text{ W m}^{-1} \text{ K}^{-1}$. Here, $d/D_0 = 0.16$ and $\alpha = \epsilon = \pi/6$.

the spin component remains negligible. Figure 9 illustrates the variation of the CYORP obliquity component with the asteroid obliquity and the crater colatitude when δ and Δ are both zero. The CYORP torque has a tendency to lead the asteroid obliquity to 90° when the crater is near the poles, while it leads to an asymptotic obliquity of 0° or 180° when the crater is near the equator.

6. Application of the CYORP effect on a real asteroid

6.1. Roughness

The surface roughness of asteroids is produced by several processes, including micrometeorite impacts, thermal fatigue, ejecta, or outgassing. It was found that the YORP torque is extremely sensitive to the small-scale surface structures

(Statler 2009; Breiter et al. 2009). The microscopic beaming effect of regolith grain-size-scale roughness ($< 1 \text{ mm}$) was shown – using the Hapke reflectance and emissivity model (Breiter & Vokrouhlický 2011) – to have a marginal influence on the YORP effect. The transverse heat conduction across thermal skin depth ($\sim 1 \text{ cm}$) causes an asymmetric thermal emission of the east and west sides of a boulder, giving rise to a systematic positive YORP torque (Golubov & Krugly 2012; Golubov & Lipatova 2022). The importance of the various self-modification effects of a concave feature on the surface was considered gradually and numerical approaches were taken to study it (Statler 2009; Rozitis & Green 2012, 2013a). It was found that the concave feature of surface roughness could dampen the YORP torque by tens of percent. While the pioneering studies by Rozitis & Green (2012) shed light on the effects of roughness, the computational expense and difficulty in studying the functional dependence means that there are severe limitations to the numerical method.

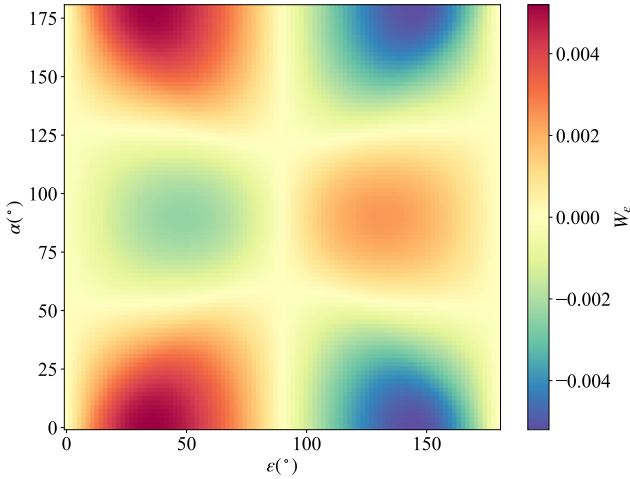


Fig. 9. Obliquity component (right panel) of the CYORP coefficient as a function of the asteroid obliquity ϵ and the crater colatitude α for $K = 2.65 \text{ W m}^{-1} \text{ K}^{-1}$. Here, $d/D_0 = 0.16$ and $\delta = \Delta = 0$.

In contrast, the analytical method that we introduce in the present study, and its computational efficiency, simplify the application of roughness-induced YORP effects to real asteroids or binary systems. Given the objective of our semi-analytical method to provide a rapid assessment of the impact of surface roughness, it is particularly well-suited for models of asteroids with rough convex shapes derived from light-curve observations. However, when dealing with high-resolution shape models, especially those that possess a resolution of a few centimetres (the scale of the thermal skin), a 3D thermal model becomes essential for accurate calculations, owing to the presence of the tangential YORP (TYORP) effect, which accounts for the transverse heat conduction inside a boulder.

For illustrative purposes, to demonstrate the application of our method, we randomly selected the main belt asteroid (272) Antonia as an example. This choice is representative of the majority of asteroids lacking detailed information obtained through in situ observations. We used the shape model obtained from Hanuš et al. (2013). To optimise the performance of our model, we assume a relatively high thermal conductivity of $1 \text{ W m}^{-1} \text{ K}^{-1}$. We uniformly distributed the roughness across the asteroid's surface and investigated the total YORP torque (NYORP + CYORP). To do so, we input the normal vector and position vector of surface elements in the shape model to our CYORP model to obtain the CYORP torque coefficient of each surface element. We then used the area of each surface element to calculate the CYORP torque and sum up all CYORP torques generated by all surface elements. The depth-to-diameter is assumed to be 0.5, following the assumption made by Rozitis & Green (2012). This has been compared with the sole NYORP torque. The result is depicted in Fig. 10. Our findings confirm that the roughness-induced CYORP torque damps the normal YORP torque. Specifically, for the asteroid (272) Antonia, the spin component of the torque experiences a damping effect of approximately 35%, while the obliquity component is damped by approximately 64%.

6.2. Rotational evolution

The rotational dynamics of asteroids are primarily governed by two key processes: collisions and the YORP effect. The timescale for reorientation of the spin axis resulting from angular

momentum transfer during a collision can be expressed as (Farinella et al. 1998)

$$\tau_{\text{imp, re-ori}} = 746 \left(\frac{R_{\text{ast}}}{1 \text{ km}} \right)^{4/3} \left(\frac{\omega}{3 \times 10^{-4} \text{ s}^{-1}} \right)^{5/6} \text{ Myr}. \quad (77)$$

On the other hand, the typical timescale associated with the YORP effect is approximately given by:

$$\tau_{\text{YORP}} \sim 4 \left(\frac{R_{\text{ast}}}{1 \text{ km}} \right)^2 \left(\frac{\omega}{3 \times 10^{-4} \text{ s}^{-1}} \right) \text{ Myr}. \quad (78)$$

Clearly, the YORP timescale is shorter than $\tau_{\text{imp, re-ori}}$, although its specific value exhibits considerable variation across different asteroids. Consequently, it is widely accepted that the YORP effect primarily governs the rotational evolution of small objects, while collisions play a dominant role in larger objects. The classic static YORP model – which assumes an invariable YORP torque until the asteroid spins up to disruption or spins down to a quasi-static rotation – has been used to study the long-term rotational evolution of asteroids (Rubincam 2000; Pravec et al. 2005; Bottke et al. 2015). A more intricate model, referred to as the ‘stochastic YORP model’ (Bottke et al. 2015), takes into account the resetting of the YORP torque caused by collisions, which arises from the high sensitivity of the YORP effect to surface morphology. Although a suggested timescale of 1 Myr has been proposed for YORP reset (Bottke et al. 2015), a quantitative assessment of the torque changes resulting from craters is yet to be explored. The CYORP effect offers a powerful tool for investigating the stochastic YORP effect. While a comprehensive examination of the stochastic YORP effect is beyond the scope of this paper, we present an example of integrating the CYORP effect into the static YORP model.

In our simulation, a random YORP coefficient is assigned within the range of -0.005 to 0.005 , with the coefficient's sign matching that of the torque. The CYORP torque is introduced specifically when a collision event takes place. The timescale for the impact by an asteroid with the size R_{imp} is

$$\tau_{\text{imp}} = \frac{1}{P_i \pi R_{\text{Antonia}}^2 \Delta N(R > R_{\text{imp}})}, \quad (79)$$

where

$$N(R > R_{\text{imp}}) = C_R \left(\frac{R_{\text{imp}}}{1 \text{ km}} \right)^{-b_R}. \quad (80)$$

Here, $P_i = 2.85 \times 10^{-18} \text{ km}^{-2} \text{ yr}^{-1}$ is the intrinsic collision probability, $C_R = 6 \times 10^5$, and $b_R = 2.2$ (Holsapple 2022). In the strength regime formulation, the crater produced by an impactor with the size of R_{imp} has a size of

$$R_{\text{crater}} = 1.306 R_{\text{imp}} \left(\frac{\rho_{\text{imp}}}{\rho_{\text{ast}}} \right)^{0.4} \left(\frac{Y}{\rho v_{\text{imp}}} \right)^{-0.205}, \quad (81)$$

with $Y = 100 \text{ Pa}$ and $v_{\text{imp}} = 5.3 \text{ km s}^{-1}$. In the gravity regime,

$$R_{\text{crater}} = 0.59 \left(\frac{\rho_{\text{ast}}}{m_{\text{imp}}} \right)^{-1/3} \left(\frac{\rho_{\text{ast}}}{\rho_{\text{imp}}} \right)^{0.00138} \left(\frac{g_{\text{ast}} R_{\text{ast}}}{v_{\text{imp}}} \right)^{-0.17}, \quad (82)$$

where g_{ast} is the surface gravity of the asteroid. In each time step ($\sim 10^3 \text{ yr}$), we calculate the numbers of impact craters of different sizes, according to Eqs. (79) and (81). We then assign each crater with a random surface element of the polyhedron

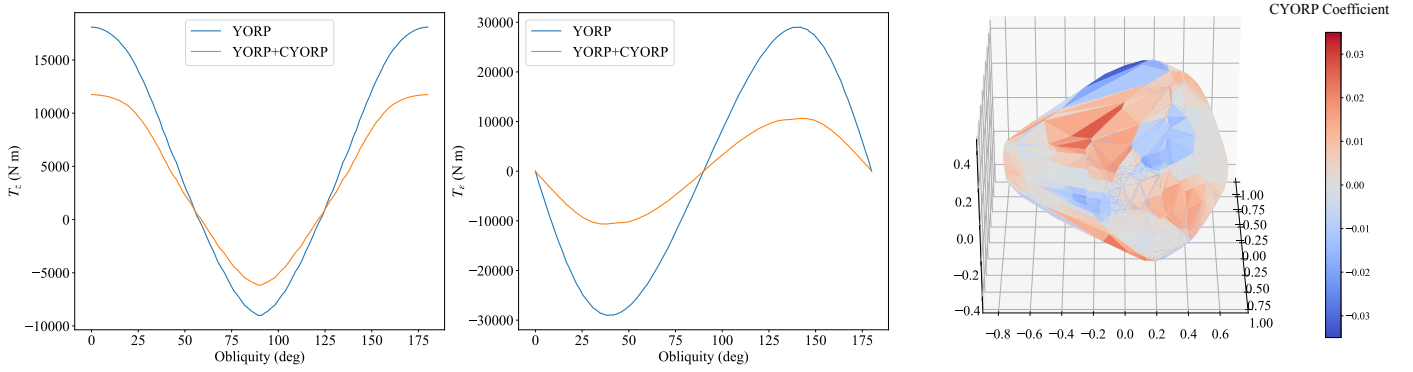


Fig. 10. YORP torque damped by the CYORP effect in the case of asteroid (272) Antonia. The spin component and the obliquity component are shown in the left and middle panels, respectively. The right panel shows the CYORP coefficient distribution over the asteroid's surface.

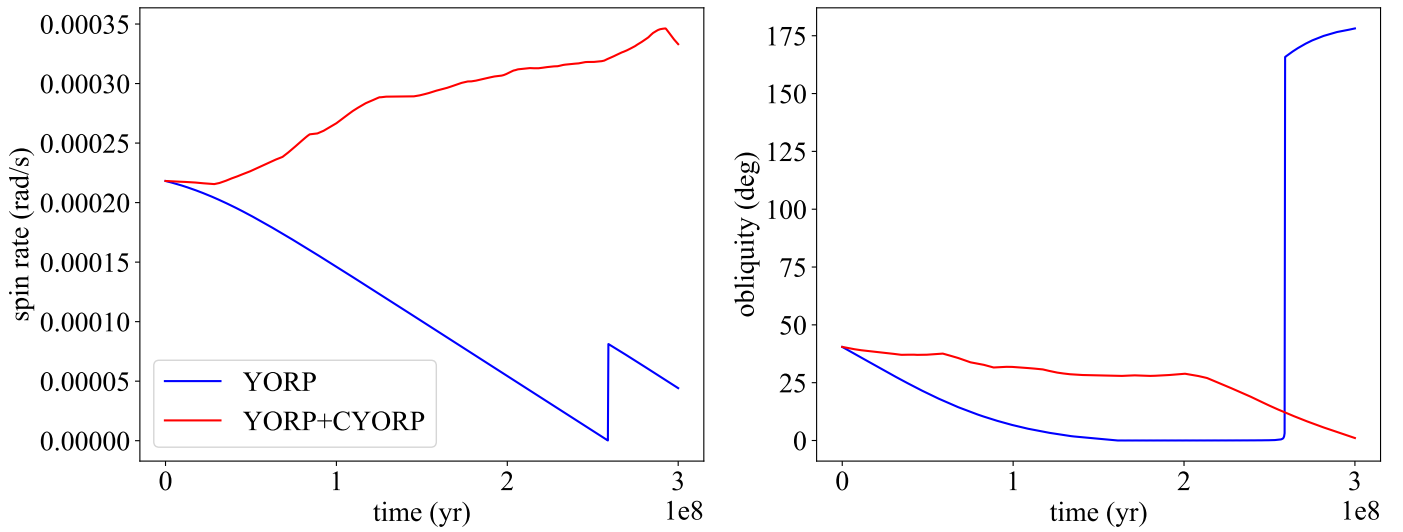


Fig. 11. Evolution of the spin rate (left panel) and the obliquity (right panel) of a 10 km synthetic asteroid. In the presence of the static YORP torque (blue line), the asteroid gradually decelerates until it reaches a quasi-non-rotational state. Subsequently, we impose a new rotational state on the asteroid by assigning random values of rotational speed and obliquity. Conversely, when incorporating the CYORP torque (red line), the asteroid follows a different path, exhibiting random fluctuations in its spin rate due to the occurrence of impacts, creating new craters that lead to changes in the CYORP torque. As a result, the asteroid experiences intermittent transitions between spin up and spin down.

model of the asteroid Antonia, after which we can calculate the CYORP torque. Finally, we add the CYORP torque to the normal YORP torque directly calculated from the shape model in order to obtain the total YORP torque. The spin rate evolves following

$$\dot{\omega} = \frac{T_z}{I}, \quad (83)$$

with I being the maximum moment of inertia and T_z being the torque component that is along a spin vector. The obliquity evolves according to

$$\dot{\epsilon} = \frac{T_\epsilon}{I\omega}, \quad (84)$$

where T_ϵ is the torque component that changes the obliquity.

There exist two possible end states in a YORP cycle: either the asteroid's rotation slows down until it reaches a quasi-non-rotational state, or it accelerates to the spin threshold for shape change or disruption with a period of approximately 2.2 h.

Upon completing a YORP cycle, the asteroid's rotational state is updated by assigning a new random rotational speed and obliquity. The impact of introducing CYORP torques can be observed in the evolution of a 10 km asteroid, as depicted in Fig. 11. Notably, significant differences arise when considering the inclusion of CYORP torques.

Nonetheless, the rotational evolution of asteroids currently lacks a standardised model. Some models propose that after spinning down to a non-rotational state, the asteroid's spin rate is assigned a new random value within a specified range (Hanuš et al. 2011; Bottke et al. 2015), while some assume it continues to spin up under the YORP effect (Pravec et al. 2008; Marzari et al. 2020). By selecting an initial spin rate for a new rotational state, Holsapple (2022) reproduces the spin evolution without the YORP effect. Hence, rather than attempting to address the entire complexity of the problem, our objective in this study is to present an illustrative example of the interaction between CYORP and the conventional YORP effect. Furthermore, we underscore the significance of the CYORP effect in the long-term rotational evolution of asteroids. A comprehensive

investigation of the rotational evolution of asteroid groups is left for future research.

7. Summary and conclusions

The YORP effect is a thermal torque produced by radiation from the irregular surface of the asteroid. It has been demonstrated that this effect is highly sensitive to surface topology (Statler 2009; Breiter et al. 2009), including small-scale roughness (Rozitis & Green 2012), boulders (Golubov & Krugly 2012), and craters (Zhou et al. 2022). In this study, we developed a semi-analytical model for calculating the temperature field of a crater, which accounts for the effects of self-sheltering, self-radiation, self-scattering, and non-zero thermal conductivity. Using this model, we investigated the crater-induced YORP (CYORP) effect in a computationally efficient manner (about three orders of magnitude faster than the numerical method), allowing for a comprehensive exploration of the functional dependence of the CYORP effect and its incorporation into the rotational and orbital evolution of asteroids. The main results and conclusions of this study can be summarised as follows.

Our semi-analytical model for the CYORP effect is valid in the high-thermal-conductivity regime ($K > 0.1 \text{ W m}^{-1} \text{ K}^{-1}$). This suggests that the model is suitable for application to materials such as solid basalt and metal, which are usually beneath the regolith on asteroid surfaces but may be exposed to sunlight due to the formation of deep craters.

The CYORP effect is significant when the crater depth-to-diameter ratio is greater than 0.05. The self-modification effects of a concave structure, including the self-sheltering effect, self-radiation effect, and self-scattering effect, are stronger with a higher depth-to-diameter ratio. For concave structures with a depth-to-diameter ratio of smaller than 0.05, the surface can be treated as a convex shape without introducing significant inaccuracies. The typical value of the CYORP coefficient for the spin component is 0.01, which is insensitive to the thermal parameter, while the obliquity component decreases from 0.004 for basalt to 0.001 for metal. For a z -axis symmetric shape (e.g. a spinning top shape), the spin component of the CYORP torque vanishes while the obliquity component survives, which implies that the spin acceleration of such symmetric shapes does not change significantly under the effect of crater formation.

Using our semi-analytical method, we confirm that the YORP torque can be damped by the surface roughness, which was first discovered by Rozitis & Green (2012). The fast computation of our semi-analytical model allows us to consider more flexible configurations of surface roughness, such as a space-varying roughness distribution, roughness on components of binary asteroids, and so on.

The magnitude and directional change of the YORP coefficient at each impact are assessed for the first time using our CYORP model. While a complete investigation of the spin evolution of asteroids is left for future work, we show that rotational evolution can be severely affected by collisions.

Acknowledgements. We acknowledge support from the Université Côte d'Azur. We thank Yun Zhang, Xiaoran Yan, and Marco Delbo for the useful discussion. Wen-Han Zhou would like to acknowledge the funding support from the Chinese Scholarship Council (No. 202110320014). Patrick Michel acknowledges funding support from the French space agency CNES and from the European

Union's Horizon 2020 research and innovation program under grant agreement no. 870377 (project NEO-MAPP).

References

- Agarwal, J., Kim, Y., Jewitt, D., et al. 2020, *A&A*, **643**, A152
- Botke, Jr, W. F., Vokrouhlický, D., Rubincam, D. P., & Nesvorný, D. 2006, *Annu. Rev. Earth Planet. Sci.*, **34**, 157
- Botke, Jr, W. F., Vokrouhlický, D., Walsh, K. J., et al. 2015, *Icarus*, **247**, 191
- Breiter, S., & Vokrouhlický, D. 2011, *MNRAS*, **410**, 2807
- Breiter, S., Bartczak, P., Czekaj, M., Oczujda, B., & Vokrouhlický, D. 2009, *A&A*, **507**, 1073
- Carruba, V., Domingos, R., Huaman, M., Santos, C. d., & Souami, D. 2014, *MNRAS*, **437**, 2279
- Carruba, V., Nesvorný, D., Aljbae, S., & Huaman, M. E. 2015, *MNRAS*, **451**, 244
- Carruba, V., Nesvorný, D., & Vokrouhlický, D. 2016, *AJ*, **151**, 164
- Čuk, M., & Burns, J. A. 2005, *Icarus*, **176**, 418
- Čuk, M., Christou, A. A., & Hamilton, D. P. 2015, *Icarus*, **252**, 339
- Delbo, M., Walsh, K., Mueller, M., Harris, A. W., & Howell, E. S. 2011, *Icarus*, **212**, 138
- Đurech, J., Vokrouhlický, D., Pravec, P., et al. 2022, *A&A*, **657**, A5
- Farinella, P., Vokrouhlický, D., & Hartmann, W. K. 1998, *Icarus*, **132**, 378
- Fatka, P., Pravec, P., & Vokrouhlický, D. 2020, *Icarus*, **338**, 113554
- Golubov, O. 2017, *AJ*, **154**, 238
- Golubov, O., & Krugly, Y. N. 2012, *ApJ*, **752**, L11
- Golubov, O., & Lipatova, V. 2022, *A&A*, **666**, A146
- Golubov, O., & Scheeres, D. J. 2019, *ApJ*, **157**, 105
- Golubov, O., Scheeres, D., & Krugly, Y. N. 2014, *ApJ*, **794**, 22
- Golubov, O., Unukovich, V., & Scheeres, D. J. 2021, *AJ*, **162**, 8
- Hanuš, J., Ďurech, J., Brož, M., et al. 2011, *A&A*, **530**, A134
- Hanuš, J., Ďurech, J., Brož, M., et al. 2013, *A&A*, **551**, A67
- Holsapple, K. A. 2022, *Planet. Space Sci.*, **219**, 105529
- Jacobson, S. A., & Scheeres, D. J. 2011, *Icarus*, **214**, 161
- Jacobson, S. A., Scheeres, D. J., & McMahon, J. 2013, *ApJ*, **780**, 60
- Jacobson, S. A., Marzari, F., Rossi, A., & Scheeres, D. J. 2016, *Icarus*, **277**, 381
- Lowry, S. C., Fitzsimmons, A., Pravec, P., et al. 2007, *Science*, **316**, 272
- Lowry, V. C., Vokrouhlický, D., Nesvorný, D., & Campins, H. 2020, *ApJ*, **160**, 127
- Lupishko, D., & Tielieusova, I. 2014, *Meteor. Planet. Sci.*, **49**, 80
- Lupishko, D., Mikhailchenko, O., & Chiorny, V. 2019, *Solar Syst. Res.*, **53**, 208
- Marzari, F., Rossi, A., Golubov, O., & Scheeres, D. J. 2020, *AJ*, **160**, 128
- Nesvorný, D., & Vokrouhlický, D. 2008, *A&A*, **480**, 1
- Polishook, D. 2014, *Icarus*, **241**, 79
- Pravec, P., Harris, A. W., Scheirich, P., et al. 2005, *Icarus*, **173**, 108
- Pravec, P., Harris, A., Vokrouhlický, D., et al. 2008, *Icarus*, **197**, 497
- Rozitis, B., & Green, S. F. 2012, *MNRAS*, **423**, 367
- Rozitis, B., & Green, S. F. 2013a, *MNRAS*, **433**, 603
- Rozitis, B., & Green, S. F. 2013b, *MNRAS*, **430**, 1376
- Rožek, A., Lowry, S., Nolan, M., et al. 2019, *A&A*, **631**, A149
- Rubincam, D. P. 2000, *Icarus*, **148**, 2
- Sánchez, P., & Scheeres, D. J. 2020, *Icarus*, **338**, 113443
- Scheeres, D. J. 2007, *Icarus*, **189**, 370
- Ševeček, P., Brož, M., Čapek, D., & Ďurech, J. 2015, *MNRAS*, **450**, 2104
- Statler, T. S. 2009, *Icarus*, **202**, 502
- Steinberg, E. & Sari, R. 2011, *AJ*, **141**, 55
- Taylor, P. A., Margot, J.-L., Vokrouhlický, D., et al. 2007, *Science*, **316**, 274
- Tian, J., Zhao, H.-B., & Li, B. 2022, *Res. Astron. Astrophys.*, **22**, 125004
- Veras, D., & Scheeres, D. J. 2020, *MNRAS*, **492**, 2437
- Vokrouhlický, D., & Čapek, D. 2002, *Icarus*, **159**, 449
- Vokrouhlický, D. & Nesvorný, D. 2008, *AJ*, **136**, 280
- Vokrouhlický, D., Milani, A., & Chesley, S. 2000, *Icarus*, **148**, 118
- Vokrouhlický, D., Nesvorný, D., & Botke, W. F. 2003, *Nature*, **425**, 147
- Vokrouhlický, D., Brož, M., Botke, W., Nesvorný, D., & Morbidelli, A. 2006, *Icarus*, **182**, 118
- Vokrouhlický, D., Botke, W. F., Chesley, S. R., Scheeres, D. J., & Statler, T. S. 2015, *Asteroids IV*, eds. P. Michel, F. E. DeMeo, & W. F. Botke (Tucson: University of Arizona Press), 509
- Zegmott, T. J., Lowry, S., Rožek, A., et al. 2021, *MNRAS*, **507**, 4914
- Zhou, W.-H., Zhang, Y., Yan, X., & Michel, P. 2022, *A&A*, **668**, A70

Part IV

CONCLUSION AND PROSPECTS

CONCLUSIONS AND PROSPECTS

CONCLUSIONS The Yarkovsky and YORP effects play a crucial role in the long-term evolution of asteroids. Studying how these forces shape the asteroid belt provides valuable insights into the history of the Solar System.

This thesis focuses on the long-term orbital and rotational evolution of main belt asteroids by addressing key challenges in Yarkovsky and YORP research, while integrating the latest observational data.

- Yarkovsky effect and orbital evolution. I present the first comprehensive study of the Yarkovsky effect on binary asteroids, introducing the concept of the “Binary Yarkovsky effect” and establishing its theoretical framework. I identify its principles, derive analytical formulas, and explore its implications for the long-term orbital evolution of binary asteroids.
- YORP effect and rotational evolution. I provide the first explanation for the spin rate distribution of slow rotators using a modified YORP theory. Additionally, I develop semi-analytical and numerical methods to study the crater-induced YORP effect, offering a potential solution to the stochastic behavior of asteroid rotation and orbital evolution.

PROSPECTS A thorough understanding of orbital and rotational evolution requires a combination of observational data and theoretical models.

Upcoming missions, including Gaia and the LSST, will usher in a golden age for asteroid and Solar System studies (Prusti et al., 2016; Ivezić et al., 2019). Gaia’s precise astrometric measurements will refine orbital parameters and reveal the rotational states of known asteroids. Gaia Data Release 4 (DR4) in 2026 will include detailed astrometry for over 150,000 objects, vastly expanding our knowledge of asteroid rotation (compared to 10,000 currently). Approximately 200,000 asteroids will have highly accurate orbital determinations, with precisions in the range of 10-100 meters, providing unparalleled opportunities to measure the Yarkovsky and YORP effects. Notably, Gaia has already obtained visible-wavelength spectra for 60,000 asteroids (compared to 3,000 before Gaia), greatly enhancing the study of asteroid compositions. The Legacy Survey of Space and Time (LSST), beginning in late 2025, will capture over 6 million main belt asteroids during its decade-long operation, increasing data collection by an order of magnitude.

Regarding Yarkovsky and YORP theory, while their mechanisms for single objects are largely understood, their effects on binary asteroids and collisional families remain largely unexplored.

The theory for binary asteroids is still developing, and several key questions remain, such as: (1) How can we derive a more general analytical solution that accounts for non-zero eccentricity and inclination? (2) What impact do different shapes have on the effect? (3) How does non-principal axis rotation influence the binary Yarkovsky effect? In terms of practical applications, further investigation is needed into: (1) How does the binary Yarkovsky effect interact with tides and BYORP in binary systems? (2) Could this theory be extended to artificial satellites, space debris, or planetary rings? Addressing these questions will require both analytical and numerical approaches.

In asteroid families, the YORP and Yarkovsky effects are complicated by their interaction with collisions. How do these effects influence the orbital evolution of asteroid families, which extends to the identification of asteroid families using the "V"-shape method, and how do they affect the age estimation of families? A comprehensive rotational evolution model, integrating the frameworks developed in Chapters 5 and 6, is needed to explore these complex interactions.

The YORP effect on tumbling asteroids remains challenging to analyze using both numerical and analytical methods. However, it may become more understandable through the framework presented in Chapter 4, especially as more slow rotators are identified as tumblers based on additional lightcurve data. The current inconsistency between the observed and theoretically predicted sign of the YORP torque could also be clarified by deriving the angular acceleration of slow rotators from long-term, high-quality observational data.

BIBLIOGRAPHY

- Avdellidou, Chrysa, Marco Delbo', David Nesvorný, Kevin J. Walsh, and Alessandro Morbidelli (Apr. 2024). "Dating the Solar System's giant planet orbital instability using enstatite meteorites." In: *Science* 384.6693, pp. 348–352. DOI: 10.1126/science.adg8092.
- Binzel, Richard P., Andrew S. Rivkin, J. Scott Stuart, Alan W. Harris, Schelte J. Bus, and Thomas H. Burbine (Aug. 2004). "Observed spectral properties of near-Earth objects: results for population distribution, source regions, and space weathering processes." In: *Icarus* 170.2, pp. 259–294. DOI: 10.1016/j.icarus.2004.04.004.
- Birnstiel, T., C. P. Dullemond, and F. Brauer (Apr. 2010). "Gas- and dust evolution in protoplanetary disks." In: *Astronomy & Astrophysics* 513, A79, A79. DOI: 10.1051/0004-6361/200913731. arXiv: 1002.0335 [astro-ph.EP].
- Bottke Jr, William F, David Vokrouhlický, David P Rubincam, and David Nesvorný (2006). "The Yarkovsky and YORP effects: Implications for asteroid dynamics." In: *Annu. Rev. Earth Planet. Sci.* 34, pp. 157–191.
- Bottke, W. F. et al. (July 2020). "Interpreting the Cratering Histories of Bennu, Ryugu, and Other Spacecraft-explored Asteroids." In: *The Astronomical Journal* 160.1, 14, p. 14. DOI: 10.3847/1538-3881/ab88d3.
- Bottke, William F., Daniel D. Durda, David Nesvorný, Robert Jedicke, Alessandro Morbidelli, David Vokrouhlický, and Hal Levison (May 2005). "The fossilized size distribution of the main asteroid belt." In: *Icarus* 175.1, pp. 111–140. DOI: 10.1016/j.icarus.2004.10.026.
- Bottke, William F., David Vokrouhlický, Miroslav Broz, David Nesvorný, and Alessandro Morbidelli (Nov. 2001). "Dynamical Spreading of Asteroid Families by the Yarkovsky Effect." In: *Science* 294.5547, pp. 1693–1696. DOI: 10.1126/science.1066760.
- Bottke, William F, David Vokrouhlický, Kevin J Walsh, Marco Delbo, Patrick Michel, Dante S Lauretta, Humberto Campins, Harold C Connolly Jr, Daniel J Scheeres, and Steven R Chelsey (2015). "In search of the source of asteroid (101955) Bennu: applications of the stochastic YORP model." In: *Icarus* 247, pp. 191–217.
- Brauer, F., C. P. Dullemond, and Th. Henning (Mar. 2008). "Coagulation, fragmentation and radial motion of solid particles in protoplanetary disks." In: *Astronomy & Astrophysics* 480.3, pp. 859–877. DOI: 10.1051/0004-6361:20077759. arXiv: 0711.2192 [astro-ph].

- Breiter, S, P Bartczak, M Czekaj, B Oczujda, and D Vokrouhlický (2009). "The YORP effect on 25 143 Itokawa." In: *Astronomy & Astrophysics* 507.2, pp. 1073–1081.
- Breiter, S, H Michalska, D Vokrouhlický, and W Borczyk (2007). "Radiation-induced torques on spheroids." In: *Astronomy & Astrophysics* 471.1, pp. 345–353.
- Breiter, S. and M. Murawiecka (May 2015). "Tumbling asteroid rotation with the YORP torque and inelastic energy dissipation." In: *Monthly Notices of the Royal Astronomical Society* 449.3, pp. 2489–2497. DOI: 10.1093/mnras/stv433.
- Čapek, D and D Vokrouhlický (2004). "The YORP effect with finite thermal conductivity." In: *Icarus* 172.2, pp. 526–536.
- Cheng, Andrew F. (June 2004). "Collisional evolution of the asteroid belt." In: *Icarus* 169.2, pp. 357–372. DOI: 10.1016/j.icarus.2004.02.002.
- Chesley, Steven R., Steven J. Ostro, David Vokrouhlický, David Čapek, Jon D. Giorgini, Michael C. Nolan, Jean-Luc Margot, Alice A. Hine, Lance A. M. Benner, and Alan B. Chamberlin (Dec. 2003). "Direct Detection of the Yarkovsky Effect by Radar Ranging to Asteroid 6489 Golevka." In: *Science* 302.5651, pp. 1739–1742. DOI: 10.1126/science.1091452.
- DeMeo, F. E. and B. Carry (Jan. 2014). "Solar System evolution from compositional mapping of the asteroid belt." In: *Nature* 505.7485, pp. 629–634. DOI: 10.1038/nature12908. arXiv: 1408.2787 [astro-ph.EP].
- Deienno, Rogerio, Kevin J. Walsh, Katherine A. Kretke, and Harold F. Levison (May 2019). "Energy Dissipation in Large Collisions—No Change in Planet Formation Outcomes." In: *The Astrophysical Journal* 876.2, 103, p. 103. DOI: 10.3847/1538-4357/ab16e1.
- Delbo', Marco, Kevin Walsh, Bryce Bolin, Chrysa Avdellidou, and Alessandro Morbidelli (Sept. 2017). "Identification of a primordial asteroid family constrains the original planetesimal population." In: *Science* 357.6355, pp. 1026–1029. DOI: 10.1126/science.aam6036.
- Dohnanyi, J. S. (May 1969). "Collisional Model of Asteroids and Their Debris." In: *Journal of Geophysical Research* 74, pp. 2531–2554. DOI: 10.1029/JB074i010p02531.
- Farinella, Paolo and David Vokrouhlický (Dec. 1996). "Thermal force effects on slowly rotating, spherical artificial satellites - I. Solar heating." In: *Planetary and Space Science* 44.12, pp. 1551–1561. DOI: 10.1016/S0032-0633(96)00073-6.
- Farinella, Paolo, David Vokrouhlický, and William K. Hartmann (Apr. 1998). "Meteorite Delivery via Yarkovsky Orbital Drift." In: *Icarus* 132.2, pp. 378–387. DOI: 10.1006/icar.1997.5872.
- Golubov, Oleksiy and Yuriy N Krugly (2012). "Tangential component of the YORP effect." In: *The Astrophysical Journal Letters* 752.1, p. L11.

- Golubov, Oleksiy and Veronika Lipatova (2022). "Analytic theory for the tangential YORP produced by the asteroid regolith." In: *Astronomy & Astrophysics* 666, A146.
- Hanuš, Josef, J Ďurech, M Brož, A Marciniak, BD Warner, F Pilcher, R Stephens, R Behrend, Benoît Carry, D Čapek, et al. (2013). "Asteroids' physical models from combined dense and sparse photometry and scaling of the YORP effect by the observed obliquity distribution." In: *Astronomy & Astrophysics* 551, A67.
- Heinze, A. N., Joseph Trollo, and Stanimir Metchev (Dec. 2019). "The Flux Distribution and Sky Density of 25th Magnitude Main Belt Asteroids." In: *The Astronomical Journal* 158.6, 232, p. 232. DOI: 10.3847/1538-3881/ab48fa. arXiv: 1910.13015 [astro-ph.EP].
- Hu, Shoucun, Derek C. Richardson, Yun Zhang, and Jianghui Ji (Apr. 2021). "Critical spin periods of sub-km-sized cohesive rubble-pile asteroids: dependences on material parameters." In: *Monthly Notices of the Royal Astronomical Society* 502.4, pp. 5277–5291. DOI: 10.1093/mnras/stab412. arXiv: 2009.12605 [astro-ph.EP].
- Ivezić, Željko, Steven M Kahn, J Anthony Tyson, Bob Abel, Emily Acosta, Robyn Allsman, David Alonso, Yusra AlSayyad, Scott F Anderson, John Andrew, et al. (2019). "LSST: from science drivers to reference design and anticipated data products." In: *The Astrophysical Journal* 873.2, p. 111.
- Izidoro, Andre, Rajdeep Dasgupta, Sean N. Raymond, Rogerio Deienno, Bertram Bitsch, and Andrea Isella (Mar. 2022). "Planetsimal rings as the cause of the Solar System's planetary architecture." In: *Nature Astronomy* 6, pp. 357–366. DOI: 10.1038/s41550-021-01557-z. arXiv: 2112.15558 [astro-ph.EP].
- Johansen, Anders, Mordecai-Mark Mac Low, Pedro Lacerda, and Martin Bizzarro (Apr. 2015). "Growth of asteroids, planetary embryos, and Kuiper belt objects by chondrule accretion." In: *Science Advances* 1, 1500109, p. 1500109. DOI: 10.1126/sciadv.1500109. arXiv: 1503.07347 [astro-ph.EP].
- Keller, H. U. et al. (Jan. 2010). "E-Type Asteroid (2867) Steins as Imaged by OSIRIS on Board Rosetta." In: *Science* 327.5962, p. 190. DOI: 10.1126/science.1179559.
- Krasinsky, G. A., E. V. Pitjeva, M. V. Vasilyev, and E. I. Yagudina (July 2002). "Hidden Mass in the Asteroid Belt." In: *Icarus* 158.1, pp. 98–105. DOI: 10.1006/icar.2002.6837.
- Kuchynka, Petr and William M. Folkner (Jan. 2013). "A new approach to determining asteroid masses from planetary range measurements." In: *Icarus* 222.1, pp. 243–253. DOI: 10.1016/j.icarus.2012.11.003.
- Lowry, Stephen C, Alan Fitzsimmons, Petr Pravec, David Vokrouhlicky, Hermann Boehnhardt, Patrick A Taylor, Jean-Luc Margot, Adrian Galád, Mike Irwin, Jonathan Irwin, et al. (2007). "Direct

- detection of the asteroidal YORP effect." In: *science* 316.5822, pp. 272–274.
- Mahlke, M., B. Carry, and P. A. Mattei (Sept. 2022). "Asteroid taxonomy from cluster analysis of spectrometry and albedo." In: *Astronomy & Astrophysics* 665, A26, A26. DOI: 10.1051/0004-6361/202243587. arXiv: 2203.11229 [astro-ph.EP].
- Métris, Gilles, David Vokrouhlický, John C. Ries, and Richard J. Eanes (Feb. 1997). "Nongravitational effects and the LAGEOS eccentricity excitations." In: *Journal of Geophysical Research* 102.B2, pp. 2711–2730. DOI: 10.1029/96JB03186.
- Milani, Andrea, Anna Maria Nobili, and Paolo Farinella (1987). *Non-gravitational perturbations and satellite geodesy*.
- Morbidelli, A., M. Lambrechts, S. Jacobson, and B. Bitsch (Sept. 2015). "The great dichotomy of the Solar System: Small terrestrial embryos and massive giant planet cores." In: *Icarus* 258, pp. 418–429. DOI: 10.1016/j.icarus.2015.06.003. arXiv: 1506.01666 [astro-ph.EP].
- Morbidelli, A. and D. Vokrouhlický (May 2003). "The Yarkovsky-driven origin of near-Earth asteroids." In: *Icarus* 163.1, pp. 120–134. DOI: 10.1016/S0019-1035(03)00047-2.
- Morbidelli, Alessandro, William F. Bottke, David Nesvorný, and Harold F. Levison (Dec. 2009). "Asteroids were born big." In: *Icarus* 204.2, pp. 558–573. DOI: 10.1016/j.icarus.2009.07.011. arXiv: 0907.2512 [astro-ph.EP].
- Pravec, Petr and Alan W. Harris (Nov. 2000). "Fast and Slow Rotation of Asteroids." In: *Icarus* 148.1, pp. 12–20. DOI: 10.1006/icar.2000.6482.
- Pravec, Petr, Alan W. Harris, P. Scheirich, P. Kušnirák, L. Šarounová, Cark W. Hergenrother, Stefano Mottola, MD Hicks, Gianluca Masi, Yu N. Krugly, et al. (2005). "Tumbling asteroids." In: *Icarus* 173.1, pp. 108–131.
- Prusti, Timo, JHJ De Bruijne, Anthony GA Brown, Antonella Valenari, C Babusiaux, CAL Bailer-Jones, U Bastian, M Biermann, Dafydd Wyn Evans, L Eyer, et al. (2016). "The gaia mission." In: *Astronomy & astrophysics* 595, A1.
- Raymond, S. N., E. Kokubo, A. Morbidelli, R. Morishima, and K. J. Walsh (Jan. 2014). "Terrestrial Planet Formation at Home and Abroad." In: *Protostars and Planets VI*. Ed. by Henrik Beuther, Ralf S. Klessen, Cornelis P. Dullemond, and Thomas Henning, pp. 595–618. DOI: 10.2458/azu_uapress_9780816531240-ch026. arXiv: 1312.1689 [astro-ph.EP].
- Rubincam, D. P. (Apr. 1982). "On the secular decrease in the semimajor axis of LAGEOS's orbit." In: *Celestial Mechanics* 26.4, pp. 361–382. DOI: 10.1007/BF01230417.
- Rubincam, David Parry (2000). "Radiative spin-up and spin-down of small asteroids." In: *Icarus* 148.1, pp. 2–11.

- Rubincam, David Parry (Oct. 2006). "Saturn's rings, the Yarkovsky effects, and the Ring of Fire." In: *Icarus* 184.2, pp. 532–542. DOI: 10.1016/j.icarus.2006.05.017.
- Rubincam, David Parry (Sept. 2014). "The thermal expansion of particles and their secular orbital evolution as they circle a planet." In: *Icarus* 239, pp. 96–104. DOI: 10.1016/j.icarus.2014.05.025.
- Somenzi, L., A. Fienga, J. Laskar, and P. Kuchynka (Apr. 2010). "Determination of asteroid masses from their close encounters with Mars." In: *Planetary and Space Science* 58.5, pp. 858–863. DOI: 10.1016/j.pss.2010.01.010.
- Statler, Thomas S. (Aug. 2009). "Extreme sensitivity of the YORP effect to small-scale topography." In: *Icarus* 202.2, pp. 502–513. DOI: 10.1016/j.icarus.2009.03.003. arXiv: 0903.1119 [astro-ph.EP].
- Taylor, Patrick A, Jean-Luc Margot, David Vokrouhlicky, Daniel J Scheeres, Petr Pravec, Stephen C Lowry, Alan Fitzsimmons, Michael C Nolan, Steven J Ostro, Lance AM Benner, et al. (2007). "Spin rate of asteroid (54509) 2000 PH5 increasing due to the YORP effect." In: *Science* 316.5822, pp. 274–277.
- Tholen, David James (Sept. 1984). "Asteroid Taxonomy from Cluster Analysis of Photometry." PhD thesis. University of Arizona.
- Vokrouhlický, D., S. Breiter, D. Nesvorný, and W. F. Bottke (Nov. 2007a). "Generalized YORP evolution: Onset of tumbling and new asymptotic states." In: *Icarus* 191.2, pp. 636–650. DOI: 10.1016/j.icarus.2007.06.002.
- Vokrouhlický, D, M Brož, WF Bottke, D Nesvorný, and A Morbidelli (2006). "Yarkovsky/YORP chronology of asteroid families." In: *Icarus* 182.1, pp. 118–142.
- Vokrouhlický, D., D. Nesvorný, L. Dones, and W. F. Bottke (Aug. 2007b). "Thermal forces on planetary ring particles: application to the main system of Saturn." In: *Astronomy & Astrophysics* 471.2, pp. 717–730. DOI: 10.1051/0004-6361:20067029.
- Vokrouhlický, D., D. Čapek, S. R. Chesley, and S. J. Ostro (Dec. 2005). "Yarkovsky detection opportunities. II. Binary systems." In: *Icarus* 179.1, pp. 128–138. DOI: 10.1016/j.icarus.2005.06.003.
- Vokrouhlicky, David, William F Bottke, Steven R Chesley, Daniel J Scheeres, and Thomas S Statler (2015). "The Yarkovsky and YORP effects." In: *arXiv preprint arXiv:1502.01249*.
- Vokrouhlický, David and D Čapek (2002). "YORP-induced long-term evolution of the spin state of small asteroids and meteoroids: Rubincam's approximation." In: *Icarus* 159.2, pp. 449–467.
- Vokrouhlický, David, Davide Farnocchia, David Čapek, Steven R. Chesley, Petr Pravec, Petr Scheirich, and Thomas G. Müller (May 2015). "The Yarkovsky effect for 99942 Apophis." In: *Icarus* 252, pp. 277–283. DOI: 10.1016/j.icarus.2015.01.011.

- Vokrouhlický, David, David Nesvorný, and William F Bottke (2003). "The vector alignments of asteroid spins by thermal torques." In: *Nature* 425.6954, pp. 147–151.
- Walsh, Kevin J., Marco Delbo', Michael Mueller, Richard P. Binzel, and Francesca E. DeMeo (Apr. 2012). "Physical Characterization and Origin of Binary Near-Earth Asteroid (175706) 1996 FG₃." In: *The Astrophysical Journal* 748.2, 104, p. 104. DOI: 10.1088/0004-637X/748/2/104. arXiv: 1203.4820 [astro-ph.EP].
- Walsh, Kevin J., Alessandro Morbidelli, Sean N. Raymond, David P. O'Brien, and Avi M. Mandell (July 2011). "A low mass for Mars from Jupiter's early gas-driven migration." In: *Nature* 475.7355, pp. 206–209. DOI: 10.1038/nature10201. arXiv: 1201.5177 [astro-ph.EP].
- Walsh, Kevin J., Derek C. Richardson, and Patrick Michel (July 2008). "Rotational breakup as the origin of small binary asteroids." In: *Nature* 454.7201, pp. 188–191. DOI: 10.1038/nature07078.
- Windmark, F., T. Birnstiel, C. W. Ormel, and C. P. Dullemond (Aug. 2012). "Breaking through: The effects of a velocity distribution on barriers to dust growth." In: *Astronomy & Astrophysics* 544, L16, p. L16. DOI: 10.1051/0004-6361/201220004. arXiv: 1208.0304 [astro-ph.EP].
- Wyatt, M. C., C. J. Clarke, and M. Booth (Oct. 2011). "Debris disk size distributions: steady state collisional evolution with Poynting-Robertson drag and other loss processes." In: *Celestial Mechanics and Dynamical Astronomy* 111.1-2, pp. 1–28. DOI: 10.1007/s10569-011-9345-3. arXiv: 1103.5499 [astro-ph.EP].
- Youdin, Andrew N. and Jeremy Goodman (Feb. 2005). "Streaming Instabilities in Protoplanetary Disks." In: *The Astrophysical Journal* 620.1, pp. 459–469. DOI: 10.1086/426895. arXiv: astro-ph/0409263 [astro-ph].
- Zsom, A., C. W. Ormel, C. Güttler, J. Blum, and C. P. Dullemond (Apr. 2010). "The outcome of protoplanetary dust growth: pebbles, boulders, or planetesimals? II. Introducing the bouncing barrier." In: *Astronomy & Astrophysics* 513, A57, A57. DOI: 10.1051/0004-6361/200912976. arXiv: 1001.0488 [astro-ph.EP].
- Đurech, J. and J. Hanuš (July 2023). "Reconstruction of asteroid spin states from Gaia DR3 photometry." In: *Astronomy & Astrophysics* 675, A24, A24. DOI: 10.1051/0004-6361/202345889. arXiv: 2305.10798 [astro-ph.EP].
- Đurech, J. et al. (Feb. 2024). "Secular change in the spin states of asteroids due to radiation and gravitation torques. New detections and updates of the YORP effect." In: *Astronomy & Astrophysics* 682, A93, A93. DOI: 10.1051/0004-6361/202348350. arXiv: 2312.05157 [astro-ph.EP].

